Evaluation of paper substrates for microfluidic application in medical diagnostic kits

by

REVESA S MOODLEY

Submitted in fulfilment of the academic requirements of

Master of Science

in Engineering

Discipline of Chemical Engineering

College of Agriculture, Engineering and Science

University of KwaZulu-Natal

Durban

South Africa

8 February 2018

Supervisor: Prof. Bruce Sithole

Co-supervisor: Dr. Kevin Land, CSIR

Co-supervisor: Mr. Jerome Andrew, CSIR

Co-supervisor: Prof. Werner van Zyl

PREFACE

The research contained in this dissertation was completed by the candidate while based in the Discipline of Chemical Engineering, School of Engineering within the College of Agriculture, Engineering and Science, University of KwaZulu-Natal, Howard College, South Africa. The work was carried out at the Council for Scientific and Industrial Research (CSIR) in Durban, based within the Biorefinery Industry Development Facility (BIDF). The research was financially supported by the National Research Foundation.

The contents of this work have not been submitted in any form to another university and, except where the work of others is acknowledged in the text, the results reported are due to investigations by the candidate.

Signed: R. S. Moodley

As the candidate's supervisor, I agree to the submission of this dissertation.

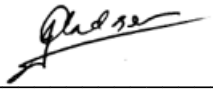

Signed: Prof. Bruce Sithole Signed: Dr. Kevin Land Signed: Mr. Jerome Andrew

Signed: Prof. Werner van Zyl

DECLARATION 1: PLAGIARISM

I, Revesa Sadasivan Moodley, declare that:

(i) the research reported in this dissertation, except where otherwise indicated or acknowledged, is my original work;

(ii) this dissertation has not been submitted in full or in part for any degree or examination to any other university;

(iii) this dissertation does not contain other persons' data, pictures, graphs or other information, unless specifically acknowledged as being sourced from other persons;

(iv) this dissertation does not contain other persons' writing, unless specifically acknowledged as being sourced from other researchers. Where other written sources have been quoted, then:

a) their words have been re-written but the general information attributed to them has been referenced;

b) where their exact words have been used, their writing has been placed inside quotation marks, and referenced;

(v) where I have used material for which publications followed, I have indicated in detail my role in the work;

(vi) this dissertation is primarily a collection of material, prepared by myself, published as journal articles or presented as a poster and oral presentations at conferences. In some cases, additional material has been included;

(vii) this dissertation does not contain text, graphics or tables copied and pasted from the Internet, unless specifically acknowledged, and the source being detailed in the dissertation and in the References sections.

Signed: R.S. Moodley

Date: 08/02/2018

ABSTRACT

Recent studies in the biomedical field have shown the use of paper in microfluidic analytical devices. However, no studies have been undertaken to ascertain what type(s) of paper substrates are ideal for such microfluidic applications. Hence, this study was conducted to determine the feasibility of using different paper substrates for implementation in microfluidic analytical devices, specifically in the South African context, compared to currently used materials such as glass and silicone. In addition, fibres in paper substrates were substituted with nanofibrillated cellulose (NFC) fibres to ascertain the impact of NFC on the microfluidics of the paper substrates. The wicking rate of the substrates was the focus of the study, with high -resolution field emission gun-scanning electron microscopy and contact angle tests being used to support the results obtained. Solid wax printing was also conducted to determine whether the paper substrates were suited to fabrication for microfluidic applications.

High-resolution morphological studies of the paper substrates showed that pore sizes of the pulp fibres were in the order sulphite> bleached kraft > unbleached kraft > Whatman No. 1 Chromatography Filter Paper > Whatman 3MM Chromatography Filter Paper > thermo-mechanical > recycled. It was concluded that the larger pore size of fibres correlated with faster wicking rates of the relevant paper substrates. The substitution of pulp fibres with NFC led to reduced pore size of the fibres thus leading to reduced wicking rates due to the presence of the small NFC particles.

Contact angle is directly linked to the hydrophobicity of the substrate and is indicative of the resistance to absorption of a liquid. The results revealed that all the paper substrates were hydrophilic. However, the hydrophilicity of two of the substrates (sheets substituted with 100% NFC unbleached kraft pulp and 100% NFC recycled pulp) were higher than those of the other substrates indicating that, although these substrates were still hydrophilic in nature, their absorption of aqueous liquid would take longer periods of time.

The results showed that Whatman glass microfiber GF/D filter paper was the fastest wicking substrate, using both dye and blood simulant as wicking liquids. Similarly, paper substrates made with recycled fibres exhibited the slowest wicking rates when using both wicking liquids. These results can be used when determining which of the substrates to use for paper-based microfluidic device (µPAD) application, whereby the desired detection time would be

the factor used to establish which of the substrates to use. Comparison of vertical and horizontal tests showed varying results. In theory, the horizontal wicking test should result in a faster wicking rate than the vertical test, taking hydrostatic pressure into consideration. The majority of the substrates showed that the horizontal wicking rate was faster when using the dye solution, whereas vertical wicking was faster when using the blood simulant. Discrepancies between the results obtained from the dye and blood simulant experiments could be attributed to the additional viscosity drag when using the higher viscosity liquid (blood simulant), as well as possible capillarity differences of the samples. The results were used in conjunction with the morphological studies, whereby the pore size was correlated with the wicking rate.

The solid wax printing test revealed that, in general, the substrates were not well suited to the fabrication method. The results showed that the wax was not able to penetrate through the depth of the sheet, hence allowing for the possibility of leakage of liquid from the channels. Two of the substrates (Whatman No. 1 Chromatography filter paper and paper made from sulphite pulp fibres containing 20% nanofibrillated cellulose) exhibited 100% wax penetration and could be considered for µPAD application. However, for paper substrates that do not meet requirements for µPAD applications, their pulp fibres could be chemically modified to induce hydrophobicity thus altering the microfluidic characteristics of the paper substrates.

ACKNOWLEDGEMENTS

"Purity, patience and perseverance are the three essentials to success, and, above all, love." – *Swami Vivekananda*

First and foremost, I would like to thank God, without who this would not have been possible. Thank You for giving me the wisdom, guidance and strength to complete this thesis.

I'd like to express my sincere gratitude to the following people for their contribution through this study:

- My supervisors, Prof. B. Sithole, Dr. K. Land, and Mr. J. Andrew for their support and guidance throughout the study. At times when I wanted to give up, you have motivated me, which I will always be grateful for.
- K. Krishna of CSIR Information Services, who helped in conducting literature searches for my thesis
- A. Mtibe of CSIR Port Elizabeth, who assisted in conducting Super mass Colloider experiments to prepare nanofibrillated cellulose from pulp samples
- S. Kumar of CSIR Pretoria, who conducted solid wax printing experiments on substrates
- Dr. P. Lekha of CSIR Durban, for conducting FEG-SEM analyses on substrates
- A. Adeniyi of Tshwane University of Technology for conducting the contact angle experiments

Sincere appreciation must be given to Mondi Merebank for provision of TMP and Recycled pulp samples.

I would like to acknowledge the CSIR-Department of Science and Technology for their financial assistance throughout the project.

To my fellow postgraduate students at CSIR: We have been through many tough and frustrating times together, but we have always made it out smiling. Thank you for your friendship, motivation and laughs.

To my friends and family, of which there are too many to mention: Thank you all for your love and support you have shown me throughout the writing of this thesis. I am truly blessed to have you in my life.

Finally, to my parents, Sada and Kisty, and my sister, Kim: Thank you for the amazing support that you have given me throughout my studies. I know there have been many days where I have wanted to give up, but you have constantly motivated me and provided much needed love and laughter in times of need. I love you all.

TABLE OF CONTENTS

Page

LIST OF TABLES

LIST OF FIGURES

Figure **Page**

ABBREVIATIONS

µPAD	Microfluidic paper-based analytical device
AKD	Alkyl ketene dimer
ALP	Alkaline phosphate
AST	Aspartate aminotransferase
BK	Bleached kraft
CA	Contact angle
CHR	Whatman No. 1 Chromatography filter paper
CHR3	Whatman 3MM Chromatography filter paper
FEG-SEM	Field emission gun-scanning electron microscopy
GM	Whatman glass microfiber GF/D filter paper
Hb	Haemoglobin
LFA	Lateral flow assay
NC	Nitrocellulose
NFC	Nanofibrillated Cellulose
PDMS	Polydimethylsiloxane
PM	Particulate matter
POC	Point-of-care
PVA	Poly (Vinyl Alcohol)
REC	Recycled
SULP	Sulphite
TMP	Thermo-mechanical
UBK	Unbleached kraft
UV	Ultraviolet

CHAPTER 1: INTRODUCTION

1.1 Background

Millions of people worldwide die from preventable diseases each year. Accurate diagnosis is of utmost importance for proper and effective treatment of diseases. However, diagnostic technologies that are produced currently are not well suited to developing countries, such as South Africa. This is due to the high costs as well as the need for trained personnel for correct diagnosis. Despite increasing urbanisation, it is still reported that approximately 55% of inhabitants in developing countries still live in rural areas, making it necessary for cheaper alternatives in diagnostic healthcare to be established (International Fund for Agricultural Development, 2011). Through the introduction of microfluidic paper-based analytical devices (µPAD), developing countries can eliminate these concerns on the medical diagnostic front.

Microfluidic devices have shown high potential in point-of-care (POC) diagnostics due to its compact size, minimal consumption of reagents and minimal generation of waste. Materials of construction for these devices consisted of silica and glass, but later expanded to various other composite materials (Whitesides, 2006). In 2007, paper was introduced to microfluidic devices by Whitesides and his team. Paper was considered a suitable material for three main reasons: (i) paper is widely available (ii) its ability to wick aqueous fluids and (iii) knowledge on paper analytical techniques is extensive and can be applied. Microfluidic paper-based analytical devices, or µPADs, are diagnostic devices produced by creating hydrophobic barriers in the hydrophilic paper, resulting in channels for wicking of aqueous fluids. These devices need to follow the ASSURED strategy of being: affordable, sensitive, specific, user-friendly, rapid and robust, equipment-free and deliverable to end-users, as stipulated by the World Health Organisation.

Academic research on µPADs has been on the increase. However, distribution of these devices in real world settings has not been as successful. Research on applications of µPADs has rapidly expanded since its inception in 2007. Applications range from medical to pharmaceutical to environmental. Besides having a large focus in the medical field, recently there have been a number of studies focusing on using µPADs in detecting contaminants in air and bodies of water.

1.2 Problem Statement

Statistics show that an estimated 43.7% of South Africa's population live in rural areas (Goede & Versteeg, 2011). With such a high population living in rural areas, concerns of accessibility to health care services are revealed. Issues such as finances and transportation create a barrier to proper diagnosis and treatment of illnesses (Goede & Versteeg, 2011).

Current diagnostic technologies, such as laboratory blood tests, are expensive and lengthy. In addition, many of these technologies are used under the supervision of trained professionals, of which there are not many.

1.3 Purpose of Study and Research Objectives

There have been various studies conducted over the decade on µPADs, mainly focussing on applications and modifications of the device to improve its user-friendliness. However, there has been minimal studies which investigated the materials of construction of the µPADs to determine which materials pose the optimal transportation properties for fluids being tested.
In this respect, the research conducted for this study aims to evaluate paper substrates in order to determine its feasibility for use in µPADs for medical applications. In order to determine this, the wicking ability of the paper substrates was tested, which showed the rate at which the fluid was absorbed through each substrate. Properties affecting the wicking ability of the substrate were investigated. Field emission gun-scanning electron microscopy and contact angle tests were conducted to determine the pore size within the substrate sheets and the wettability of the sheet, respectively. Lastly, solid wax printing was conducted to investigate whether the substrates were well suited to this fabrication method for µPAD application. Paper substrates were prepared from pulp samples (either base samples or nanofibrillated pulp samples). The nanofibrillated sheets were used to investigate the effect of smaller pore size on the wicking ability of a substrate.

1.4 Research Questions

A. What paper substrates show suitable fluid transport properties for use in microfluidic applications?
B. How does the addition of nanofibrillated pulp affect the wicking ability of substrates?
C. Are these substrates well suited to µPAD fabrication techniques, more specifically solid wax printing?

1.5 Significance of Study

Considering that this research has not been conducted before, results from this study are an important addition to the database of possible materials to use for µPAD fabrication. The overall expectation is that this work would be implemented in South Africa and in other developing countries, for development of cheaper alternative diagnostic technologies in the medical diagnostics field.

1.6 Format of Dissertation

This dissertation has 8 chapters with 5 appendices. Each chapter and appendix has an introduction, body and conclusion.

Chapter 1 gives an introduction to the research topic investigated. The chapter gives the background to the study, the research questions, protocol and significance of the study.

Chapter 2 provides the reader with an understanding of microfluidic devices, in terms of its operation, fabrication, materials of construction, application and limitations. Previous studies conducted on paper-based microfluidics are highlighted in this chapter.

Chapter 3 gives information on the equipment used and research methodology followed when conducting this study. Appendix A supports this chapter by providing an overview of the major pieces of equipment used.

Chapters 4, 5, 6 and 7 focus on the results obtained from the experimentation and provide a discussion on each of the results. Chapter 4 gives an analysis of the FEG-SEM results

obtained from FEG-SEM. Chapter 5 provides an investigation of the contact angle test results. Chapter 6 is a discussion of the wicking test results, where the transport properties of each substrate were studied. Chapter 7 focused on the solid wax printing results, which assisted to determine the suitability of the substrates for µPAD manufacture.

Lastly, Chapter 8 summarises the findings from the study and links it back to the research questions and objectives of the study. Recommendations are also provided to improve the study for future research in the field.

CHAPTER 2: LITERATURE REVIEW

2.1 Introduction

Healthcare in developing countries has been a cause for concern due to the high costs involved in diagnosing and treating diseases in rural areas. Millions of people worldwide die from preventable diseases each year. Accurate diagnosis is of utmost importance for proper and effective treatment of diseases. However, diagnostic technologies are often unsuitable in developing countries due to high costs as well as the need for trained personnel required for correct diagnosis. Paper has been introduced to medical diagnostics as a simple and low-cost alternative to existing diagnostic technologies. Creation of paper-based microfluidic devices occurs through the patterning of the paper into microfluidic hydrophilic channels and hydrophobic barriers, which allows the transportation of liquids in a controlled manner. Paper was considered an appropriate substrate for application in microfluidic systems due to (i) its wide availability; (ii) knowledge on paper analytical techniques is extensive and can be applied; and (iii) its ability to wick aqueous fluids without the need for external forces.

This chapter gives an overview of µPADs, highlighting the history of research conducted as well as the relevant information necessary in understanding the operation of these microfluidic devices.

This chapter is split up into seven subsections, each providing background on microfluidic devices, its operation and more importantly, for this study, the substrates used in its manufacture. Section 2.2 highlights the operation and base substrates used in µPADs currently. Section 2.3 focuses on the fabrication techniques that have been used to date for µPADs. Section 2.4 looks at the fluid transport in microfluidic devices and the models used to describe the fluid flow in porous media. Section 2.5 gives an overview of the detection methods used in µPADs, while section 2.6 highlights applications and possible applications of these devices. Finally, sections 2.7 and 2.8 summarise the limitations and future perspectives of µPADs, respectively.

2.2 Microfluidic paper-based analytical devices

Microfluidics is the study of systems involving small volumes of fluids, that is 10^{-9} to 10^{-18} litres, transported in microchannels with dimensions of tens to hundreds of micrometers (Whitesides, 2006). Microfluidic devices are becoming increasingly popular due to its

analytical advantages such as: (i) small sample volumes, (ii) shorter analysis times compared to macro devices, (iii) easy handling of fluids, (iv) easy transportation and accurate control of fluids in the system and (v) ability to perform separations, reactions and other complex processes within a simple, low-cost device (Baker et al., 2009).

2.2.1 Principle of Operation

Microfluidic paper-based analytical devices (µPADs) are designed to transport aqueous fluid through patterning paper into hydrophilic capillary channels bounded by hydrophobic barriers. These channels can be open to the atmosphere or can alternatively be sealed to prevent leakage (Lisowski & Zarzycki, 2013). Patterning of paper can be done in numerous methods, discussed in 2.3.1, which determines the dimensions of width and length of the microfluidic channels. The height of the channels is controlled by the thickness of the paper substrate used for fabrication (Martinez et al., 2010). The hydrophilic cellulose fibres provide support for reagents, filtering samples or executing chromatographic separations (Martinez et al., 2010).

The principle of operation of µPADs involves the wicking of fluids along the hydrophilic channels to various detection zones containing specific reagents, which react with the sample fluid, as seen in Figure 2.1 (Martinez et al., 2010). The result of this reaction can be analysed to obtain information about the fluid, which is useful in diagnosis.

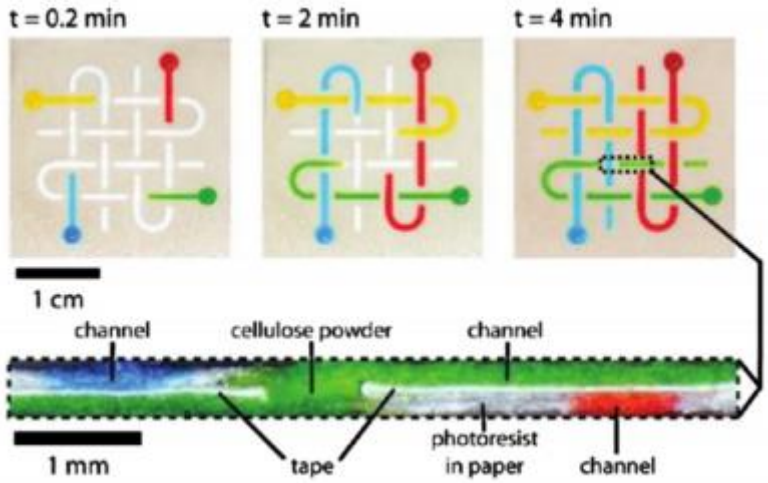

Figure 2.1 Typical µPAD showing the operation and fluid flow through the device (Martinez, et al., 2008)

2.2.2 Base Substrates

Before the introduction of microfluidics, microchannels were designed using glass or quartz used for applications in gas chromatography and capillary electrophoresis (Ren et al., 2013). Thereafter, microfluidics was conceptualised and the first known materials for production of microfluidic chips were silica or glass (Whitesides, 2006). A few years later, materials such as elastomers, plastics, hydrogels and other composite materials were introduced into fabrication of typical microfluidic devices (Ren et al., 2013). For a cheaper alternative, paper was also studied and found to be suitable for microfluidic applications for three main reasons: (i) paper is inexpensive and widely available, (ii) its ability to wick aqueous fluids without the use of external forces and (iii) knowledge on paper analytical techniques is extensive and can be applied in the field (Martinez et al., 2010). Other advantages of paper include: (i) it is thin, lightweight, available in various thicknesses and easy to transport and store, (ii) it can be used in a variety of applications due to it cellulose composition, which has chemical compatibility, (iii) it has the ability to be chemically modified to include other functional groups for binding with proteins, DNA and small molecules, (iv) it is suitable for colourimetric tests as it is normally white in colour, (v) it can be easily disposed of through incineration due to its high flammability, (vi) it is flexible and compatible with various fabrication techniques and (vii) the physical properties lends itself to µPAD production (Martinez et al., 2010; Ren et al., 2013; Yetisen et al., 2013).

For a certain grade of paper to be used as a suitable substrate for µPADs, numerous properties have to be considered. The surface area of the substrate is important as reagent deposition, reproducibility, sensitivity and specificity are dependent on it (Yetisen et al., 2013). The substrate should allow for fastgraph, capillary flow of fluids and penetration of hydrophobising agents throughout its depth. Paper thickness, together with porosity, plays a major role in the volume of fluid absorbed by the substrate. Another important factor to take into consideration with thickness is opacity, which determines the visibility of a signal produced by a reaction in the device for analysis. If the substrate is too thick, the signal from the reagent will not be seen by the end-user. For good colourimetric analysis on µPADs, paper substrates must be white and avoid discolouration, which can occur when stored for prolonged periods (Koivunen, 2014; Yetisen et al., 2013).

From previous studies, the most frequently used paper substrate is filter and chromatography paper, although other grades of paper have been investigated. A few common grades from previous research have been discussed.

2.2.2.1 Filter and chromatography paper

Filter paper is a semi-permeable barrier used for the separation of solids from liquids, allowing liquids to pass through its pores. Therefore, the paper must have a high porosity, controlled pore size distribution and pore connectivity for permeability of fluids, yet still be impermeable to solid material. The solid material is unable to pass through the pores in the paper, and form a layer on top of the paper, called filter cake. Filter paper has various applications, generally in laboratory and diagnostic work, air conditioning, fuel and oil filters and household uses such as teabags. Chromatography paper is similar to that of filter paper, however is used for the separation of chemicals/substances (Koivunen, 2014).

Whatman filter and chromatography papers have been popular in numerous studies, with Whatman no.1 filter paper being most commonly used (Bhakta et al., 2014; Evans et al., 2014; Jayawardane et al., 2014; Noiphung et al., 2013; Rattanarat et al., 2013; Sechi et al., 2013; Ge et al., 2012; Mentele et al., 2012; Shi et al., 2012; Martinez et al., 2010). It is a medium flow filter paper, widely used for laboratory purposes, and made from cellulose with a particle retention of 11 µm for liquids at 98% efficiency, an average thickness of 180 µm and a basis weight of 88 g/m^2 (ACEFESA, 2015). Whatman grade no.1 chromatography paper has also been widely used as it is a clean paper substrate, made out of pure cellulose, has a uniform thickness and good wicking properties (Martinez et al., 2010). It has specifications of 87 g/m^2 basis weight and a thickness of 170 µm (Adventec MFS Inc., 2006).

A study conducted between six different Whatman filter and chromatography papers to determine its applications yielded that the thicker substrates (i.e. grade 3 filter paper and 3MM chromatography paper) displayed higher resistances to flow, transferred solutions at a slower rate and showed poor colour development in µPADs (Evans et al., 2014). Grade 3 filter paper has a particle retention of 6 µm, with a thickness of 390µm and a basis weight of 187 g/m^2 (ACEFESA, 2015). Grade 3MM chromatography paper has specifications of 185 g/m^2 basis weight and a thickness of 320 µm (Adventec MFS Inc., 2006). Thinner substrates (i.e. grade 1 filter and chromatography papers) showed faster transfers of the solution and an overall enhanced analytical performance (Evans et al., 2014).

Filter paper can experience issues during the fabrication process of µPADs due to its high surface roughness, low surface and bulk strength and uneven pore size distribution, which

was found to be problematic during flexographic printing (Koivula et al., 2013). Therefore, suggested methods include screen and inkjet printing, with preference being given to inkjet printing due to its non-contact approach (Koivunen, 2014).

2.2.2.2 Nitrocellulose

Nitrocellulose (NC) is cellulose which has undergone a nitration process by exposing it to a nitrating agent, usually nitric acid. Nitrocellulose membranes have been introduced into paper-based microfluidics in 2010, where fabrication of µPADs was conducted using NC membranes and wax printing for applications in protein immobilisation. The membrane was reported to have small, uniform pores of 0.45 µm and a smooth surface, which results in a stable flow within the paper. However, it was discovered that the penetration of wax was slow compared to filter paper (Lu et al., 2009).

Caution must be taken when working with NC as it is highly flammable, having a flash point of approximately 200°C (Lu et al., 2009). Other disadvantages include low mechanical properties, which make it difficult for patterning and its high cost (Rosen et al., 2009).
A nitrocellulose membrane was also used in the extraction of nucleic acid from various pathogenic samples. Here, photolithography patterning was conducted using SU-8 photoresist. It was found that NC, in comparison to cellulose, is more effective at isolating larger nucleic acids (Fronczek et al., 2013).

2.2.2.3 Printing paper

Printing paper, also known as office copy paper, is manufactured for use in photocopy machines or xerographic printers (Koivunen, 2014). They have a basis weight of between 70-90 g/m^2.

A few studies on printing paper for microfluidic applications have been conducted. Research conducted by Zhong et al. (2012) and Lu et al. (2009), using wax printing, showed that printing paper has low wicking capabilities, which is expected due to the low porosity level and surface tension of the substrate, therefore making it unsuitable for µPAD fabrication. Lu et al. (2009) proposed a method for improved properties by oxidising the substrate with oxygen plasma, or through the addition of a surfactant to the sample fluid.

Another study by Maattanen (2014) made use of Optitext surface sized copy paper for fabrication using Polydimethylsiloxane (PDMS) patterning techniques. This substrate was chosen for its low cost, wide availability and intermediate absorbance properties. Results showed an 89° contact angle with water, which is used as an indirect measurement of surface energy for information on the adhesion properties of the substrate and the hydrophobising agent, as well as the penetration of the sample. Water absorption was reported to be relatively fast, implying that the paper had retained hydrophobicity (Maattanen, 2014; Maattanen et al., 2011).

2.2.2.4 Handsheets

Handsheets are produced on a laboratory-scale by using equipment such as a Rapid- Köthen handsheet maker. This results in a circular paper sheet whose properties vary depending on the type of pulp used. Böhm et al. (2014) investigated properties of two different laboratory-engineered paper sheets: one made of eucalyptus sulphate pulp and the other produced from cotton linters pulp. Improved fluid transport was seen in these paper sheets when compared to commercially available filter papers (Whatman No. 1 chromatography paper and Roth 15A). The laboratory-engineered paper sheets allowed for control over the composition of paper, specifically with regards to porosity, and the addition of unnecessary chemicals was avoided. These chemicals were shown to affect the fluid transport kinetics. Eucalyptus sulphate handsheets had the following properties: a pore radius of 4.2 µm with a porosity of 0.62, a thickness of 180 µm and a basis weight of 95 g/m^2 (Böhm et al., 2014). The cotton linter substrate had a 4.3 µm pore radius with a porosity of 0.69, a thickness of 160 µm and a basis weight of 76 g/m^2 (Böhm et al., 2014).

2.2.2.5 Other substrates

Numerous other substrates have been studied for use in µPAD fabrication. They have been listed:

- ✓ Pigment coated paper (LumiArt), printed with PDMS. Unfavourable results have been obtained as the ink was unable to penetrate the substrate (Maattanen et al., 2011).
- ✓ Kitchen towel, thin paper napkins and laboratory paper towels patterned with wax pencils. It was shown that the laboratory paper towels and napkins had good wicking capabilities, with the laboratory paper towel being the most rapid and reliable. The

paper napkin showed leakage due to its thinness. The kitchen towel was a poor substrate due to its high porosity, resulting in irregular and incomplete spreading of the wax barriers (Zhong et al., 2012).

- ✓ Steri-Pak LF indicator test sheets tested with PDMS have a high permeability and water absorbing abilities (Maattanen, 2014).
- ✓ Parchment paper, a fibre sheet coated with silicone, was tested using CO_2 laser cutting. This resulted in a highly porous structure, which assists in trapping/localising reagents for assays (Chitnis et al., 2011).
- ✓ Hydroxypropyl cellulose, which is reacted with methacrylic anhydride for photo cross-linkability. The cross-linking occurs through photolithography. It has shown promising results for use with µPADs for application in protein and cell assays (Qi et al., 2014).
- ✓ Silica gel plate patterned using a marker pen. The plate is widely used in thin-layer chromatography and is inexpensive, uniform, portable and widely available with chemical stability and useful for biological assays. It was found to be useful in protein and glucose assays (Fang et al., 2011).

2.3 Fabrication

Patterning is a process whereby channel networks are created on the base substrate through the creation of hydrophobic barriers. This process, besides creating hydrophobicity, can be used for other purposes such as depositing analytical elements (reagents or electrically conductive materials) and graphics onto a substrate (Koivunen, 2014).

Paper lends itself to microfluidic applications due to its hydrophilic and porous nature (Hu et al., 2014). µPADs were first introduced by Whitesides' group at Harvard University in 2007. The µPADs were made by patterned photoresist onto chromatography paper, producing distinct hydrophobic barriers on the hydrophilic paper, which provided spatial control and transportation of biological fluids (Martinez et al., 2007).

Since then, various methods of µPAD fabrication have been developed. These methods can be categorised into two general groups: (i) physical blocking within paper through the creation of barriers and (ii) two-dimensional cutting/shaping for production of multifunctional µPADs (Yetisen et al., 2013). The first group involves the production of hydrophobic barriers through selective hydrophobisation of a hydrophilic substrate using a

hydrophobising agent. With this method, penetration of the hydrophobising agent through the depth of the substrate is crucial to avoid leakages from the hydrophilic channels (Koivunen, 2014). Another approach involves hydrophobising the entire substrate using a hydrophobising agent and subsequently selectively creating hydrophilic areas on the substrate for production of channels (Koivunen, 2014). The cutting/shaping approach uses a computer-controlled plotter cutter to cut a shape on a substrate. The cut pattern is then sealed with sticky tape, which is used as a backing for μPADs (Li et al., 2012).

A table of advantages and disadvantages of the main fabrication methods can be seen in Table 2.1.

Table 2.1 Advantages and disadvantages of fabrication techniques.

Fabrication Technique	Advantages	Disadvantages	Refs
Photolithography	Sharp resolution Hydrophilic channel widths up to 200µm	Expensive equipment Extra washing step µPADs susceptible to bending clogs pores of substrate due to SU-8 photoresist	(Li et al., 2012; Yetisen et al., 2013)
Plotting	µPADs flexible Patterning agent (PDMS) is cheap	Low throughput of devices Formation of hydrophobic barriers difficult to control Curing step necessary	(Bruzewicz et al., 2008; Li et al., 2012)
Inkjet printing	AKD cheap patterning agent Fast fabrication (<10 mins) Minimal equipment needed	Specialised equipment necessary Extra heating step required Prior treatment of paper necessary	(Li et al., 2012)
Wax printing	Simple and fast fabrication (5-10 mins)	Expensive wax printers Extra heating step required Unstable at high temperatures	(Lu et al., 2009; Li et al., 2012)
Flexography	No heat applied for patterning	Multiple printing steps Specialised equipment needed Low throughput Frequent cleaning needed Printed pattern dependent on smoothness of paper	(Olkkonen et al., 2010; Cate et al., 2015)
Cutting/shaping	Easy to fabricate	Stability of structure needed Limited geometry Wastage of raw materials	(Fenton et al., 2008; Fu et al., 2010)

2.3.1 Fabrication methods

2.3.1.1 Wax patterning

Of the methods available for patterning, wax patterning has proven to be simple, rapid, inexpensive and suitable for laboratory-scale production of µPADs due to the non-toxic reagents used in the process (Yetisen et al., 2013; Carrilho et al., 2009). The fabrication of µPADs through wax patterning involves two fundamental operations: (i) printing patterns of wax onto the paper surface and (ii) melting the wax into the paper to create hydrophobic barriers (Carrilho et al., 2009).

There are three known wax patterning methods available, namely wax screen printing, wax dipping and solid wax printing (as seen in Figure 2.2). Wax screen printing involves rubbing solid wax onto paper filters through a screen. The printed wax is then melted into the paper using a hotplate or oven, thus forming hydrophobic barriers (Dungchai et al., 2011). Wax dipping is another simple method using an iron mould created by laser cutting (Songjaroen et al., 2011). The assembled mould is dipped into melted wax and placed onto paper, thereby transferring the pattern and creating hydrophobic barriers (Songjaroen et al., 2011). The optimal melting temperature and dipping times are between 120 – 130°C and 1 s, respectively (Songjaroen et al., 2011).

Although both these techniques are simple and inexpensive, they suffer from loss of feature resolution due to wax spreading (Sameenoi et al., 2014), inflexibility in patterning and low reproducibility between batches (Yetisen et al., 2013). To overcome these downfalls, solid wax printing was explored. A sheet of paper is inserted into a wax printer and processed by a heat source (hotplate or oven). The process usually takes a few minutes and can produce tens to hundreds of copies of devices (Yetisen et al., 2013).

The spreading of molten wax on paper poses some difficulty in the patterning process, as the printed pattern does not directly translate to the dimensions of the hydrophobic carriers in the paper (Carrilho et al., 2009). Washburn's equation for capillary flow in porous materials can be used to model the spreading of molten wax in paper (eq. 2.1):

$$L = \sqrt{\frac{\gamma D t}{4\eta}} \qquad (2.1)$$

where L is the distance the wax spreads through the paper in time t, γ is the surface tension, η is the viscosity (as a function of temperature) and D is the average pore diameter (Carrilho et al., 2009). Assuming the temperature is constant and all parameters in eq. 1 are consistent, leads to the conclusion that the distance L is constant. Using these assumptions and eq. 1, the width of a hydrophilic channel can be defined using the following equation (eq. 2.2):

$$W_c = W_G - 2L \tag{2.2}$$

where W_c is the width of the hydrophilic channel and W_G is the width of the printed channel (in µm), measured from the edge of the line (Carrilho et al., 2009). Additional assumptions for this model include that the amount of wax is not a limiting factor and natural convection is negligible (Yetisen et al., 2013).

Wax patterning produces various size hydrophobic barriers depending on the fabrication method. Typical sizes of hydrophilic channels range from 0.5 to 4 mm, with the average being between 1 and 2 mm, and the hydrophobic barrier is approximately 1 mm in width (Yetisen et al., 2013).

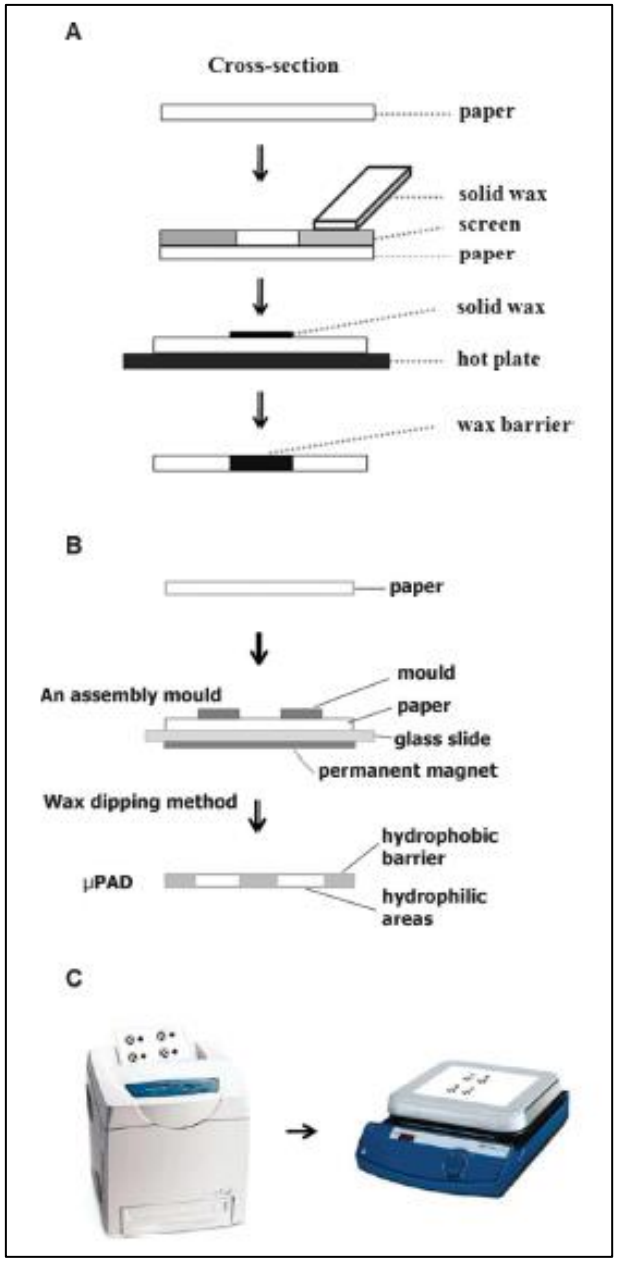

Figure 2.2 Wax fabrication techniques. A: wax-screen printing, B: wax dipping and C: solid wax printing (Yetisen et al., 2013).

2.3.1.2 Inkjet printing

Inkjet printing is a non-impact printing technique in which individual droplets of ink, produced in print heads, is sprayed onto paper directly. The ink used during this process is usually liquid, however holt-melt inks, which become liquid upon heating, are also used as an alternative due to their advantages such as rapid drying and ability to print on various paper substrates (Kipphan, 2001).

"Continuous inkjet" and "drop on demand inkjet" are the two developed inkjet technologies available, shown in Figure 2.3. In the "continuous inkjet" technology, a steady stream of small ink droplets are generated, which have a charge according to the image and are electronically controlled. An electric field is used to deflect the charged droplets, while the uncharged droplets are deposited onto the paper. This means that only small percentage of the stream of droplets flow to the paper, with the larger portion fed back into the system. With the "drop on demand inkjet" technology, production of droplets only occurs if they are required by the image. "Drop on demand inkjet" has two important technologies, these being thermal inkjet (bubble jet) and piezo inkjet printing, which differ based on the method of generation of droplets. Production of droplets in thermal inkjet printing occurs by heating and vapourisation of liquid in a jet chamber. On the other hand, in piezo inkjet printing, the formation of the droplet is based on the mechanical deformation of the jet chamber, due to an electronic signal and piezoelectric characteristics of the chamber wall (Kipphan, 2001).

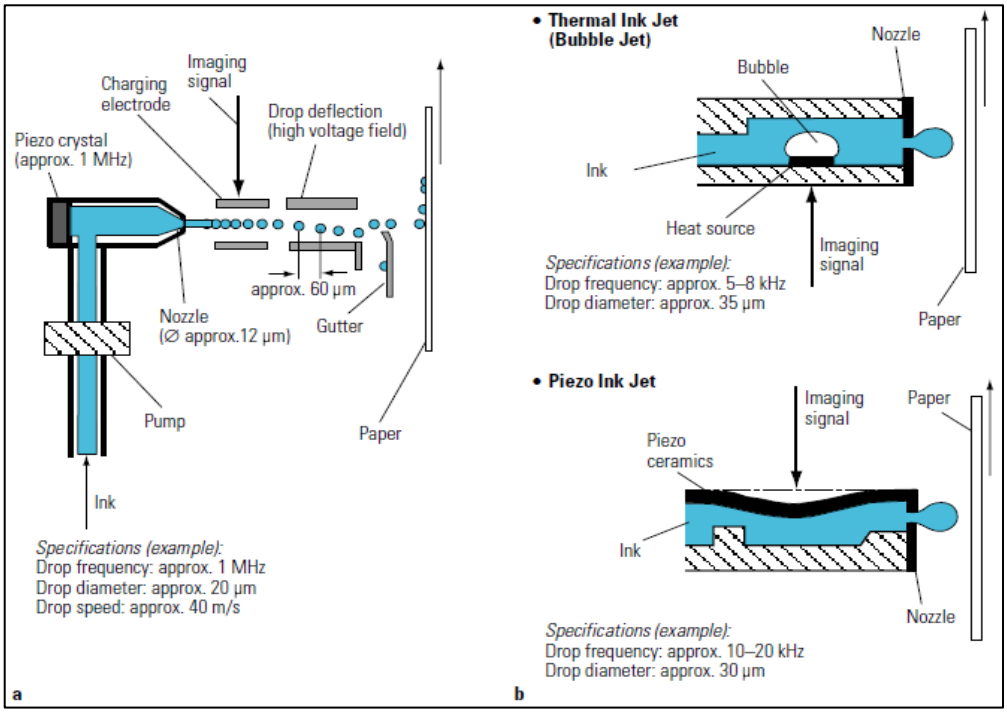

Figure 2.3 Inkjet fabrication techniques. a: continuous inkjet and b: drop on demand inkjet (Kipphan, 2001).

Printing inks generally consist of colourants, binders, additives and solvents (Kipphan, 2001). Recently, the development in inkjet printing has been used to create barriers in paper substrates. Modified inkjet printing was investigated using alkyl ketene dimer (AKD), a cellulose reactive hydrophobisation agent (Yetisen et al., 2013). Alkyl ketene dimer was deposited onto paper and thereafter heated for production of hydrophilic and hydrophobic patterns (Yetisen et al., 2013). With this technique, hydrophobic barriers remain invisible to the naked eye and the paper substrate maintains its flexibility (Yetisen et al., 2013). Similarly, UV curable inks have been investigated as an alternative to the typical inks used, which provides an environmentally-friendly approach to inkjet printing (Maejima et al., 2013).

Inkjet etching is an interesting application of inkjet printing. While inkjet printing adds substances onto a substrate, etching works in an opposite manner, by removing, displacing or changing the material on the substrate (Koivunen, 2014). Inkjet etching is a process whereby a solvent is printed onto a polymer layer, which is previously deposited through another process (de Gans et al., 2007). When the solvent drops onto the polymer layer, the polymer dissolves and forms a crate-like hole (de Gans et al., 2007). In paper-based microfluidics, inkjet etching can be applied to selectively create hydrophilic areas in a hydrophobic substrate (Abe et al., 2008).

2.3.1.3 Flexographic printing

Flexographic printing, also known as flexography, is a fabrication technique that uses the principles of letterpress printing (Koivunen, 2014). A paper substrate is placed on an impression roll. An ink reservoir is filled with the required amount of ink and is transferred to an anilox roll, which is a cylinder with microfluidic patterns indented into its hard surface (Olkkonen et al., 2010). The anilox then transfers the ink to the printing plate, which prints the pattern on the paper substrate (Koivunen, 2014; Olkkonen et al., 2010). Operation of printing can be optimised by controlling the anilox, either accelerating or decelerating its speed, or controlling the pressure between the printing plate and impression roll (Olkkonen et al., 2010).

Currently, only a few studies have reported the use of flexography for µPAD fabrication and were conducted on a laboratory-scale. Polystyrene ink dissolved in toluene and xylene has been used to print hydrophobic barriers (Olkkonen et al., 2010). Polydimethylsiloxane

(PDMS), in a widely available ink form, was also used in flexography applications (Maattanen et al., 2011).

2.3.1.4 Photolithography

Photolithography or optical lithography is a technique which is used for fabricating microstructures onto paper substrates. A paper substrate is covered with photoresist, a photosensitive material, and undergoes a selective polymerisation process where it is exposed to UV light through a photo mask (transparency film with black ink print). A washing step follows, which removes the unexposed photoresist leaving behind the desired microfluidic pattern. (Martinez et al., 2010).

Various photoresists have been experimented with in paper-based microfluidic applications. Paper was soaked in SU-8 photoresist in a study conducted by Martinez et al. (2010). Recently, OuYang and team investigated the use of trichloromethane diluted photoresist, which decreased photoresist consumption and shortened drying time (OuYang et al., 2014).

2.3.1.5 Two-dimensional cutting/shaping

Two-dimensional shaping and cutting have been a popular method for µPAD fabrication. There are two methods for shaping and cutting, these being: (i) X-Y knife plotters controlled by computers (Fenton et al., 2008) and (ii) CO_2 laser cutting (Fu et al., 2010).

The X-Y knife plotter method makes use of a computer controlled knife on a rotating platform for creation of different patterns and features on a substrate. The device operates at various pressures and blade angles depending on the application. The cutting action can cause damage to the substrate, therefore decreasing cutting force with multiple passes and adding a backing to the substrate are advised during the process. Nitrocellulose was investigated as a substrate using this method, where a polyester backing was necessary for prevention of damage (Fenton et al., 2008). Recently, the knife plotter technique was used for the production of open channels for fluid flow control in µPADs (Giokas et al., 2014).

CO_2 laser cutting uses a similar technique as the X-Y knife plotter method, however here a computer is used to control a CO_2 laser. This method has an added advantage as the substrate

can be cut in one pass without the use of a backing. However, it makes use of expensive equipment (Nie et al., 2013).

2.3.1.6 Other techniques

Numerous other methods have been developed. However, due to the high costs and/or multi-step processes involved, they have been replaced by the above-mentioned methods. These fabrication techniques include:

- ✓ Using X-Y plotting for production of hydrophilic channels by printing a solution of PDMS dissolved in hexanes onto filter paper (Bruzewicz et al., 2008).
- ✓ Plasma treatment introduced by Xu Li's group in 2008: Paper is hydrophobised and subsequently a metal mask, with patterns, is placed on the paper and treated with plasma to create hydrophilic channels (Li et al., 2008).
- ✓ Laser treatment of hydrophobic substrates: Hydrophilic channels are formed on hydrophobic substrates using a CO_2 laser, through selective modification of surface and properties of the substrate (Chitnis et al., 2011).
- ✓ Using photolithography for embossing of parafilm, and transferring the pattern from the parafilm onto the paper substrate through a heating step (Yu & Shi, 2015).
- ✓ Handheld stamping: A stainless steel stamp with microfluidic patterns was designed. The paper substrate was chemically modified through oxidation. Thereafter a filter paper covered in paraffin was placed on top of the paper substrate. The stamp was heated and placed on the paraffined paper for transfer of hydrophobic barriers onto the substrate (de Tarso Garcia et al., 2014).

2.3.1.7 Three-dimensional µPADs

Paper-based microfluidic devices can be grouped into 1D, 2D and 3D devices, depending on the number of dimensions of fluid flow within the device. One dimensional devices, called lateral flow assays (LFAs), transport fluid in one direction along the channel. Tests are conducted on a strip of paper substrate, which is divided into sample application pad, conjugate pad, nitrocellulose membrane and an absorption pad (Sajid et al., 2014). Reagents are deposited onto the strip and are active by the flow of fluid (Sajid et al., 2014). The most common LFAs are pregnancy test kits.

The fabrication techniques discussed in section 2.3 deal with two-dimensional µPADs, which transport fluid in a 2D network of hydrophilic channels (Koivunen, 2014). To introduce added functionality to these devices, fabrication of 3D µPADs was developed. They have been proven to be advantageous due to (i) the accommodation of more assays on a device without an increase in size, (ii) the ability of a fluid to move in three dimensions through numerous layers of paper, allowing for multi-step assays on a single device and (iii) the ability of a fluid to move through the thickness of paper (z direction) and laterally (x-y direction), which minimises sample loss, increases distribution time and minimises the amount of sample required for an assay (Yetisen et al., 2013).

Studies have reported three methods for fabrication of 3D µPADs, as seen from Figure 2.4. The original method uses alternating layers of paper and double-sided tape, both with microfluidic patterns. Due to the thickness of the double-sided tape, a gap is formed between layers, breaking the flow of fluid through the device (Martinez et al., 2010; Martinez et al., 2008). The gap is closed by either making a hole in the tape and filling it with hydrophilic materials or by compressing the paper layers by punching a hole in the tape between the paper (Martinez et al., 2010; Martinez et al., 2008). As fabrication using this method is time-consuming, an alternative approach has been developed where hydrophilic spray adhesive is used in place of double-sided tape (Lewis et al., 2012). This method provides a high throughput and rapid assembly of devices on a laboratory-scale (Lewis et al., 2012).

The second method involves cutting and stacking individual layers of paper. Wax patterns are printed on layers of paper, where one layer is printed with toner. The layers are folded to create a 3D µPAD and passed through a laminator to melt the toner for binding of layers (Schilling et al., 2013).

The third method uses the principles of origami by folding layers of the µPAD from a sheet of paper and using a clamp or lamination to hold the device together (Liu et al., 2012).

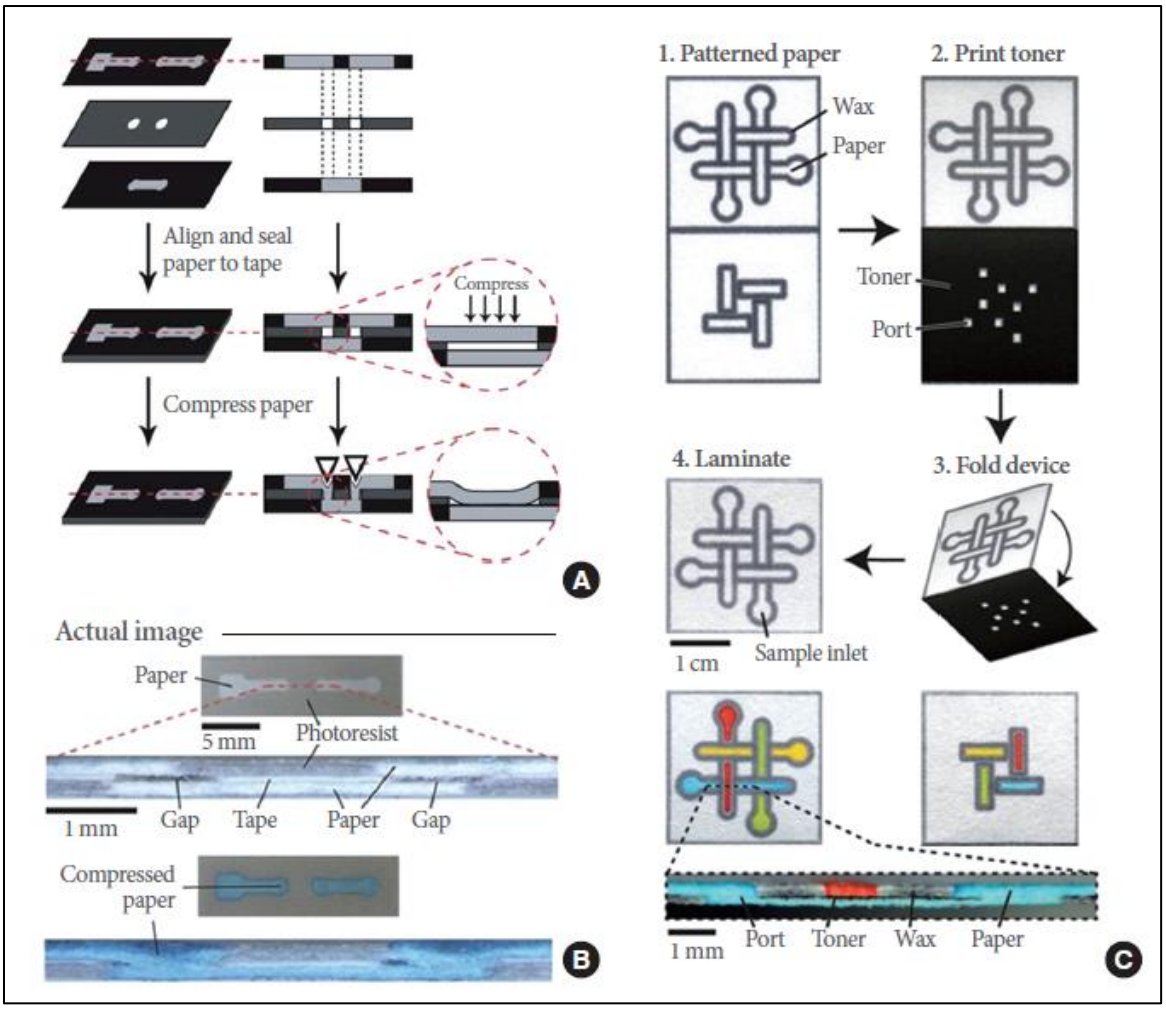

Figure 2.4 Schematic of fabrication of 3D µPADs. A: fabrication through stacking of layers with tape, B: cross section of µPAD with closed gap between layers and C: fabrication using toner (Jeong et al., 2013).

2.3.2 Finishing of µPADs

A large portion of µPADs developed on a laboratory-scale is left with open channels and testing zones. However, it can be useful to consider packaging of the devices. It can assist in avoiding issues such as: (i) potential contamination due to transportation or operation, (ii) effect of evaporation on sample and reagent, (iii) contamination or leakage of sample when contacting other surfaces and (iv) light receptibility (Yetisen et al., 2013). In addition, enclosed µPADs protects reagents on the stored device and can be handled easily (Schilling et al., 2012).

Various materials have been studied for the use of sealants in µPADs, which also act as support structures. Adhesive tapes have been utilised for sealing and packaging, and have the

added advantage of being transparent, making the test zones visible. It is inexpensive and widely available (Cate et al., 2015). Pressure sensitive tapes were shown to have poor adhesion properties when applied to wet channels, and at temperatures above ambient, it disperses into the paper substrate, thereby affecting the flow of fluid in µPAD (Yetisen et al., 2013). Toner can also be used as a sealant, which prevents natural convection and controls moisture within an assay (Yetisen et al., 2013). Toner is deposited onto the surface of the paper substrate using a laser printer, which forms a layer of plastic on the substrate. Four to five layers of toner must be used for complete sealing of the µPAD. Disadvantages of toner as a sealant include: (i) disturbance of wicking process, (ii) reagents which cannot withstand high temperatures are not suitable and (iii) the reagents must be added prior to the toner deposition (Yetisen et al., 2013). Cold lamination is used to seal the top and bottom of µPADs. Self-adhesive laminating sheets are similar to that of adhesive tape and protect the assay while providing mechanical support (Pollock et al., 2012; Vella et al., 2012). However, this process requires specialised equipment, which is expensive to purchase.

2.3.3 Functional Features

Paper-based microfluidic devices can incorporate added functionality for better fluid control and independent operation. The increasing functionalities in paper-based microfluidics can soon lead to fully automated µPADs.

2.3.3.1 Switches and valves

Switches play an important role in the control of wicking in the channels. This function was achieved by cutting a microfluidic channel into two and separating them to either allow or impede flow (Li et al., 2008).

Valves are designed for use in µPADs for flow control. The principle of valve operation in a 3D µPAD relies on closing a gap between two channels, which are vertically aligned using pressure (Martinez et al., 2010). This operation allows the fluid to wick along the channel, by using a single-use “on” button, which is triggered by applying pressure using a pen (Martinez et al., 2010). Other valve mechanisms involve altering the geometry of the channel, depicted in Figure 2.5 (Fu et al., 2010; Kauffman et al., 2010; Osborn et al., 2010). By changing the

width of the channel, so too does the flowrate in the channel. A change in the channel width from narrow to wide decreases the flowrate.

Recently, fluidic barriers used as time delays were developed using soluble materials, as seen in Figure 2.5. Sucrose is commonly used due to its low cost and wide availability. The fluid in the channel passes through the barrier of soluble material for a duration of minutes to a few hours (Lutz et al., 2013).

Razor-cutting was also presented as a technique for controlling fluid flow, as seen in Figure 2.6. This is done by cutting slits in the paper, either parallel or perpendicular to the direction of flow of fluid. The flowrate is a function of slit length, direction and quantity (Giokas et al., 2014). A cutting method for cellulose removal from the fluid path using a craft cutter was introduced by Renault et al. (2014). This resulted in an increased fluid flowrate in the paper substrate.

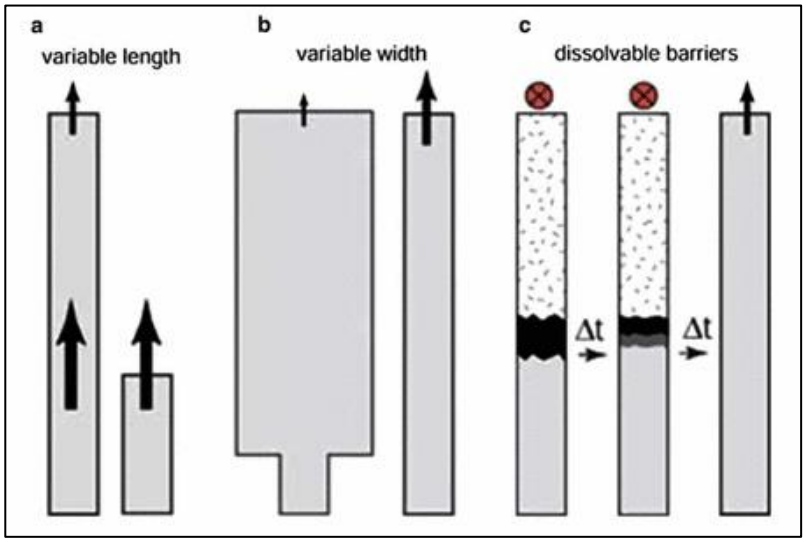

Figure 2.5 Schematic of different valve designs for control of fluid flow (Fu, et al., 2010).

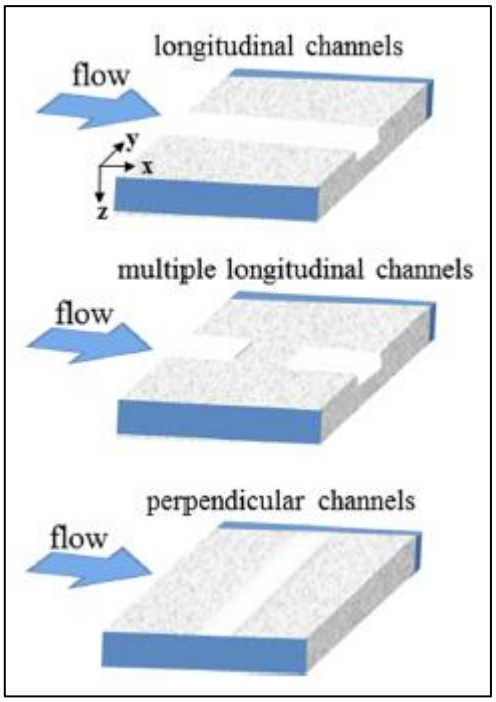

Figure 2.6 Razor-cut channels for fluid control (Giokas et al., 2014).

2.3.3.2 Mixing

Mixing in channels can be incorporated through threads, which will increase uniformity and control of fluids. A thread consists of fibres and pores, which allows for the transportation of fluids through the process of wicking without any barriers. Threads are sewn onto channels to produce a 3D pathway for fluid transportation. These µPADs incorporating threads have potential applications in the medical, environmental, food and beverage industries. (Ballerini et al., 2012; Li et al., 2010; Reches et al., 2010)

2.3.3.3 Timers

An important factor in µPAD operation is the end-point of an assay. Recent studies using 3D devices have successfully managed to monitor the end-point of a time-dependent assay, without the use of external equipment. A timing mechanism is built into the µPAD and is composed of paraffin wax and a chemical used for signalling the end of an assay (for example, a dye). The operation of the timer depends on the wicking time of the sample, which starts as soon as the sample is added to the device and does not require reset buttons or

maintenance throughout its usage (Noh & Phillips, 2010). Figure 2.7 shows the operation of timers in microfluidic applications using a glucose assay.

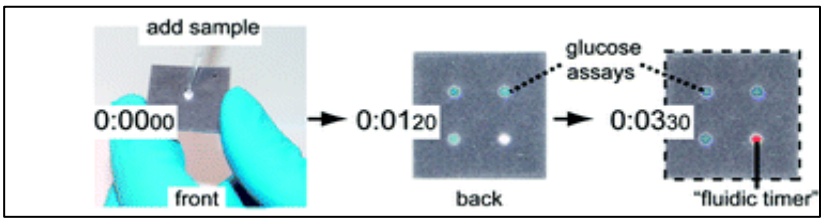

Figure 2.7 Fluidic timer operation using a glucose assay (Noh&Phillips, 2010).

2.3.3.4 Multi-step processes

Fully automated multi-step processes, depicted in Figure 2.8, are useful in µPADs for delivery of reagent to detection zones. Fu et al. (2011) and Lutz et al. (2011) investigated the delivery of multiple reagents to detection zones by adding numerous constant-width sections of filter paper for each addition of reagent. Apilux et al. (2013) varied the lengths of the channel paths for each reagent, thereby allowing reagents to arrive at the detection zones at different times, i.e. shorter channels will allow the reagent to reach zone faster. An additional feature includes baffles, which lengthens the flow path, thereby delaying flow (Cate et al., 2015).

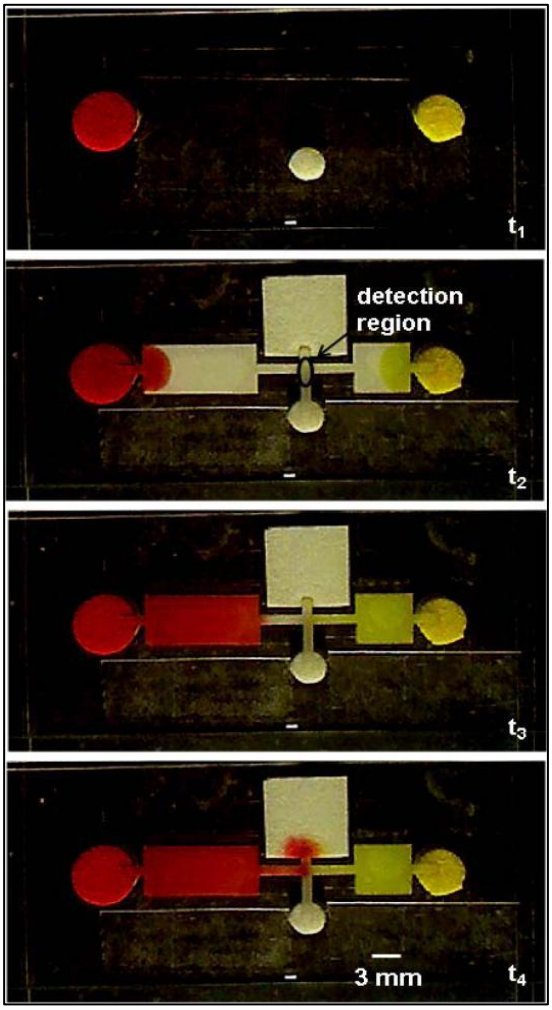

Figure 2.8 Multi-step process demonstration with delivery of three different reagents to detection zone. t_1 shows the reagents in the sample inlet, t_2 shows the white reagent at detection zone, followed by yellow reagent at t_3 and lastly the red reagent at t_4 (Fu et al., 2011).

2.3.3.5 Other functionalities

By altering the surface chemistry of the substrate, the fluid flow in channels can be controlled, uniform colour can be produced in detection, chemical stability can be improved and microfluidic valves can be created (Guan et al., 2014; Zhu et al., 2014).

Paper-based microfluidic devices can incorporate a power source in the form of fluidic batteries. One such example is a galvanic cell placed in channels for power generation (Thom et al., 2012). The batteries are only activated when fluid is introduced into the device.

2.4 Fluid transport

The operation of µPADs relies on fluid transportation within the paper substrate, which is through the process of wicking. Wicking is defined as the movement of fluids through the pores of a substrate as a result of capillary pressure. A capillary force is formed due to the difference between dry and wet surface energies, which can cause certain liquids to be pulled into the pores (Masoodi & Pillai, 2012a).

The wicking rate is dependent on the substrate properties as well as the properties of the fluid being transported. In an open environment, external factors such as temperature and vapour pressure also affect wicking due to evaporation of liquid, which can bring about viscosity changes. The substrate can also change during the wicking process, where swelling through liquid absorption can occur or the liquid can bring about the bond breakage of the matrix (Koivunen, 2014).

Principles of wicking in porous media and factors affecting it will be discussed in detail in this subchapter.

2.4.1 Properties affecting wicking rate

2.4.1.1 Fluid properties

Viscosity, η, can be defined as the resistance of a fluid to shear stress. Fluid viscosity is a function of temperature and pressure. An increase in liquid temperature weakens the attractive forces between molecules, thereby increasing the speed of molecules, decreasing the viscosity (Kamyabi, 2014). Change in pressure alters the viscosity on a small scale.

Surface tension is the surface property of a liquid which allows it to withstand external forces due to its cohesive forces of molecules (USGS, 2015). It can also be defined as the force required to increase the length of contact line between two substances, i.e. liquid and another substance such as air (Barnes & Gentle, 2011). Surface tension is a function of temperature, where an increase in temperature results in a decrease in surface tension (Barnes & Gentle, 2011).

Liquid transport through porous media relies on the wetting of the surface before capillary action can take place (Patnaik et al., 2006). Wetting can be defined as the spreading of a

liquid on a solid medium, thereby allowing for absorption of the liquid into the medium (Dullien, 2012). It is strongly dependent on surface energy and the roughness of the material. The balance between adhesive and cohesive forces determines the degree of wetting of a material. The phenomenon of wetting can be physically observed through the measurement of the contact angle. Contact angle, θ, is defined as the angle formed by the triple interface, where liquid-solid and liquid-vapour interfaces intersect (Yuan & Lee, 2013). The contact angle of a material is related to its hydrophobicity properties, where a contact angle of less than 90º indicates a hydrophilic material and a contact angle of greater than 90º indicates a hydrophobic material.

Contact angles have been proven difficult to measure on porous media. This is due to the complex porous and fibrous structure of cellulosic surfaces (Hubbe et al., 2015). To overcome the complexity of determining the contact angle, the apparent contact angle was proposed by Wenzel for wetting on a rough surface (see Figure 2.9) (Wenzel, 1936). This model was based on the Young equation, which was strictly developed for smooth, chemically homogeneous surfaces (Song & Rojas, 2013). Characteristics of the porous structure need to be known for determination of the contact angle, using the Wenzel model. The apparent θ is calculated based on the roughness of the porous medium, taking into consideration a smooth surface made of the same substrate:

$$cos\theta_a = r cos\theta_r \tag{2.3}$$

where θ_a is the equilibrium contact angle, θ_r is the contact angle of the smooth surface and r is the roughness of the surface (Maattanen, 2014).

Another focus point with the study is the hydrophobicity of nanofibrillated (NFC) cellulose. Nanofibrillated cellulose refers to cellulose fibres that have been broken down into smaller fibre particles. These materials have a typical diameter of less than 100 nm and a length of a few micrometers (Thakur & Kessler, 2015). It is typically used as mechanical reinforcement in biocomposites. Mechanical properties of this cellulose are that it has a high number of hydroxyl groups and a high hydrophilicity. In order to expand the applications of NFC, surface modifications are recommended. It has been seen from a previous study by Kord et al. (2016) that the addition of NFC to composite polyvinyl alcohol (PVA) films (0% to 20%), increased the contact angles from 73º to 111º. The NFC addition resulted in a decreased surface energy and a higher surface roughness for the PVA films. The expectation, which was

realised in the study, was an improved water resistance of the film due to a stronger hydrogen bonding between the components, resulting in a higher contact angle (Kord et al., 2016).

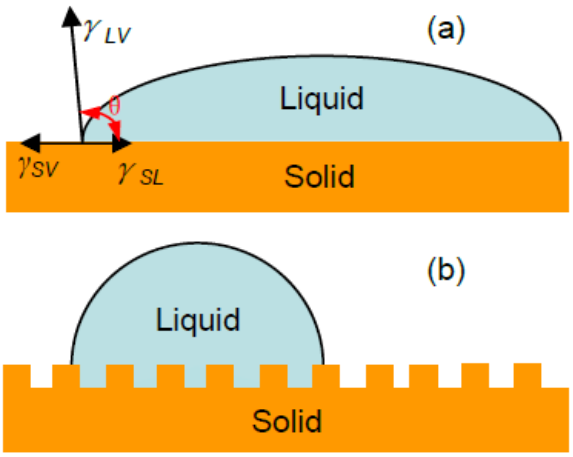

Figure 2.9 (a) Young equation model and (b) Wenzel model (Song & Rojas, 2013).

2.4.1.2 Paper substrate properties affecting wicking

Paper is composed of cellulosic fibres from wood or any other plant source. The fibre properties used in the papermaking process can be one of two types, these being hardwood or softwood. The difference between softwood and hardwood is observed in the fibre properties such as fibre length, diameter and wall thickness. These properties determine the strength and collapsibility of the fibre (Kerr, 2014).

Table 2.2 shows the difference between softwood and hardwood fibres.

Table 2.2 Morphology of softwood and hardwood fibres (Kerr, 2014).

Characteristic	Softwood	Hardwood
Origins	Conifers	Broad-leafed
Fibre Length (mm)	3 – 7	1 – 2
Fibre Diameter (µm)	20 – 50	10 – 40
Fibre Wall Thickness (µm)	3 – 7	-
Composition	Fibre elements	Fibre and non-fibrous elements

In comparison to softwoods, hardwoods contain non-fibrous elements such as vessel segments, ray cells and parenchyma cells, which affect the papermaking process and paper properties. Other components of wood, which can be carried over into paper include hemicellulose, lignin and extractives. Hemicellulose is a polymer of 5 different sugars, whose function is not well understood (Kerr, 2014). It has an effect on the bonding strength of fibres. Lignin is an aromatic polymer which binds cells together and causes a yellowing in paper. Due to its high binding capacity and molecular weight, it could prove to retard the movement of liquid through paper (Kerr, 2014). Extractives contribute a small percentage of the wood constituents. It is derived from wood parenchyma cells and is usually not present in paper (Kerr, 2014).

Papermaking significantly determines the paper structure, which is a result of how the fibres are orientated in the process. In the handmaking process, the fibres are isotropic, while using a Fourdrinier machine, the fibres are orientated in the machine direction. The papermaking process has an effect on the thickness of paper, as well as the shrinkage (McDonald, 2006).
Paper is a complex structure, as there is no uniform pore size or pore orientation. A pore size distribution is usually determined for the paper substrate, which shows the average pore size within the sheet. Pore size, which is usually the pore radius measurement, is important for the penetration of fluid. Pore size and duration for absorption of fluid can be seen to have a directly proportional relationship, where larger pores absorb fluid faster (Rioux, 2003).

Porosity, ε, is a dimensionless number which indicates the pore volume portion of a medium, where the rest is the solid material (Koivunen, 2014). The porosity gives an indication of the amount of fluid that can be absorbed by the medium.

Another significant factor influencing the capillary flow through paper is the hydrogen bonding between fibre networks. Once wet, by coming into contact with water, the hydrogen bonds can be broken apart. Fibre swelling and expansion will also result, affecting the pore shape and size (McDonald, 2006).

The permeability of paper is directly related to its wicking rates. Permeability, κ, is used to determine the fluid conductivity of porous media or how easily a fluid can penetrate the medium (Amico, 2000). The Carman-Kozeny equation is the most commonly used model for the determination of permeability, based on the laminar flow in granular particle beds (Koivunen, 2014). It is used to relate permeability to the medium's physical properties expressed as:

$$\kappa = \frac{\rho g \varepsilon^3}{\eta C_{kc} S_o{}^2 (1+\varepsilon)} \quad (2.4)$$

where ρ is the density of the fluid, g is the gravitational acceleration, C_{kc} is the Carman-Kozeny equation, usually taken as 5, and S_o is the specific surface area per unit volume of particle (Koivunen, 2014). The permeability of a material can be affected by various factors, for example, the deposition of particles on the pore surface, which could lead to blocking of pores, lowering permeability (Rattanarat et al., 2013). Another factor could be the swelling of substrate material, such as cellulose fibres, by absorption of fluid, which reduces porosity and permeability of the medium (Masoodi & Pillai, 2012b).

2.4.2 Wicking

Wicking is the transportation of fluid through a channel using only capillary pressure. The capillary pressure, P_c, can be determined using the Young-Laplace equation (eq. 2.5):

$$P_c = \frac{2\gamma_{LV} cos\theta}{r} \quad (2.5)$$

where r is capillary radius, γ_{LV} is liquid-vapour surface tension and θ is the contact angle between liquid-solid interface (Masoodi & Pillai, 2012b).

Wicking is dependent on the intermolecular forces of cohesion and adhesion. The forces of adhesion between the fluid and capillary wall must be greater than the forces of cohesion between the molecules of the fluid for wicking to occur. (Simile, 2004).

There are two methods used for modelling capillary flow in porous media. The first approach is the Lucas-Washburn equation (eq. 2.8), a first-order approximation of fluid transport, which models the porous medium as a bundle of capillary tubes. Derivation of the model uses the Laplace model for capillary pressure and flow rate expressed by the Poiseuille equation (eq. 2.6).

$$\frac{dV}{dt} = \frac{\pi r^2 dl}{dt} = \frac{\pi r^4 \Delta P}{8\eta l} = \frac{\pi r^4}{8\eta l}\left(\frac{2\gamma_{LV} cos\theta}{r}\right) \quad (2.6)$$

$$\rightarrow l\frac{dl}{dt} = \left(\frac{r\gamma_{LV} cos\theta}{4\eta}\right) \quad (2.7)$$

$$\rightarrow l^2 = \frac{r\gamma_{LV} cos\theta}{2\eta}\, t \quad (2.8)$$

where *l* is the distance travelled in time t, r is the capillary radius and $^{r\gamma_{LV}cos\theta}/_{2\eta}$ is known as the coefficient of penetrance (Cate et al., 2015; Koivunen, 2014).

Various assumptions were made for the development of this model (Cate et al., 2015; Yetisen et al., 2013):

- ✓ Constant cross-section/cylindrical pores
- ✓ Effects of gravity are negligible
- ✓ Chemical homogeneity
- ✓ Reservoir volume is unlimited
- ✓ Flow within porous medium is straight
- ✓ No impurities on medium
- ✓ Constant-width channels

According to the Lucas-Washburn equation (2.8), the graph of *l* versus $t^{1/2}$ should follow a linear relationship, given that the system holds true to the assumptions.

In the case of vertical wicking, the hydrostatic pressure must be accounted for, which results in the following differential equation (eq. 2.9):

$$\frac{dl}{dt} = \frac{r^2 cos\theta}{8\eta l}\left(\frac{2\gamma_{LV}}{r} - P_H\right) \qquad (2.9)$$

where P_H is the hydrostatic pressure, which can be represented as

$$P_H = l\rho g \qquad (2.10)$$

Vertical wicking is dependent on capillary pressure as well as the hydrostatic pressure. Once the capillary pressure is equal to the hydrostatic pressure, movement of the fluid through the substrate stops as the net driving force for fluid transport is zero. Viscous drag also plays a significant role in retarding the motion of fluid through the substrate. (Simile, 2004).

The height at which movement of the fluid ceases can be used in a theoretical calculation of the capillary pressure of the system by using equation 2.10.

A relationship between *r*, *l* and *t* can be deduced from equation (2.8), for any fluid flowing through a porous medium. Specifically looking at vertical wicking, it can be expected that a faster wicking rate would be observed for the larger pore sizes. However, a study conducted

by Miller disproved this hypothesis (Miller, 2000). The study used 4 paper substrates, 3 being paper towels and 1 laboratory grade filter paper. Vertical wicking was observed through a camera at 1 second intervals. Figure 2.10 shows the larger pore sized substrate initially being the faster wicker, however is overtaken by the smaller pore size after a certain period of time.

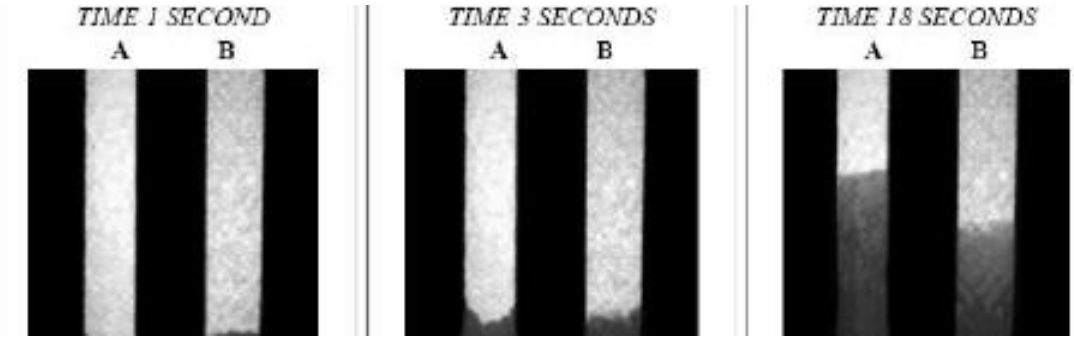

Figure 2.10 Miller's experimental results from vertical wicking tests for two paper towel samples, A with a small pore size and B with a large pore size, at 1, 3 and 18 seconds (Miller, 2000).

Despite being a good approximation, the Lucas-Washburn method tends to overestimate wicking speed in the x-y plane together with the distance of fluid penetration (Roberts et al., 2003). Other variables not taken into consideration are the property changes after wetting, which is the swelling of fibres and increased hydrodynamic resistance to flow (Zhu & Takatera, 2013).

Studies have been conducted on the modification of the equation by taking into consideration viscous drag, gravity and inertia (Fries & Dreyer, 2008; Reed & Wilson, 1993).

The second and more recent fluid transport model uses Darcy's Law, which is based on the Navier-Stokes equations by making the assumption of homogeneity (Nordbotten et al., 2007). This models fully-wetted flow in porous media with constant-width channels.

$$Q = -\frac{\kappa A \Delta P}{\eta L} \qquad (2.11)$$

where Q is the volumetric flowrate, κ is the permeability, A is the area of the channel perpendicular to the fluid movement, ΔP is the pressure change throughout the direction of

fluid flow along the distance L and η is the viscosity (Yetisen et al., 2013). This model can be modified for varying-width channel applications.

2.5 Detection methods

Results from assays conducted on µPADs need to be portrayed to end-users for quantitative analysis. There are five reported methods for quantitative detection of analytes, which are colourimetric, electrochemical, chemiluminescence, electrochemiluminescence and electrical conductivity.

2.5.1 Colourimetric method

Colourimetric detection is the most widely used method in paper-based microfluidic devices and is used when a semi-quantitative result is adequate for analysis. It is considered one of the easiest detection methods, as the colour change can be seen by the end-user due to the chemical or enzymatic reaction that occurs from the assay (Liana et al., 2012). The first colourimetric detection was conducted on a glucose and protein assay, where the colour change was initiated when the sample filled the detection zone (Martinez et al., 2010).

The simplest of detection methods using colourimetry relies on the principle of reflectance. The colour intensity as the reaction proceeds in the reaction zones is a function of the concentration of the analytes present. Figure 2.11 shows an example of colourimetry detection of uric acid and NO_2^-. A desktop scanner or digital camera is used to capture the amount of light reflected off the surface from the test zone. This image is then used to calculate the concentration of analyte using imaging software, where pixel values are calibrated with the concentration (Martinez et al., 2010).

Colourimetric detection is advantageous in paper-based microfluidics as it is easy to conduct and uses simple equipment. However, this detection method is dependent on the quality of the image and lighting, therefore can produce inaccurate results. Desktop scanners are able to produce better results as the focus and lighting during the image capture are constant. (Martinez et al., 2010)

Detectors such as spectrophotometers, charge-coupled devices (CCD) and complementary metal-oxide sensors (CMOS) are also used for colourimetric detection and are relatively inexpensive and user-friendly (Pires et al., 2014; Schwarz & Hauser, 2001).

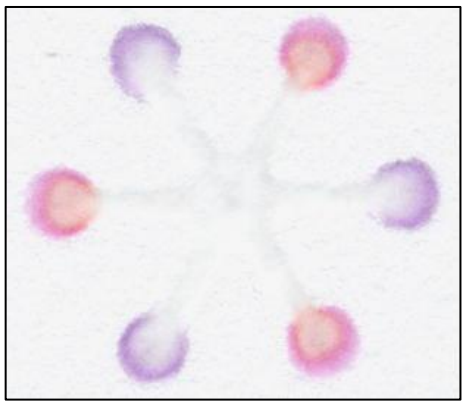

Figure 2.11 Colourimetric detection on a µPAD with multiple detection zones for uric acid (purple zones) and NO_2^- (pink zones) (Li et al., 2010).

2.5.2 Electrochemical method

Electrochemical detection requires electrodes or probes, which interact with chemicals to produce varying electrical signals allowing for the quantitative analysis of sample (Pires et al., 2014). There are two principles in electrochemistry, these being: (i) chemical reactions occurring due to a flow of electrical current through the electrode system, or (ii) electrode response as a result of chemical reactions (Pires et al., 2014). For electrochemical detection of analytes, a three-electrode system is generally required, which consists of a counter electrode, reference electrode and an operational electrode (Liana et al., 2012). The operational electrode detects the analyte, the reference electrode undergoes the standard oxidation/reduction and the counter electrode minimises the electric current flowing within the reference electrode, which is important in keeping a constant potential (Pires et al., 2014). This system must be installed onto the paper substrate through an additional step in the fabrication process, where the electrodes (usually conductive inks), are added (Liana et al., 2012). Voltammetry, the study of the relationship between potential and current, is used for analysis of results (Flanagan et al., 2005). A potentiostat, which is low in power, is required for detection of voltages in assays. Various inks can be used for detection, however the most common are carbon inks for the operational and counter electrodes and silver/silver chloride ink for the reference electrode (Nie et al., 2010; Dungchai et al., 2009).

Dungchai et al. (2009) pioneered the use of electrochemical detection for analysis of glucose, lactate and uric acid on µPADs, using cyclic and square wave voltammetry (as seen in Figure 2.12). A study conducted by Nie et al. (2010) used a four electrode system: a working electrode, a counter electrode and two reference electrodes all produced from graphite ink, with silver ink electronic wires. A handheld glucometer was used to analyse glucose and alcohol content (Nie, et al., 2010).

Electrochemical detection is well suited for application in µPADs as it is highly sensitive, gives a rapid response and can be performed on a wide range of analytes (Nie et al., 2010).

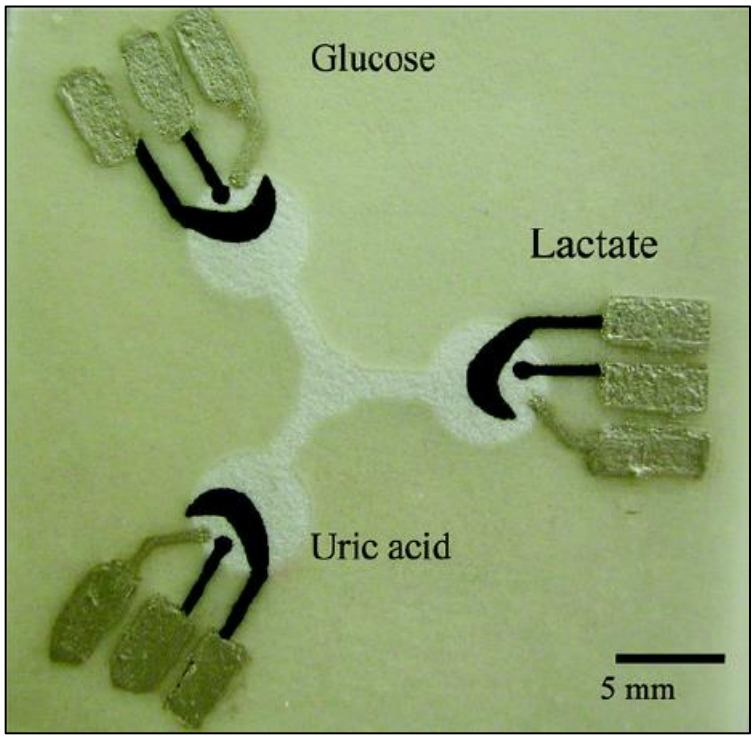

Figure 2.12 µPAD with electrochemical detection, using a three electrode system, for analysis of glucose, lactate and uric acid (Dungchai et al., 2009).

2.5.3 Electrical conductivity

Electrical conductivity detection determines the changes in conductance of a material in contact with a chemical substance for quantitative analysis (Liana et al., 2012). There have only been a few studies on this method, with only gas phase applications. Arena et al. (2010)

performed studies for ethanol detection by measuring the current in the air using triangular applied voltage.

2.5.4 Chemiluminescence and electrochemiluminescence

Chemiluminescence detection is an optical detection technique in which a reaction is caused by the addition of a chemical substance to the analytes to produce a photochemical emission, which in turn can be related to the concentration of analyte in the sample (Ge et al., 2012). This method provides simplicity, portability and low cost, which is well suited for use in µPADs (Ge et al., 2012). An additional advantage is that excitation light sources and emission filters are not necessary; however highly sensitive, specialised equipment is required for accurate analysis (Pires et al., 2014). Yu et al. (2011) used chemiluminescence for detection of glucose and uric acid through the reaction rhodamine derivative and hydrogen peroxide.

Electrochemiluminescence detection combines the principles of chemiluminescence and electrochemistry for increased selectivity. Both these techniques are conducted in the dark to avoid disturbance caused by ambient light (Li et al., 2012).

2.5.5 Interpretation of data

Despite the simplicity of µPADs, trained healthcare workers are still required for interpretation of results and prescribing treatment accordingly. Trained personnel are scarce in developing countries and it is an expensive feat transporting them into rural areas. Telemedicine is an attractive solution for providing healthcare in remote areas, where untrained personnel can assist in the testing, while professionals can be contacted by telephone for diagnosis. This operation involves a technician, with little medical training, conducting tests using µPADs. Thereafter, photographing results using a camera phone and sending results to a laboratory, where an expert will interpret the data and reply with proper treatment through text message or a phone call (Martinez et al., 2010).

A limitation of telemedicine is the interpretation of images in the laboratory. Images are dependent on the resolution of the camera, focus of the image and environmental conditions,

such as the lighting (Martinez et al., 2010). These problems may be solved through a printed calibration chart on µPADs.

2.6 Applications of paper-based microfluidic devices

Paper-based microfluidic devices were developed as a means for inexpensive, simple and rapid diagnostics for people living in developing countries. Applications of µPADs can be categorised into two groups, namely "on-demand" and "ready-to-use" devices. "On-demand" devices are blank µPADs, where users are required to select reagents prior to testing based on samples being analysed. "Ready-to-use" devices are inclusive of reagents in detection zones and are specifically designed for testing of particular samples, depending on reagents deposited. Most of the µPADs developed are in the "ready-to-use" category, with numerous applications found in the medical, pharmaceutical and environmental fields (Li et al., 2012).

2.6.1 Medical applications

Bodily fluids carry important information, which can be helpful in the detection of diseases in the human body. Blood, saliva, urine and tears have been used for various µPAD diagnostic tests and are discussed in detail.

2.6.1.1 Blood

Whole blood consists of approximately 55% plasma while the remaining 45% are formed elements, which are made up of blood cells (i.e. erythrocytes and leukocytes) and platelets (Virtual Medical Centre, 2015). It has three major functions in the body: (i) transportation of gases, nutrients, waste products, hormones and heat; (ii) protection in the form of leukocytes and antibodies; and (iii) regulation of pH and water balance (Virtual Medical Centre, 2015).

Using whole blood in diagnostics often requires separation of plasma from the formed elements. This is generally done by centrifugation, however other methods are required for use in paper-based microfluidics. Incorporating blood separation membranes have been common practice in many assays. Songjaroen et al. (2012) developed a µPAD using this technique for quantification of proteins. Noiphung et al. (2013) used whole blood samples for

determination of glucose content using electrochemical detection. The plasma from the blood was isolated through a separating zone in the device and subsequently used in the assay (Noiphung et al., 2013). Vella et al. (2012) used a blood filter membrane to separate plasma from erythrocytes for liver function analysis, which detects alkaline phosphate (ALP) and aspartate aminotransferase (AST).

Another approach for plasma separation is through erythrocyte agglutination, allowing for plasma to flow through the paper substrate (Yang et al., 2012). Using this technique, Yang (2013) investigated the use of µPADs for diagnosis of sickle cell disease based on the solubility of haemoglobin [Hb]. The test uses a drop of blood mixed with a solution for solubility of Hb, which is deposited onto a chromatography paper (Yang, 2013). The pattern created by the blood indicates the presence or absence of sickle cell disease in the patient. If the blood solution is absorbed by the substrate, the patient is healthy. However, if the blood solution forms a layer on the surface of the substrate, the patient has sickle cell disease.

2.6.1.2 Saliva

Saliva is a secretion produced by the salivary gland consisting of approximately 99% water and the remaining 1% is made up of numerous electrolytes, proteins, immunoglobulins and other compounds such as albumin. Glucose and nitrogenous compounds are also present. Saliva has a variety of functions. It aids in the digestion process, assists in acid neutralisation and kills certain types of bacteria. Other functions include assisting in: (i) taste, (ii) protection and lubrication, (iii) dilution and cleaning, and (iv) maintaining integrity of tooth enamel for prevention of tooth decay (De Almeida et al., 2008).

Nitrite in saliva has been proposed to have a link to the occurrence of periodontitis, a gum disease caused by plaque build-up below the gum line (American Academy of Periodontology, 2015). Bhakta et al. (2014) developed a µPAD for the quantification of nitrite through colourimetric detection.

2.6.1.3 Urine

Urine is a liquid waste product secreted by the kidneys with a composition of 95% water and 5% solutes. The solutes contain a wide variety of compounds such as urea, sodium chloride, potassium chloride, creatinine, uric acid, phosphates, sulphates, calcium and magnesium. A

variety of diseases can cause abnormal compounds to be found in urine such as glucose, free [Hb], albumin, ketones and bile pigments (Saladin, 2010).
Urine tests are also useful for detection of alcohol or illegal drugs for application in competitive sports. Early pregnancy tests use lateral flow assays to detect the presence of human chorionic gonadotropin in urine, which can be detected within 6 to 12 days after fertilisation (Sino Biological Inc., 2015).

In paper-based microfluidics, urinalysis has been used in detection of glucose and proteins on 3D µPADs (Sechi et al., 2013). Glucose in urine is an indication of diabetes, whereas protein in urine could be an early sign of kidney disease (American Kidney Fund, 2015). Klasner et al. (2010) used µPADs to monitor glucose and ketone levels in urine for detection of diabetes.

2.6.1.4 Tears

Tears are a secretion from the lacrimal gland, which acts as transportation and excretion of nutrients and metabolic products. In addition, it provides protection and lubrication for the eye. Human tears usually consist of water, electrolytes, proteins, lipids, mucins and other small compounds (Tiffany, 2003).

Yamada et al. (2014) focussed on the fabrication of µPADs through inkjet printing for detection of lactoferrin, a glycoprotein, in tear fluid. Protein is important in protection of the eye, therefore a low level of lactoferrin indicates poor ocular health.

2.6.2 Pharmaceutical applications

Paper-based microfluidic devices have recently been investigated in the pharmaceutical industry, where two studies have shown promising results. Weaver et al. (2013) have designed µPADs for detection of substandard medication through the screening of ampicillin, amoxicillin, rifampicin, isoniazid, ethambutol and pyrazinamide and certain substitute compounds for beta-lactam antibiotics and antituberculosis medication. Koesdjojo et al. (2014) used a similar concept, using µPADs for detection of counterfeit antimalarial drugs.

2.6.3 Environmental applications

An increase in environmental awareness has led to the development of µPADs for usage in the environmental field. It has become appealing, when compared to the current detection methods, due to it's low-cost and accurate testing abilities.

2.6.3.1 Airborne

Exposure to harmful particulate matter (PM) in the air can bring about severe and numerous health issues. High levels of exposure to these PM can cause health issues relating to: (i) pulmonary diseases, (ii) cardiovascular diseases, (iii) cerebrovascular diseases, (iv) cancer, and (v) neurodevelopmental diseases (Oregon PSR, 2015).

Various metals, such as chromium, iron, nickel and copper, have been used for production of pigment dyes, plastics, coatings and various other products, however have harmful effects when inhaled (Rattanarat et al., 2013). This is a cause for concern as these metals, when inhaled, affects the respiratory, digestive, reproductive, developmental, immune and haematological systems and is carcinogenic (Rattanarat et al., 2013).

Rattanarat et al. (2013) used wax printing and colourimetric detection for determination of chromium in PM. Mentele et al. (2012) and Cate et al. (2015) developed colourimetric assays for detection of iron, nickel and copper. Sameenoi et al. (2013) have developed a method for measuring the toxicity of PM through the determination of its oxidative activity using µPADs.

2.6.3.2 Waterborne

Contamination of water supplies causes a great problem currently due to the health concerns associated with it. Nitrate contamination from fertilisers, animal waste and disposal of sewage is a high risk in many areas (Kurunc et al., 2011). Nitrates and nitrites pose a threat due to their high water solubility, low soil retention and inability to be volatised, thus remaining in the water source until consumption by organisms (Kurunc et al., 2011). These compounds are carcinogenic and can lead to methemoglobinemia, a blood disorder which produces an abnormal amount of methemoglobin, if ingested (Kurunc et al., 2011).

Jayawardane et al. (2014) fabricated a low-cost µPAD for the determination of nitrate and nitrite levels in water sources.

Cadmium and lead contamination were also studied due to their harmful effects if ingested. Water containing cadmium can lead to kidney damage, while lead affects kidneys, reproductive and nervous systems and can cause developmental defects, high blood pressure and anaemia (World Health Organization, 2001). Dirty groundwater was tested for the presence of cadmium and lead using electrochemical detection (Shi et al., 2012). In the same manner, salty soda water was also tested for signs of cadmium and lead (Shi et al., 2012).

2.7 Limitations

Paper-based microfluidic devices have been able to provide a cost-effective, rapid and simple approach to point-of-care diagnostics. However, as research is still in its early stages, there are limitations with regards to its clinical performance, substrate characteristics, fabrication techniques and detection methods (Hu et al., 2014; Li et al., 2012). Paper-based microfluidic devices have been criticised for its varying sensitivity and specificity, which can result in false-positives and false-negatives (Hu et al., 2014). This can have psychological consequences for end-users and can lead to suicide in extreme cases. Improvement in performance of µPADs should focus on four major aspects, these being: (i) detection methods, as results can vary depending on end-user, and in the case of colourimetric testing, low concentrations of substances can go undetected; (ii) coupling of detection methods, substrates and fabrication techniques; (iii) environmental factors and (iv) reproducibility of the tests (Hu et al., 2014).

The operation of µPADs also has certain limitations. The transport of fluid through the channels has a low efficiency due to evaporation occurring (Li, et al., 2012). The volume of sample arriving at detection zone compared to the sample entering the system is reported to be less than 50% (Li et al., 2012). Patterning with certain hydrophobic agents has limitations as the strength of the hydrophobic barriers formed is weak and cannot withstand fluids with low surface tensions. (Li et al., 2012).

2.8 Future perspectives

With paper-based diagnostics being a fairly new concept, there are opportunities for further development and improvement in the field. Currently, studies have been conducted on chemically and biologically complex assays. However, research into 3D assays for multiple reactions is required for solving these complex problems (Cate et al., 2015).

As was discussed, µPADs have a variety of applications from medical to environmental purposes. Although there has been rapid development, expansion in applications must be focussed on, for example, the introduction of µPADs in the food and beverage industry for detection of unwanted compounds.

Various paper substrates should be designed for specified use in point-of-care diagnostics. Paper sheet structures, integration of novel and biofunctional materials (such as nanoparticles) into substrates through polyelectrolytes and printing technology will increase capabilities of µPADs (Ngo et al., 2011; Olkkonen et al., 2010).

Transportation of fluid through paper substrates is an area that should gain interest in the future. Lateral and vertical flow can be investigated for control of sample in the channels (Cate et al., 2015).

Emphasis on read-out from the tests may lead to new display methods. Text displays may gain popularity as it is simple and user-friendly (Li et al., 2012).

2.9 Conclusions

As seen from the overview provided, there have been various studies conducted in the field of paper-based microfluidic devices. However, a large majority of the research focuses on the applications of µPADs, more specifically in the pharmaceutical, environmental and medical fields. Another area of research which has been on the increase, as seen from the literature, is the addition of functionalities to microfluidic devices, such as switches and valves.

From the literature provided, it can be seen that minimal research has been conducted on the types of substrates used in µPADs. Although previous work has shown the use of various substrates, such as filter and chromatograph paper, the focus has not been on which of the substrates would be better suited for µPAD production. The gaps in this overview will be addressed in this study, to increase the knowledge base in this field.

CHAPTER 3: MATERIALS AND METHODS

3.1 Introduction

This chapter will provide an overview of the materials used in experimentation, as well the equipment used to reach the objectives of the study. A short description of the equipment is given, with the major equipment overview provided in Appendix A. In addition, an overview of the experimental procedures followed during the study is provided. The chapter is divided into 6 sub-sections, these being the source of paper substrates, materials used, equipment used, research protocol, methodology and limitations, and recommendations.

3.2 Source of paper substrates

Pulp for the production of handsheets was sourced from various mills around KwaZulu-Natal. Paper substrates were sourced from Capital Lab Suppliers in Durban. The nanofibrillation of pulp was conducted at the CSIR in Port Elizabeth. Table 3.1 lists the sources of the different pulp and paper substrates used in the study.

Table 3.1 showing the source of pulp and paper substrates used in experimentation.

Type of pulp/substrate	Source
Bleached Kraft	CSIR Durban
Bleached Sulphite	CSIR Durban
Bleached Thermo-mechanical	Mondi Merebank
Unbleached Recycled	Mondi Merebank
Unbleached Kraft	CSIR Durban
Nanofibrillated unbleached kraft	CSIR Port Elizabeth
Nanofibrillated bleached sulphite	CSIR Port Elizabeth
Nanofibrillated Whatman 3MM	CSIR Port Elizabeth
Nanofibrillated unbleached recycled	CSIR Port Elizabeth
Nanofibrillated Whatman No. 1	CSIR Port Elizabeth
Whatman No.1	Capital Lab Suppliers
Whatman 3MM	Capital Lab Suppliers
Whatman Glass Fibre Filters GF/D	Capital Lab Suppliers

Whatman No.1 Chromatography Filter Paper (CHR) and Whatman 3MM Chromatography Filter Paper (CHR3) sheets were commercially produced, through the use of a Fourdrinier machine. Pure cellulose was used to produce the filter papers. Repulping and further disintegration of the filter paper could result in fines to be formed, which could in turn resist the motion of liquid through the sheet.

3.3 Materials used in experiments

For each experiment conducted, a number of different materials were used, besides the pulp and paper substrates mentioned in 3.2. These are summarised in Table 3.2.

Table 3.2 showing materials used in each experiment.

Materials	Description
Hydrogen peroxide Sodium hydroxide Sodium metasilicate Sodium hydrosulfite	Bleaching agents
Water	Dilution of pulp
Pulp	Produce handsheets
Food dye	Wicking liquid
Glycerol	Wicking liquid
Wax	Solid wax printing
NFC	Addition to pulps to produce handsheets

The wicking liquids used were yellow food dye and a blood simulant consisting of a mixture of glycerol and water, at a ratio of 52:48. These liquids were chosen to represent bodily fluids that would normally be used in µPADs in medical applications. The properties of the wicking liquids can be seen in Table 3.3.

Table 3.3 showing the properties of the wicking liquids in comparison to bodily fluids

	Food dye		**Glycerol-water**
Comparative bodily fluid	Tears, saliva, urine		Blood
Dynamic viscosity	Saliva (mixed) Urine	1.0 cP (Davis, 1970) 1.1 cP (Putnam, 1971)	3.2 cP
Colour	Colourless		Dark brown/ red

* cP represents centipoise

3.4 Equipment used

A description of the major equipment used in this study is summarised in Table 3.4. A detailed description of the equipment is available in Appendix A.

Table 3.4 showing the major equipment used during experimentation.

Experiment	Equipment	Description
Bleaching (Recycled pulp only)	Water bath	Medium for bleaching to occur
Handsheet making	Rapid Kothen sheet former	Handsheet formation
	Oven	For consistency tests
	Scale	Weighing samples for consistency tests
	Dryer	Drying of the handsheet after handsheet formation
	Disintegrator	Separation of pulp fibres, preparing it for handsheet making
	Stock divider	Provides constant mixing of pulp mixture for uniformity of handsheets
Nanofibrillation	Super mass colloider	Grinding of the pulp fibres to produce nanofibrils
Wicking tests	Beakers	Reservoirs for wicking liquid
	Stopwatch	Timing of wicking rates
Field emission gun-scanning electron microscopy	Carl Zeiss Ultra Plus FEG-SEM	Microscopy imaging of paper samples for analysis
	Polaron SC500 sputter coater	Coating of sample with gold
Solid wax printing	Wax printer Xerox ColorQube 8870	Printing of wax onto paper substrates
Contact angle measurement	DataPhysics Optical Contact Angle 15EC	Measurement of contact angle between surface of substrate and drop

3.5 Research Protocol

The research protocol shows the general guideline followed for setting out experiments for the study, with details in the subsequent methodology section.

- Obtain Whatman paper substrates from lab suppliers
- Produce handsheets from pulp
- Produce nanofibrillated pulp for handsheet making
- Conduct wicking tests on the paper substrates
- Put paper through channel printer for production of hydrophobic barriers and analyse the feasibility of using paper in this capacity
- Conduct field emission gun-scanning electron microscopy experiments
- Conduct contact angle experiments
- Evaluate the microfluidics of resulting paper and compare the different pulp to determine which is the most suitable for application in diagnostic devices

A detailed diagram summarising the research steps taken in this study can be seen in Figure 3.1.

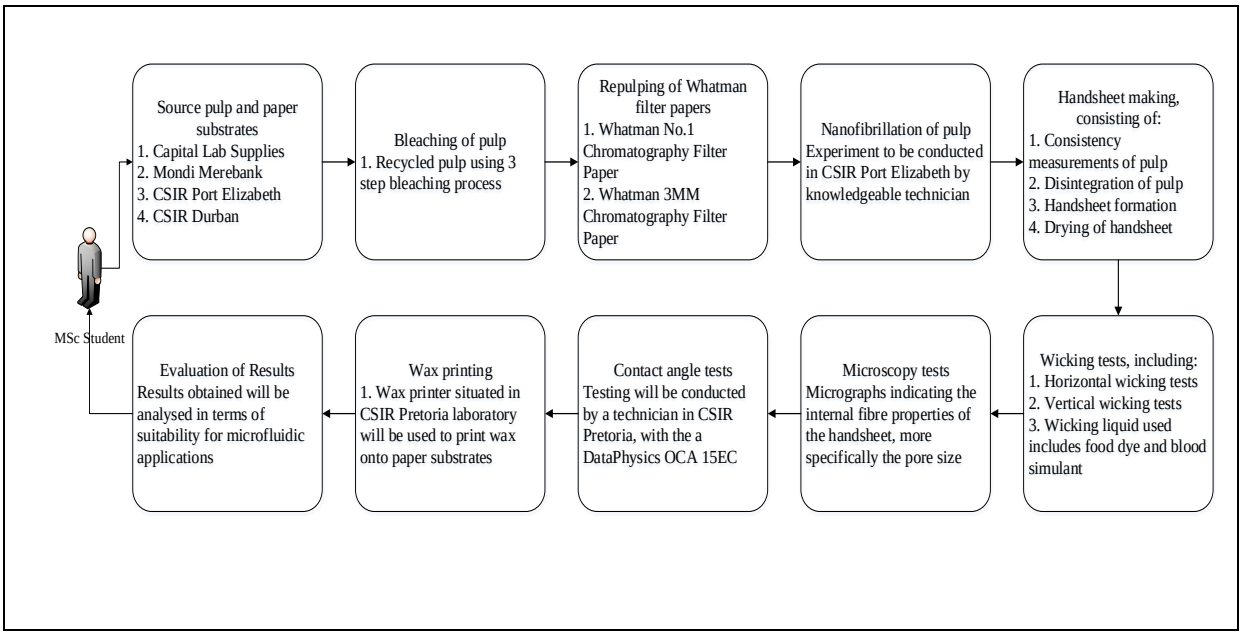

Figure 3.1: Summary of research protocol.

3.6 Methodology

3.6.1 Bleaching

Bleaching was conducted for the recycled pulp. A bleaching process called P-FAS-P bleaching process with the following 3 stages was carried out:

Hydrogen peroxide (1st stage) – P

Sodium hydrosulfite (2nd stage) – FAS

Hydrogen peroxide (3rd stage) – P

Table 3.5 shows the bleaching conditions for each stage.

Table 3.5 showing the bleaching conditions used for recycled pulp.

Conditions	P bleaching	FAS bleaching
Dosages (%) *		
Hydrogen peroxide	2	-
Sodium hydroxide	1.5	-
Sodium silicate	1	-
Sodium hydrosulfite	-	1
pH	9 – 11	6 – 7
Temperature (ºC)	60	60
Consistency (%)	15	15
Duration (hr)	3	1
* based on oven dry pulp mass		

The moisture of the pulp sample was determined. This was done by weighing out a sample of pulp (approximately 5 g) and drying the sample overnight in an oven. The oven dried sample was weighed and the moisture was calculated using the following equation (3.1):

$$Moisture\ (\%) = \frac{wet\ pulp\ weight - dry\ pulp\ weight}{wet\ pulp\ weight}\ x\ 100 \qquad (3.1)$$

The moisture content was used to calculate the weight of dry pulp in the sample.

The pulp was diluted to the desired consistency of 15% through the addition of deionised water. The amount of water added was determined by using equation (3.2):

$$Mass\ of\ water\ to\ add = \frac{Dry\ pulp\ mass}{Desired\ consistency} - amount\ of\ H_2O_2 - initial\ wet\ pulp\ mass \quad (3.2)$$

The pulp was added to a plastic bag together with the bleaching chemicals (indicated in Table 3.4). The pulp was mixed thoroughly and placed in a water bath set at the 60ºC for the duration stipulated in Table 3.4. Thereafter, the pulp was washed with water using filtration to remove the bleaching chemicals. The washed pulp was spin-dried for 10 minutes and moisture content was calculated using equation 3.1. This method was followed for each of the three stages.

3.6.2 Repulping

The Whatman filter papers (No. 1 and 3MM) were repulped in preparation for handsheet making. This was done in order to keep the grammage of the paper substrates consistent for comparison purposes. The filter papers were shredded and soaked in water overnight. Thereafter, the soaked paper was disintegrated for 10 minutes, which created pulp for handsheet making.

3.6.3 Nanofibrillation of pulp

Nanofibrillation of the pulp was conducted to determine the effect of the addition of smaller fibres on the wicking ability of the paper substrate. This experiment was conducted by a trained technician, with the use of a super mass colloider.

2% of sample (cellulosic material) was soaked in water overnight. The samples were dispersed by mechanical stirring for 30 minutes at a speed of 1000 rpm. The samples were subsequently subjected to treatment in a super mass colloider (model: MKCA6-3, Masuko Sangyo Co, Ltd., Japan) at a speed of 1500 rpm. The samples were allowed to pass 10 times at 0 spaces between grinding stones and then 15 times at minus 160 microns to obtain very fine materials.

3.6.4 Handsheet making

Before handsheet making could take place, the moisture content of the pulp samples was determined using equation 3.1. Thirty grams of oven dry equivalent pulp was weighed out and added to the disintegrator. Approximately 1L of water was also added and the pulp suspension was disintegrated for 5 minutes. The disintegrated pulp was then added to the stock divider, into which air was injected in order to continuously mix the pulp. Water was added to pulp to a total volume of 11 L, resulting in a stock solution of 0.3% consistency. A 1 L aliquot of the pulp suspension was then taken out to make a test sheet, to ensure that the handsheet produced was within the desired grammage range of 90 (±1) g/m^2. 1L aliquots were added to the Rapid Kothen sheet former to produce the handsheets. The handsheets were pressed for 5 minutes to remove excess water. Thereafter, the handsheets were dried for 4 minutes and placed in the oven for 1 minute. The resulting handsheets were weighed. If the test handsheet was not in the required range of between 2.85 and 2.91 g, water was either removed (in the case of the sheet weight being below the range value) or added (in the case where the sheet was too heavy), which was determined by equations 3.3 and 3.4. When the handsheet produced was within the acceptable range, the remaining pulp solution was used to produce handsheets, following the procedure mentioned.

$$Total\ Volume = \frac{Volume\ of\ water\ remaining\ in\ divider \times weight\ of\ handsheet\ produced}{1.885} \tag{3.3}$$

$$Volume\ to\ remove\ or\ add = Total\ Volume - Volume\ remaining \tag{3.4}$$

3.6.5 Wicking tests

Wicking tests were used to determine the rate at which liquids absorb into the paper substrates. Horizontal and vertical wicking tests were conducted on each of the paper substrates. The handsheet was cut into 12 cm × 2 cm strips in preparation for the wicking tests. Markings were made on the sheets at 1 cm intervals along the length of the strip. Each experiment was conducted in triplicate for data integrity and accuracy. The wicking liquids, mentioned in section 3.3, were used in the experimentation.

3.6.5.1 Horizontal wicking

Horizontal wicking was conducted in a temperature controlled environment, using constant temperature surroundings of 23ºC. Each strip of paper substrate was placed in a reservoir of liquid, approximately 1 cm deep, positioned in a horizontal orientation supported by a block (see Figure 3.2). Once the liquid reached the 0 cm mark on the strip, the stopwatch was started. For each centimeter of liquid wicked, a time was recorded, eventually reaching the 10 cm mark, whereby the experiment ended.

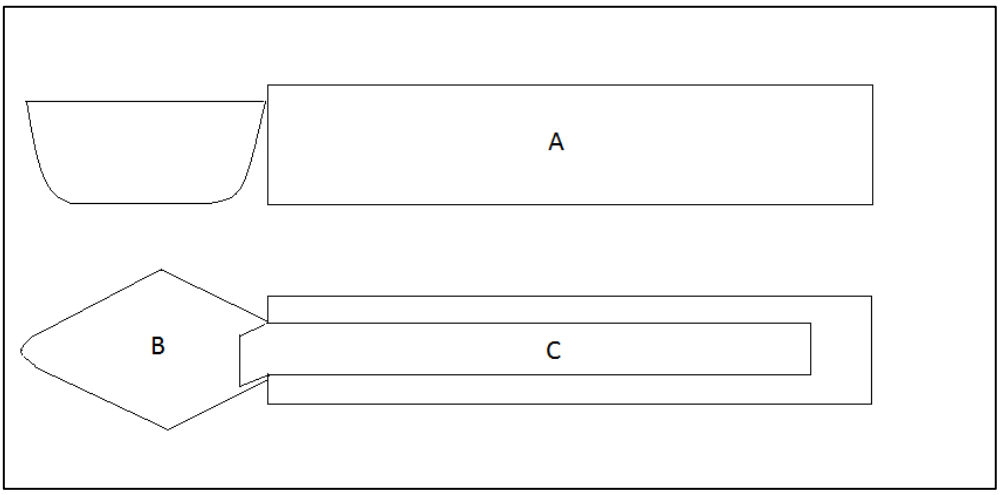

Figure 3.2: Set-up for horizontal wicking, where A is the horizontal support for the paper substrate, B is the reservoir for the wicking liquid and C is the paper substrate.

3.6.5.2 Vertical wicking

Vertical wicking tests were conducted in the same environment as the horizontal wicking tests. The paper substrate strip was placed in a reservoir of wicking liquid (see Figure 3.3 for set-up). The time was recorded on a stopwatch as soon as the liquid reached the 0 cm mark. For each centimeter wicked, a time was recorded until 10 cm was reached.

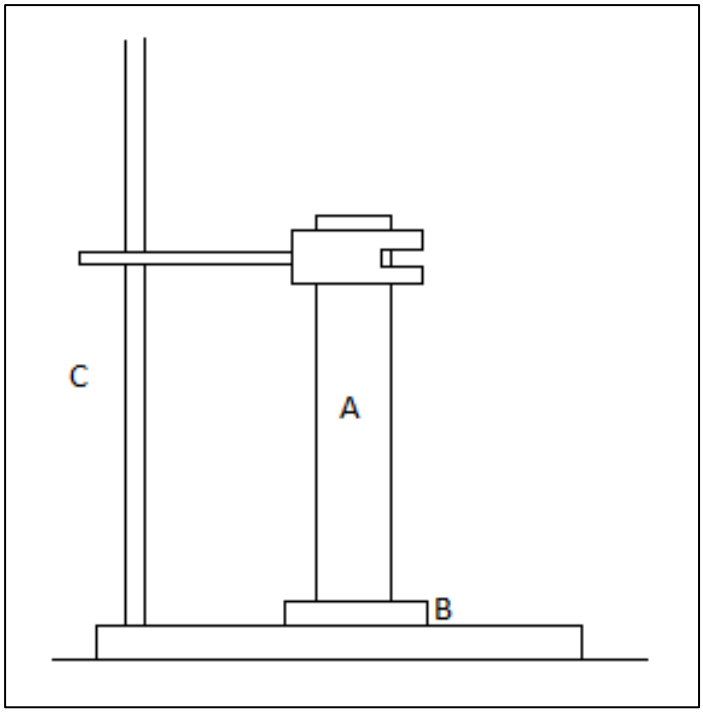

Figure 3.3: Set-up for vertical wicking, where A is the paper substrate, B is the reservoir for wicking liquid and C is a burette stand to hold paper in a vertical position vertical wicking.

3.6.6 Field emission gun-scanning electron microscopy

The microscopy was conducted by a trained technician, using Field Emission Gun-Scanning Electron Microscopy (FEG-SEM). The sheet samples were oven-dried to ensure no moisture was present during experimentation. The dry samples were mounted on aluminium stubs using double-sided carbon tape. Thereafter, a Polaron SV500 sputter coater was used to coat the samples with gold and observed using a Carl Zeiss Ultra Plus FEG-SEM at an accelerating voltage of 5 kV. Various magnifications, ranging from 100× to 20 000×, were used to obtain the FEG-SEM images.

3.6.7 Contact angle measurements

The contact angle test was used to determine the wettability and in turn the hydrophobicity of the substrates. Determining these properties was essential for understanding the transport of liquid through the sheet, which was used to investigate the feasibility of the substrate to be used in the fabrication of µPADs.

The experiment was conducted by a trained technician. The contact angle measurements were recorded at room temperature using a DataPhysics Optical Contact Angle (OCA) 15EC, which was equipped with video capture. Five measurements were conducted for each substrate at different positions per sample. The contact angle was recorded and images were taken for samples where the droplet remained on the sheet for a period of 30 seconds. The contact angle for the samples which immediately absorbed the droplet, within 5 seconds, could not be measured.

3.6.8 Solid wax printing

Solid wax printing is one of the most common fabrication techniques for µPAD production. The solid wax printing test was conducted to determine which of the paper substrates would be suitable for this fabrication technique for application in microfluidic devices.

A standard procedure for solid wax printing was performed by a trained technician. The Y-shaped design used for the wax printing was prepared in computer-aided design (CAD). The design was printed on the sheets that were produced using the method described in section 3.6.3. The Xerox ColorQube 8870 wax printer was used, with black solid wax cartridges. The wax was melted to form droplets and distributed on the paper surface, with a line width of 0.4 mm. Once the wax contacted the paper surface, the wax droplets reverted back to the solid phase. Thereafter, the paper sheet was placed onto a hot plate at 120ºC in order for penetration of wax through the sheet. A stopwatch was used to record the time taken for the wax to fully melt through the sheet. The depth through which the wax penetrated was analysed visually, which resulted in a wax penetration as a percentage.

3.7 Limitations and Recommendations

- For the wicking tests, timing of the wicking rate was done manually, therefore experimentation took a longer period of time. For future investigations, an electronic timing approach could be used, together with a camera to record the experiment, to improve the accuracy of the results obtained.
- In this study, a more qualitative approach was adopted for sheet properties, more specifically for the pore size analysis. In future studies, a quantitative approach could be used, such a mercury porosimetry, for in-depth analysis of the substrates.
- Other methods of fabrication could be investigated, which would assist in determining the substrates suitable for use in µPAD production.

3.8 Conclusions

This chapter gives an overview and description of equipment and materials used. In addition, methodologies followed for each experiment is described, with further detail given in Appendix A. It serves as a prelude to Chapter 4 to Chapter 7, which contains the results and discussions of the experiments conducted, giving context to the results obtained.

CHAPTER 4: MORPHOLOGY AND PORE SIZE OF BASE AND NANOFIBRILLATED SUBSTRATES

4.1 Introduction

The wicking ability of paper substrates is strongly dependent on the porosity of the sheet. Therefore, field emission gun-scanning electron microscopy (FEG-SEM) was conducted to observe the differences in sheet pore sizes for each of the different substrates. This chapter provides the differences between each substrate in terms of the pore sizes of the sheets used, which will then be referenced when discussing the wicking tests results (in Chapter 6). In this thesis, pore size was defined as the spaces between the fibre particles that form part of the sheet structure.

This chapter is split into 2 subsections. Section 4.2 focuses on the base substrate results and provides a comparison between these substrates. Section 4.3 focuses on the comparison between base substrates and NFC (20%, 50% and 100%) substrate results. The images displayed were taken at 200× and 500× magnification for the surface and cross-sectional images, respectively.

4.2 RESULTS AND DISCUSSION

4.2.1 Base Substrates

The FEG-SEM images obtained from the experiment can be seen in Figures 4.1 – 4.7. The movement of liquid through the sheet is highly dependent on the voids between the fibres in the sheet. Through visual observations, it was seen that each of the substrates have varying fibre network structures.

Evaluation of the sulphite (SULP) FEG-SEM images, Figure 4.1 showed that the sheet morphology contained long, rod-like fibres in a disorderly manner, with the formation of pores between the fibres. From the cross-sectional image, it can be observed that the fibre walls have collapsed implying that the fibre wall was thin, thereby compacting the fibres to form a tightly packed structure. Through the thickness of the sheet, it can be seen that spaces were formed between the fibres. These voids allowed for the movement of liquid through the sheet.

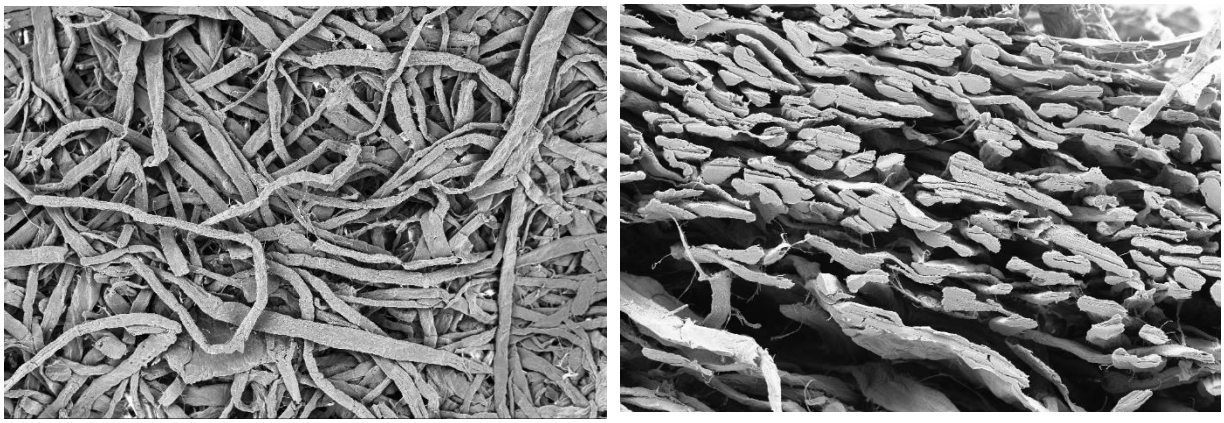

Figure 4.1: FEG-SEM images of SULP sheet showing surface images (left) at 200 × magnification and the cross-sectional image (right) at 500 × magnification.

Similar observations were seen with the bleached kraft (BK) sheet to that of the SULP sheet. Morphologically, the fibres followed the same pattern, whereby the surface image showed flat, rod-like structures, with pores in between the fibres. However, visual observation led to the conclusion that BK had smaller voids between the fibres, which would directly affect the transport of liquid through the sheet. Similarly, the cross-sectional image showed that the fibre walls were thin, shown by the collapsed walls. Through the compression of fibres in the handsheet making stage, it can be expected that the fibres were tightly packed. Small voids were seen between the fibres through which liquid flowed.

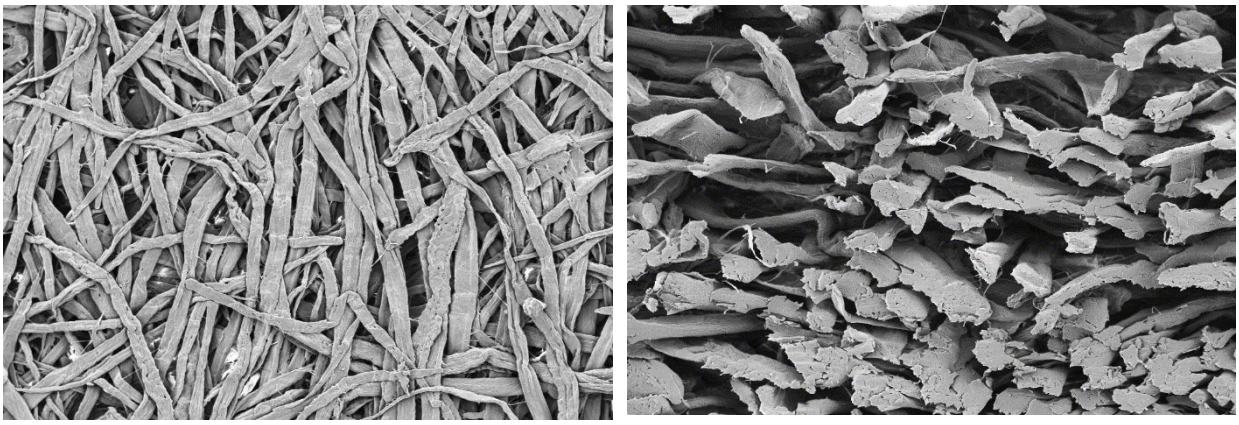

Figure 4.2: FEG-SEM images of BK sheet showing surface images (left) at 200 × magnification and the cross-sectional image (right) at 500 × magnification.

FEG-SEM images on the unbleached kraft (UBK) sheet showed slightly different structure to that of the BK and SULP. From the surface image, it can be seen that the fibres were more flat-shaped and broader. As a result, smaller pore sizes can be expected, which can be seen in Figure 4.3. From this, a slower wicking rate could be anticipated. In addition, the unbleached nature of the pulp would result in the presence of lignin, which would minimise the space available for liquid flow. The cross-sectional image showed similar results to the previous substrates. It can be observed that the fibres are tightly packed in the structure, with collapsed fibre walls. From one of the fibres in the image, it can be seen that the fibre wall was not fully collapsed, showing that the walls are thicker than the BK and SULP.

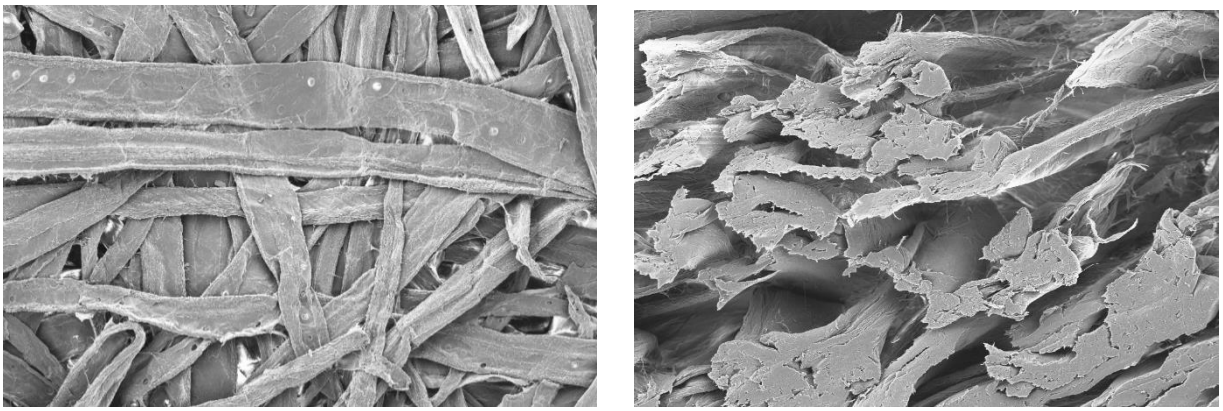

Figure 4.3: FEG-SEM images of UBK sheet showing surface images (left) at 200 × magnification and the cross-sectional image (right) at 500 × magnification.

Figure 4.4 shows the CHR sheet images with a fibre network is packed closely. The fibres were flat and thin, however the pore size can be seen to be smaller than the previous substrates. A slower wicking rate would be expected, when comparing SULP, BK and UBK, due to the limited space available for liquid absorption. The cross-sectional image also showed a tightly packed network with restricted space for flow of liquids.

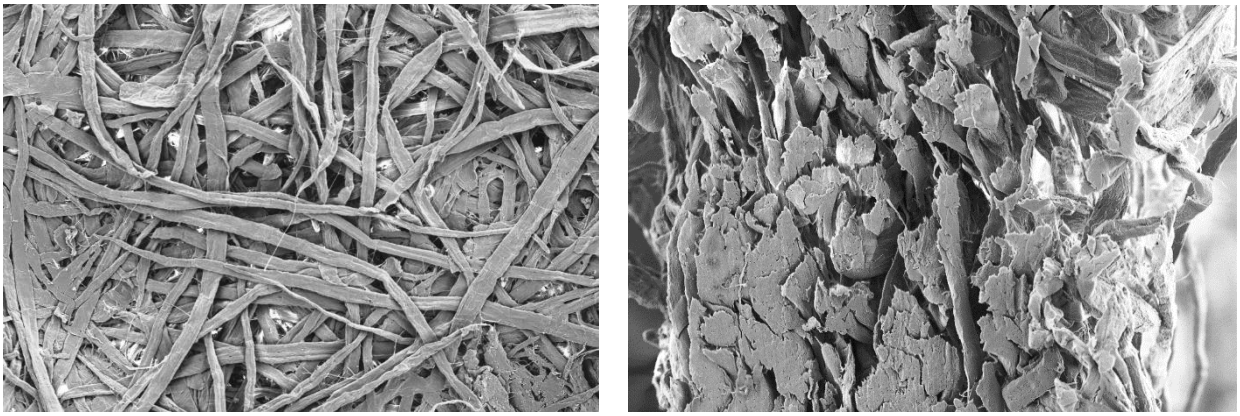

Figure 4.4: FEG-SEM images of CHR sheet showing surface images (left) at 200 × magnification and the cross-sectional image (right) at 500 × magnification.

The CHR3 image (Figure 4.5) showed a different network in comparison to the other substrates. It was observed that the fibre network contained fines, which were observed to fill the voids in the structure. This could result in the retardation of liquids through the sheet. The fibres were long and had a rod-like structure. The cross-sectional image showed that the fibres were fully collapsed from the handsheet making process. It can also be observed that the spaces between the fibres were larger, which could result in an improved rate of wicking within the sheet.

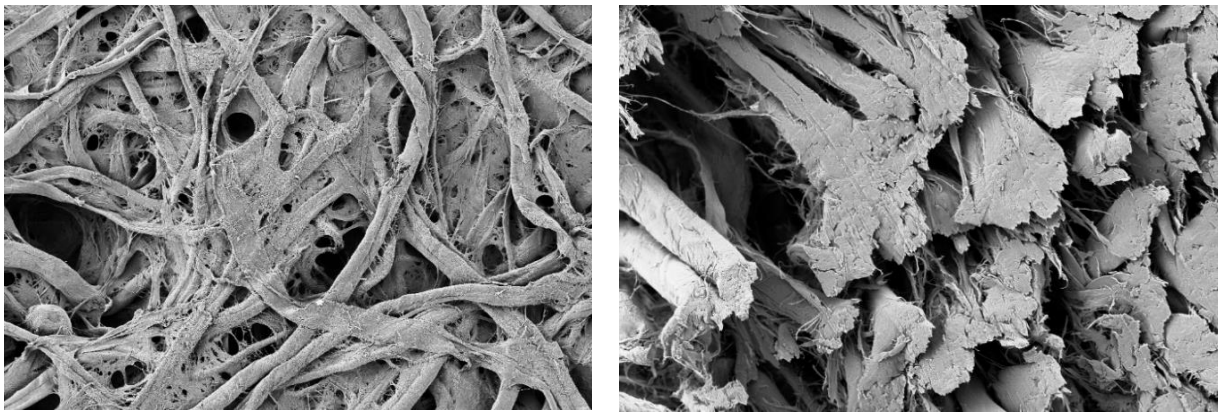

Figure 4.5: FEG-SEM images of CHR3 sheet showing surface images (left) at 200 × magnification and the cross-sectional image (right) at 500 × magnification.

The FEG-SEM images of the thermo-mechanical pulp (TMP) sheet showed a different morphology when compared to the previous sheet structures. Here it can be seen that the single fibres form a network where fibres are not defined, with very minimal voids in network structure. The composition of the pulp could result in this structure, whereby

contaminants and elements, such as lignin, were still present in the sheet. This can be directly related to the wicking ability of the sheet. A slower wicking rate could be expected from the smaller voids between the fibres. A compressed fibre structure could also be observed from the cross-sectional image. This is an additional factor affecting the wicking ability of the sheet, due to the minimal space between the fibres for possible liquid flow.

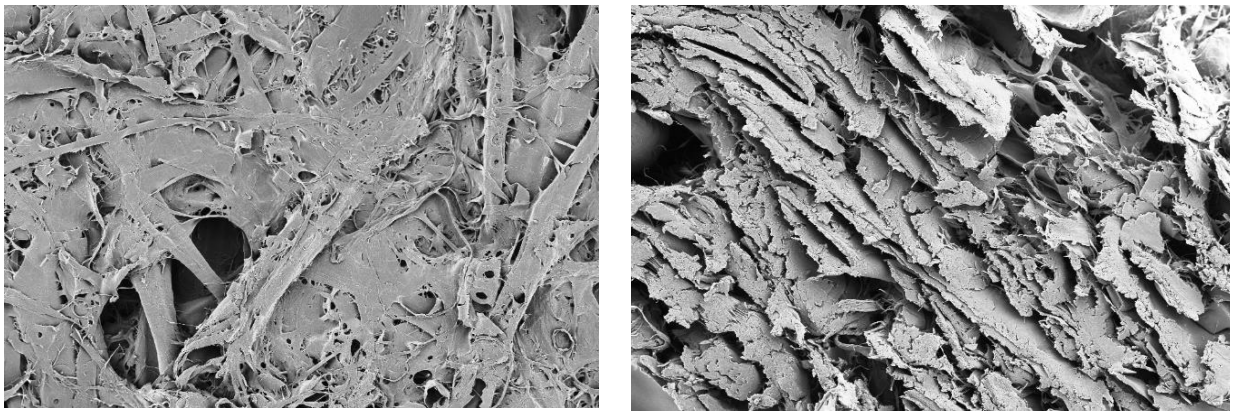

Figure 4.6: FEG-SEM images of TMP sheet showing surface images (left) at 200 × magnification and the cross-sectional image (right) at 500 × magnification.

The recycled (REC) sheet can be seen to have the smallest voids in between the fibres, as seen from Figure 4.7. It can be observed that the fibre coverage on the flat surface of the sheet was almost complete. Similar to that of the TMP sheet, the composition of the pulp was lignin, as well as contaminants such as inks and stickies found in the recycling process. The cross-sectional image showed that the fibres were compact during the handsheet making process. This was an added factor to the flow of liquid through the sheet. It can be expected that the wicking rate would be the slowest in comparison to the other substrates due to the minimal free capacity available for liquid flow.

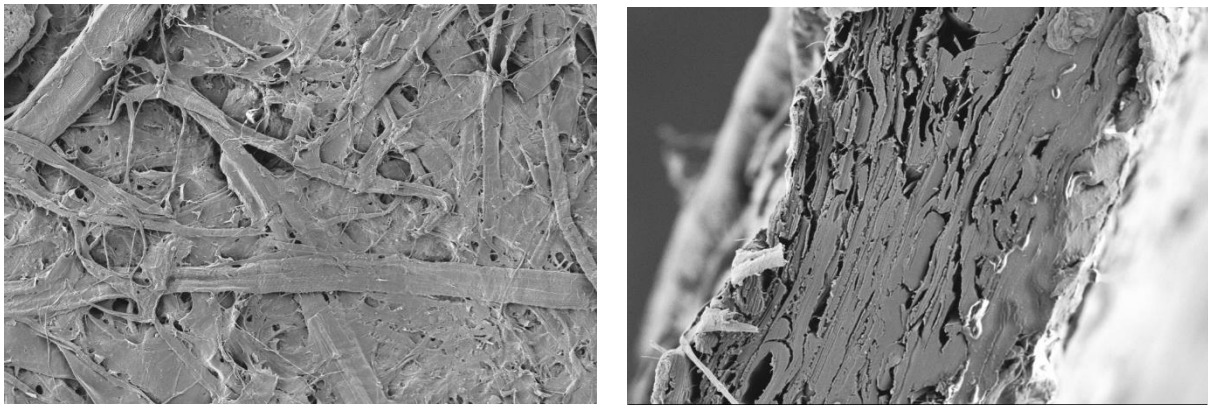

Figure 4.7: FEG-SEM images of REC sheet showing surface images (left) the cross-sectional image (right).

4.2.2 Nanofibrillated Substrates

Sulphite, unbleached kraft, Whatman No.1 chromatography filter paper, Whatman 3MM chromatography filter paper and recycled pulp underwent nanofibrillation, resulting in smaller fibres available for the formation of handsheets. The anticipated effect of the substitution of the nanofibrillated pulp should be a slower wicking rate, due to the expected smaller voids in the sheets.

Analysing the SULP sheets, in Figure 4.8, it can be seen from the surface images (A, C and E) that the voids between the fibres became progressively smaller as the NFC pulp in the sheet increased. This was expected as the fibres would form a tighter network with smaller fibres. In addition, through nanofibrillation, the production of fines increased, therefore reducing the voids between the fibre particles. The cross-sectional images (B, D and F) showed that with an increase in NFC pulp, the more compact the fibres network in the sheet. It can be seen from Figure 4.8 B that the fibres are clearly defined and separate. Moving towards Figure 4.8 F, it can be seen that the fibres are merged and closer together, thus resulting in smaller spaces for liquid motion and a slower wicking rate through the sheet.

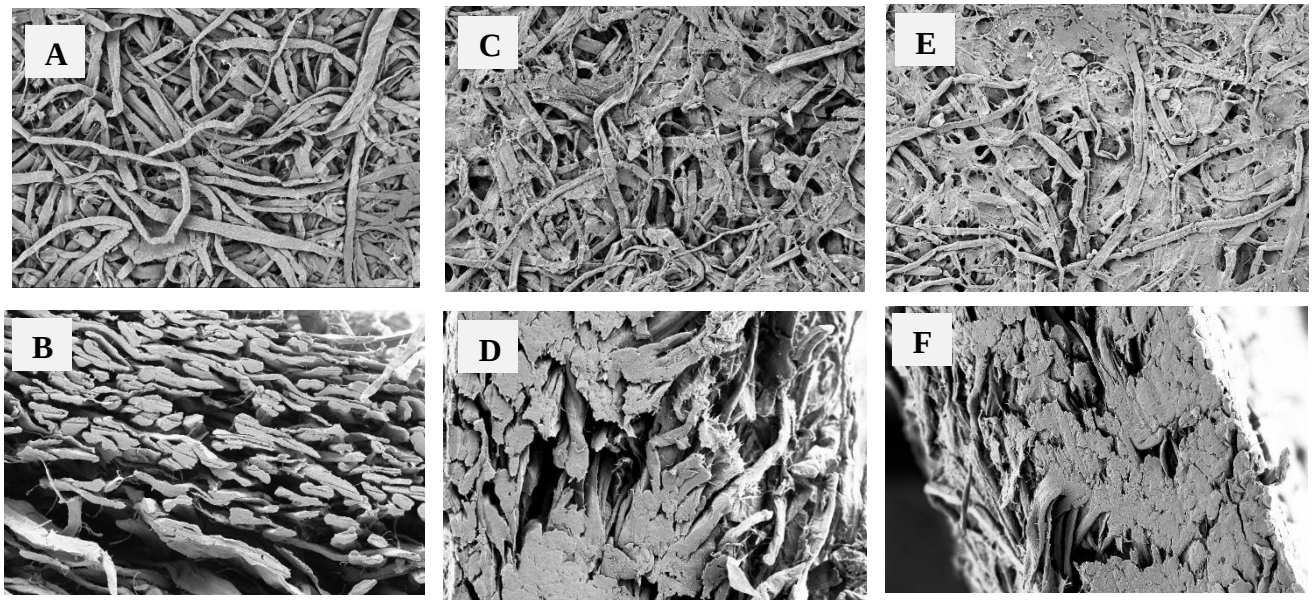

Figure 4.8: FEG-SEM images of SULP sheets at NFC substitutions of 0% (A-B), 20% (C-D) and 50% (E-F) showing surface images (top) at 200 × magnification and the cross-sectional image (bottom) at 500 × magnification.

Similarly, the UBK sheets were analysed at different substitution of NFC pulp (Figure 4.9). The 0% NFC sheet showed distinct fibre particles with voids in between the fibres. As the NFC pulp increased from 0% to 100% (A, C, E and G), it can be observed that the fibres merged into an indistinguishable network, with minute spaces between the fibres. The substitution of NFC pulp introduced nanoparticles, which during handsheet making, filled the voids between the fibres, hence creating an interwoven network of fibre particles. Thus, the substitution of NFC fibres would lead to slower absorption of liquids through the sheet, with very minimal fluid transport in the 100% NFC sheet. The cross-sectional images (B, D, F and H) support the theory formulated, whereby the voids between the fibres can be seen to reduce, allowing for less liquid uptake in the sheets as the NFC substitution increased. From these observations, an inversely proportional relationship could be expected between the substitution of NFC pulp and the pore size.

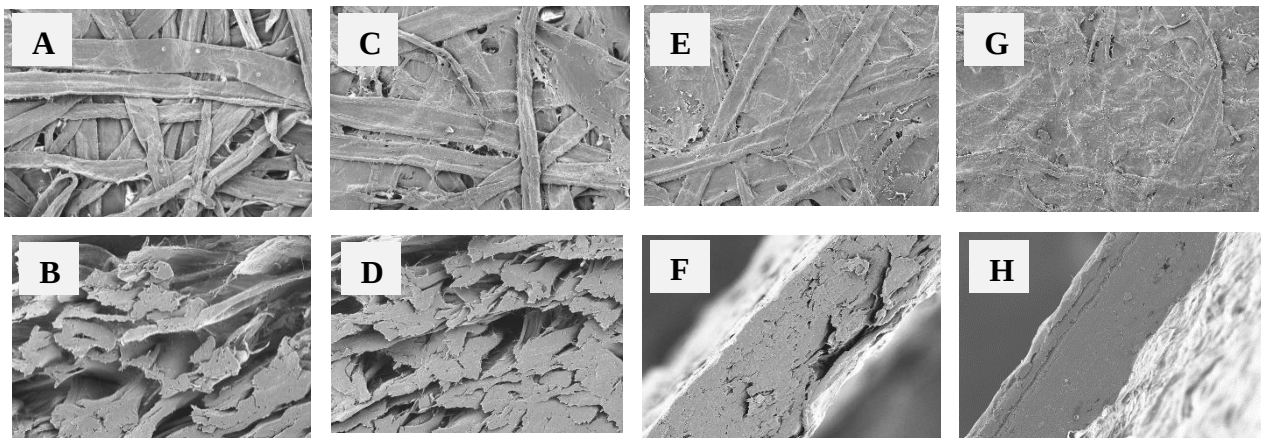

Figure 4.9: FEG-SEM images of UBK sheets at NFC substitutions of 0% (A-B), 20% (C-D), 50% (E-F) and 100% (G-H) showing surface images (top) at 200 × magnification and the cross-sectional image (bottom) at 500 × magnification.

The substitution of NFC pulp had the same effect on the CHR sheets as previously seen with the SULP and UBK sheets. It can be observed from surface images of Figure 4.10 (A, C, E and G) that there is a distinct reduction in the voids between the fibre particles. Image A showed defined fibre strands. The substitution of the finer NFC fibres resulted in a merged fibre network (as seen in image C), where the pore size decreased, which would negatively affect the wicking properties of the sheet. Images E and G can be seen to have almost full coverage of fibres due to the fine nature of the fibres, with minute voids between the fibres. The wicking rate in these sheets would be expected to be slower than the 0% and 20% NFC sheets. Similarly, the cross-sectional images (B, D, F and H) showed that as the NFC pulp substitution increased, the amount of space between the fibres decreased, thus supporting the surface image results, whereby slower liquid motion is expected in the higher substitutions of NFC pulp.

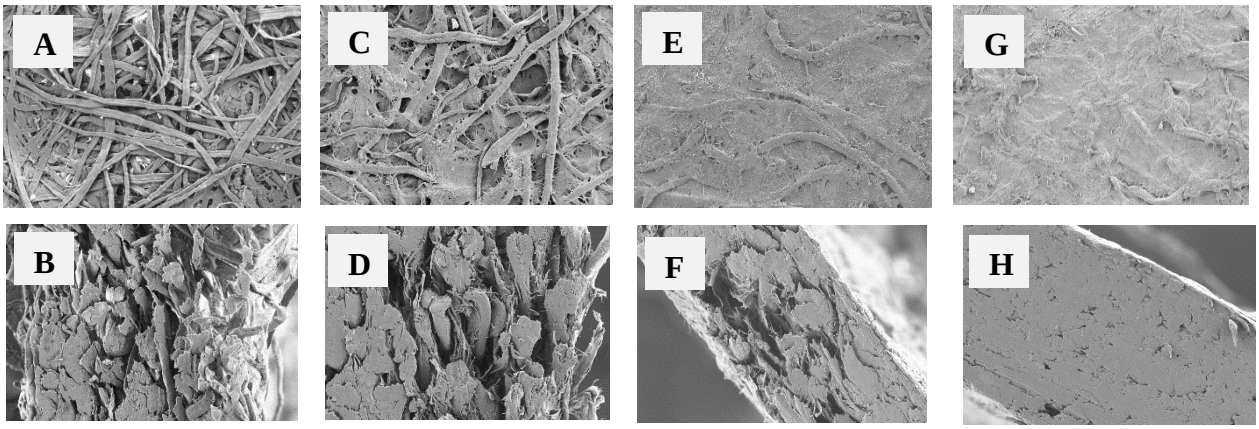

Figure 4.10: FEG-SEM images of CHR sheets at NFC substitutions of 0% (A-B), 20% (C-D), 50% (E-F) and 100% (G-H) showing surface images (top) at 200 × magnification and the cross-sectional image (bottom) at 500 × magnification.

The CHR3 sheets followed the same distinct pattern as the CHR sheets in Figure 4.11. Here, it could be seen that the surface images (A, C, E and G) followed the general trend, which was the decrease in pore size as the substitution of NFC pulp increased. The 0% NFC sheet (image A) showed a network of fibres, whereby individual rod-like structures could be observed. Increasing the NFC pulp, decreased the pore size within the sheet, due to the substitution of finer particles filling the voids in the structure. The cross-sectional images (B, D, F and H) support the observations seen from the surface FEG-SEM images. Image B showed distinct fibre strands with voids between the fibres. Increasing the NFC pulp in the sheet (from image D, F and G) resulted in a decrease in the spaces between the fibres, forming an indistinguishable network of fibres. The wickability of the sheets would be expected to decrease with an increase in NFC pulp, due to the decrease in space available for the liquid to flow through.

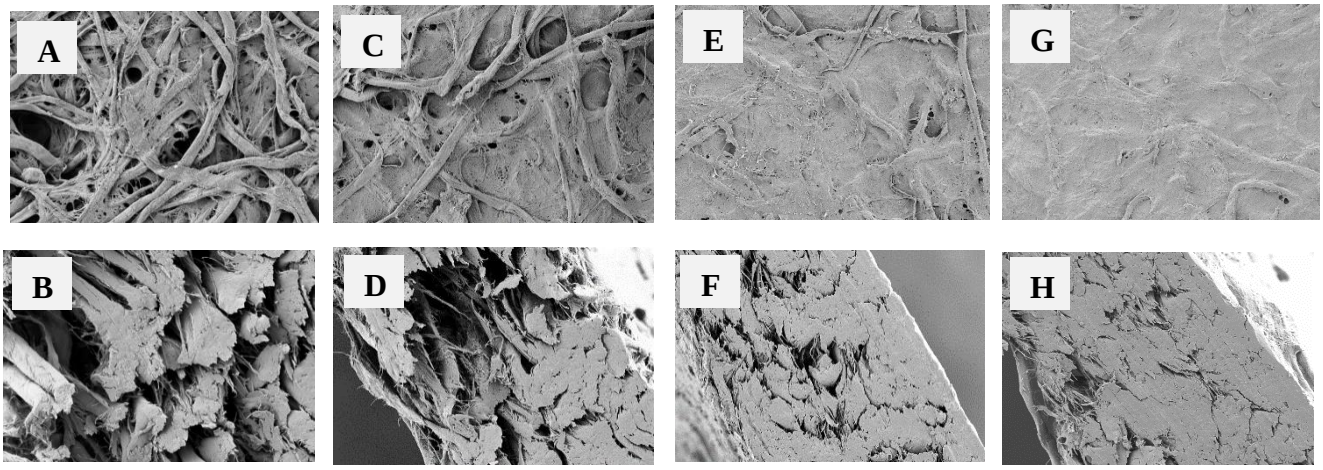

Figure 4.11: FEG-SEM images of CHR3 sheets at NFC substitutions of 0% (A-B), 20% (C-D), 50% (E-F) and 100% (G-H) showing surface images (top) at 200 × magnification and the cross-sectional image (bottom) at 500 × magnification.

Lastly, REC sheets were considered (Figure 4.12). The images showed a slightly different view as opposed to the previous substrates, in that the pore sizes in the 0% NFC sheet were already relatively small, which would be expected to result in slow wicking rate. From the surface images (A, C, E and G) showed a gradual decrease in the pore size through the substitution of NFC pulp. Eventually, the 100% NFC pulp sheet had no distinguishable fibres, showing that the finer particles were taking up the space of the voids. The 0% NFC sheet cross-sectional image (B) showed a fairly compressed structure with very minimal space for liquid movement. As the NFC pulp substitution increased, the sheets showed similar results to that of the 0% NFC sheet. It could be observed that the 100% NFC sheet was compact, where no individual fibres were seen. The nanoparticles replaced the voids in the sheets, resulting in fairly non-porous structure, with tiny voids. As previous substrates concluded, it would be expected that the wicking rate would decrease with the increase in NFC pulp.

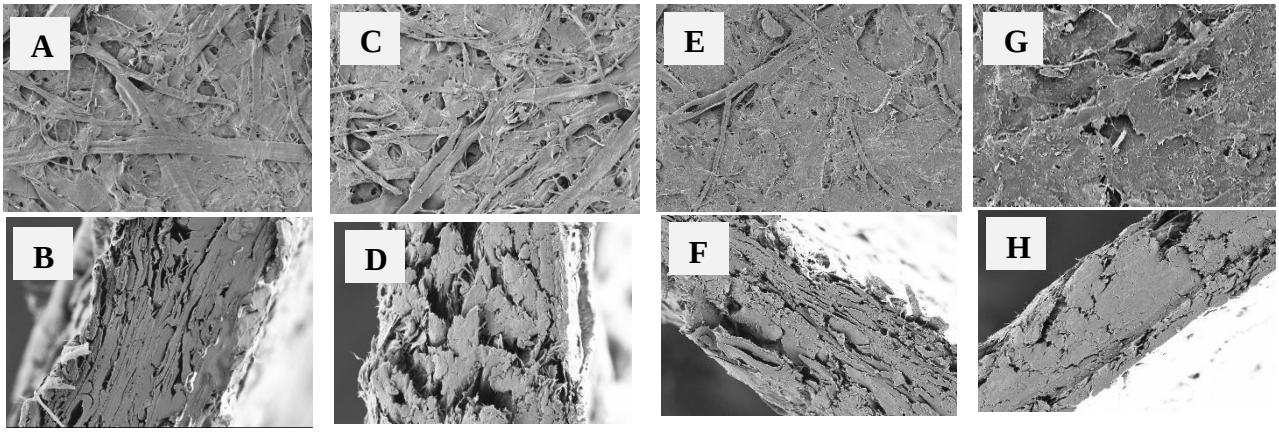

Figure 4.12: FEG-SEM images of REC sheets at NFC substitutions of 0% (A-B), 20% (C-D), 50% (E-F) and 100% (G-H) showing surface images (top) at 200 × magnification and the cross-sectional image (bottom) at 500 × magnification.

4.3 Conclusions

- FEG-SEM on the base substrates showed that SULP had the biggest pore size in comparison to the other substrates, followed by BK, UBK, CHR, CHR3, TMP and REC. This related to the wicking ability of the sheet, whereby the bigger the pore size, the higher the wicking rate.
- The substitution of NFC pulp to the sheet resulted in smaller pore sizes due to the increase in finer fibre particles, which would be expected to lead to a slower wicking rate.

CHAPTER 5: WETTABILITY DETERMINATION OF BASE AND NANOFIBILLATED SUBSTRATES

5.1 Introduction

Wettability is the ability of a substrate to allow liquids to spread, thereby allowing for absorption of liquid into the substrate. This property is vital for fluid transport in microfluidic paper-based devices. Hydrophobicity is linked to the wettability, in that if a substrate is non-wettable, it is deemed hydrophobic and vice versa for wettable surfaces being hydrophilic.

Contact angle (CA) was used in determining the wettability and hydrophobicity of the substrates. The chapter contains the data.

5.2 Results

The results from the CA tests revealed that all the substrates were hydrophilic and the majority of the substrates exhibited CA of 0º. In other words, water droplets were instantly absorbed into the paper samples, showing that these substrates are highly hydrophilic. This result showed that the substrates were wettable, therefore allowing absorption of liquids into the sheet, where capillary action can occur to transport the liquid through the sheet. Two of the substrates, these being sheets substituted with 100% NFC unbleached kraft pulp and 100% NFC recycled pulp, exhibited CA behaviours that could be measured. This corroborates data from for wicking studies where increase in NFC content resulted in slower wicking times in the paper substrates. The observations are also in agreement with a study by Kord et al. (2015) who reported that increase in NFC cellulose content to a PVA composite material resulted in increase of contact angle.

The data on five replicate measurements are shown in Table 5.1.

Table 5.1 Contact angle measurements on substrates used in this study.

Substrate	Average contact angle measurement
SULP	
0% NFC substitution	0º
50% NFC substitution	0º
100% NFC substitution	0º
UBK	
0% NFC substitution	0º
20% NFC substitution	0º
50% NFC substitution	0º
100% NFC substitution	53.27°
BK	0º
CHR	
0% NFC substitution	0º
20% NFC substitution	0º
50% NFC substitution	0º
100% NFC substitution	0º
CHR3	
0% NFC substitution	0º
20% NFC substitution	0º
50% NFC substitution	0º
100% NFC substitution	0º
TMP	0º
REC	
0% NFC substitution	0º
20% NFC substitution	0º
50% NFC substitution	0º
100% NFC substitution	46.85°

5.2.1 Substrate substituted with 100% NFC unbleached kraft pulp

The CA measurements were variable in the sheet had varying contact angles at different points in the sheet: the five replicates ranged from 56.51º to 48.54º (as seen from Figure 5.1). The variability in the values could be a result of uneven distribution of NFC mass in the

substrate – the higher CA values are most probably from areas that had high aggregations of NFC mass thus resulting in slower liquid absorption rates.

Although the contact angle of this sample was highest among the samples tested, it is nevertheless hydrophilic since the CA values were less than 90º. This result showed that the substrate would allow liquids to be absorbed, however the absorption time would be longer than that of the other substrates with a CA of 0º. Therefore, this factor must be noted when looking at the feasibility of using this substrate in µPAD applications.

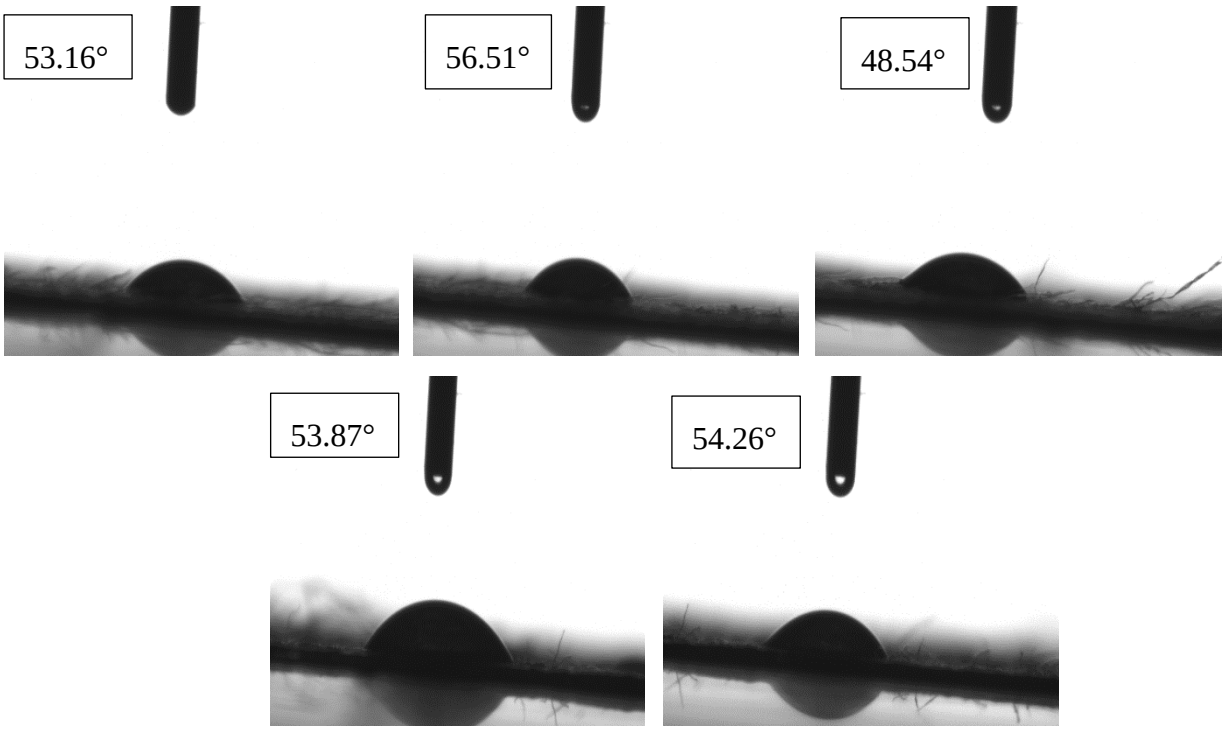

Figure 5.1: Contact angle images at different points in the UBK sheet.

5.2.2 Substrate substituted with 100% NFC recycled pulp

Similar to the UBK substrate, the CA of the REC sheet was also higher than 0º and the values ranged from 43.66º to 50.68º from five points in the sheet. Again this can be explained by non-uniformity of grammage in the sheet.

The result of the experiment showed that the REC sheet had a similar CA to that of the UBK sheet. Due to the CA being less than 90º, the substrate can be considered hydrophilic, thereby allowing for wetting to occur and absorption of liquid. However, a longer period for

absorption is expected in comparison to the 0º CA substrates, which must be considered when determining the feasibility of REC for µPAD applications.

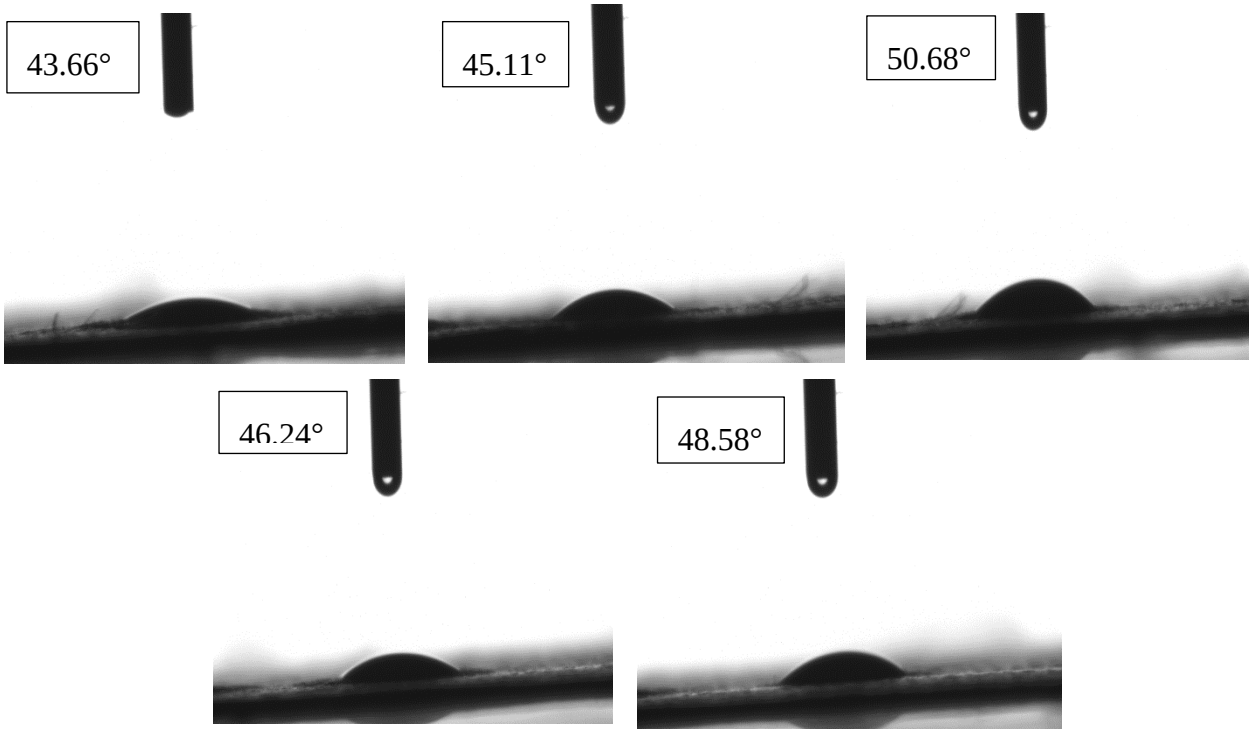

Figure 5.2: Contact angle images at different points in the REC sheet.

5.3 Conclusions

The CA test measurements indicate that all the substrates tested were very hydrophilic with no measurable CA values except for two, these being sheets substituted with 100% NFC unbleached kraft pulp and 100% NFC recycled pulp, that exhibited lower hydrophilicity properties. Increase in NFC content in the sheets resulted in higher CA, that increased the resistance to absorption of liquids into the substrates.

CHAPTER 6: WICKING BEHAVIOUR OF BASE AND NANOFIBRILLATED SUBSTRATES

6.1 Introduction

This chapter will be focusing on experimental results obtained from the horizontal and vertical wicking tests for each substrate. The experiments were designed to determine the time taken for a liquid to travel a distance of 10 cm along the substrate. The results presented in this chapter were obtained from studies of three different factors, namely, the wicking test (either horizontal or vertical), the wicking liquid, and paper substrate type.

The results obtained from the tests were analysed in depth, which can be used as a guideline when determining a substrate for use in µPADs. This is eventually dependent on the wicking liquid, which would be bodily fluids in a case of medical kits, and the desired time for wicking.

The chapter is split into 4 subsections. Section 6.2 looks at the results obtained from the horizontal wicking tests. Section 6.3 focuses on vertical wicking test results of the substrates. Section 6.4 will compare the trends in relation to the horizontal and vertical tests. Lastly, section 6.5 incorporates Lucas-Washburn equation to determine how closely the substrates follow the model for porous media.

6.2 Horizontal Wicking

6.2.1 Base substrates

From Figure 6.1, it can be observed that the Whatman glass microfiber GF/D filter paper (GM) substrate had the fastest wicking rate compared to the other substrates when using dye as the wicking liquid. The GM line followed a steep, linear graph, showing that the liquid wicked through the substrate uniformly at approximately the same rate throughout the paper. Sulphite was the second fastest wicker. The graph followed a linear path, with a slight curvature at the end. This showed that the absorption rate of the dye slowed down as the wicking height increased. The FEG-SEM conducted in Chapter 4.2 supported the results obtained from this test, as the pore size can be seen to be the largest of the substrates, resulting in quicker absorption of the wicking liquid. Bleached kraft (BK) and unbleached kraft (UBK) substrates followed a similar wicking pattern, which showed an increasing linear trend together with the SULP graph, levelling off. The substrates had the same wicking rate

as the SULP substrate until the 8 cm mark, where the rate of wicking slowed down. Observations from FEG-SEM results in Chapter 4.2 showed that BK had slightly bigger pore sizes when compared to UBK. From this, it can be derived that BK should have a quicker wicking rate. The discrepancies seen in this experiment could be due to the morphology of the fibres and thickness of the sheet. Whatman No.1 chromatography filter paper (CHR) and Whatman 3MM chromatography filter paper (CHR3) substrates had a similar wicking rate, which can be seen from the overlapping red and blue graphs in Figure 6.1. From this result, the expectation would be that the pore sizes of these substrates had similar dimensions. However, from the FEG-SEM images in Chapter 4.2, it can be observed that there are slight variations between the size of the voids found between the fibres in CHR and CHR3, thus allowing for differing wicking rates. The inconsistencies in the expected result and what experimental results showed could be due to the fibre network structure being different to that of the FEG-SEM image. Thermo-mechanical pulp (TMP) substrate followed a different pattern to the other substrates. The graph resembled an exponential decay graph, showing that the wicking rate is fast initially, slowing down with distance covered. The latter of the graph levelled off, showing that wicking reached a uniform rate. The TMP substrate was significantly slower than the other substrates. This can be attributed to the fact that the pulp used for sheet production contained lignin, which would retard the wicking. The FEG-SEM results also supported this result, showing that the pore size is smaller in comparison to the other substrates previously mentioned in Chapter 4.2. It can also be observed that the dye stopped wicking at 6 cm and did not wick through the full distance of the substrate. This may be a result of the equilibrium of hydrostatic pressure and capillary pressure (Simile, 2004). The REC substrate showed the slowest wicking, similar to that of the TMP substrate. The recycled pulp sheet was expected to produce the slowest wicking as it contains lignin and other contaminants such as ink and stickies, which are residues from the recycling process. From FEG-SEM, it can be seen that REC had the smallest pore size, resulting in slower absorption of liquid (seen from Chapter 4.2). As with the TMP substrate, REC also did not allow the liquid to wick through the length of the sample and stopped at 4 cm.

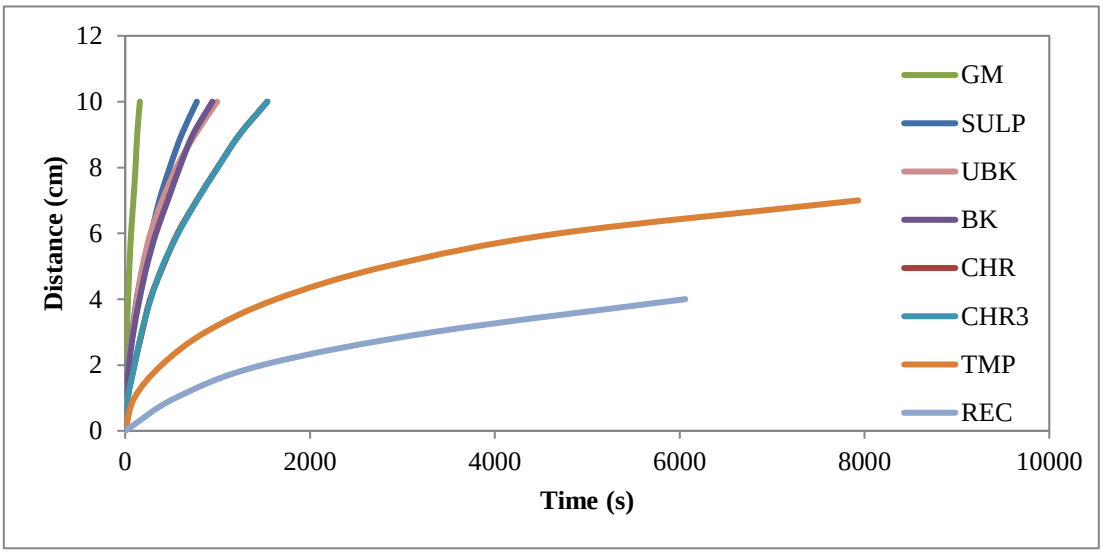

Figure 6.1: Horizontal wicking rates for different substrates with dye as wicking liquid.

From Figure 6.2 with blood simulant as a wicking liquid, it can be seen that GM was the fastest wicking substrate. The wicking rate initially increased linearly then deviated to an exponential decay graph after 8 cm, showing that the wicking rate decreased. The sulphite (SULP) substrate followed being the second fastest wicking material. However, it was observed that the substrate had an initial fast absorption of liquid, with a gradual decrease in the wicking rate, which started levelling off at approximately 6 cm. The UBK and CHR3 substrates eventually overtook the SULP substrate during its levelling period, where SULP slowed down significantly, which could be attributed to a high hydrostatic pressure, which would counteract the capillary pressure. The unbleached kraft (UBK) substrate was the third faster wicker, however due to its fairly consistent wicking rate, as seen from the slightly curved graph, it eventually wicked faster than the SULP after a distance of 8 cm. The CHR3 substrate followed UBK in wicking rates. As with UBK, CHR3 overtook SULP toward the 9 cm mark. It was observed that the wicking rate deviated from the UBK graph at a distance of approximately 3 cm. From Chapter 4.2, the FEG-SEM images provided an overall understanding of which substrate should wick fastest, by observation of the pore sizes. It can be concluded that the wicking rates obtained from the vertical wicking experiments did not correspond to the FEG-SEM results and expectations. The deviation from the expected results could be due to a number of factors, these being: a variation in fibre network structure from the sheet used in the experiment to the fibre structure found in the FEG-SEM images, as well as a difference in thickness of the sheets. The BK substrate was the fifth fastest wicker, however from Figure 6.2, it was seen that the BK graph initially had a steep gradient,

overtaking the UBK and CHR3 graphs. But with time, the wicking rate decreased and began to level off, similar to that of the SULP graph. It can also be observed that the BK substrate wicking stops at 8 cm, showing that an equilibrium between hydrostatic and capillary pressure had been reached. This point could be referred to as the saturation point. The CHR substrate followed BK in wicking rate. From observation, the graph increased gradually and followed an exponential graph. As with the BK substrate, CHR reached a saturation point at a distance of 5 cm. The thermo-mechanical pulp sheet was the second slowest wicking substrate, which was expected due to the lignin present in the substrate. The FEG-SEM images (in Chapter 4.2) also supported this result. As with the previous 2 substrates, the motion of liquid through TMP stopped at a distance of 3 cm. The slowest wicking substrate was REC. This was expected due to the contaminants present in the REC substrate such as lignin, which retard the motion of liquid. The FEG-SEM (Chapter 4.2) also showed the substrate to have small pores, resulting in a slow wicking rate. The graph followed a linear pattern, which indicated that the wicking rate is fairly uniform throughout the substrate.

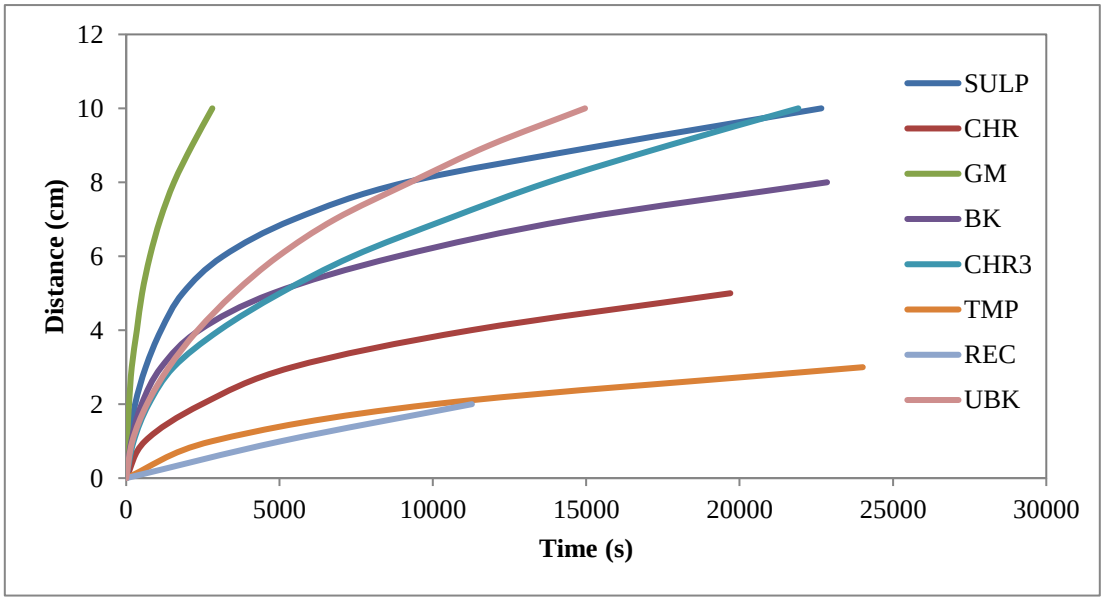

Figure 6.2: Horizontal wicking rates for different substrates with blood simulant as wicking liquid.

As each of the experiments were conducted 3 times for each of the substrates, the averages were used and standard deviations were calculated and tabulated in Appendix D 2.1. In general, it was observed that the wicking times for each run for the substrates were fairly

accurate and consistent. This could be seen from the low standard deviations, indicating that the data points were close to the average values.

Comparing Figure 6.1 and 6.2, it was observed that the time of wicking liquid could significantly change the wicking rates of each substrate. Due to the high viscosity of the blood simulant, as compared to that of the dye, the wicking rates were significantly longer than that of the dye.

6.2.2 Nanofibrillated substrates

This subsection is split up into 6 subsubsections, with one section focusing on the wicking rates of the 50% NFC pulp sheets and the others focusing on a different substrate and its NFC equivalents. The substrates discussed in the following sections include SULP, CHR, CHR3, UBK and REC.

6.2.2.1 Substrates substituted with 50% NFC pulp

From Figure 6.3, a comparison between the wicking rates of the substrates substituted with 50% NFC pulp could be observed. It can be seen that the SULP sheet was the fastest wicking substrate. The SULP graph followed an initial linear path, with a slight curvature at the end. This implied that the absorption rate of the dye slowed down as the wicking height increased. From the FEG-SEM images in Chapter 4.3, it was seen that the SULP sheet had the largest pore size, thereby resulting in the quickest wicking rate. The CHR substrate followed, with a similar wicking trend of increasing rate, eventually levelling off. From the microscopy analysis in Chapter 4.3, it was observed that the CHR and CHR3 substrates had similar pore sizes. Therefore, the wicking rates of these sheets would be expected to be similar. From the results, it was seen that the CHR3 substrate followed CHR, thereby indicating that the pore sizes were inconsistent. The difference in these results could be explained by a variance in sheet thickness and morphology of the sheet. The UBK and REC were observed to have the slowest wicking rates. This was expected from FEG-SEM analysis (Chapter 4.3), as these substrates had the smallest pore size. In the latter stage of the experiment, the REC graph is seen to overtake the UBK and CHR3 graphs. This anomaly could be as a result of a variation in fibre structure within the REC sheet, which could affect the pore size.

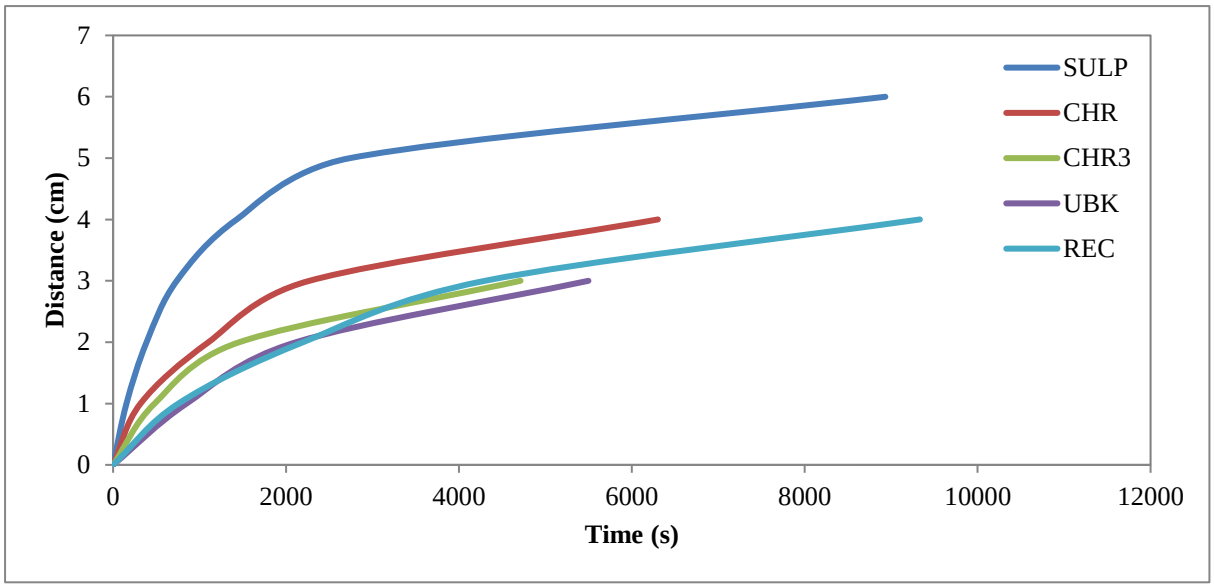

Figure 6.3: Horizontal wicking rates for substrates substituted with 50% NFC pulp samples at different substitutions of nanofibrillated pulp with dye as wicking liquid.

Figure 6.4 shows the comparison between the 50% NFC pulp substituted sheets using blood as a wicking liquid. Similar to Figure 6.3, it was observed that SULP was the fastest wicking substrate with a fairly linear path, with a slight curvature. The FEG-SEM images in Chapter 4.3, SULP sheet had the largest pore size, supporting the result obtained in this experiment. The CHR substrate followed, with a similar linear wicking trend which levels off. CHR3, UBK and REC followed the same path and were the slowest wicking substrates. The FEG-SEM analysis (Chapter 4.3) showed that the UBK and REC had the smallest pore size, which corresponds to the results obtained. The CHR3 and CHR substrates had similar pore sizes, however the wicking rates differ, where CHR3 was slower than CHR, as in Figure 6.3. As previously stated, a difference in sheet thickness and morphology of the sheet could be factors affecting the wicking rate.

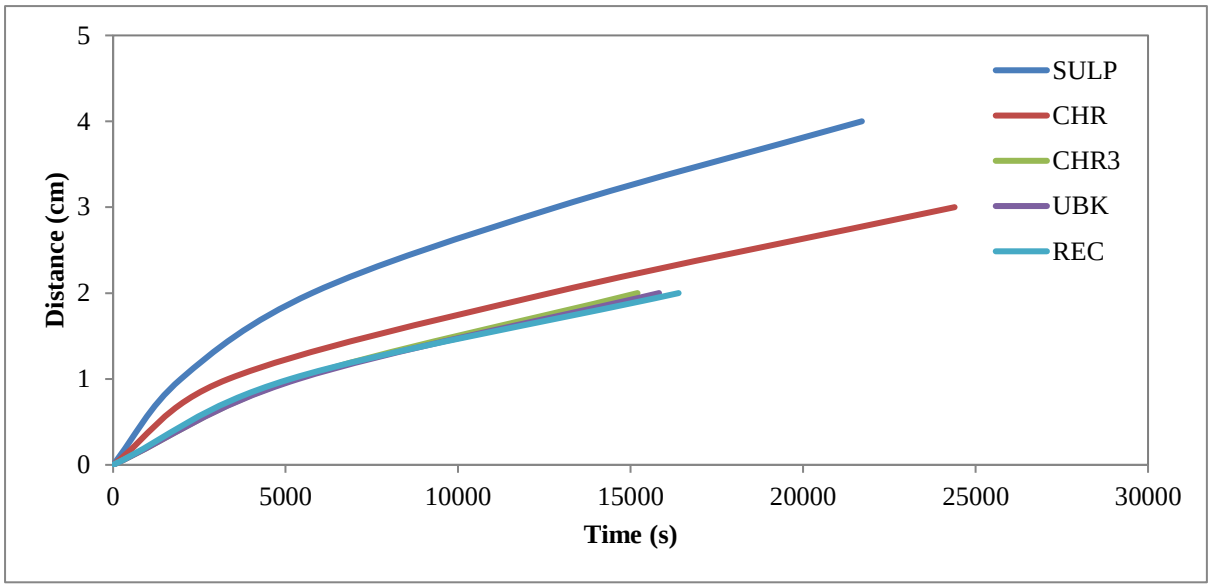

Figure 6.4: Horizontal wicking rates for substrates substituted with 50% NFC pulp samples at different substitutions of nanofibrillated pulp with blood simulant as wicking liquid.

6.2.2.2 Sulphite

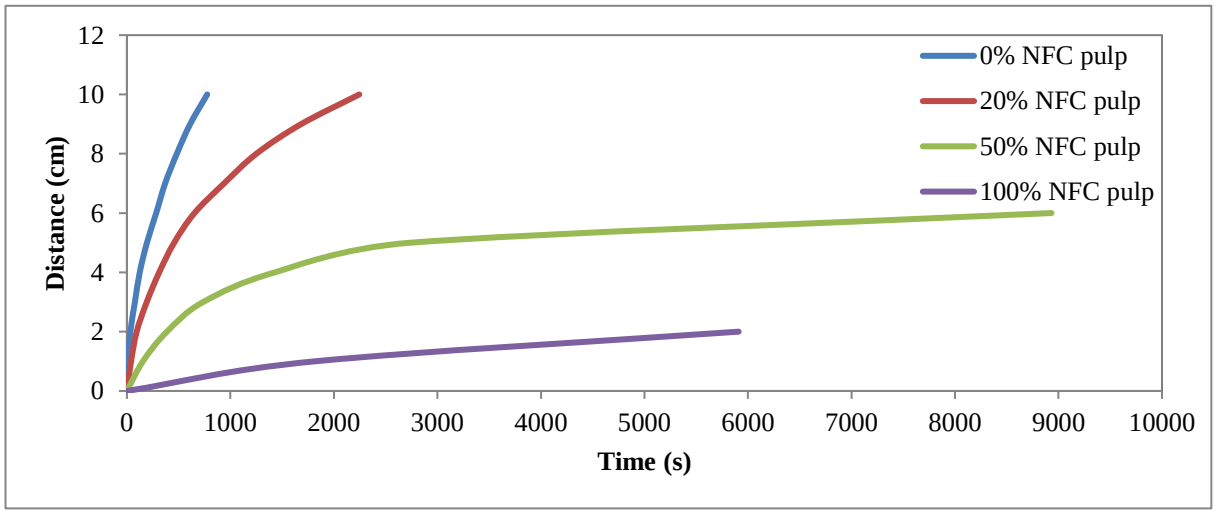

Figure 6.5: Horizontal wicking rates for SULP samples at different substitutions of nanofibrillated pulp with dye as wicking liquid.

As observed from Figure 6.5, as the amount of NFC pulp in the sample increased, the slower the wicking of liquid through the substrate. The results showed that the substrate with no

substitution of NFC pulp was the fastest wicking. This result was expected from FEG-SEM conducted. It was seen that the 0% NFC sample had the largest pore size, therefore a quicker absorption rate of the dye. The 20% NFC sample was the second fastest wicker, which was seen to have a pore size smaller than that of the 0% sample, allowing for slower wicking through the substrate. The 50% NFC sample followed, with the liquid motion stopping at a distance of 6 cm. The FEG-SEM accounts for the wicking rate as the pore size was smaller than the previous 2 samples. Lastly, the 100% NFC sample was the slowest wicker. The slow wicking rate was due to the small pore size in the paper substrates as confirmed by FEG-SEM images. From the results, it was observed that the sample reached saturation at 2 cm.

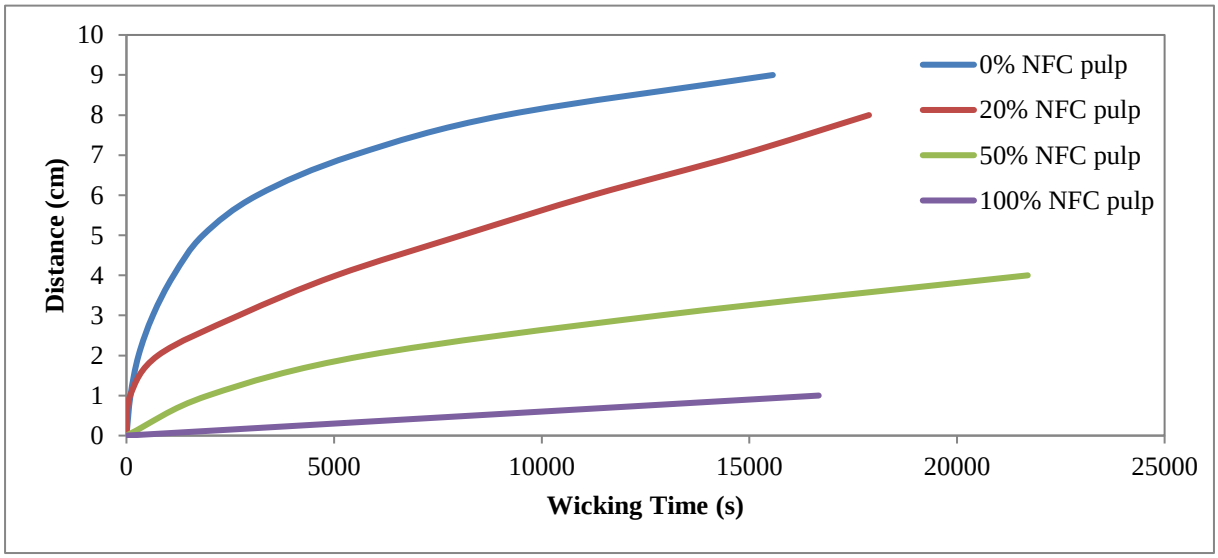

Figure 6.6: Horizontal wicking rates for SULP samples at different substitutions of nanofibrillated pulp with blood simulant as wicking liquid.

Based on the results from Figure 6.6, the same conclusion from the dye experiment could be stated using blood simulant as the wicking liquid: the wicking rate decreases with the increase in NFC pulp. The results for the blood simulant followed that of the dye, shown in Figure 6.3. The 0% sample was the fastest wicker, followed by 20% sample, 50% sample and lastly, the 100% sample. The 0% and 50% samples followed an exponential decay path, showing that the wicking rate was quick initially, gradually slowing down with distance covered. The 20% sample was initially quick, eventually following an increasing linear trend. The 100% sample followed a linear path, with wicking rate uniformly decreasing along the substrate. However, it was observed that these substrates reached saturation. The 0% sample

stopped at a distance of 9 cm, the 20% sample at 8 cm, the 50% sample at 4 cm and the 100% sample at 1 cm. Due to the viscosity of the blood simulant being higher than that of the dye, the time taken for wicking through the samples was greater.

Field emission gun-scanning electron microscopy image analysis, conducted in Chapter 4.3, could be used to support the results obtained from this experiment. It was concluded that as the amount of NFC pulp increased in the sheet, the pore size decreased, resulting in a decrease in wicking rate of the sheet.

Statistical analysis of the data from this experiment was conducted and summarised in Appendix D 3.1.1. In general, it can be observed that the data is spread close to the mean value for most of the experiments. However, for the higher NFC pulp samples, it can be seen that there is a higher standard deviation. This implied that the wicking times for these samples were dispersed widely. A possible explanation for this could be due to a difference in the sheet properties, such as thickness, which affects the absorption of liquid through the sheet.

6.2.2.3 Chromatography No.1 Filter Paper

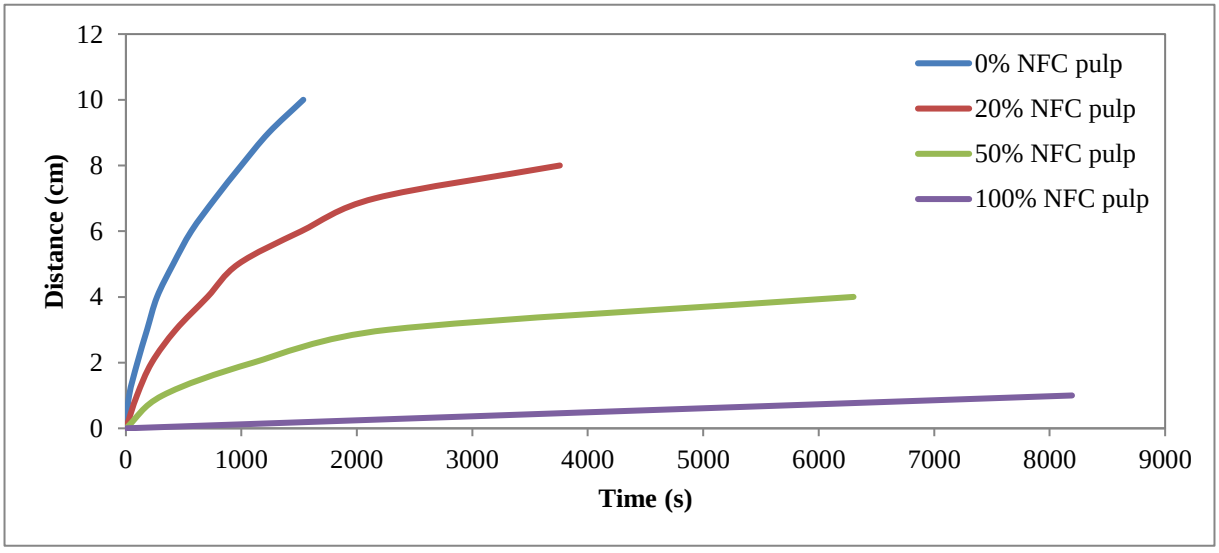

Figure 6.7: Horizontal wicking rates for CHR samples at different substitutions of nanofibrillated pulp with dye as wicking liquid.

The general trend of Figure 6.7 followed that of SULP samples seen in sections 6.2.2.2 – 6.2.2.5, where there was an inversely proportional relationship between the wicking rate and

amount of NFC pulp. The 0% sheet was the fastest wicker, which was expected as FEG-SEM results showed that it contained the largest pore size in comparison to the other samples. Similarly, the 20% sample, 50% sample and 100% sample followed in wicking rates respectively. The results obtained showed that the 20% sample reached a saturation at 8 cm, the 50% sample at 4 cm and the 100% sample at 1 cm.

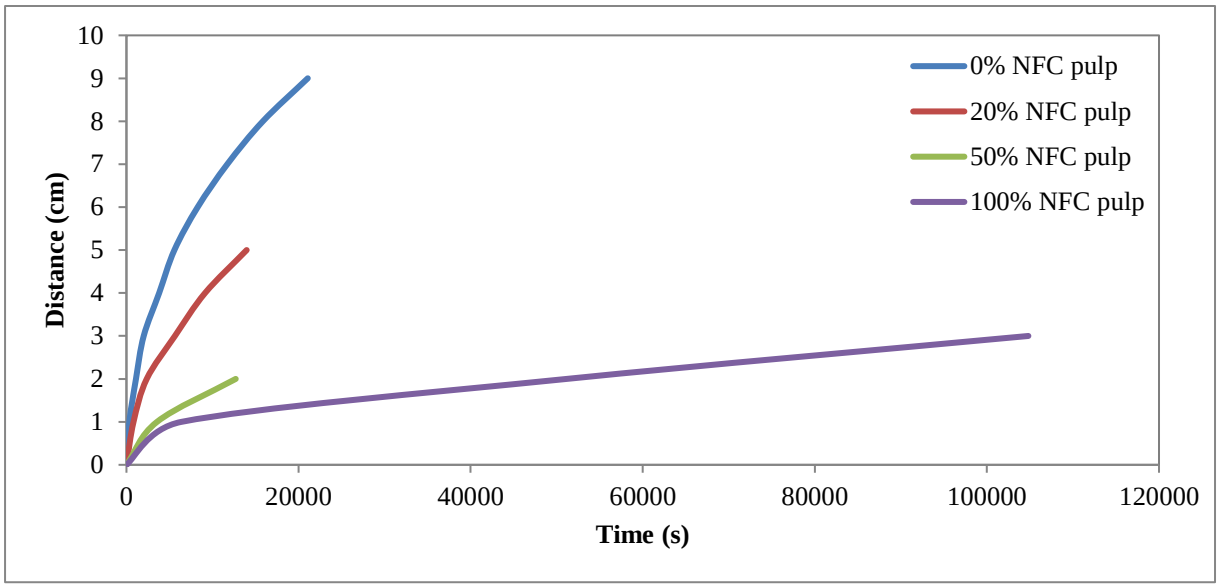

Figure 6.8: Horizontal wicking rates for CHR samples at different substitutions of nanofibrillated pulp with blood simulant as wicking liquid.

From Figure 6.8, a similar trend from the dye experiment was observed when using the blood simulant. The 0% NFC sample had the fastest wicking rate, followed by the 20% sample, 50% sample and lastly, the 100% NFC sample. The samples followed a general exponential decay graph, which started off with a quick wicking rate, eventually levelling off. These samples experienced an equilibrium between hydrostatic and capillary pressure. The 0% NFC sample reached equilibrium at a distance of 9 cm, the 20% NFC sample at 5 cm, the 50% NFC sample at 2 cm and the 100% NFC sample at 3 cm. The blood simulant was expected to wick at a slower rate due to its high viscosity, which was observed.

Taking into account the FEG-SEM images of these substrates (from Chapter 4.3), the results obtained were expected, due to the decrease in pore size as the increase of NFC pulp increased.

Looking at the statistical aspect, it can be seen from Appendix D 3.1.3 that the spread of data varied from run to run. In general, most of the data were spread in close proximity to the average value. However, for the higher distances, it can be seen that there is a higher standard deviation for a number of samples. As explained previously, this could be due to a difference in the sheet properties, such as thickness and dispersion of NFC pulp within the sheet.

6.2.2.4 Chromatography 3MM Filter Paper

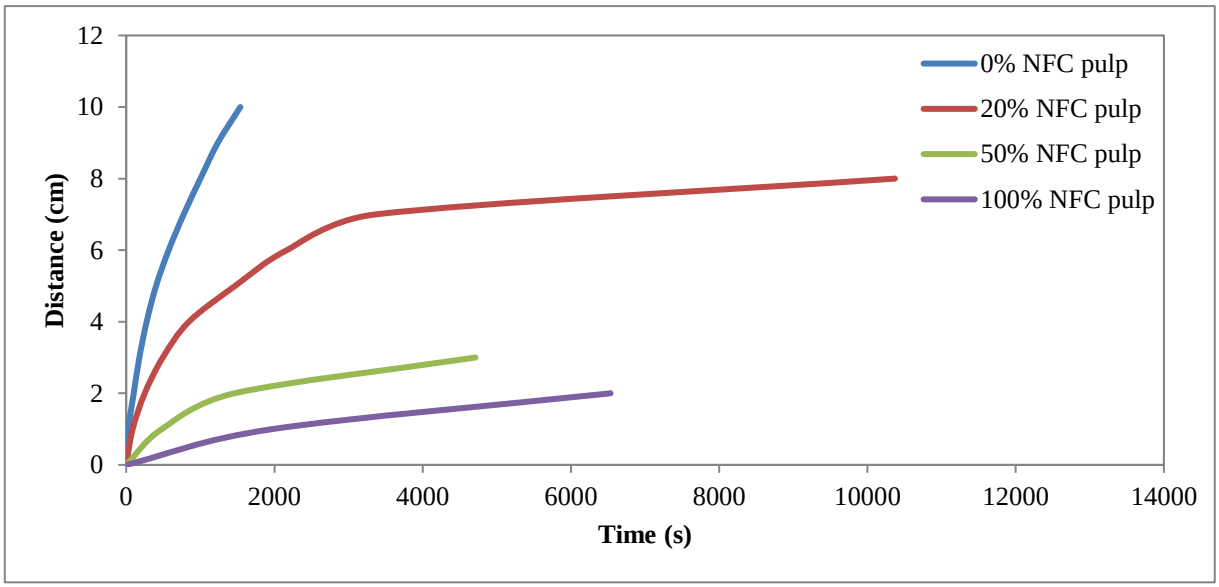

Figure 6.9: Horizontal wicking rates for CHR3 samples at different substitutions of nanofibrillated pulp with dye as wicking liquid.

From Figure 6.9, it was observed that the 0% NFC sample wicked the fastest, followed by the 20% NFC sample, 50% NFC sample and 100% NFC sample. This result was expected, as seen from sections 6.2.2.1 and 6.2.2.2. The FEG-SEM results showed that the 0% NFC sample had the largest pore size. Similarly, the 20% NFC sample, 50% NFC sample and 100% NFC sample pore sizes decreased with wicking rate. The results obtained showed that the 20% NFC sample reached a saturation at 8 cm, the 50% NFC sample at 3 cm and the 100% NFC sample at 2 cm.

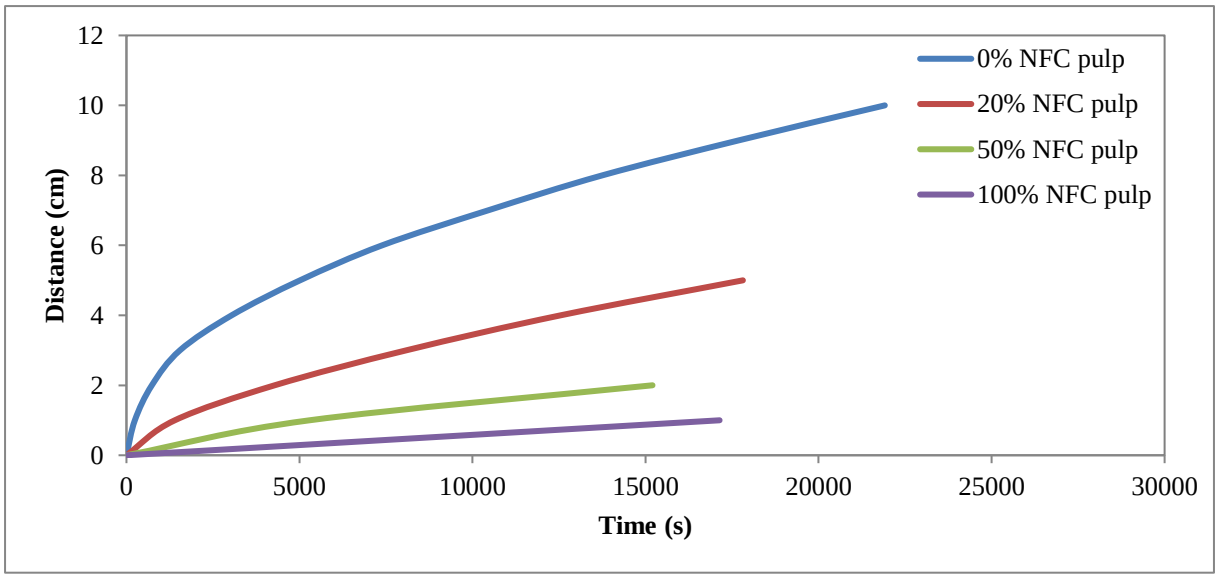

Figure 6.10: Horizontal wicking rates for CHR3 samples at different substitutions of nanofibrillated pulp with blood simulant as wicking liquid.

Figure 6.10 followed the same trend as in Figure 6.9. The 0% NFC sample had the fastest wicking rate, followed by 20% NFC sample, 50% NFC sample and lastly, the 100% NFC sample. The graphs followed an exponential decay graph, with an initial steep rate, slowing down to a uniform gradient. The 20%, 50% and 100% NFC samples reached a saturation point, where the motion of liquid ceased. The 20% sample stopped at 5 cm, the 50% NFC sample at 2 cm and the 100% NFC sample at 1 cm.

The field emission gun-scanning electron microscopy results, from Chapter 4.3, showed that the pore size decreased with an increase in NFC pulp. The results from the experiment can be seen to be consistent with that of the FEG-SEM, thereby supporting the results obtained.

From the 3 runs conducted for each substrate, it can be seen that the data has been consistent and clustered around the average value (as seen from Appendix D 3.1.4). The standard deviation values calculated showed the range between the values was low, resulting in acceptable data.

6.2.2.5 Unbleached Kraft

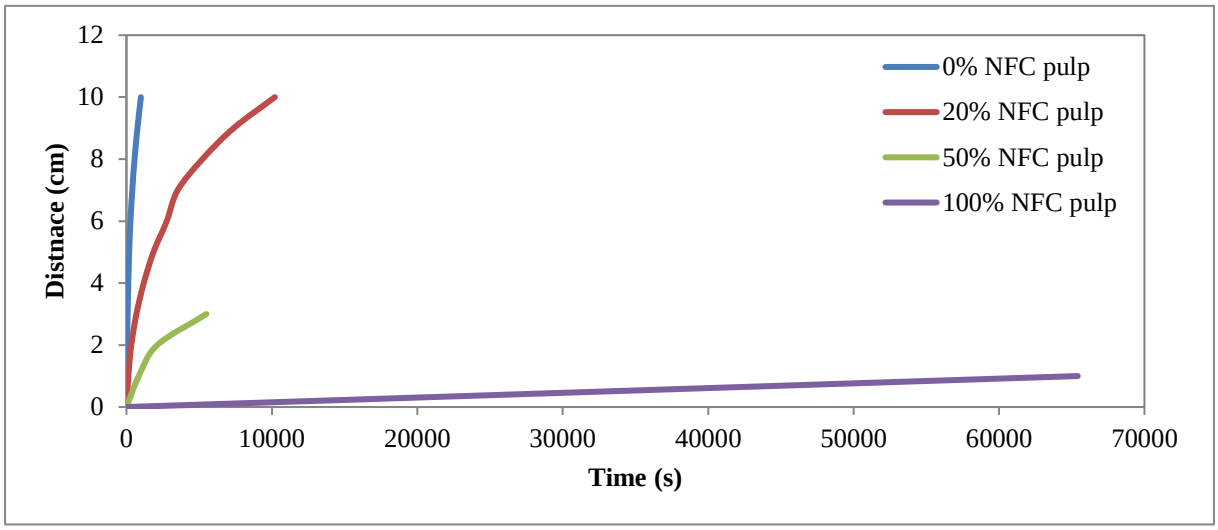

Figure 6.11: Horizontal wicking rates for UBK samples at different substitutions of nanofibrillated pulp with dye as wicking liquid.

The results observed from Figure 6.11 showed that the 0% NFC sample wicked the fastest, with a steep linear graph, showing that wicking was uniform throughout the substrate. The 20% NFC sample was the second fastest wicker, with a slightly curved graph, showing that the wicking rate was uniform, slowing down at a distance of approximately 7 cm. The 50% NFC samples, followed the same pattern as the 20% NFC sample, however it was observed that there was a resistance to absorption of the liquid, as seen from the saturation point. The 100% NFC sample followed a linear graph, showing consistent wicking rates, however it was seen that the substrate takes a long period to wick liquid through 1 cm, in comparison to the other samples. The field emission gun-scanning electron microscopy results showed that the 0% NFC sample had the largest pore size, with a decrease in pore size from 20% to 100% NFC samples. The graph indicated that the 50% NFC sample reached a saturation at 3 cm, while the 100% NFC sample stopped at 1 cm.

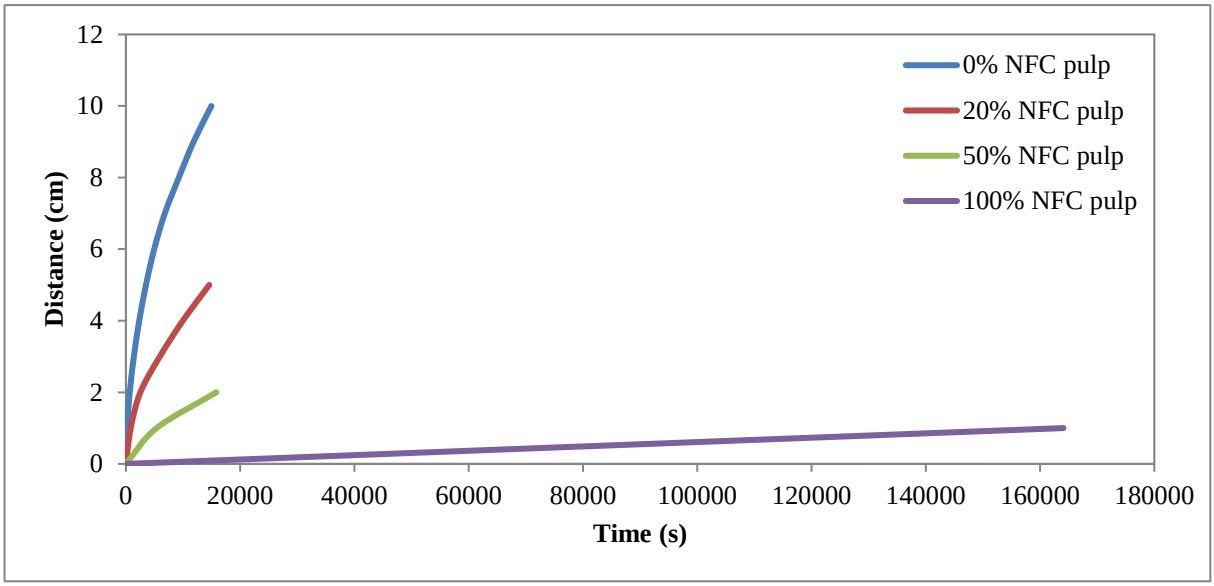

Figure 6.12: Horizontal wicking rates for UBK samples at different substitutions of nanofibrillated pulp with blood simulant as wicking liquid.

Figure 6.12 was observed to have a similar pattern of wicking rates as compared to Figure 6.11. The 0%, 20% and 50% NFC samples followed a curved graph path, which showed that the wicking rate decreased with increasing distance. The 100% NFC sample followed that of a linear graph, with a gradual gradient, showing that resistance to wicking was experienced. The 20%, 50% and 100% NFC samples reached a point where the motion of the blood simulant stopped. The 20% NFC sample stopped at 5 cm, 50% NFC sample at 2 cm and the 100% NFC sample at 1 cm.

Similar to the previous substrates, the FEG-SEM images, seen in Chapter 4.3, showed that the wicking rate would be expected to decrease as the amount of NFC pulp in the sheet increased, which was obtained from the wicking test.

Statistical analysis of the experimental data showed that the wicking times were similar, which shows integrity of the data. However, from Appendix D 3.1.2, it can be seen that there were instances where the data deviated from the averages significantly. This can be seen in the 50% samples, where the standard deviation is high. This could be the result of deviation in sample physical properties.

6.2.2.6 Recycled

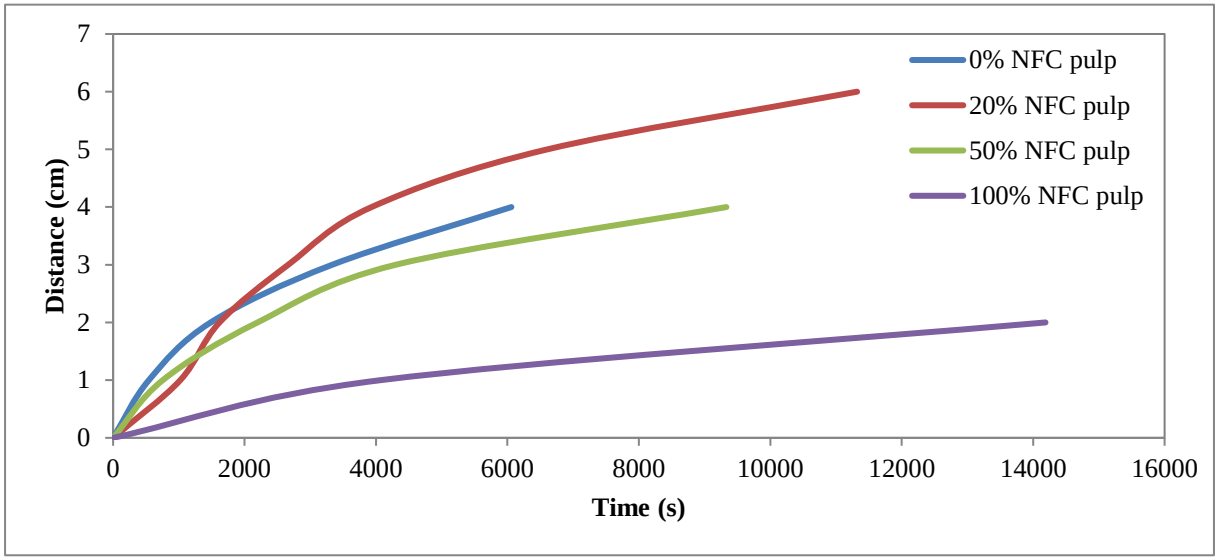

Figure 6.13: Horizontal wicking rates for REC samples at different substitutions of nanofibrillated pulp with dye as wicking liquid.

From Figure 6.13, it was observed that the graphs did not follow the same trend as the previous substrates, as seen in 6.2.2.2 – 6.2.2.5. Here it was seen that the 0% NFC sample initially was the quickest wicker, however the 20% sample eventually overtook the 0% NFC sample at a distance of approximately 2 cm. The 0%, 50% and 100% NFC samples followed. All the graphs followed an exponential graph, indicating the wicking rate slowed down with distance wicked. It was observed that the dye did not wick throughout the length of the substrate strip. The wicking stopped at 6 cm for the 20% NFC sample, 4 cm for the 0% and 50% NFC samples, and 2 cm for the 100% NFC sample.

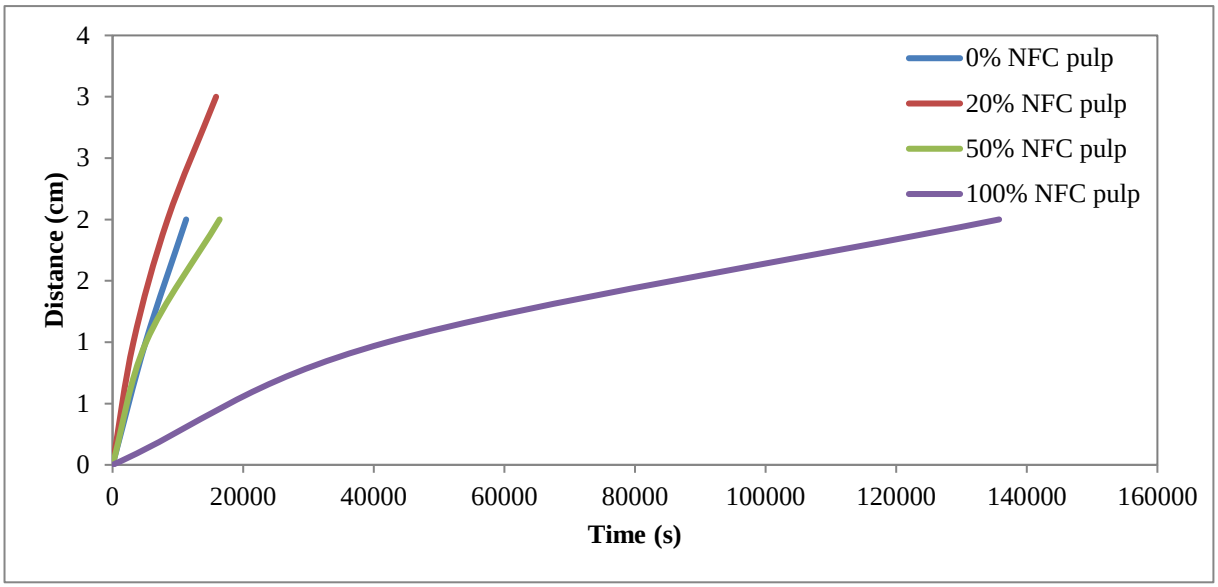

Figure 6.14: Horizontal wicking rates for REC samples at different substitutions of nanofibrillated pulp with blood simulant as wicking liquid.

Figure 6.14 followed the same trend as Figure 6.13, showing that the 20% NFC sample is the fastest wicking substrate followed by 0%, 50% and 100% NFC samples. The 0%, 20% and 50% NFC samples followed a fairly linear graph pattern, which showed a uniform wicking rate. The 100% NFC sample followed that of an exponential graph, showing that wicking rate decreased over the distance covered. Due to the composition of recycled pulp, with contaminants such as lignin, stickies and inks, there was a high resistance to wicking. This was observed in the ceasing of liquid motion during the experiment. The 20% NFC sample stopped at 3 cm, the 0%, 50% and 100% NFC samples at 2 cm.

Conclusion from the FEG-SEM experiments (Chapter 4.3) was different to those from the wicking results. The 20% sheet was seen to wick the fastest, however the FEG-SEM showed that the 0% sheet should produce the fastest wicking rate. Discrepancy in the data could be a result of contaminants within the sheets, such as lignin or stickies, which would cause a difference in wicking rates.

Statistical analysis was conducted on the data (Appendix D 3.1.5). It was found that there was a deviation in wicking times in certain samples. The NFC pulp samples, i.e. 20%, 50% and 100% NFC samples showed the highest deviations in wicking times, especially as the

wicking distance increased. A possible explanation of this result could come from factors such as paper substrate properties (thickness and uniformity).

6.3 Vertical Wicking

6.3.1 Base substrates

Analysing Figure 6.15, it was observed that the GM substrate was the fastest wicking substrate. The graph followed a linear graph with a steep gradient, showing that the wicking rate is fast in comparison to the other substrates. The substrates with the second fastest wicking rates were SULP and UBK, which had a similar wicking path, as seen from the overlaid graphs. The substrates wicking profiles followed a slightly curved graph, showing that the wicking rate decreased as the liquid moved throughout the substrates. The BK substrate was fourth fastest wicking, followed closely by CHR3. The SULP, UBK, BK and CHR3 graphs followed the same curved graph path, which starts off as a linear graph, representing a fast wicking rate initially, which slowed down as the experiment progressed. The CHR substrate followed the CHR3 substrate in wicking rate. The graph resembled an exponential decay graph, displaying a fast wicking rate initially, slowing down with distance covered and eventually levelled off toward the latter of the graph. It was observed that the dye did not wick throughout the substrate, where motion ceased at 9 cm. The FEG-SEM conducted for these substrates showed variances from the experimental data found from the wicking test. This could be a result of a variety of factors, these being the morphology of the fibres and thickness of the sheet being different to that from the micrographs. The TMP substrate had the second slowest wicking rate. As previously discussed in section 6.2.1, this result was expected due to the lignin present in the substrate, which is known to retard motion. Field emission gun-scanning electron microscopy, from Chapter 4.2, supported this result as the pore size was smaller when compared to the other 6 substrates mentioned. During experimentation, it was seen that the dye stopped wicking at 6 cm. The REC substrate was the slowest wicking substrate as was expected. From the previous section 6.2.1, it was stated that the contaminants within the substrate would negatively affect wicking rate. The FEG-SEM results backed the end result, which showed that REC had the smallest pore size (as seen in Chapter 4.2). Similar to TMP, the REC substrate did not allow the dye to move the full distance of the substrate. The dye stopped at a distance of 3 cm.

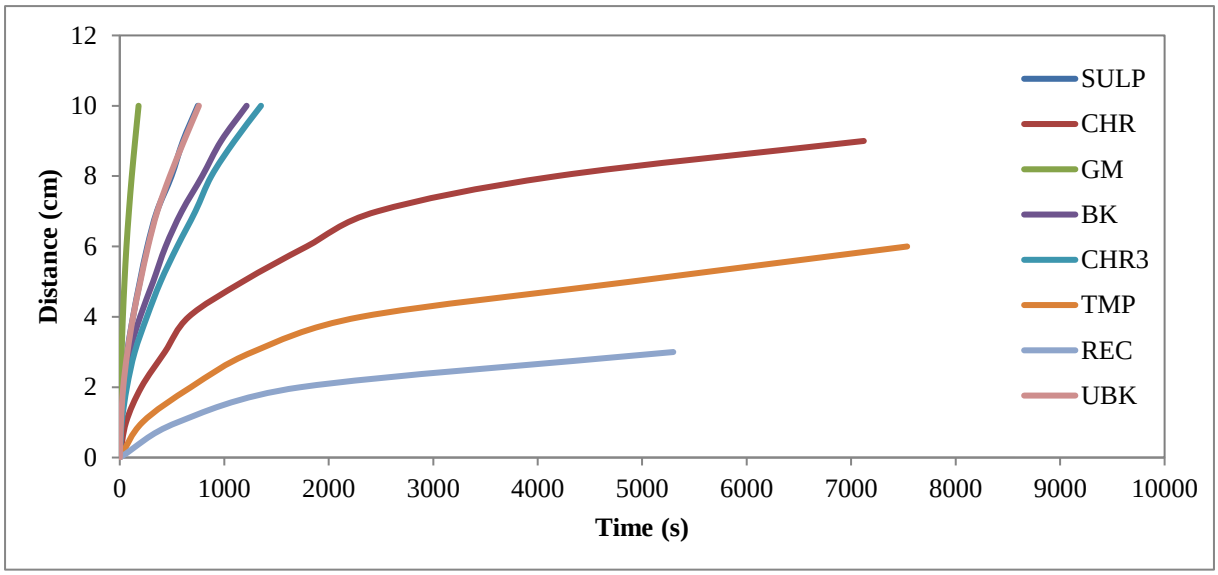

Figure 6.15: Vertical wicking rates for different substrates with dye as wicking liquid.

Figure 6.16 showed that GM was the fastest wicking substrate, using blood simulant as the wicking liquid. The wicking rate initially followed a linear graph, changing into an exponential graph showing that the wicking rate decreased. The second fastest wicking material was found to be SULP followed closely by BK. This was expected from the FEG-SEM images in Chapter 4.2. It was seen that these substrates were exponential by nature. However, it was seen that the BK graph deviated from the graph at a distance of approximately 7 cm. A spike in wicking rate was experienced, which could be attributed to a possible decrease in thickness of the sheet due to non-uniformity, allowing for quicker uptake of liquids. The UBK substrate was the fourth fastest wicking substrate, which followed BK closely. From field emission gun-scanning electron microscopy (Chapter 4.2), it was observed that BK had a larger pore size than the UBK, thereby supporting the data obtained. The CHR3 and CHR sheets were the fifth and sixth fastest wicking substrates respectively. The FEG-SEM results showed that CHR had larger voids between the fibres than CHR3, therefore it was expected to have a higher wicking rate. The inconsistencies from the experiments could be due to a variation in fibre network structure to that of the micrographs in Chapter 4.2. The graphs followed exponential decay paths. The CHR substrate reached a saturation point at a distance of 9 cm. The TMP sheet was the second slowest wicker, which was expected as from Figure 6.2. Similar to CHR, TMP reached a point where liquid motion stopped at a distance of 5 cm. The recycled pulp sheet was the slowest wicking substrate, as

expected from FEG-SEM (see Chapter 4.2). The REC substrate reached a saturation point at 3 cm, where the motion of the blood simulant stopped. Both the TMP and REC graphs followed an exponential path, showing a decrease in wicking rate with distance.

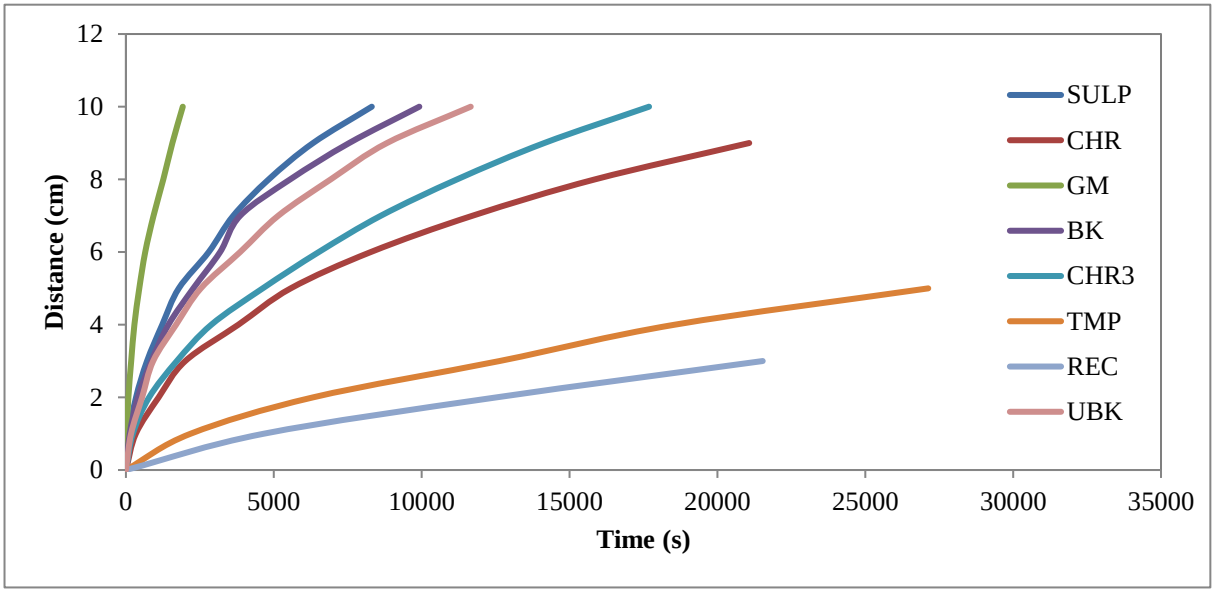

Figure 6.16: Vertical wicking rates for different substrates with blood simulant as wicking liquid.

With each wicking test conducted, statistical analysis was carried out to ascertain if the data was consistent and within an acceptable range. This was determined by calculation of standard deviation (see Appendix D 2.2). Upon analysis of the standard deviations, it was concluded that the data points were similar to that of the averages calculated. Therefore, the averages were a good representation of the original data obtained.

When comparing Figure 6.15 and 6.16, it was found that the when using a high viscosity liquid, such as the blood simulant, wicking times increased significantly. It can also be seen that the wicking liquid did not change the order of fastest wicking substrates, apart from the anomalies mentioned.

6.3.2 Nanofibrillated substrates

6.3.2.1 Substrate substituted with 50% NFC pulp

A comparison between the vertical wicking rates of the substrates substituted with 50% NFC pulp could be observed in Figure 6.17. Similar to Figure 6.3 showing horizontal wicking,

SULP was the fastest wicking substrate. The SULP graph followed an exponential path, where the wicking rate slowed down as the wicking distance increased. The FEG-SEM images in section 4.3 supported this result, showing that the pore size of the SULP sheet was the largest. The CHR sheet was the second fastest wicking substrate followed by CHR3. From the microscopy analysis in section 4.3, it was observed that the CHR and CHR3 substrates had similar pore sizes. This indicated that the wicking rates of these sheets should be similar. The difference in these results could be explained by a variance in sheet thickness and morphology of the sheet. The UBK and REC were observed to have the slowest wicking rates. This was expected from FEG-SEM analysis (section 4.3), as these substrates had the smallest pore size.

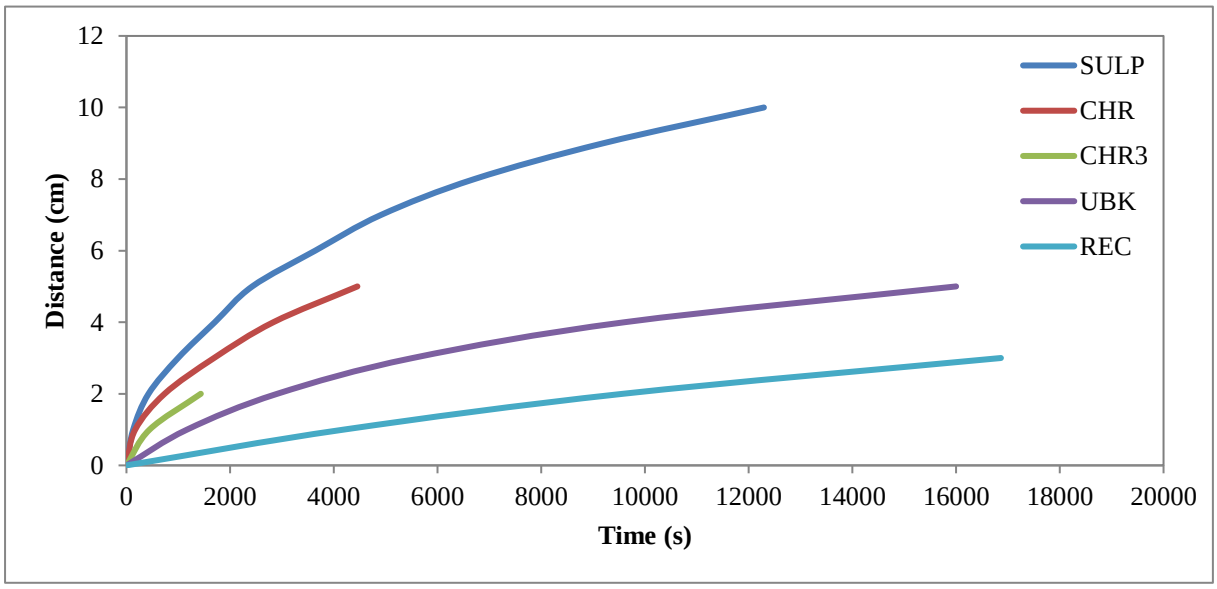

Figure 6.17: Vertical wicking rates for substrate substituted with 50% NFC pulp samples at different substitutions of nanofibrillated pulp with dye as wicking liquid.

Figure 6.18 shows the vertical wicking results for the 50% NFC pulp substituted sheets using blood as a wicking liquid. It can be observed that Figure 6.17 and 6.18 follow different trends as will be explained. The results showed that SULP was the fastest wicking substrate, which was expected from the FEG-SEM in section 4.3. The UBK and REC substrates followed, with a linear wicking trend which levels off. The microscopy results showed that this substrate had the smallest pore size, therefore would be predicted to have the slowest wicking rates. CHR and CHR3 were the slowest wicking substrates. These results were unexpected, as CHR and CHR3 had the larger pore sizes than UBK and REC. The discrepancies in the

results, as previously discussed, could be the factors such as differences in thickness and fibre structure within the sheet.

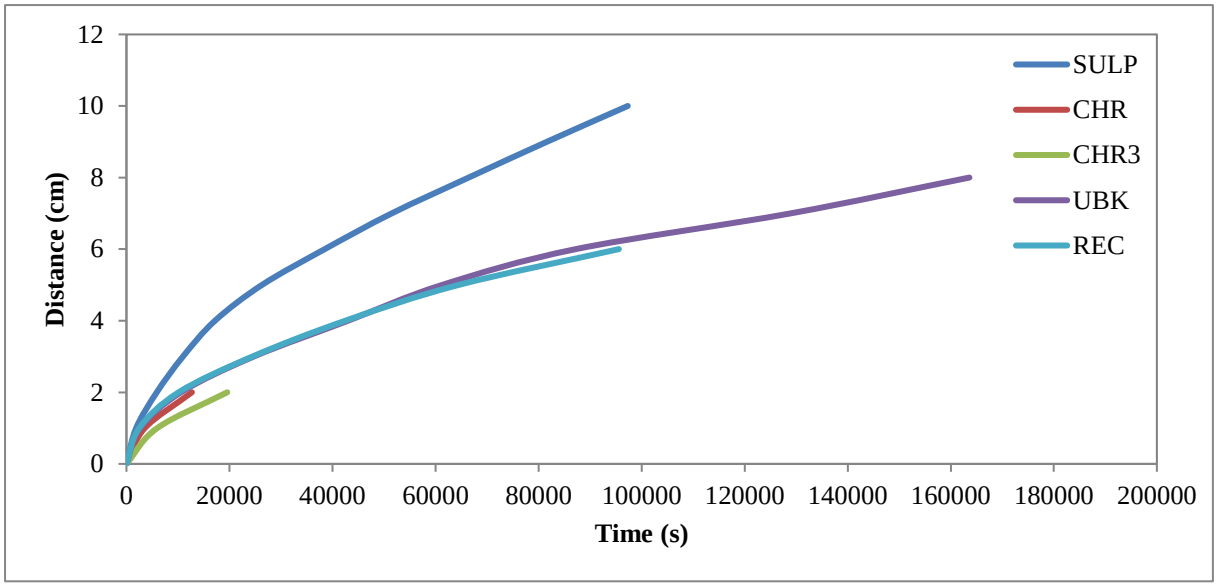

Figure 6.18: Vertical wicking rates for substrate substituted with 50% NFC pulp samples at different substitutions of nanofibrillated pulp with blood simulant as wicking liquid.

6.3.2.2 Sulphite

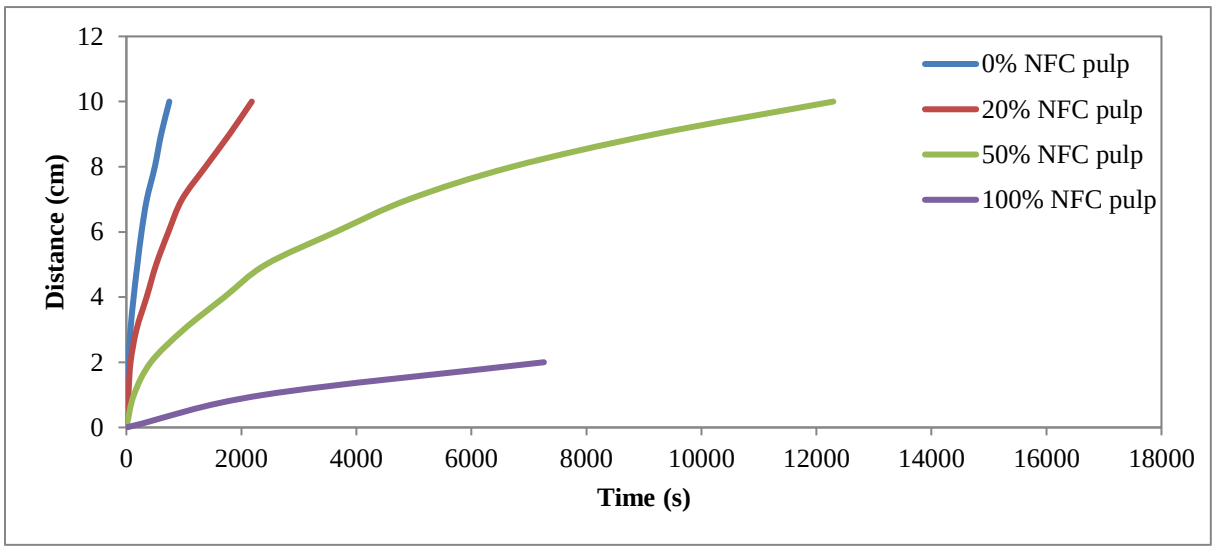

Figure 6.19: Vertical wicking rates for SULP samples at different substitutions of nanofibrillated pulp with dye as wicking liquid.

From Figure 6.19, it was seen that an increase in percentage of NFC pulp in the sample resulted in a decrease in the wicking rate. The 0% NFC sample was the quickest wicking followed by the 20% NFC sample. Both the 0% and 20% NFC sample follow a linear trend, transitioning into an exponential graph toward the end. The 50% NFC sample followed, with an exponential graph. Lastly, the 100% NFC sample was the slowest wicking. The substrate reached a point when liquid motion stopped. This was at a distance of 2 cm. From the experiment, it was observed that the 100% NFC sample did not wick well.

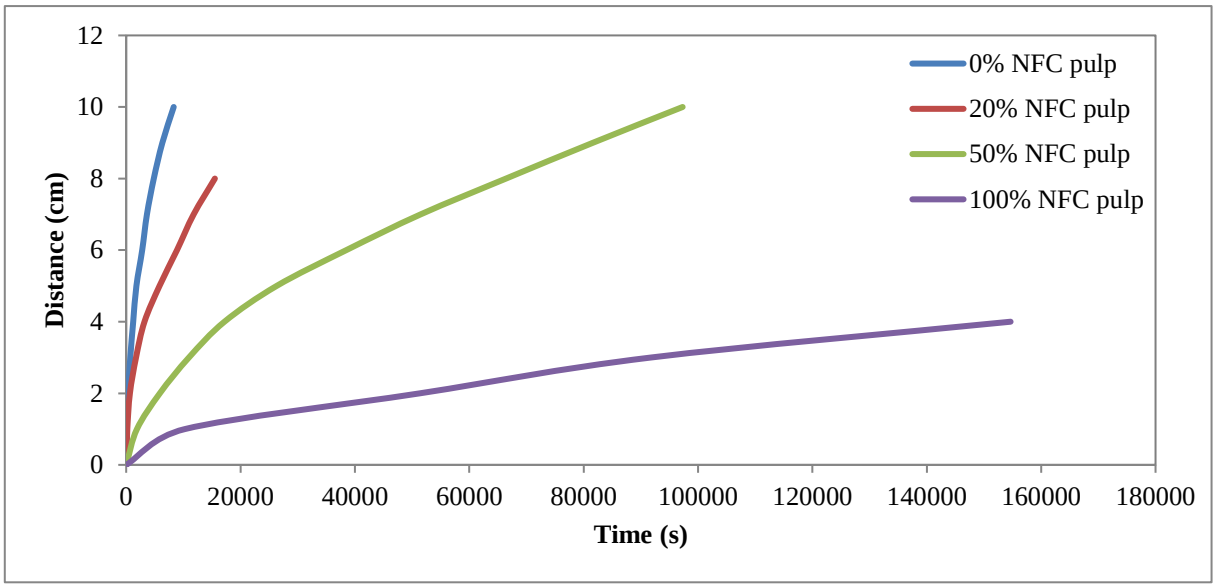

Figure 6.20: Vertical wicking rates for SULP samples at different substitutions of nanofibrillated pulp with blood simulant as wicking liquid.

Based on the results from Figure 6.20, the same trend was seen in the blood simulant experiment as the dye experiment. This showed that the substitution of NFC pulp slowed the motion of liquid through the substrate. The 0% NFC sample was the fastest wicker, followed by 20% NFC sample, 50% NFC sample and lastly, the 100% NFC sample. The 0% and 20% samples followed a linear path and eventually diverted to an exponential path. The 50% and 100% NFC samples followed an exponential graph, showing an initial quick wicking rate, levelling off toward the latter of the experiment. It was observed that the 20% and 100% NFC substrates reached saturation. The 20% NFC sample stopped at a distance of 9 cm and the 100% NFC sample at 4 cm. Comparing figures 6.19 and 6.20, it can be seen that the time taken for the blood simulant to wick is greater than that of the dye, due to the high viscosity of the blood simulant.

The images obtained from FEG-SEM analysis, conducted in section 4.3, could be used to support the results obtained from this experiment. It was expected that as the amount of NFC pulp increased in the sheet, the pore size decreased, resulting in a decrease in wicking rate of the sheet.

Statistical analysis (summarised in Appendix D 3.2.1), showed that the data was fairly closely spread around the average values. A general trend can be seen that as the wicking distance

increased, the standard deviation increased. This implied that the data was dispersed at higher wicking distances. This was expected as the wicking times increased with wicking distance, allowing for the higher standard deviations.

6.3.2.3 Chromatography No.1 Filter Paper

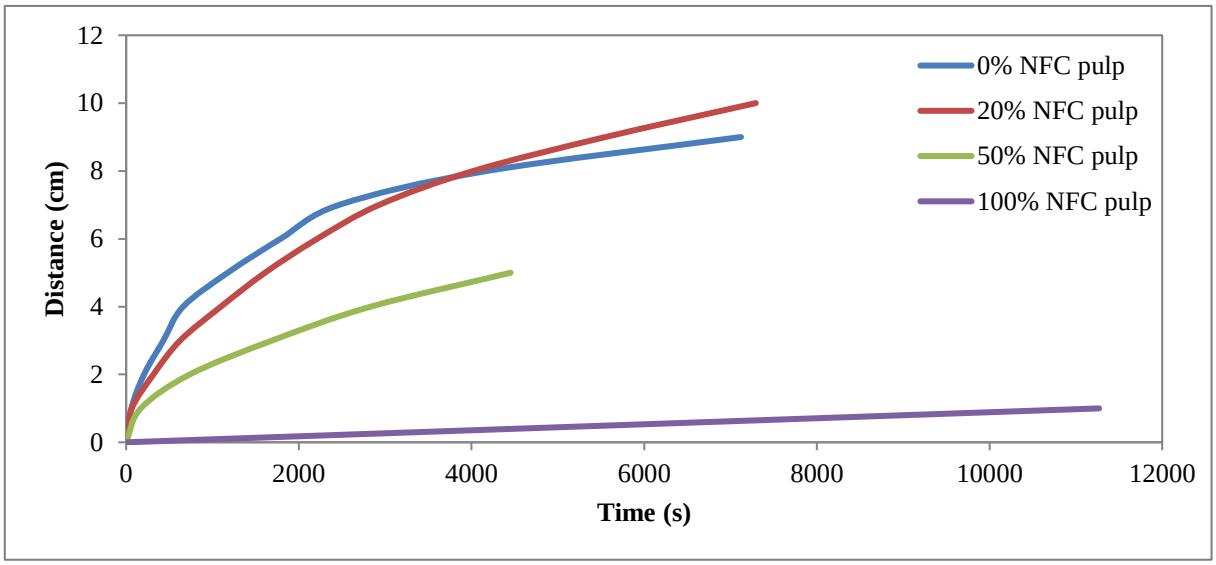

Figure 6.21: Vertical wicking rates for CHR samples at different substitutions of nanofibrillated pulp with dye as wicking liquid.

Figure 6.21 showed a different trend to that found in section 6.3.2.2. As it can be observed that the 0% NFC sample initially was the fastest wicking substrate, but is overtaken by the 20% NFC sample. This anomaly could be a result of the handsheet making of the sheets. Should the sheets not have a uniform distribution of fibre, the thickness of the sheet could be affected, resulting in quicker wicking in thinner sheets, and vice versa for thicker sheets. The 50% NFC sample followed, with an exponential graph. The 100% NFC substrate was the slowest wicking, which followed a linear graph with a gradual gradient, showing that the wicking rate was uniform and slow. The 0%, 50% and 100% NFC samples reached a saturation point at 9 cm, 5 cm and 1 cm respectively.

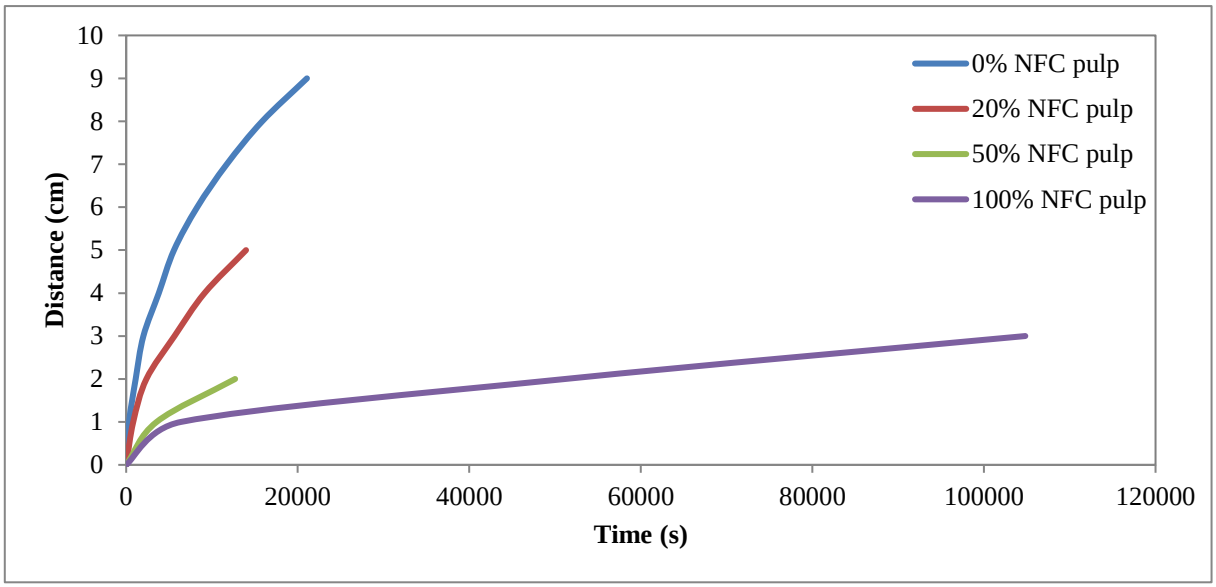

Figure 6.22: Vertical wicking rates for CHR samples at different substitutions of nanofibrillated pulp with blood simulant as wicking liquid.

Figure 6.22 followed the trend from section 6.3.2.2. It can be seen that the wicking rate decreases with the increase in NFC pulp. The 0% NFC sample had the fastest wicking rate, followed by 20% NFC sample, 50% NFC sample and lastly, the 100% NFC sample. The 0% and 20% NFC samples followed a linear graph, with a fast initial wicking rate, curving towards the end. The 50% and 100% NFC samples followed a general exponential decay graph, which started off with a quick wicking rate, eventually levelling off. It was observed that the 20% and 100% NFC samples experienced an equilibrium between hydrostatic and capillary pressure. The 20% NFC sample reached saturation at 8 cm and the 100% NFC sample at 4 cm.

Focusing on the FEG-SEM images of these substrates (from section 4.3), the results obtained from the wicking experiment were expected, whereby the increase in NFC pulp in the sheet caused a decrease in the wicking rate.

Taking statistical analysis into account, it can be seen that, in general, the averages represent the data accurately (Appendix D 3.2.3). It can be observed that the higher distances had a higher standard deviation. Possible influencing factors of this results could be a difference in the sheet properties, such as thickness and distribution of NFC pulp within the sheet.

6.3.2.4 Chromatography 3MM Filter Paper

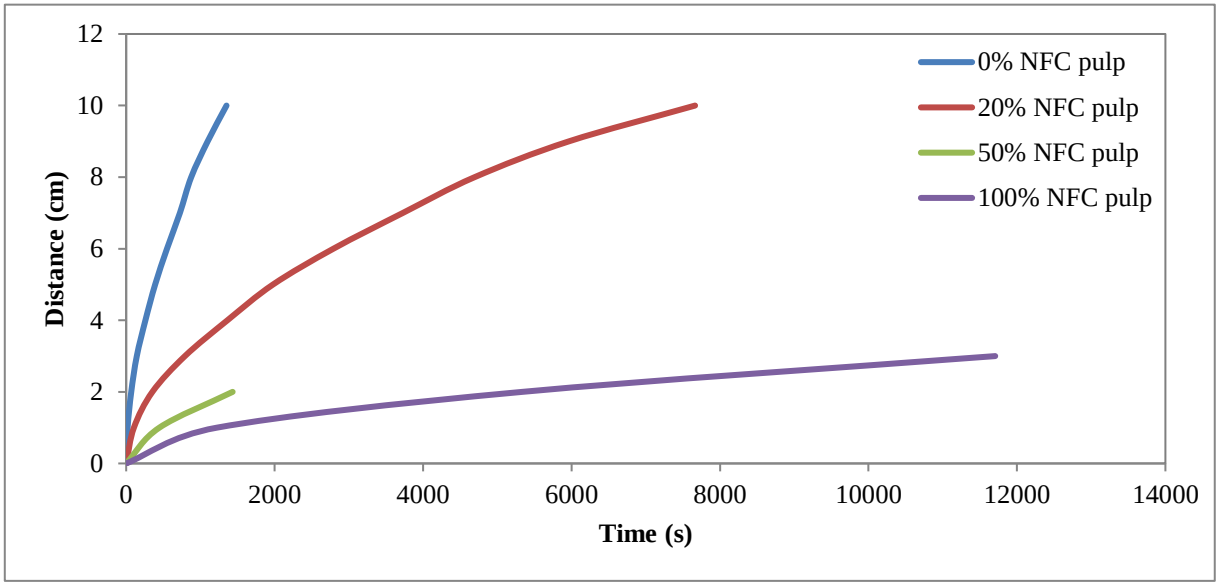

Figure 6.23: Vertical wicking rates for CHR3 samples at different additions of nanofibrillated pulp with dye as wicking liquid.

The trend from section 6.3.2.2 was observed in Figure 6.23. This showed that the 0% NFC sample wicked the fastest, followed by the 20% NFC sample, 50% NFC sample and 100% NFC sample. The 0% NFC sample started off as a linear graph until 8 cm, where it diverted to a curved line. This showed that the wicking rate decreased as distance increased. The 20%, 50% and 100% NFC samples followed exponential curves, which showed a distant decrease in the wicking rate. From the experiment, it was observed that the 50% and 100% NFC samples reached a saturation point at 2 cm and 3 cm respectively. The contact angle test revealed that the 100% NFC sample had the highest contact angle as expected, resulting in a slow wicking rate.

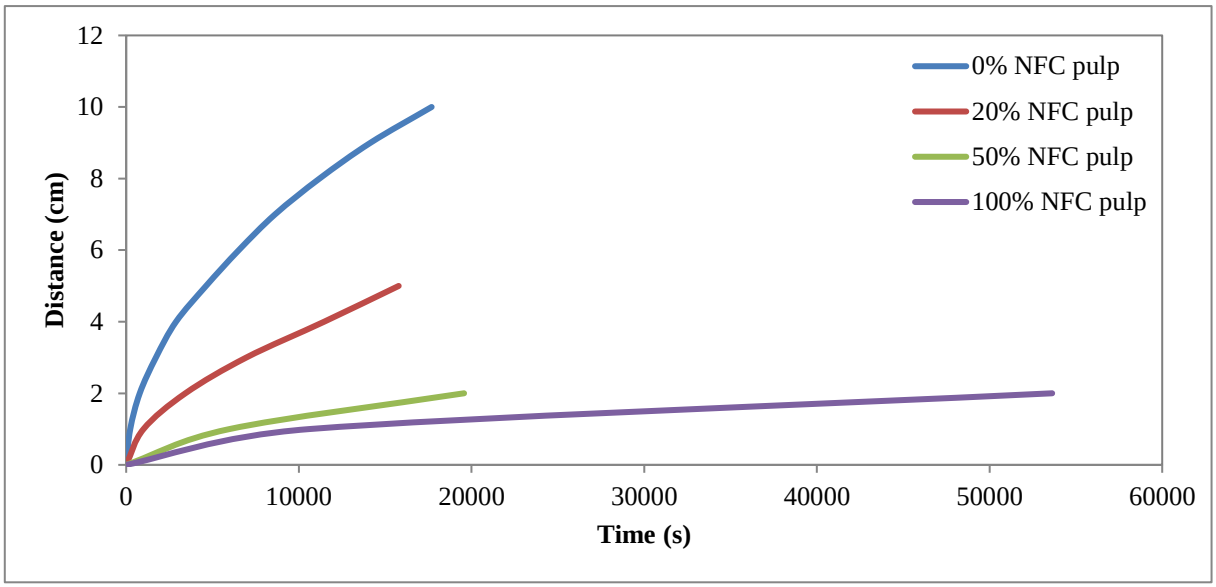

Figure 6.24: Vertical wicking rates for CHR3 samples at different substitutions of nanofibrillated pulp with blood simulant as wicking liquid.

Figure 6.24 followed the same trend as in Figure 6.23. The 0% NFC sample was the fastest wicking substrate, followed by 20%, 50% and the 100% NFC sample. The graphs followed an exponential decay graph, with an initial steep rate, which started to level off to a uniform gradient. The 100% NFC sample was seen to level off to, showing no change in the wicking rate as distance increased. The 20%, 50% and 100% NFC samples reached a saturation point at 5 cm, 2 cm and 2 cm respectively.

The FEG-SEM results, from section 4.3, showed that the pore size decreased with an increase in NFC pulp. The results from the wicking experiment can be seen to be consistent with that of the FEG-SEM.

From the statistical analysis, it was observed that the 3 runs conducted for each substrate were consistent and clustered around the average value (see Appendix D 3.2.4). The standard deviation values calculated showed the range between the values was low, resulting in acceptable data for experimental analysis.

6.3.2.5 Unbleached Kraft

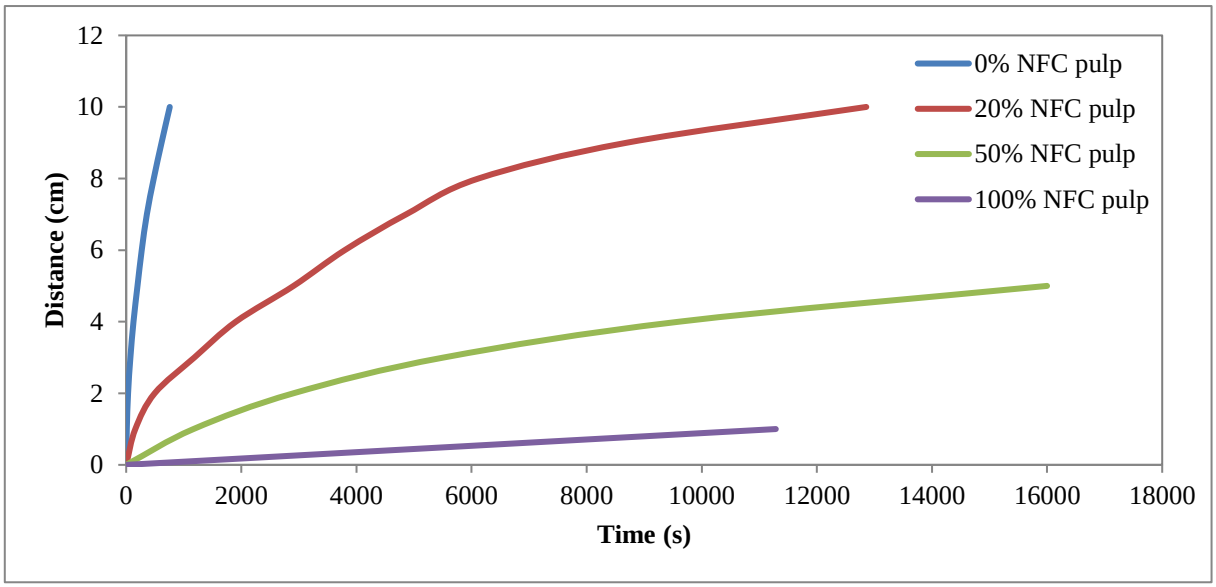

Figure 6.25: Vertical wicking rates for UBK samples at different substitutions of nanofibrillated pulp with dye as wicking liquid.

Observation from Figure 6.25 showed that the 0% NFC sample wicked the fastest, with a steep linear graph, showing that wicking was uniform throughout the substrate when compared to the other samples. The 20% NFC sample was the second fastest wicker, which followed an exponential graph, showing that the wicking rate was uniform, slowing down at a distance of approximately 8 cm. The 50% NFC sample also followed an exponential graph, however it was observed that there was a resistance to absorption of the liquid, as seen from the saturation point at 5 cm. The 100% NFC sample followed a linear graph, showing consistent wicking rates, however it was seen from the experiments that the substrate takes a long period to wick liquid through 1 cm. The FEG-SEM results proved that the 0% NFC sample had the largest pore size, which is directly related to the wicking rate. The pore size decreased from the 20% NFC sample to the 50% NFC sample to the 100% NFC sample.

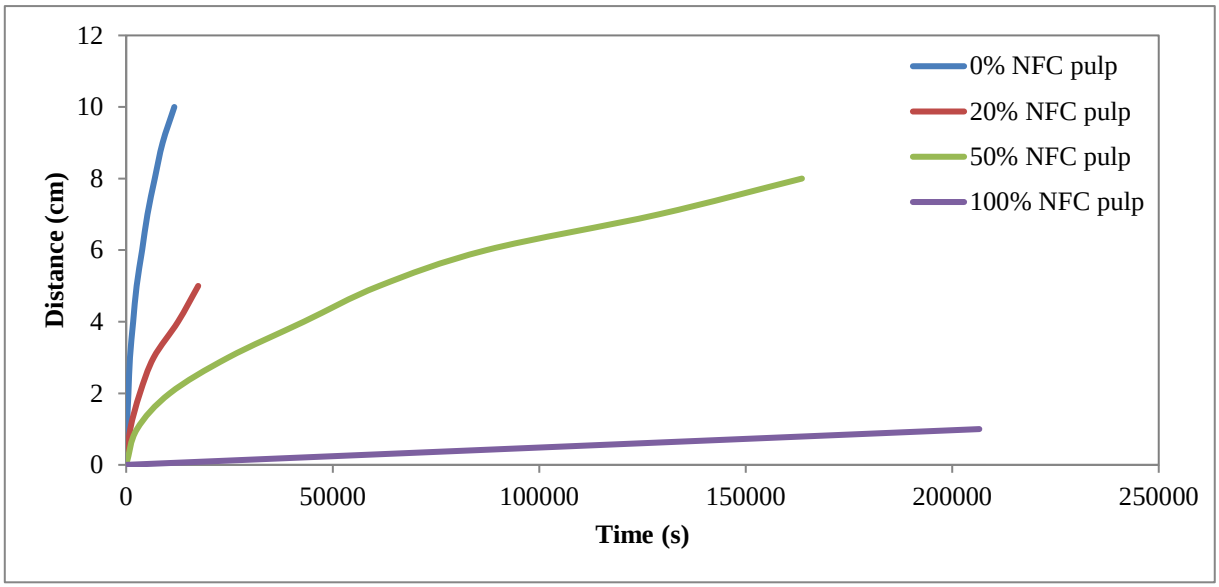

Figure 6.26: Vertical wicking rates for UBK samples at different substitutions of nanofibrillated pulp with blood simulant as wicking liquid.

Figure 6.26 was observed to have the same trend of wicking rates as compared to Figure 6.25. The 0% and 20% NFC samples followed a linear path eventually transitioning into a curved graph path, which showed that the wicking rate decreased with increasing distance, but was initially consistent. The 50% NFC sample followed an exponential graph, with a decrease in wicking rate as liquid moved through the sample. The 100% NFC sample followed that of a linear graph, with a gradual gradient, indicating that resistance to wicking was experienced. The 20%, 50% and 100% NFC samples reached a point where the motion of the blood simulant stopped. The 20% NFC sample stopped at 5 cm, 50% NFC sample at 8 cm and the 100% NFC sample at 1 cm.

The micrographs obtained, as seen in section 4.3, showed that the pore size decreased with the increase in NFC pulp, thereby resulting in a slower wicking rate, which was observed from the wicking experiment.

Statistical analysis of the experimental data showed that the wicking times were similar and spread close to the mean value, from Appendix D 3.2.2. The standard deviations showed that the data did not deviate excessively in comparison to the wicking time averages, deeming the results acceptable for analysis.

6.3.2.6 Recycled

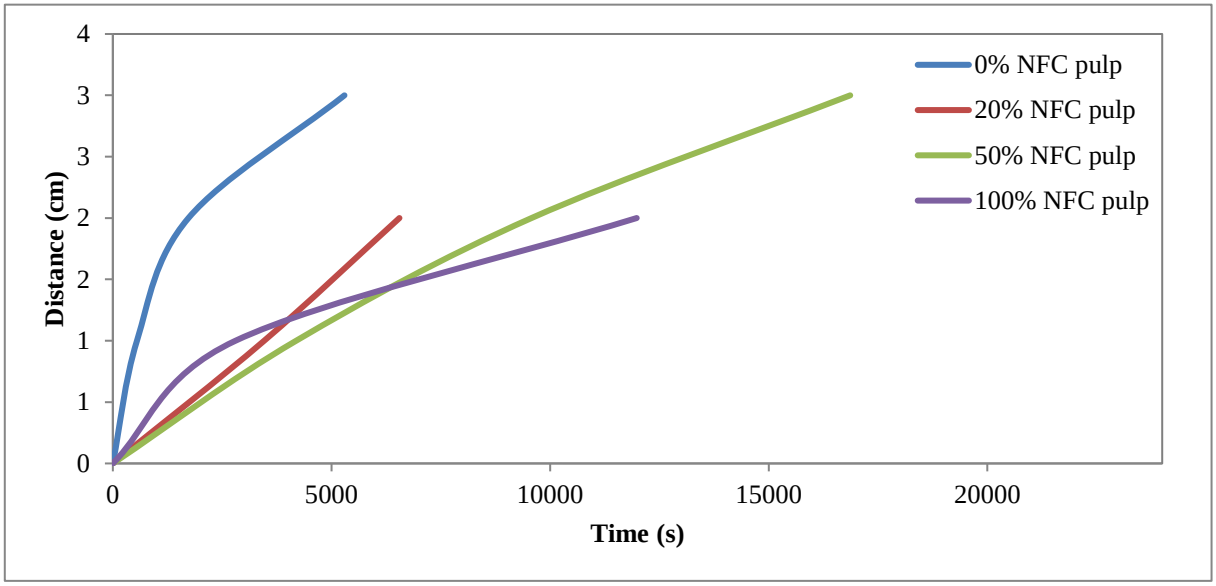

Figure 6.27: Vertical wicking rates for REC samples at different substitutions of nanofibrillated pulp with dye as wicking liquid.

From Figure 6.27, it was observed that the graphs did not follow the same trend as the previous substrates, as seen in sections 6.3.2.2 – 6.3.2.5. The 0% NFC sample is the fastest wicking substrate. Thereafter, the 100% NFC sample was the second had the second fastest wicking rate, until approximately 1 cm, where the 20% NFC sample overtook. The 100% NFC sample eventually became the slowest wicker after a distance of 1.5 cm. This was an anomaly, which could be a result of uneven sheet grammage, allowing for quicker uptake of liquid at certain areas on the substrate strip. The 50% NFC sample was the slowest wicker initially, however became the second slowest after a distance of 1.5 cm. The 0%, 50% and 100% graphs followed an exponential graph, indicating the wicking rate slowed down with distance wicked. The 20% NFC sample followed a linear graph. It was observed that the dye did not wick throughout the length of the substrate strip. The wicking stopped at 3 cm for the 0% NFC sample, 2 cm for the 20% and 50% NFC samples, and 3 cm for the 100% NFC sample.

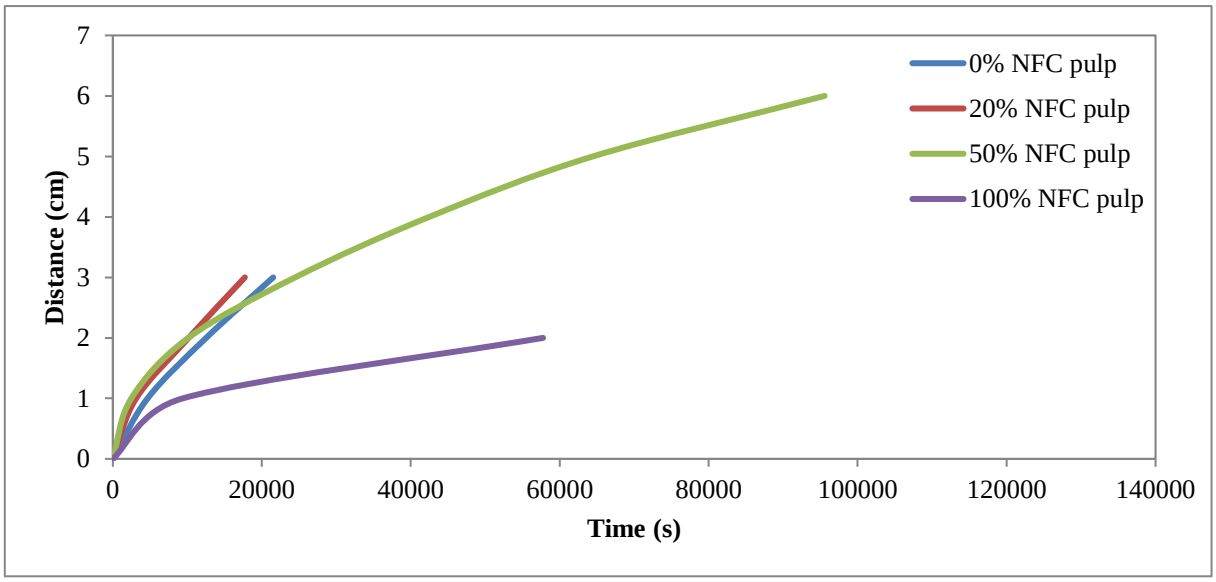

Figure 6.28: Vertical wicking rates for REC samples at different substitutions of nanofibrillated pulp with blood simulant as wicking liquid.

Figure 6.28 showed a different trend to that of Figure 6.27. This graph showed that the 0%, 20% and 50% NFC samples initially had similar wicking rates until approximately 2 cm. Thereafter, the 20% NFC sample was the fastest wicking substrate, followed by the 0% NFC sample and then the 50% NFC sample. These samples followed a fairly linear graph pattern, which showed a uniform wicking rate. However, the 50% NFC sample diverted into an exponential graph, which started to level off. The 100% NFC sample, which had the slowest wicking rate, followed that of an exponential graph, showing that wicking rate decreased over the distance covered. It was observed that ceasing of liquid motion was present during the experiment. The 0% and 20% NFC samples stopped at 3 cm, 50% NFC sample at 6 cm and 100% NFC sample at 2 cm.

The FEG-SEM experiments (section 4.3) showed different to those obtained from the wicking results, specifically in the blood simulant experiment. The 20% NFC sheet was seen to wick the fastest in the blood simulant experiment, however the FEG-SEM showed that the 0% NFC sheet had the largest pore size, therefore a quicker wicking rate. Factors affecting the results could be the presence of contaminants within the sheets, such as lignin or stickies, which would cause a difference in wicking rates.

Statistical analysis was conducted on the data (Appendix D 3.2.5). It was found that the data was fairly consistent in wicking times. The standard deviations showed that the data was spread in close proximity to the average value, leading to integrity of the data.

6.4 Comparison of horizontal and vertical wicking test results

From theoretical knowledge, the motion of the liquid in the vertical wicking tests will be retarded due to the hydrostatic pressure (Simile, 2004). Therefore, horizontal wicking is expected to be faster in comparison to vertical wicking. Comparing the horizontal and vertical wicking tests for each base substrate showed that this is not always the case, wherein tests using the blood simulant as a wicking liquid, the vertical wicking rate was, in fact, quicker than the horizontal wicking rate.

For the case of the SULP substrate using dye as the wicking liquid, (Figure 6.29) it was observed that the vertical and horizontal wicking rate were similar. However, when the blood simulant was used, there was a discrepancy in the wicking rates, where the vertical wicking was faster than that of the horizontal wicking. A previous study by Simile (2004) showed that there were inconsistencies in capillarity of the substrates to account for this result. Another possibility could be as a result of the higher viscosity of the blood simulant, which produced a higher viscosity drag in the horizontal tests, producing slower wicking rates.

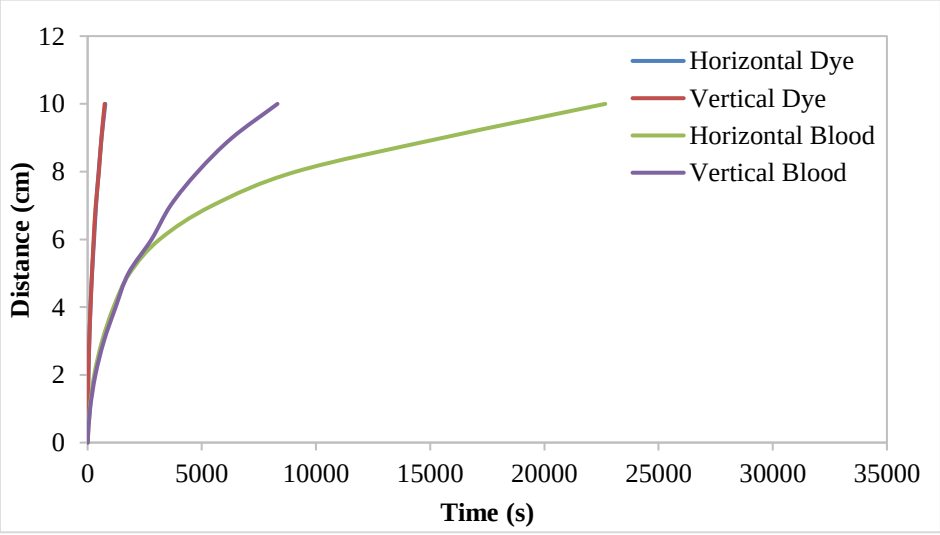

Figure 6.29: Comparison of horizontal and vertical wicking rates for base SULP samples with dye and blood simulant as wicking liquid.

CHR, BK, GM and TMP substrates showed differing results from SULP, where it was seen that the horizontal wicking rate was faster compared to the vertical wicking rate for the dye. This result was expected from theoretical knowledge (Simile, 2004). However, the opposite could be seen for the blood simulant (see Figures 6.30 – 6.33). The GM substrate can be seen to have similar wicking rates for horizontal and vertical tests, with slight deviations toward the latter of the graphs (Figure 6.32). Similarly to that of the SULP substrate, a possible explanation for these results could be a higher retarding force due to viscosity in the horizontal direction, as well as capillary differences within the samples.

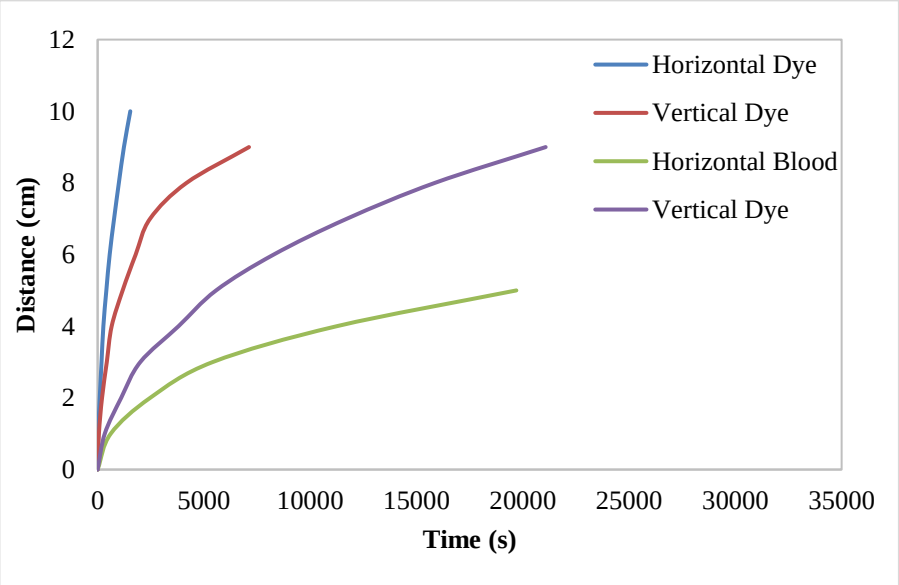

Figure 6.30: Comparison of horizontal and vertical wicking rates for base CHR samples with dye and blood simulant as wicking liquid.

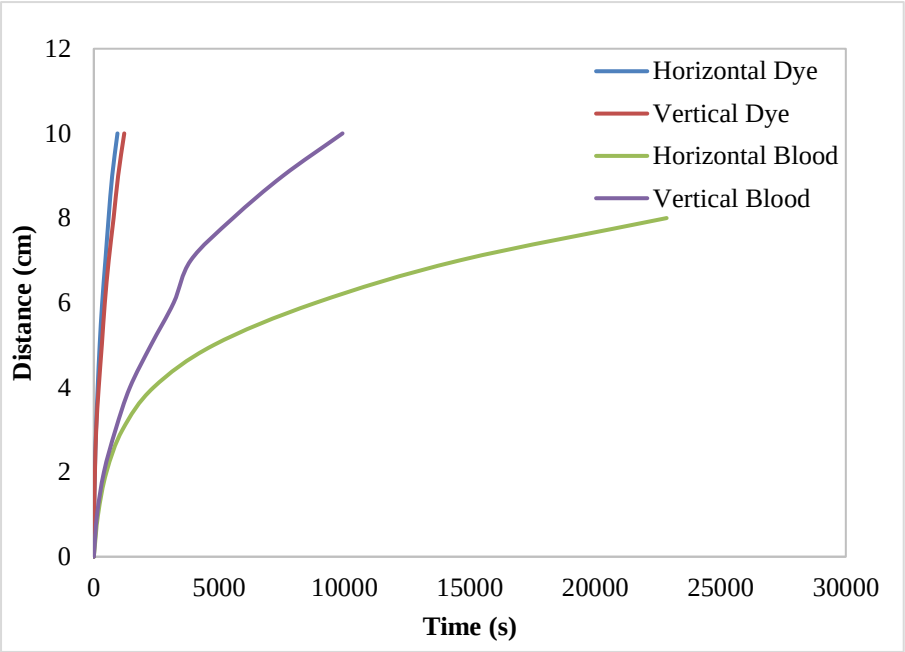

Figure 6.31: Comparison of horizontal and vertical wicking rates for base BK samples with dye and blood simulant as wicking liquid.

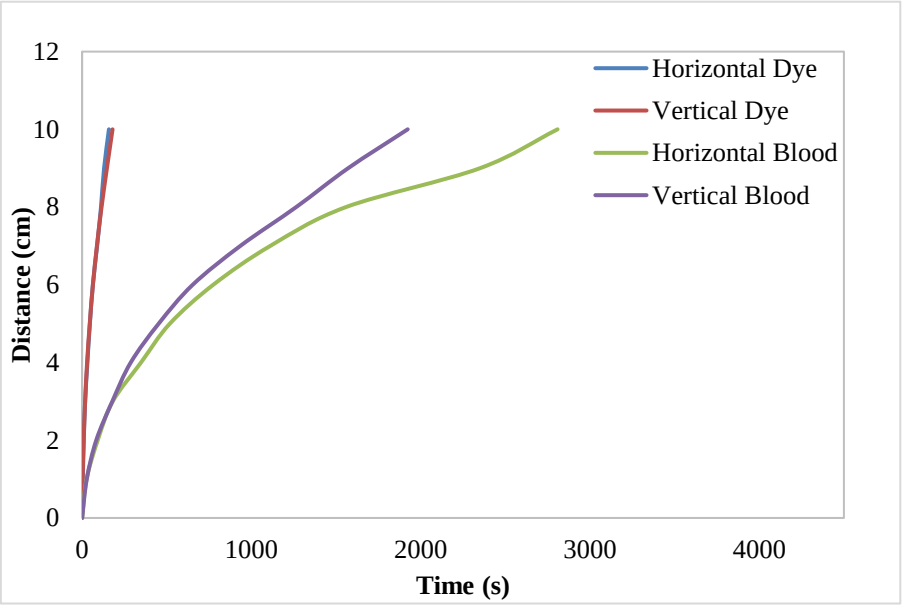

Figure 6.32: Comparison of horizontal and vertical wicking rates for base GM samples with dye and blood simulant as wicking liquid.

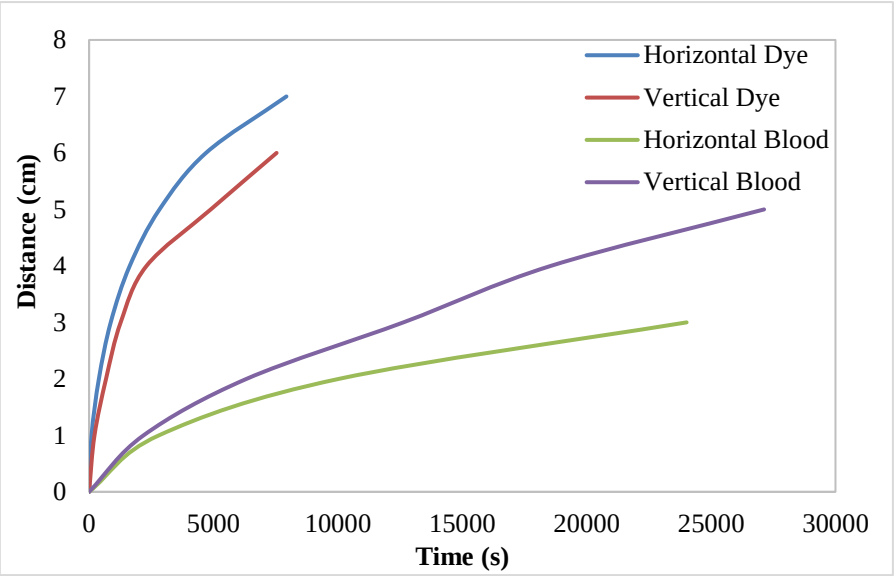

Figure 6.33: Comparison of horizontal and vertical wicking rates for base TMP samples with dye and blood simulant as wicking liquid.

For the REC substrate, using both dye and blood simulant as the wicking liquid (Figure 7.34), it was observed that the horizontal wicking rate was faster than that of the vertical. The wicking test with blood simulant showed similar wicking rates for both tests, however the horizontal wicking rate slightly exceeds the vertical wicking rate.

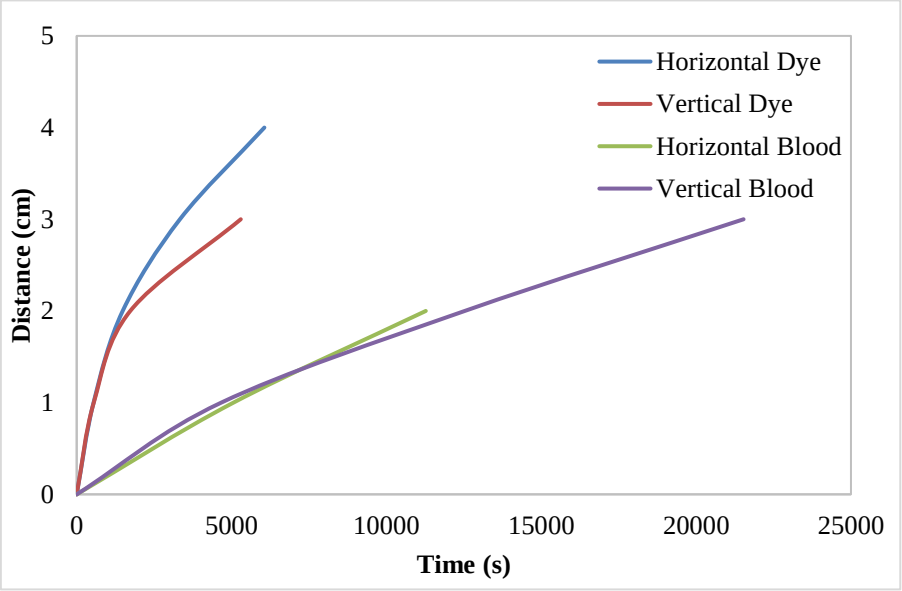

Figure 6.34: Comparison of horizontal and vertical wicking rates for base REC samples with dye and blood simulant as wicking liquid.

UBK and CHR3 substrates follow the same trend (Figures 6.35 and 6.36). It was observed that for both cases (dye and blood simulant), the vertical wicking rates were faster than that of the horizontal wicking test. This was not an expected result, as from theory, the vertical wicking rates should be slower due to the forces of gravity acting against the motion. As discussed, there could be inconsistencies in capillarity of the substrates which account for the anomaly.

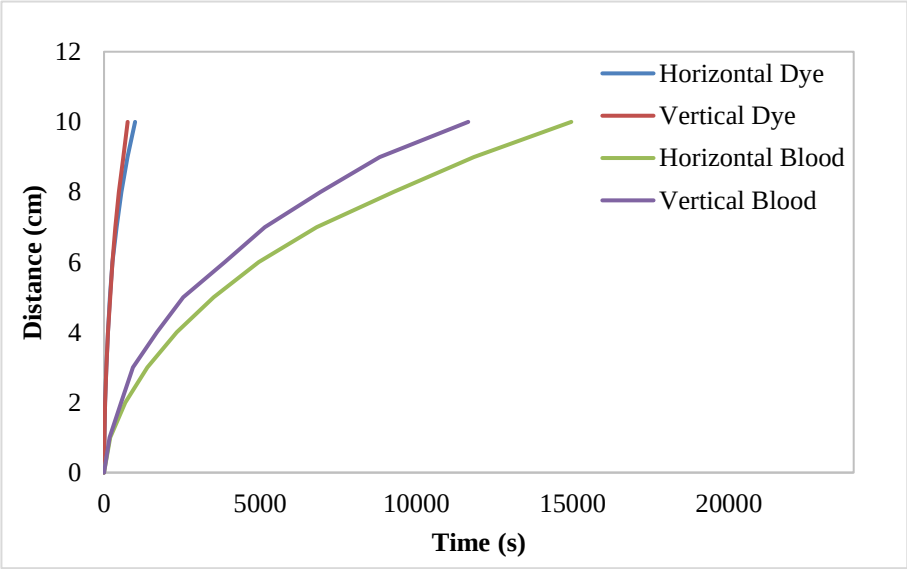

Figure 6.35: Comparison of horizontal and vertical wicking rates for base UBK samples with dye and blood simulant as wicking liquid.

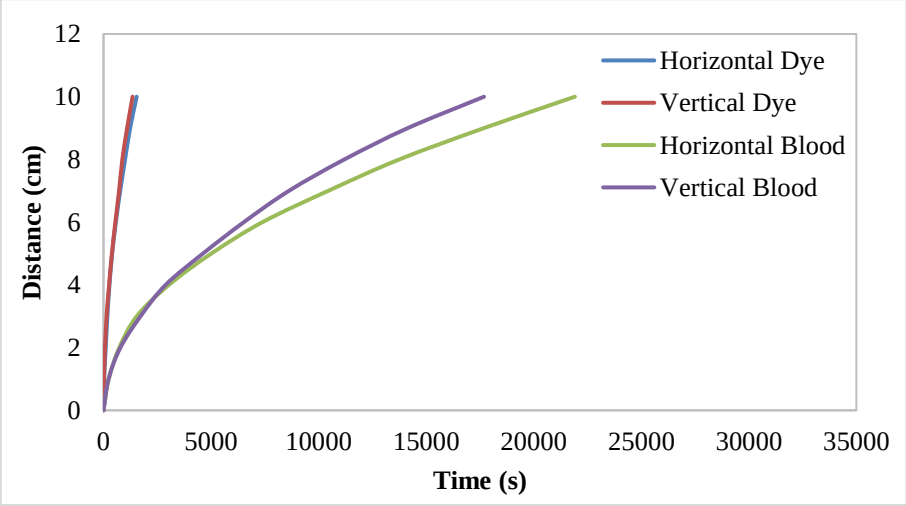

Figure 6.36: Comparison of horizontal and vertical wicking rates for base CHR3 samples with dye and blood simulant as wicking liquid.

From the results obtained, it can be seen that there is no consistency when it comes to whether horizontal or vertical wicking rates are quicker. Therefore, it can be said that each substrate produces a different result, which is based on the capillarity of the sample as well as the wicking liquid used in the experiment.

6.5 Modelling data using Lucas-Washburn model

The Lucas-Washburn model is used for modelling capillary flow in porous media, where the medium of choice is modelled as a bundle of tubes. The model follows equation (6):

$$l^2 = \frac{r\gamma_{LV}cos\theta}{2\eta}\ t \qquad (6)$$

Should the flow of fluid through the medium follow this model, the resulting graph of distance squared (l^2) vs time (t) will follow a directly proportional relationship.

6.5.1 Base substrates

Figure 6.37 plotted l^2 vs t for the base substrates using dye as the wicking liquid in a horizontal wicking test. Linear trend lines were inserted, with a coefficient of determination (R^2) attached to each graph. It can be seen that the substrates followed a close linear relationship with l^2 and t, showing that the substrates followed the Lucas-Washburn model. The R^2 values, from Table 6.1, showed that the data points fit the linear regression line, with the lowest R^2 value being 0.981.

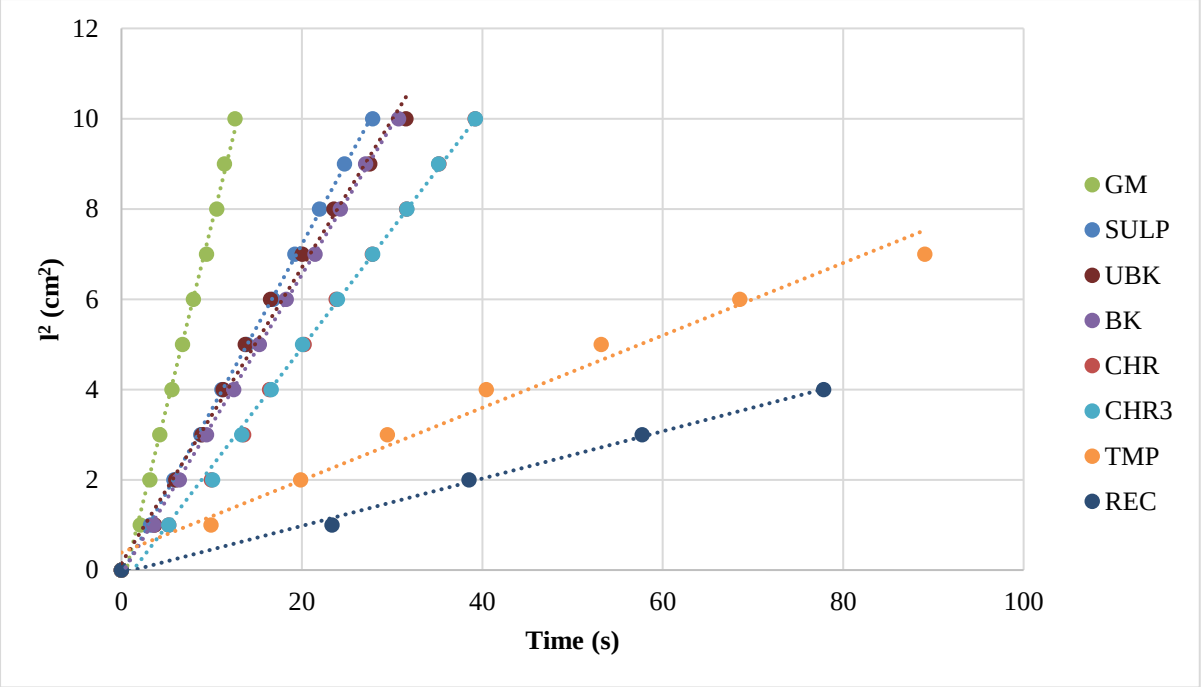

Figure 6.37: Relationship between l^2 and t for horizontal wicking test base substrates and dye as wicking liquid.

Table 6.1 showing the R^2 value from the linear regression of data for the horizontal wicking test for dye as wicking liquid.

Substrate	R^2 value
GM	0.9961
SULP	0.9995
UBK	0.9996
BK	0.992
CHR	0.9976
CHR3	0.9976
TMP	0.981
REC	0.9967

Looking at the vertical test results, Figure 6.38, it can be seen that the substrates followed the Lucas-Washburn model. The R^2 values, as seen from Table 6.2, showed a linear relationship between l^2 and t, with the lowest R^2 value being 0.9581 for the CHR substrate.

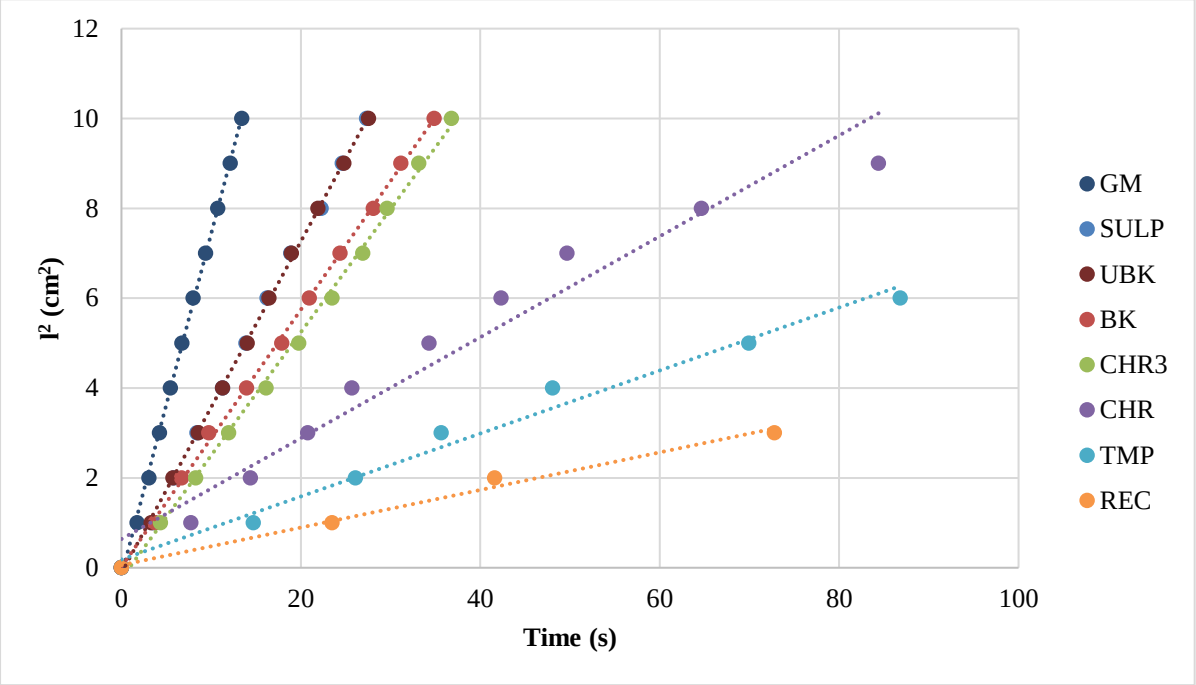

Figure 6.38: Relationship between l^2 and t for vertical wicking test base substrates and dye as wicking liquid.

Table 6.2 showing the R^2 value from the linear regression of data for the vertical wicking test for dye as wicking liquid.

Substrate	R^2 value
GM	0.9992
SULP	0.9995
UBK	0.9995
BK	0.9993
CHR	0.9581
CHR3	0.9978
TMP	0.9835
REC	0.9887

Analysing the horizontal test results for blood simulant as the wicking liquid, Figure 6.39, a discrepancy in the graphs can be seen. The coefficient of determination (R^2) for the substrates allowed for modelling with the Lucas-Washburn model. The SULP graph showed the lowest R^2 value of 0.9335, as seen from Table 6.3. As previously mentioned, the Lucas-Washburn model uses ideal conditions.

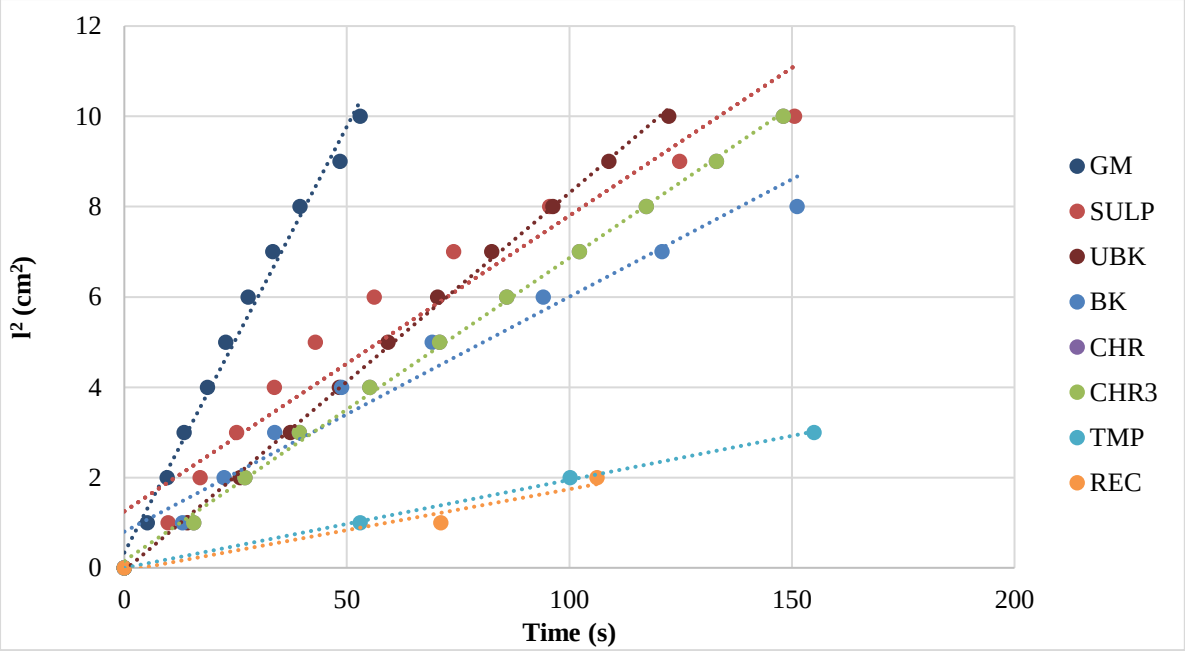

Figure 6.39: Relationship between l^2 and t for horizontal wicking test base substrates and blood simulant as wicking liquid.

Table 6.3 showing the R^2 value from the linear regression of data for the horizontal wicking test for blood simulant as wicking liquid.

Substrate	R^2 value
GM	0.99
SULP	0.9335
UBK	0.9988
BK	0.9599
CHR	0.9986
CHR3	0.9986
TMP	0.9993
REC	0.9629

Figure 6.40 shows the vertical test results for the base substrates using blood simulant. It can be observed that the substrates followed the Lucas-Washburn equation, with a linear relationship between l^2 and t. For the TMP and REC substrates, a lower R^2 value was obtained, being 0.9877 and 0.9756 respectively (from Table 6.4).

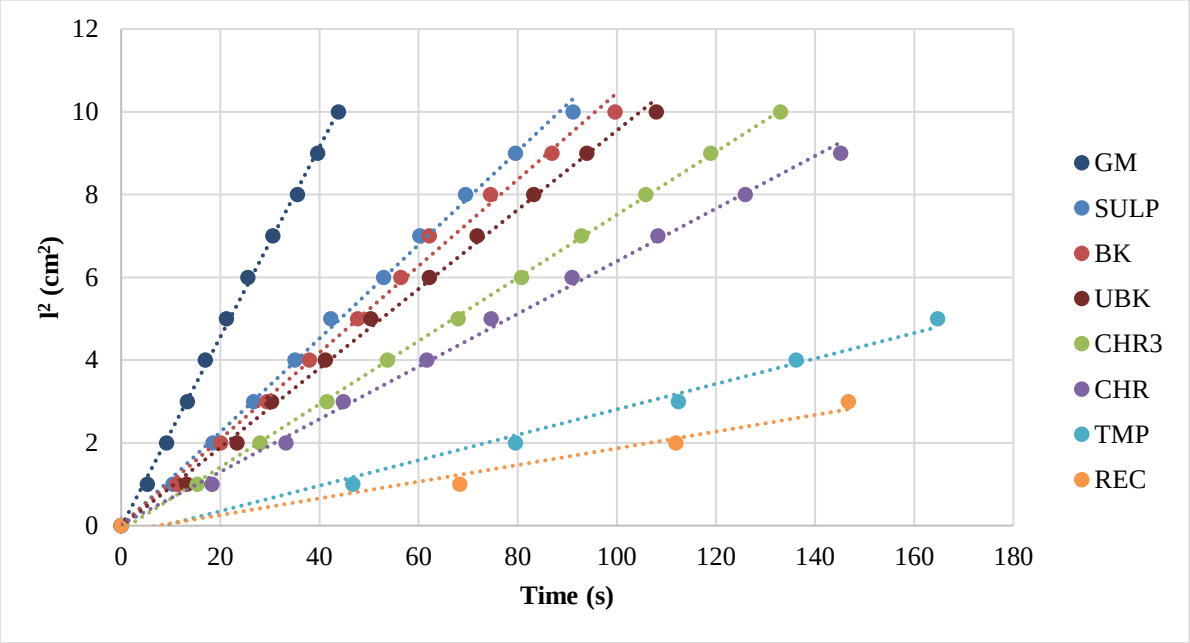

Figure 6.40: Relationship between l^2 and t for vertical wicking test base substrates and blood simulant as wicking liquid.

Table 6.4 showing the R^2 value from the linear regression of data for the vertical wicking test for blood simulant as wicking liquid.

Substrate	R^2 value
GM	0.9988
SULP	0.9978
UBK	0.9973
BK	0.9951
CHR	0.9971
CHR3	0.9997
TMP	0.9877
REC	0.9756

6.5.2 Nanofibrillated substrates

6.5.2.1 Substrates substituted with 20% NFC pulp

Figures 6.41 – 6.44 shows the horizontal and vertical test results for substrates substituted with 20% NFC pulp using dye and blood simulant as wicking liquids. From the figures, it can be seen that the substrates followed the Lucas-Washburn equation, with a linear relationship between l^2 and t. The R^2 values for the regression ranged between 0.8746 and 0.9989 (from Table 6.5), confirming that the substrates could be modelled using the Lucas-Washburn equation.

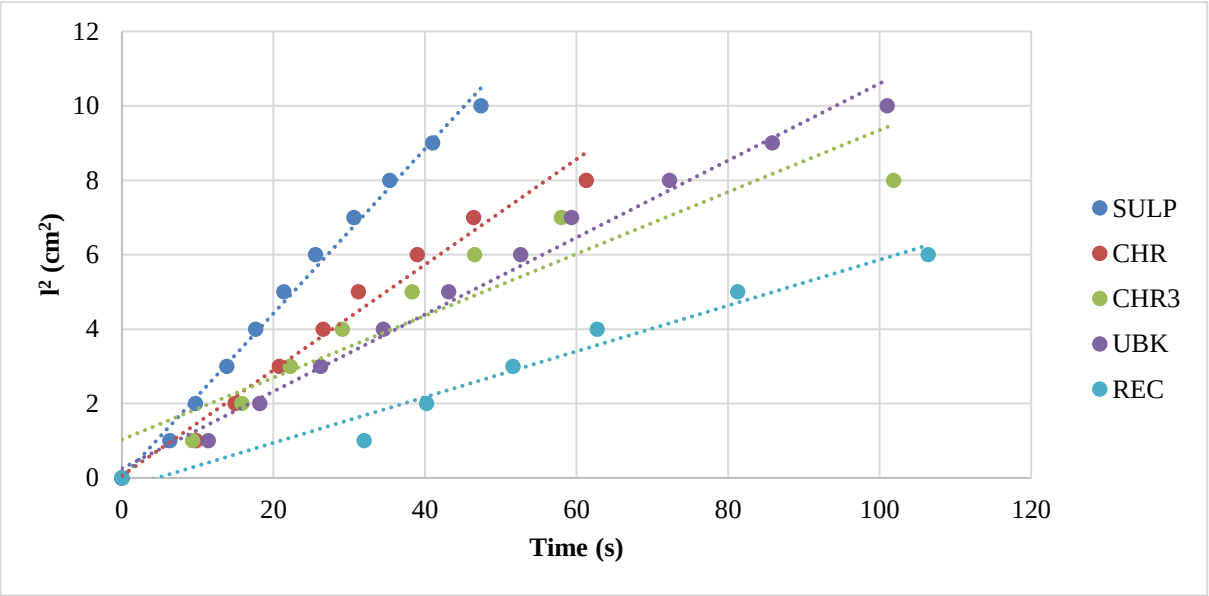

Figure 6.41: Relationship between l^2 and t for horizontal wicking test on 20% NFC pulp substrates using dye as wicking liquid.

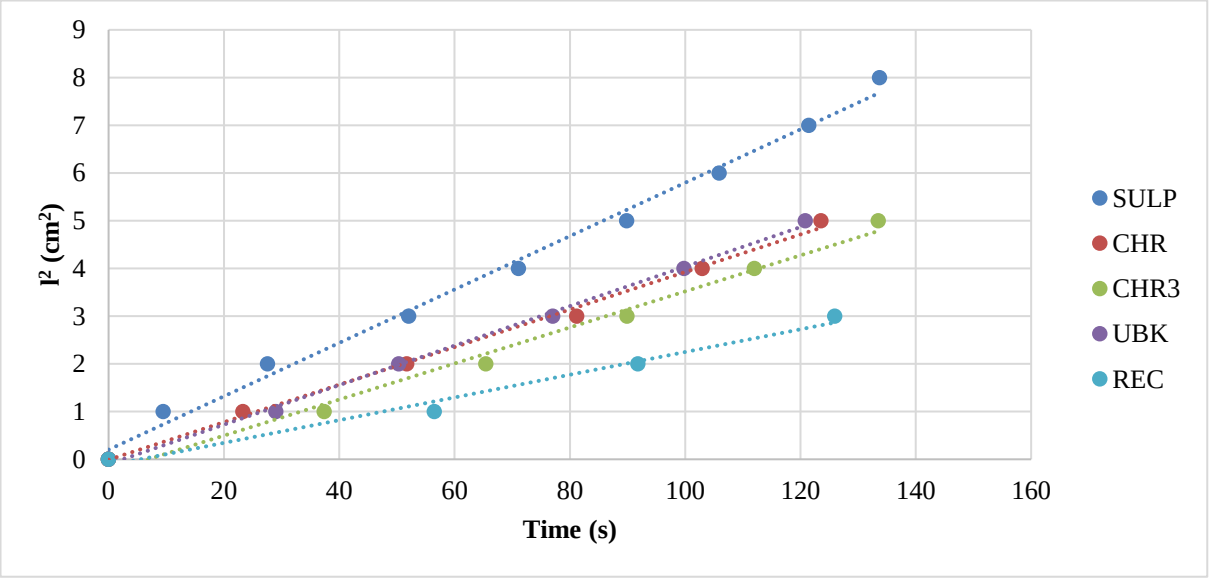

Figure 6.42: Relationship between l^2 and t for horizontal wicking test on 20% NFC pulp substrates using blood simulant as wicking liquid.

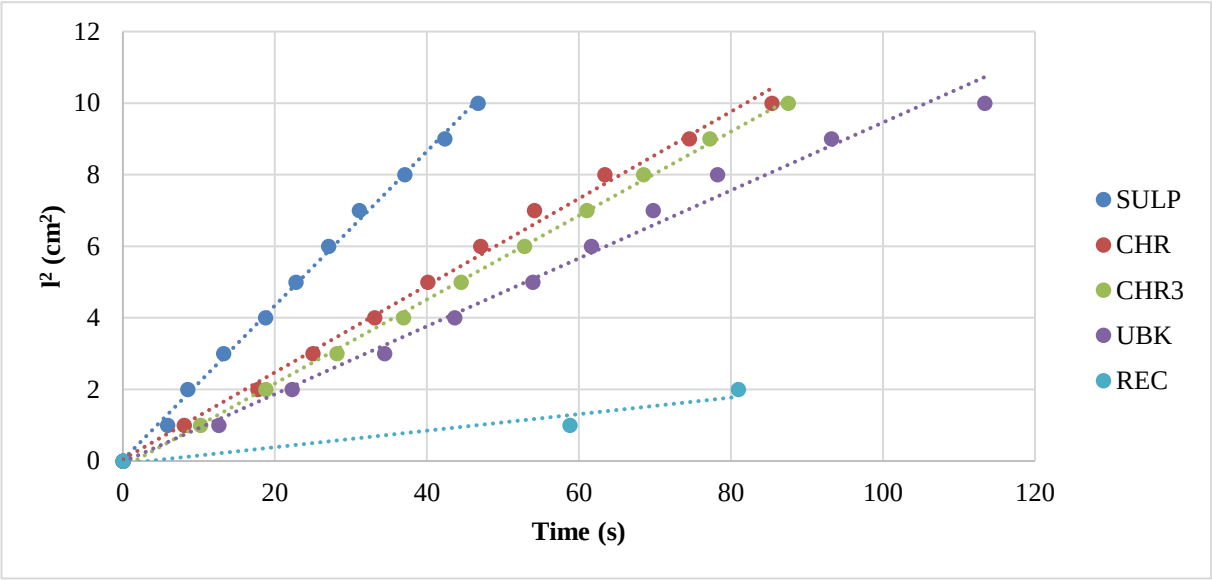

Figure 6.43: Relationship between l^2 and t for vertical wicking test on 20% NFC pulp substrates using dye as wicking liquid.

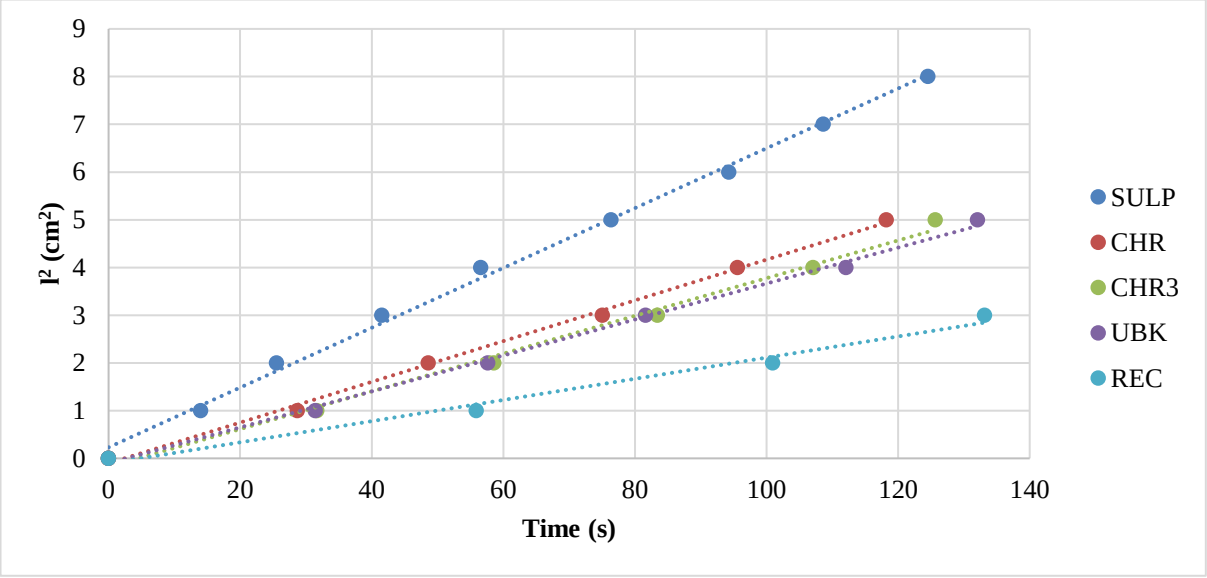

Figure 6.44: Relationship between l^2 and t for vertical wicking test on 20% NFC pulp substrates using blood simulant as wicking liquid.

Table 6.5 showing the R^2 value from the linear regression of data for the wicking tests for 20% NFC pulp substrates using dye and blood simulant as wicking liquid.

Substrate	R^2 value			
	Horizontal wicking		Vertical wicking	
	Dye	Blood simulant	Dye	Blood simulant
SULP	0.9936	0.9934	0.9977	0.9968
UBK	0.987	0.9978	0.9886	0.997
CHR	0.9767	0.9962	0.9954	0.9977
CHR3	0.8746	0.9884	0.9989	0.9933
REC	0.967	0.9833	0.9359	0.986

6.5.2.2 Substrates substituted with 50% NFC pulp

Figures 6.45 – 6.48 shows the horizontal and vertical test results for substrates substituted with 50% NFC pulp using dye and blood simulant as wicking liquids. The R^2 values for the linear regression ranged between 0.8838 and 0.9997, as seen from Table 6.6. These values indicated a linear relationship between l^2 and t, thus following the Lucas-Washburn model for fluid flow through porous media.

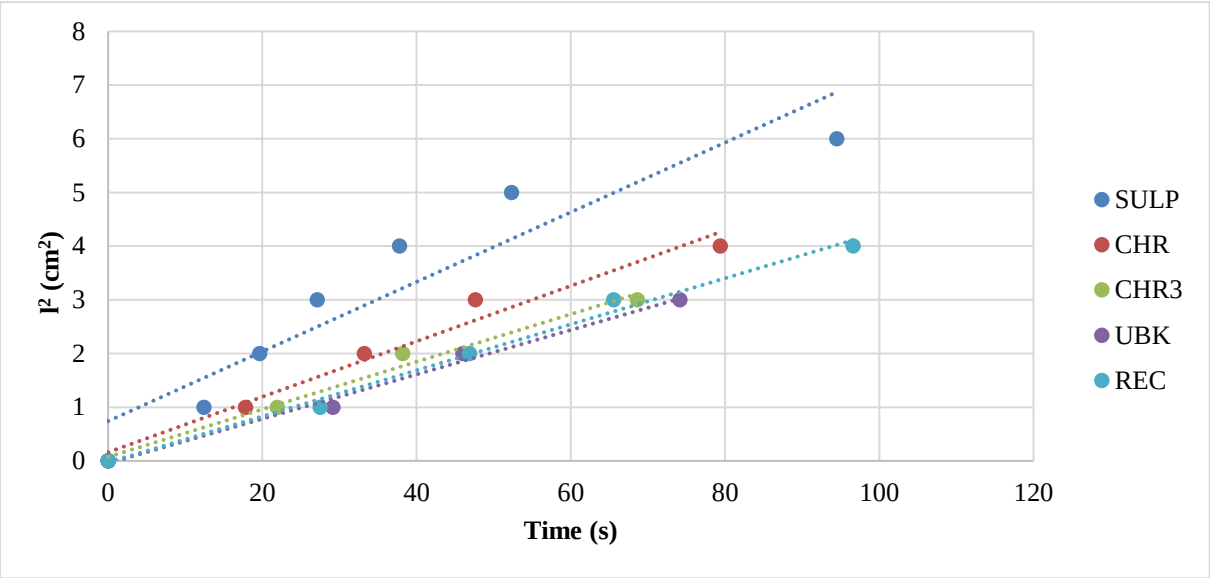

Figure 6.45: Relationship between l^2 and t for horizontal wicking test on 50% NFC pulp substrates using dye as wicking liquid.

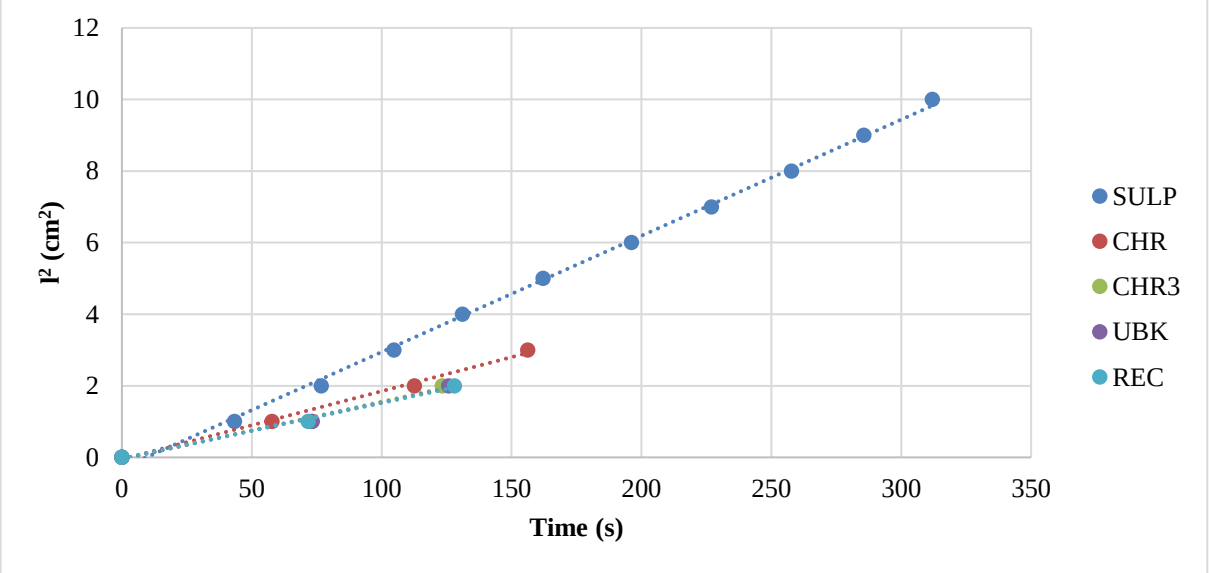

Figure 6.46: Relationship between l^2 and t for horizontal wicking test on 50% NFC pulp substrates using blood simulant as wicking liquid.

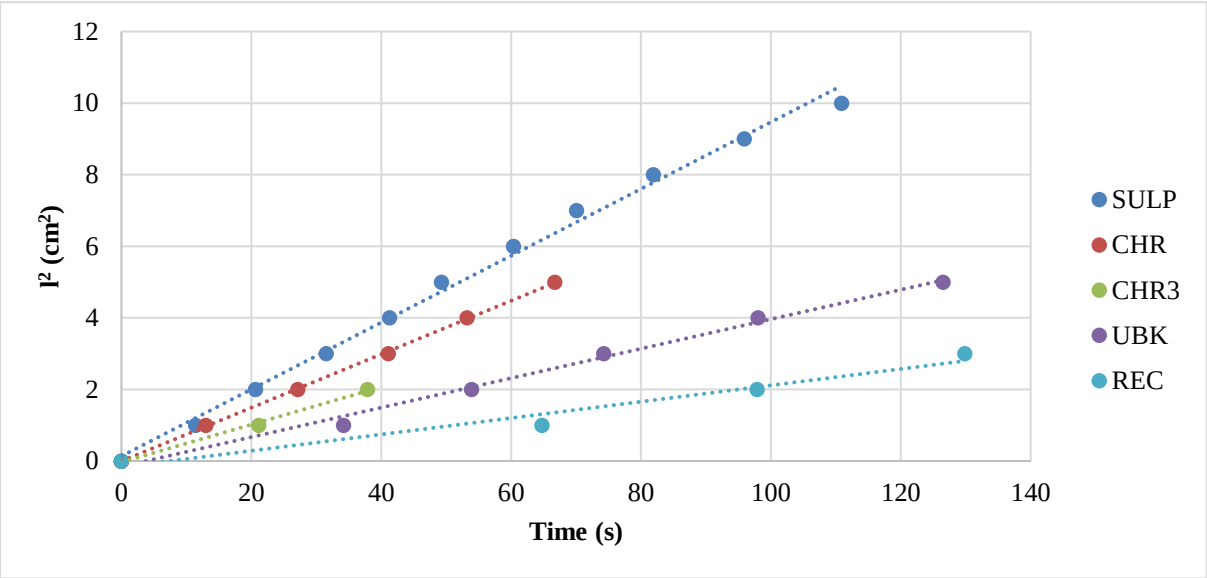

Figure 6.47: Relationship between l^2 and t for vertical wicking test on 50% NFC pulp substrates using dye as wicking liquid.

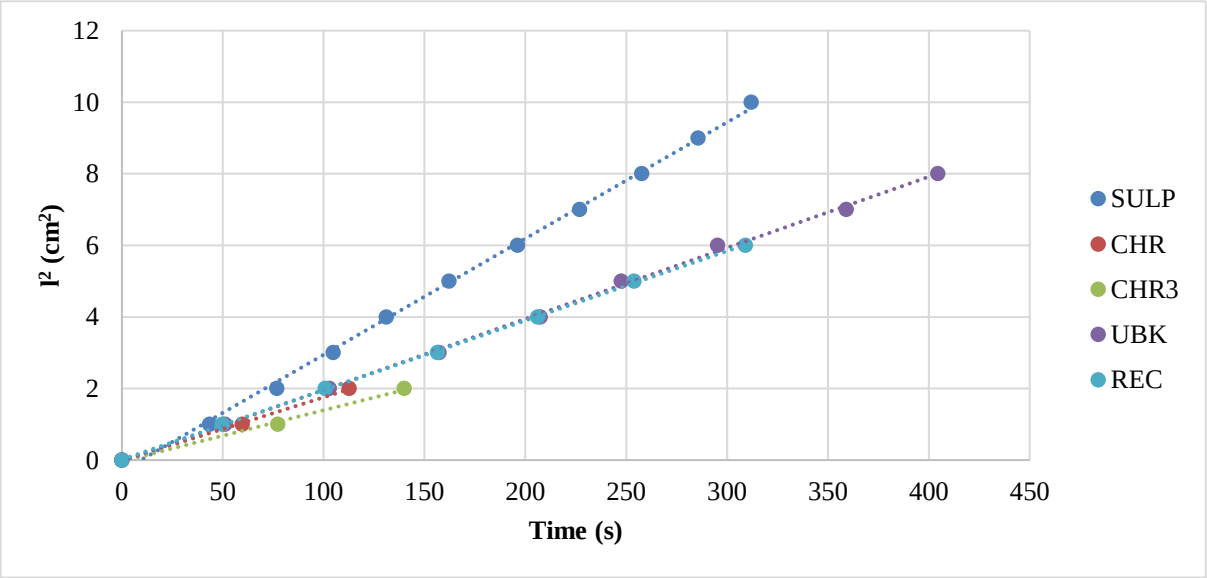

Figure 6.48: Relationship between l^2 and t for vertical wicking test on 50% NFC pulp substrates using blood simulant as wicking liquid.

Table 6.6 showing the R^2 value from the linear regression of data for wicking tests for 50% NFC pulp substrates using dye and blood simulant as wicking liquid.

Substrate	R^2 value			
	Horizontal wicking		Vertical wicking	
	Dye	Blood simulant	Dye	Blood simulant
SULP	0.8838	0.9982	0.9947	0.9982
UBK	0.985	0.9953	0.9932	0.9989
CHR	0.9741	0.9961	0.9996	0.9997
CHR3	0.985	0.9953	0.9955	0.9963
REC	0.9916	0.9953	0.966	0.9989

6.5.2.3 Substrates substituted with 100% NFC pulp

Figures 6.49 – 6.52 shows the horizontal and vertical test results for substrates substituted with 100% NFC pulp using dye and blood simulant as wicking liquids. Certain substrates were not taken into consideration as only one data point was obtained, therefore linear regression would not be possible. From the figures, it was observed that the substrates followed a linear relationship between l^2 and t, as could be seen from the R^2 values in Table 6.7. The values ranged from 0.9876 and 0.9996. Therefore, the substrates can be modelled by the Lucas-Washburn equation.

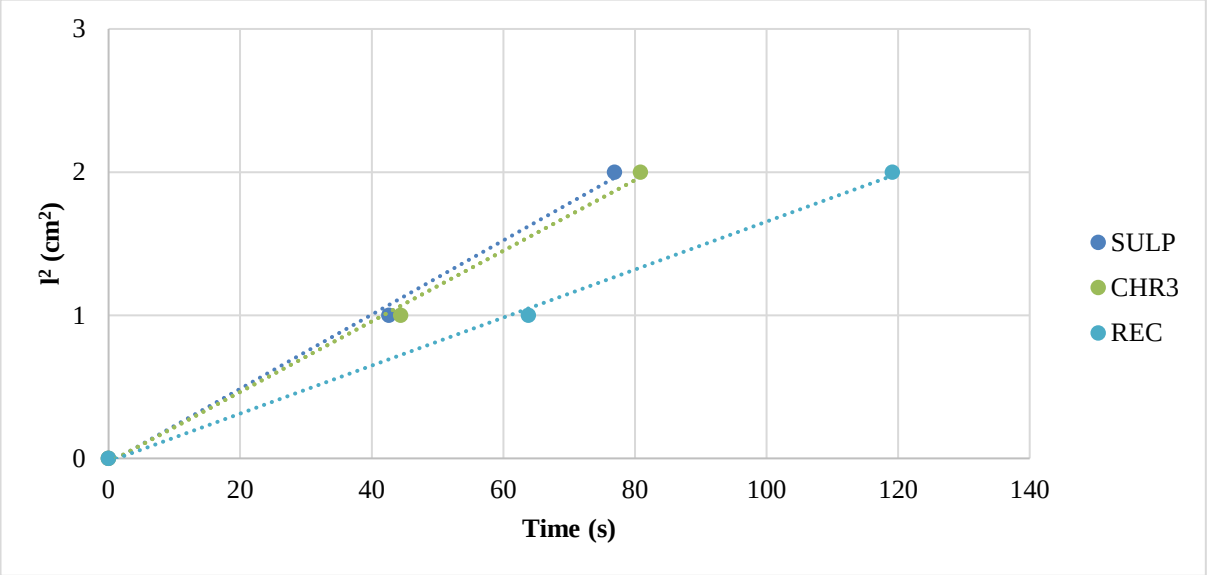

Figure 6.49: Relationship between l^2 and t for horizontal wicking test on 100% NFC pulp substrates using dye as wicking liquid.

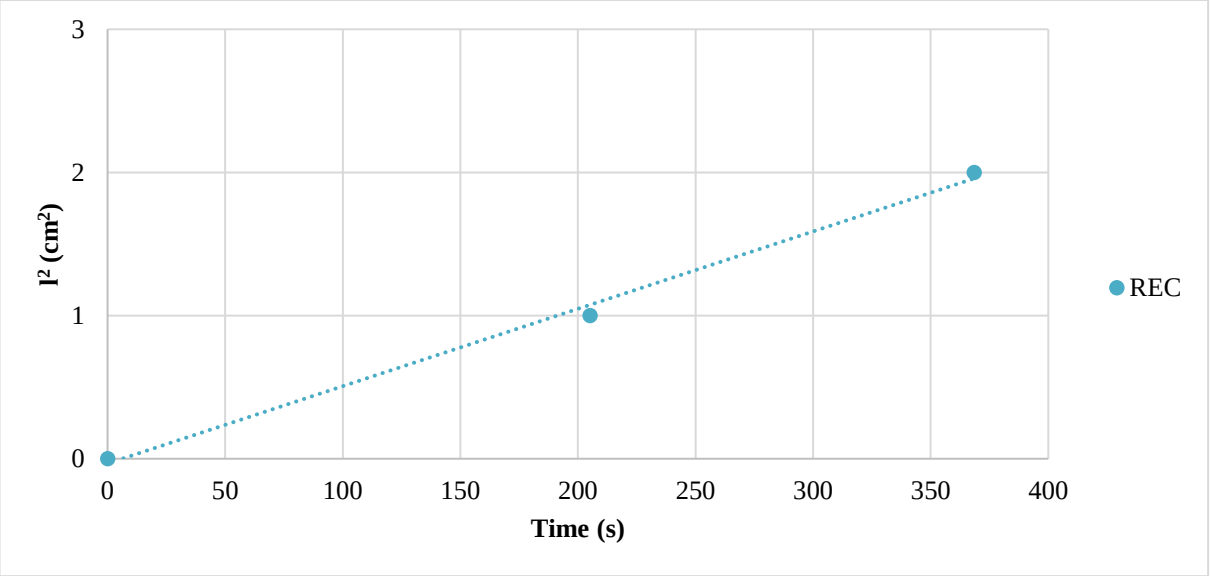

Figure 6.50: Relationship between l^2 and t for horizontal wicking test on 100% NFC pulp substrates using blood simulant as wicking liquid.

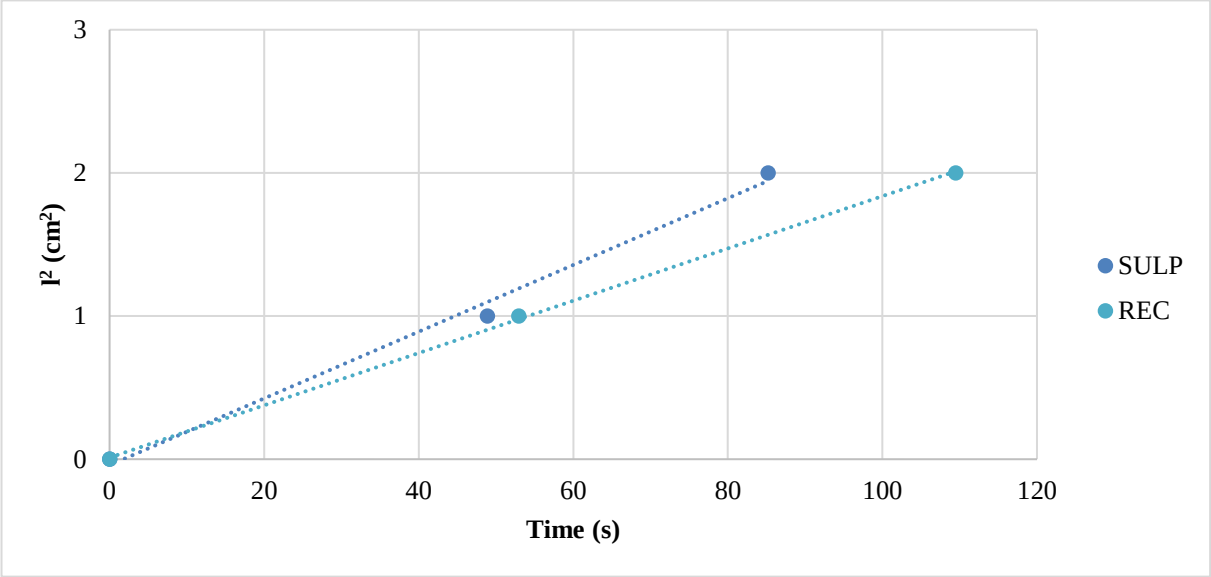

Figure 6.51: Relationship between l^2 and t for vertical wicking test on 100% NFC pulp substrates using dye as wicking liquid.

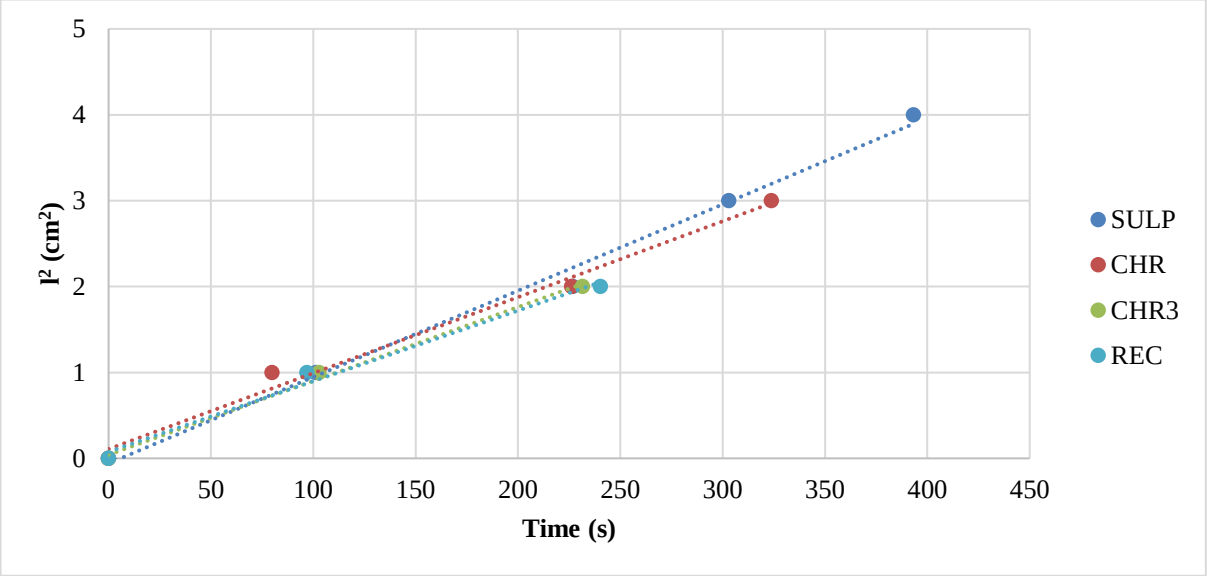

Figure 6.52: Relationship between l^2 and t for vertical wicking test on 100% NFC pulp substrates using blood simulant as wicking liquid.

Table 6.7 showing the R^2 value from the linear regression of data for wicking tests for 100% NFC pulp substrates using dye and blood simulant as wicking liquid.

Substrate	R^2 value			
	Horizontal wicking		Vertical wicking	
	Dye	Blood simulant	Dye	Blood simulant
SULP	0.9961	-	0.9929	0.9935
UBK	-	-	-	-
CHR	0.9983	-	-	0.9883
CHR3	0.9968	-	-	0.9876
REC	-	0.9957	0.9996	0.9876

6.6 Conclusions

- The wicking liquid used affects the substrates wicking rate. The higher the viscosity of the liquid, the longer the wicking through the substrate.
- Each substrate produced different wicking rates for the dye and blood simulant. In general, it was found that GM was the fastest wicker and REC the slowest wicker for base substrates. For the substrates substituted with 50% NFC pulp, it was found that SULP was the fastest wicker and REC the slowest wicker.
- The substitution of NFC pulp slowed down the wicking rate of the substrates. This was attributed to the smaller pore size, resulting in resistance to absorption of liquids, hence longer wicking times.
- When comparing the vertical and horizontal tests, it was found that each substrate produced different results. CHR, BK, GM and TMP showed that the horizontal wicking rate was faster for dye, but faster in the vertical direction for the blood simulant. UBK and CHR3 and showed that for both wicking liquids, the vertical wicking rate was faster than the horizontal wicking rate. The SULP substrate showed similar results for horizontal and vertical wicking for the case of the dye and faster

vertical wicking using the blood simulant. REC showed that horizontal wicking rates were faster using both wicking liquids.

- In general, it was found that both the base and NFC substituted substrates followed the Lucas-Washburn model.

CHAPTER 7: RESULTS AND DISCUSSIONS – SOLID WAX PRINTING

7.1 Introduction

Solid wax printing was conducted to determine whether the paper substrates would be well suited for use in microfluidic devices. This method was chosen as it is one of the most common fabrication methods used for paper-based µPADs. Should these substrates show that solid wax printing was not successful, it can be concluded that the substrate will not be beneficial during the fabrication of µPADs.

The results presented in this chapter focus on whether the substrates have the ability to be wax fabricated and the percentage penetration of wax through the substrate. Images of penetration of wax through the sheet substrates are shown in Appendix C. This chapter is split into 2 subsections, showing results from the base substrates and the results from the NFC samples. The results are tabulated to show the major findings from the experiments conducted.

7.2 Base Substrates

From the 5 experiments conducted for the SULP substrates, it was ascertained that the substrates had the ability to withstand the solid wax printing, as shown in Table 7.1. It took 30 minutes for a wax barrier of width 0.4 mm to melt through the substrates, however it was found that the wax penetrated through only 90% of the substrate. This result was undesirable as this could lead to leaking of liquid out of the barrier, hampering the objective of the µPAD.

Similarly, UBK was found to be wax printable, as seen from Table 7.1. A wax barrier of 0.4 mm was printed onto the substrates, which took a period of 30 minutes to penetrate through the substrates. Here, it was found that there were varying depths that the wax penetrated through the samples. Results showed that the wax penetration ranged from 50-70%. Discrepancy in the results could be a result of varying thicknesses of the sheets, thus affecting the depth of wax through the sheet. In addition, as the pulp is unbleached, the lignin in the sheets could also be affecting the melting of wax into the sheet. It can be observed that UBK is not recommended for use in µPADs when using solid wax printing as a fabrication method as there is a possibility of leakage through the hydrophobic wax barrier.

Table 7.1 showed that BK had a higher penetration of wax through the sheets. Within the 30 minutes of melting, it was seen that the wax reached a depth of between 80% and 90% through the sheet. As explained previously, this could be a result of different thicknesses in sheet samples. The 0.4 mm line of wax took 30 minutes to melt through the sheet at a temperature of 120°C. Although the substrate had a high wax penetration, there would still be a possibility of leakage of the liquid flowing through the barrier.

Looking at CHR (Table 7.1), it can be observed that this substrate has the necessary properties for solid wax printing for µPAD application. The wax melted through the sheets at various time intervals, ranging from 9 – 15 minutes. This would be a result of the thicknesses of the sheets, where a shorter time would represent a thinner sheet. It was seen that there was a 100% penetration of wax through the substrate. This result indicated that liquid would not leak through the wax barrier printed on the CHR sheet.

From Table 7.1, it can be observed that the CHR3 substrate showed unfavourable results for solid wax printing fabrication. After 30 minutes of melting, the wax partially penetrated through the sheet. This result implied that the sheets would allow for leakage of liquid from the wax barrier. Therefore, it can be mentioned that CHR3 substrates are not suitable for µPAD applications when using solid wax printing as a fabrication method.

Results from the TMP experiment can be seen in Table 7.1. It can be seen that substrate is wax printable. The 0.4 mm wax barrier was melted for 30 minutes, which resulted in a wax penetration of 60-70%. This difference can be attributed to a possibility of varying sheet thicknesses as well as the presence of lignin, which would resist the melting of wax through the sheet. As with the majority of the previous substrates, it can be concluded that the substrate is not appropriate for µPAD production with solid wax printing.

Lastly, solid wax printing on the REC substrate was evaluated (Table 7.7). Here, it was found that the wax was able to melt through the sheet at a depth of 65-85% of the sheet thickness. Although the pulp was bleached before handsheet making, lignin was still present, accounting for the fluctuating penetration levels in the sheets. In addition, the thickness of the sheets would affect the depth of wax, resulting in varying depths of wax. The 0.4 mm wax barrier took 30 minutes to melt through the sheets at a temperature of 120°C. These results showed that REC was not an option for use in wax printed µPADs.

Table 7.1 showing the results from solid wax printing conducted for substrates.

Sample	Substrate	Wax Printable (Y/N)	Line Width (mm)	Wax Penetration (%)	Melting Temperature (°C)	Melting Time (min)
1						
2						
3	SULP	Y	0.4	90	120	30
4						
5						
1				65		
2				60		
3	UBK	Y	0.4	50	120	30
4				50		
5				70		
1				90		
2				90		
3	BK	Y	0.4	80	120	30
4				90		
5				90		
1						15
2						10
3	CHR	Y	0.4	100	120	9
4						9
5						9
1						
2						
3	CHR3	Y	0.4	Partial	120	30
4						
5						
1				65		
2				70		
3	TMP	Y	0.4	60	120	30
4				65		
5				65		
1				85		
2				85		
3	REC	Y	0.4	80	120	30
4				65		
5				80		

7.3 Nanofibrillated substrates

Solid wax printing was conducted on the NFC pulp sheets. It can be expected that with the substitution of NFC for pulp fibres, the lower the wax penetration. This is due to the smaller pore size, while would make it harder for the wax to melt through the sheet. The results for the 20% NFC pulp sheets can be seen in Table 7.2. It was observed that the SULP and CHR substrate both had a 100% wax penetration through the sheet. The wax depth through the UBK substrate was 95%. Comparing these results to the base substrates, it can be seen that the wax penetration increased with the substitution of NFC for pulp fibres. Sheet properties, such as grammage and fibre orientation could be responsible for the unexpected result. Whatman No.1 chromatography filter paper (CHR) had a 90% wax penetration, whereas REC had the lowest wax penetration at 60%. The depth of wax melted through these sheets, when compared to the base substrates, decreased with the substitution of NFC for pulp fibres.

Table 7.2 showing the results from solid wax printing conducted for 20% nanofibrillated pulp substrates.

% Nanofibrillated pulp	Substrate	Wax Printable (Y/N)	Line Width (mm)	Wax Penetration (%)	Melting Temperature (°C)	Melting Time (min)
20	SULP	Y	0.4	100	120	30
	UBK			95		
	CHR			90		
	CHR3			100		
	REC			60		

Table 7.3 shows the solid wax printing results for the 50% NFC samples. It can be seen that SULP, UBK and CHR3 have wax penetrations of 75%, 50% and 70% respectively. Comparing this to the 20% NFC samples, it can be observed that the depth of wax through the sheets have decreased, which is expected due to the increase in smaller pores. CHR wax penetration was recorded at 90%, which was the same as the 20% NFC sample. The recycled sheet, however, showed an increase in wax penetration from 60% to 95% from the 20% NFC sample to the 50% NFC sample. As previously discussed, this could be an inconsistency in sheet properties, more specifically distribution of NFC fibres within the sheet.

Table 7.3 showing the results from solid wax printing conducted for 50% nanofibrillated pulp substrates.

% Nanofibrillated pulp	Substrate	Wax Printable (Y/N)	Line Width (mm)	Wax Penetration (%)	Melting Temperature (°C)	Melting Time (min)
50	SULP	Y	0.4	75	120	30
	UBK			50		
	CHR			90		
	CHR3			70		
	REC			95		

The 100% solid wax printing showed similar results for CHR3 and REC as in the 50% NFC sample (see Table 7.4). The CHR3 substrate had a 70% wax penetration through the sheet, with a melting time of 30 minutes, which was the same as the 50% NFC sample. The REC substrate had a 98% penetration rate, similar to the 50% NFC sample, however the melting times differed. The melting time for the 100% NFC sample was 20 minutes, while the 50% NFC sample was 30 minutes. This demonstrated that the melted wax flowed easier through the 100% NFC sample. The UBK substrate showed that the wax penetrated through the sheet, however was insufficient to quantify.

Table 7.4 showing the results from solid wax printing conducted for 100% nanofibrillated pulp substrates.

% Nanofibrillated pulp	Substrate	Wax Printable (Y/N)	Line Width (mm)	Wax Penetration (%)	Melting Temperature (°C)	Melting Time (min)
100	UBK	Y	0.4	Penetrates	120	30
	CHR3			70		
	REC			98		20

7.4 Conclusions

- The CHR base substrate and the SULP 20% NFC substrate were the only samples to show desired results, where 100% wax penetration was achieved. Therefore, these substrates are recommended for use in µPAD manufacture, using solid wax printing as the method of fabrication.
- The other substrates were wax printable, however, the wax was not able to penetrate through the depth of the sheet. It was determined that these substrates would not be well suited for the production of µPADs, as there is a high possibility of leakage of liquid from the barrier.
- However, the chemistry of the fibres could be chemically modified to induce hydrophobicity and thus enable facile wax penetration. This can be achieved for example by sizing of fibres, for example, with alkyl ketene dimer that is commonly used to size printing and writing papers or by addition of functional groups to NFC particles (Sithole & Ambayec, 2000; Sithole et al., 1995).

CHAPTER 8: CONCLUSIONS AND RECOMMENDATIONS

8.1 Summary of findings

- Field emission gun-scanning electron microscopy studies on the base substrates showed that the sulphite (SULP) substrate had the biggest pore size in comparison to the other substrates, followed by bleached kraft (BK), unbleached kraft (UBK), Whatman No.1 chromatography filter paper (CHR), Whatman 3MM chromatography filter paper (CHR3), thermo-mechanical (TMP) and recycled (REC). It was expected that the larger pore size results in a quicker wicking rate.
- Pore size decreased with increase in the amount of NFC in the paper substrates resulting in slower wicking rates of the substrates.
- The contact angle test results for the substrates showed that all the substrates were hydrophilic in nature, therefore there was no resistance to wetting. The sheets substituted with 100% NFC unbleached kraft pulp and 100% NFC recycled pulp substrates exhibited higher CA than the other substrates, albeit still hydrophilic.
- The absorption time of liquids for the sheets substituted with 100% NFC unbleached kraft pulp and 100% NFC recycled pulp substrates would be greater than the other substrates. It was also observed that an increase of NFC pulp in the sheets resulted in a higher CA, which increased the resistance to absorption of liquids into the substrates.
- The wicking liquid used affects the substrates wicking rate. The higher the viscosity of the liquid, the longer the wicking through the substrate.
- In determining the wicking ability of each substrate, it was found that these substrates produced different wicking rates for the dye and blood simulant. In general, it was found that GM was the fastest wicker and REC the slowest wicker.
- The substitution of NFC for pulp in the substrates slowed down the wicking rate of the substrates. This was attributed to the smaller pore size is the sheets, resulting in resistance to absorption of liquids, hence longer wicking times.
- Comparison of the vertical and horizontal wicking tests resulted in different outcomes for each substrate. In general, the vertical test results were expected to be slower than those of the horizontal tests, due to the added element of gravity. However, the tests showed that the wicking rates were dependent on the wicking liquid as well as the retardation forces acting on the liquid.
- The substrates followed the Lucas-Washburn model for fluid transport.

- The CHR base substrate and the SULP with 20% NFC substrate were the only samples to show desired results for the solid wax printing experiment. These substrates showed a 100% wax penetration, therefore, these substrates are recommended for use in µPAD manufacture when using this method of fabrication.

8.2 Conclusions

The overall objective of this study was to ascertain which of the paper substrates studied would be suitable for use in microfluidic applications. This was answered through the wicking experiments, where the transport of liquid was investigated. The wicking rates differed for each substrate. GM paper substrate exhibited the fastest wicking, and REC substrate the slowest. These results can be used to determining which of the substrates to use for µPAD applications. If the µPAD requires a long period for detection, a slower wicking substrate, such as CHR or CHR3, should be considered. However, if the wicking substance needs to reach the detection zone quickly, a quicker wicking substrate, such as SULP or BK could be considered.

Substrates that do not meet requirements for µPAD applications can be modified by chemical modifications to allow for such applications.

The substitution of NFC for pulp in the paper substrates led to slower wicking rates for both liquids studied. From the microscopy evaluations, it was observed that the pore sizes decreased with the increase of NFC in the paper substrates. This resulted in slower absorption of liquid. From the results, it can be concluded that these substrates would be suitable for microfluidic applications where long detection periods for analytes are required.

The contact angle test measurements showed that the substrates were all hydrophilic, therefore allowing liquids to be absorbed into the sheets. This result showed that the substrates could be considered for µPAD application, as there was no resistance to wetting.

The solid wax printing experiment was considered last, where it was determined whether the substrates could be fabricated using wax. Here, it was observed that only the CHR base substrate and the 20% NFC substituted SULP sheet allowed for 100% wax penetration.

Therefore, it was concluded that for solid wax printing as a method of fabrication, only two of the substrates could be used in microfluidic applications.

8.3 Contributions of this study

As this is one of the first studies to determine which paper substrates are best suited for µPAD applications, the results presented in this thesis add valuable knowledge to the paper microfluidics field.

8.4 Recommendations for future studies

- Testing of other fabrication methods to determine which of the methods can be used when producing µPADs
- Use of various wicking liquids to test the substrates, and consideration of using bodily fluids to simulate application in a µPAD
- Addition of the detection zone into the substrates to determine its diagnostic abilities
- Chemical modification of surfaces of paper substrates to tailor their microfluidic properties for specific applications.

REFERENCES

Abe, K. & Citterio, D., 2008. Inkjet-Printed Microfluidic Multianalyte Chemical Sensing Paper. *Analytical Chemistry,* 80(18), pp. 6928-6934.

ACEFESA, 2015. *Filter Papers and Membranes.* [Online] Available at: http://www.acefesa.es/filtra/membrana.pdf [Accessed 14 September 2015].

Advantec MFS, Inc., 2006. *Specialty Products.* [Online] Available at: www.advantecmfs.com/catalog/filt/specialty.pdf [Accessed 14 September 2015].

American Academy of Periodontology, 2015. *Types of Gum Disease.* [Online] Available at: https://www.perio.org/consumer/types-gum-disease.html [Accessed 27 September 2015].

American Kidney Fund, 2015. *Protein in Urine.* [Online] Available at: http://www.kidneyfund.org/kidney-problems/protein-in-urine/?referrer=https://www.google.co.za/ [Accessed 27 September 2015].

Amico, S., 2000. *Permeability and capillary pressure in the infiltration of fibrous porous media in resin transfer moulding.* Ph.D Thesis: University of Surrey.

Apilux, A., Ukita, Y., Chikae, M., Chailapakul, O. & Takamura, Y., 2013. Development of automated paper-based devices for sequential multistep sandwich enzyme-linked immunosorbent assays using inkjet printing. *Lab on a Chip,* 13(1), pp. 126-135.

Arena, A., Donato, N., Saitta, G., Bonavita, A., Rizzo, G. & Neri, G., 2010. Flexible ethanol sensors on glossy paper substrates operating at room temperature. *Sensors and Actuators B: Chemical,* 145(1), pp. 488-494.

Baker, C., Duong, C., Grimley, A. & Roper, M., 2009. Recent advances in microfluidic detection systems. *Bioanalysis,* 1(5), pp. 967-975.

Barnes, G. & Gentle, I., 2011. *Interfacial Science: An Introduction.* Second ed. Oxford: Oxford University Press.

Bhakta, S., Borba, R., Taba Jr, M., Garcia, C.D. & Carrilho, E., 2014. Determination of nitrite in saliva using microfluidic paper-based analytical devices. *Analytica Chimica Acta,* Volume 809, pp. 117-122.

Bruzewicz, D., Reches, M. & Whitesides, G., 2008. Low-Cost Printing of Poly(dimethylsiloxane) Barriers to Define Microchannels in Paper. *Analytical Chemistry,* 80(9), pp. 3387-3392.

Carrilho, E., Martinez, A. & Whitesides, G., 2009. Understanding Wax Printing: A Simple Micropatterning Process for Paper-Based Microfluidics. *Analytical Chemistry,* 81(16), pp. 7091-7095.

Cate, D., Adkind, J., Mettakoonpitak, J. & Henry, C., 2015. Recent Developments in Paper-Based Microfluidic Devices. *Analytical Chemistry,* Volume 87, pp. 19-41.

Cate, D., Noblitt, S., Volckens, J. & Henry, C., 2015. Multiplexed paper analytical device for quantification of metals using distance-based detection. *Lab on a Chip,* Volume 15, pp. 2808-2818.

Chitnis, G., Ding, Z., Chang, C., Savran, C.A. & Ziaie, B., 2011. Laser-treated hydrophobic paper: an inexpensive microfluidic platform. *Lab on a Chip,* Volume 11, pp. 1161-1165.

DataPhysics, 2017. *OCA 15EC.* [Online] Available at: http://www.dataphysics.de/2/start/products/contact-angle-measuring-and-contour-analysis-systems/oca-measuring-instruments/oca-15ec/ [Accessed 11 November 2107].

Davis, S., 1970. *The rheological properties of saliva.* [Online] Available at: https://link.springer.com/article/10.1007/BF01972473 [Accessed 13 September 2017].

de Almeida, P. D., Gregio, A.M.T., Machado, M.A.N., de Lima, A.A.S. & Azevedo, L.R., 2008. Saliva Composition and Functions: A Comprehensive Review. *Journal of Contemporary Dental Practice,* 9(3), pp. 1-10.

de Gans, B. H. S. & Schubert, U., 2007. polymer relief microstructures by inkjet etching. *Journal of Materials Chemistry,* Volume 17, pp. 3045-3050.

de Tarso Garcia, P., Cardoso, T.M.G., Garcia, C.D., Carrilho, E. & Coltro, W.K.T., 2014. A handheld stamping process to fabricate microfluidic paper-based analytical devices with chemically modified surface for clinical assays. *RSC Advances,* 4(71), pp. 37637-37644.

Dungchai, W., Chailapakul, O. & Henry, C., 2009. Electrochemical Detection for Paper-Based Microfluidics. *Analytical Chemistry,* 81(14), pp. 5821-5826.

Dungchai, W., Chailapakul, O. & Henry, C., 2011. A low-cost, simple, and rapid fabrication method for paper-based microfluidics using wax-screen printing. *Analyst,* 136(1), pp. 77-82.

Evans, E., Gabriel, E., Coltro, W. & Garcia, C., 2014. Rational selection of substrates to improve color intensity and uniformity on microfluidic paper-based analytical devices. *Analyst,* Volume 139, pp. 2127-2132.

Fang, X., Chen, H., Jiang, X. & Kong, J., 2011. Microfluidic Devices Constructed by a Marker Pen on a Silica Gel Plate for Multiplex Assays. *Analytical Chemistry,* Volume 83, pp. 3596-3599.

Fenton, E., Mascarenas, M., Lopez, G. & Sibbett, S., 2009. Multiplex lateral-flow test strips fabricated by two-dimensional shaping. *ACS Applied Materials & Interfaces*, 1(1), pp. 124-129.

Flanagan, R., Perrett, D. & Whelpton, R., 2005. *Electrochemical Detection in HPLC: Analysis of Drugs and Poisons.* Cambridge: The Royal Society of Chemistry.

Fries, N. & Dreyer, M., 2008. An analytical solution of capillary rise restrained by gravity. *Journal of Colloid and Interface Science,* Volume 320, pp. 259-263.

Fronczek, C., Park, T. & Yoon, J., 2013. *Paper microfluidic extraction of bacterial and viral nucleic acid from field and clinical samples towards a direct microtas apparatus.* Freiburg, 17th International Conference on Miniaturized Systems for Chemistry and Life Sciences, pp. 1114-1116.

Fu, E., Lutz, B., Kauffman, P. & Yager, P., 2010. Controlled Reagent Transport in Disposable 2D Paper Networks. *Lab on Chip,* 10(7), pp. 918-920.

Fu, E., Ramsey, S.A., Kauffman, P., Lutz, B. & Yager, P., 2011. Transport in two-dimensional paper network. *Microfluidics and Nanofluidics,* 10(1), pp. 29-35.

Ge, L., Yan, J., Song, X., Yan, M., Ge, S. & Yu, J., 2012. Three-dimensional paper-based electrochemiluminescence immunodevice for multiplexed measurement of biomarkers and point-of-care testing. *Biomaterials,* Volume 33, pp. 1024-1031.

Giokas, D., Tsogas, G. & Vlessidis, A., 2014. Programming fluid transport in paper-based microfluidic devices using razor-crafted open channels. *Analytical Chemistry,* 86(13), pp. 6202-6207.

Goede, B. & Versteeg, M., 2011. *The State of the Right to Health in Rural South Africa.* [Online] Available at: http://rhap.org.za/wp-content/uploads/2013/11/Chap-9-State-of-right-Rural-Health-pgs-99-106.pdf [Accessed 11 September 2017].

Guan, L., Cao, R., Tian, J., McLiesh, H., Garnier, G. & Shen, W., 2014. A preliminary study on the stabilization of blood typing antibodies sorbed into paper. *Cellulose,* 21(1), pp. 717-727.

Hubbe, M., Gardner, D. & Shen, W., 2015. Contact Angles and Wettability of Cellulosic Surfaces: A Review of Proposed Mechanisms and Test Strategies. *BioResources,* 10(4), pp. 8657-8749.

Hu, J., Wang, S., Wang, L., Li, F., Pingguan-Murphy, B., Lu, T.J. & Xu, F., 2014. Advances in paper-based point-of-care diagnostics. *Biosensors and Bioelectronics,* Volume 54, pp. 585-597.

International Fund for Agricultural Development, 2011. *Rural Poverty in the Developing World.* [Online] Available at: https://www.ifad.org/documents/10180/c1bbf5fa-bdc3-4ea6-9366-d163b95b1180 [Accessed 11 April 2017].

Jayawardane, B., Wei, S., Mckelvie, I. & Kolev, S., 2014. Microfluidic Paper-Based Analytical Device for the Determination of Nitrite and Nitrate. *Analytical Chemistry,* Volume 86, pp. 7274-7279.

Jeoung, S., Kim, J., Nam, J., Song, Y.S. & Lee, C., 2013. Paper-Based Analytical Device for Quantitative Urinalysis. *International Neurourology Journal,* 17(4), pp. 155-161.

Kamyabi, F., 2014. *Multiphase Flow in Porous Media.* MSc Thesis: Norwegian University of Science and Technology.

Kauffman, P., Fu, E., Lutz, B. & Yager, P., 2010. Visualization and measurement of low in two-dimensional paper networks. *Lab on a Chip,* Volume 10, pp. 2614-2617.

Kerr, I., 2014. *Nature of Wood.* Durban: s.n.

Kipphan, H., 2001. *Handbook of Print Media: Technologies and Production Methods.* Heidelberg: Springer.

Klasner, S., Price, A.K., Hoeman, K.W., Wilson, R.S., Bell, K.J. & Culbertson, C.T., 2010. Paper-based microfluidic devices for analysis of clinically relevant analytes present in urine and saliva. *Analytical and Bioanalytical Chemistry,* 397(5), pp. 1821-1829.

Koesdjojo, M., Wu, Y., Boonloed, A., Dunfield, E.M. & Remcho, V.T., 2014. Low-cost, high-speed identification of counterfeit antimalarial drugs on paper. *Talanta,* Volume 130, pp. 122-127.

Koivula, H., Pelton, R., Brennan, J.D., Grenon, J. & Manfred, T., 2013. Flexographic printability of sol-gel precursor dispersions for bioactive paper. *Nordic Pulp and Paper Research Journal,* 28(3), pp. 450-457.

Koivunen, R., 2014. *Inkjet-printed hydrophobic patterning of porous substrates for microfluidic applications.* MSc Thesis: Aalto University.

Kord, B., Malekian, B., Yousefi, H. & Najafi, A., 2016. Preparation and characterization of nanofibrillated Cellulose/Poly (Vinyl Alcohol) composite films. *Maderas, Ciencia y tecnologia,* 18(4).

Kurunc, A., Ersahin, S., Uz, B.Y., Sonmez, N.K., Uz, I., Kaman, H., Bacalan, G.E. & Emekli, Y., 2011. Identification of nitrate leaching hot spots in a large area with contrasting soil texture and management. *Agricultural Waste Management,* 98(6), pp. 1013-1019.

Lewis, G., DiTucci, M., Baker, M. & Phillips, S., 2012. High throughput method for prototyping three-dimensional, paper-based microfluidic devices. *Lab on a Chip,* 12(15), pp. 2630-2633.

Liana, D., Raguse, B., Gooding, J. & Chow, E., 2012. Recent Advances in Paper-Based Sensors. *Sensors,* Volume 12, pp. 11505-11526.

Lisowski, P. & Zarzycki, P., 2013. Microfluidic Paper-Based Analytical Devices and Micro Total Analysis Systems: Development, Applications and Future Trends. *Chromatographia,* Volume 76, pp. 1201-1214.

Liu, H., Xiang, Y., Lu, Y. & Crooks, R., 2012. Aptamer-based Origami Paper Analytical Device for Electrochemical Detection of Adenosine. *Angewandte Chemie,* 51(28), pp. 6925-6928.

Li, X., Ballerini, D. & Shen, W., 2012. A perspective on paper-based microfluidics: Current status and future trends. *Biomicrofluidics,* Volume 6, p. 011301.

Li, X., Tian, J., Nguyen, T. & Shen, W., 2008. Paper-Based Microfluidic Devices by Plasma Treatment. *Analytical Chemistry,* 80(23), pp. 9131-9134.

Li, X., Tian, J. & Shen, W., 2010. Quantitative biomarker assay with microfluidic paper-based analytical devices. *Analytical and Bioanalytical Chemistry*, 396(1), pp. 495-501.

Li, X., Tian, J. & Shen, W., 2010. Thread as a versatile material for low-cost microfluidic diagnostics. *ACS Applied Materials & Interfaces,* 2(1), pp. 1-6.

Lutz, B., Liang, T., Fu, E., Ramachandran, S., Kauffman, P. & Yager, P., 2013. Dissolvable fluidic time delays for programming multi-step assays in instrument-free paper diagnostics. *Lab on a Chip,* 13(14), pp. 2840-2847.

Lutz, B., Trinh, P., Ball, C., Fu, E. & Yager, P., 2011. Two-dimensional paper networks: programmable fluidic disconnects for multi-step processes in shaped paper. *Lab on a Chip*, 11(24), pp. 4274-4278.

Lu, Y., Shi, W., Jiang, L., Qin, J. & Lin, B., 2009. Rapid prototyping of paper-based microfluidics with was for low-cost, portable bioassay. *Electrophoresis,* 30(9), pp. 1497-1500.

Lu, Y., Shi, W. & Qin, J. L. B., 2010. Fabrication and Characterization of Paper-Based Microfluidics Prepared in Nitrocellulose Membrane By Wax Printing. *Analytical Chemistry*, 82(1), pp. 329-335.

Maattanen, A., 2014. *Printed platforms for paper-based analytical applications.* Ph. D Thesis: Abo Akademi University.

Maattanen, A., Fors, D., Wang, S., Valtakari, D., Ihalainen, P. & Peltonen, J., 2011. Paper-based planar reaction arrays for printed diagnostics. *Sensors and Actuators B: Chemical,* 160(1), pp. 1404-1412.

Maejima, K., Tomikawa, S., Suzuki, K. & Citterio, D., 2013. Inkjet printing: an integrated and green chemical approach to microfluidic paper-based analytical devices. *RSC Advances,* 3(24), pp. 9258-9263.

Martinez, A., Phillips, S., Butte, M. & Whitesides, G., 2007. Patterned Paper as a Platform for Inexpensive, Low-Volume, Portable Bioassays. *Angewandte Chemie,* Volume 46, pp. 1318-1320.

Martinez, A., Phillips, S.T., Cheng, C.M., Carrilho, E., Wiley, B.J. & Whitesides, G.M., 2010. Programmable diagnostic devices made from paper and tape. *Lab on a Chip*, 10(19), pp. 2499-2504.

Martinez, A., Phillips, S. & Whitesides, G., 2008. Three-dimensional microfluidic devices fabricated in layered paper and tape. *Proceedings of the National Academy of Sciences USA,* 105(50), pp. 19606-19611.

Martinez, A., Phillips, S. & Whitesides, G., 2010. Diagnostics for the Developing World: Microfluidic Paper-Based Analytical Devices. *Analytical Chemistry,* 82(1), pp. 3-10.

Masoodi, R. & Pillai, K., 2012. A general formula for capillary suction-pressure in porous media. *Journal of Porous Media,* 15(8), pp. 775-783.

Masoodi, R. & Pillai, K., 2013. *Wicking in Porous Materials: Traditional and Modern Modeling Approaches.* Florida: CRC Press.

Masuko Sangyo Co., Ltd, 2017. *Ultra-fine friction grinder "Supermasscolloider".* [Online] Available at: http://www.masuko.com/English/product/Masscolloder.html [Accessed 14 October 2017].

McDonald, P., 2006. *Wicking in Multi-Ply Paper Structures with Dissimilar Plies,* Georgia: Georgia Institute of Technology.

Mentele, M., Cunningham, J., Koehler, K., Volckens, J. & Henry, C.S., 2012. Microfluidic Paper-Based Analytical Device for Particulate Matter. *Analytical Chemistry,* Volume 84, pp. 4474-4480.

Miller, B., 2000. Critical Evaluation of Upward Wicking Tests. *International Nonwovens Journal,* Volume 9, pp. 35-40.

Ngo, Y., Simon, G. & Garnier, G., 2011. Paper surfaces functionalized by nanoparticles. *Advances in Colloid and Interface Science,* 163(1), pp. 23-38.

Nie, J., Liang, Y., Zhang, Y., Le, S., Li, D. & Zhang, S., 2013. One-step patterning of hollow microstructures in paper by laser cutting to create microfluidic analytical devices. *Analyst,* 138(2), pp. 671-676.

Nie, Z., Nijhuis, C.A., Gong, J., Chen, X., Kumachev, A., Martinez, A.W., Narovlyansky, M. & Whitesides, G.M., 2010. Integration of paper-based microfluidic devices with commercial electrochemical readers. *Lab on a Chip,* 10(22), pp. 3163-3169.

Nie, Z., Deiss, F., Liu, X., Akbulut, O. & Whitesides, G.M., 2010. Electrochemical sensing in paper-based microfluidic devices. *Lab on a Chip,* Volume 10, pp. 477-483.

Noh, H. & Phillips, S., 2010. Fluidic Timers for Time-Dependent, Point-of-Care Assays on Paper. *Analytical Chemistry,* 82(19), pp. 8071-8078.

Noiphung, J., Songjaroen, T., Dungchai, W., Henry, C.S., Chailapakul, O. & Laiwattanapaisal, W., 2013. Electrochemical detection of glucose from whole blood using paper-based microfluidic devices. *Analytica Chimica Acta,* Volume 39, pp. 39-45.

Nordbotten, J., Celia, M., Dahle, H. & Hassanizadeh, S., 2007. Interpretation of macroscale variables in Darcy's Law. *Water Resources Research,* 43(8), p. W08430.

Olkkonen, J., Lehtinen, K. & Erho, T., 2010. Flexographically Printed Fluidic Structures in Paper. *Analytical Chemistry,* 82(24), pp. 10246-10250.

Oregon PSR, 2015. *Airborne Particulate Matter and Public Health.* [Online] Available at: http://www.psr.org/chapters/oregon/assets/pdfs/airborne-particulate-matter.pdf [Accessed 27 September 2015].

Osborn, J., Lutz, B., Fu, E., Kauffman, P., Stevens, D.Y. & Yager, P., 2010. Microfluidics without pumps: reinventing the T-sensor and H-filter in paper networks. *Lab on a Chip,* 10(20), pp. 2659-2665.

OuYang, L., Wang, C., Du, F., Zheng, T. & Liang, H., 2014. Electrochromatographic separations of multi-component complexes on a microfluidic paper-based device with a simplified photolithography. *RSC Advances,* 4(3), pp. 1093-1101.

Pires, N., Dong, T., Hanke, U. & Hoivik, N., 2014. Recent Developments in Optical Detection Technologies in Lab-on-a-Chip Devices for Biosensing Applications. *Sensors,* 14(8), pp. 15458-15479.

Pollock, N., Rolland, J.P., Kumar, S., Beattie, P.D., Jain, S; Noubary, F., Wong, V.L., Pohlmann, R.A., Ryan, U.S. & Whitesides, G.M., 2012. A paper-based multiplexed transaminase test for low-cost, point-of-care liver function testing. *Science Translational Medicine,* 4(152), p. 152ra129.

Putnam, D., 1971. *Composition and Concentrative Properties of Human Urine.* [Online] Available at: https://ntrs.nasa.gov/archive/nasa/casi.ntrs.nasa.gov/19710023044.pdf [Accessed 13 September 2017].

Qi, A., Hoo, S.P., Freiend, J., Yeo, L., Yue, Z. & Chan, P.P., 2014. Hydroxypropyl cellulose methacrylate as a photo-patternable and biodegradable hybrid paper substrate for cell culture and other bioapplications. *Advanced Healthcare Materials*, 3(4), pp. 543-554.

Rattanarat, P., Dungchai, W., Cate, D.M., Siangproh, W., Volckens, J., Chailapakul, O. & Henry, C.S., 2013. A microfluidic paper-based analytical device for rapid quantification of particulate chromium. *Analytica Chimica Acta,* Volume 800, pp. 50-55.

Reches, M., Mirica, K.A., Dasgupta, R., Dickey, M.D., Butte, M.J. & Whitesides, G.M., 2010. Thread as a matrix for biomedical assays. *ACS Applied Materials & Interfaces,* 2(6), pp. 1722-1728.

Reed, C. & Wilson, N., 1993. The fundamentals of absorbency of fibers, textile structures and polymers: The rate of rise of a liquid in glass capillaries. *Journal of Physics D: Applied Physics,* 26(9), pp. 1378-1381.

Renault, C., Anderson, M. & Crooks, R., 2014. Electrochemistry in Hollow-Channel Paper Analytical Devices. *Journal of the American Chemical Society,* Volume 136, pp. 4616-4623.

Ren, K., Zhou, J. & Wu, H., 2013. Materials for Microfluidic Chip Fabrication. *Accounts of Chemical Research,* 46(11), pp. 2396-2406.

Research Equipment Database, 2017. *Carl Zeiss Ultra Plus Field emission Scanning Electron Microscope (FEGSEM) Electron Microscopes.* [Online] Available at: http://eqdb.nrf.ac.za/equipment/microscope/carl-zeiss-ultra-plus-field-emission-scanning-electron-microscope-fegsem [Accessed 14 October 2017].

Rioux, R., 2003. *The rate of fluid absorption in porous media.* MSc Thesis: University of Maine.

Roberts, R., Senden, T., Knackstedt, K. & Lyne, M., 2003. Spreading of Aqueous Liquids in Unsized Papers is by Film Flow. *Journal of Pulp and Paper Science,* 29(4), pp. 123-131.

Sajid, M., Kawde, A. & Daud, M., 2014. Designs, format and applications of lateral flow assay: A literature review. *Journal of Saudi Chemical Society.*

Saladin, K., 2010. *Anatomy & Physiology: The Unity of Form and Function.* Fifth ed. New York: McGraw-Hill.

Sameenoi, Y., Nongkai, P.N., Nouanthavong, S., Henry, C.S. & Nacapricha, D., 2014. One-step polymer screen-printing for microfluidic paper-based analytical device fabrication. *Analyst,* Volume 139, pp. 6580-6588.

Sameenoi, Y., Panymeesamer, P., Supalakorn, N., Koehler, K., Chailapakul, O., Henry, C.S. & Volckens, J., 2013. Microfluidic Paper-Based Analytical Device for Aerosol Oxidative Activity. *Environmental Science & Technology,* Volume 47, pp. 932-940.

Schilling, K., Jaurequi, D. & Martinez, A., 2013. Paper and toner three-dimensional fluidic devices: programming fluid flow to improve point-of-care diagnostics. *Lab on a Chip,* 13(4), pp. 628-631.

Schilling, K., Lepore, A., Kurian, J. & Martinez, A., 2012. Fully Enclosed Microfluidic Paper-Based Analytical Devices. *Analytical Chemistry,* Volume 84, pp. 1579-1585.

Schwarz, M. & Hauser, P., 2001. Recent developments in detection methods for microfabricated analytical devices. *Lab on a Chip,* 1(1), pp. 1-6.

Sechi, D., Greer, B., Johnson, J. & Hashemi, N., 2013. Three-Dimensional Paper-Based Microfluidic Device for Assays of Protein and Glucose in Urine. *Analytical Chemistry,* Volume 85, pp. 10733-10737.

Shi, J., Tang, F; Xing, H., Zheng, H., Bi, L. & Wang, W., 2012. Electrochemical Detection of Pd and Cd in Paper-Based Microfluidic Devices. *Journal of the Brazilian Chemical Society,* 23(6), pp. 1124-1130.

Simile, C. B., 2004. *Critical Evaluation of Wicking in Performance Fabrics,* Georgia: Georgia Institute of Technology.

Sino Biological Inc., 2015. *ELISA for Home Pregnancy Test.* [Online] Available at: http://www.elisa-antibody.com/ELISA-applications/home-pregnancy-test [Accessed 27 September 2015].

Sithole, B. & Ambayec, B., 2000. Identification and determination of surface sizing agents on sized papers. *PULP PAPER,* 101 (9), pp. 53-57.

Sithole, B., Nyarku, S & Allen, L., 1995. Chromatographic Methods for Determination of Alkylketene Dimer in Pulp and Paper Matrices. *Analyst,* 120, pp.1163-1169.

Songjaroen, T., Dungchai, W., Chailapakul, O., Henry, C.S. & Laiwattanapaisal, W., 2012. Blood separation on microfluidic paper-based analytical devices. *Lab on a Chip,* 12(18), pp. 3392-3398.

Songjaroen, T., Dungchai, W., Chailapakul, O. & Laiwattanapaisal, W., 2011. Novel, simple and low-cost alternative method for fabrication of paper-based microfluidics by wax dipping. *Talanta,* 85(5), pp. 2587-2593.

Song, J. & Rojas, O., 2013. Approaching super-hydrophobicity from cellulosic materials: A Review. *Nordic Pulp and Paper Research Journal,* 28(2), pp. 216-238.

Thakur, V. & Kessler, M., 2015. *Green Biorenewable Biocomposites: From Knowledge to Industrial Applications.* Oakville: Apple Academic Press, Inc.

Thom, N., Yeung, K., Pillion, M. & Phillips, S., 2012. "Fluidic batteries" as low-cost sources of power in paper-based microfluidic devices. *Lab on a Chip,* 12(10), pp. 1768-1770.

Tiffany, J., 2003. Tears in health and disease. *Eye,* Volume 17, pp. 923-926.

University of Oulu, 2013. *Zeiss ULTRA Plus FESEM.* [Online] Available at: http://www.oulu.fi/cmnt/node/15439 [Accessed 14 October 2017].

USGS, 2015. *Surface Tension and Water*. [Online] Available at: http://water.usgs.gov/edu/surface-tension.html [Accessed 22 September 2015].

Vella, S., Beattie, P., Cademartiri, R., Laromaine, A., Martinez, A.W., Phillips, S.T., Mirica, K.A. & Whitesides, G.M., 2012. Measuring markers of liver function using a micropatterned paper device designed for blood from a fingerstick. *Analytical Chemistry,* 84(6), pp. 2883-2891.

Virtual Medical Centre, 2015. *Blood Function and Composition.* [Online] Available at: http://www.myvmc.com/anatomy/blood-function-and-composition/ [Accessed 27 September 2015].

Weaver, A., Reiser, H., Barstis, T., Benvenuti, M., Ghosh, D., Hunckler, M., Joy, B., Koenig, L., Raddell, K. & Lieberman, M., 2013. Paper Analytical Devices for Fast Field Screening of Beta-Lactam Antibiotics and Antituberculosis Pharmaceuticals. *Analytical Chemistry,* 85(13), pp. 6453-6460.

Wenzel R.N., 1936. Resistance of solid surfaces to wetting by water. *Industrial & Engineering Chemistry*, 28(8), pp. 988-994.

Whitesides, G., 2006. The origins and future of microfluidics. *Nature,* Volume 442, pp. 368-373.

Wong, R. & Tse, H., 2009. *Lateral Flow Immunoassay.* New York: Springer.

World Health Organization, 2001. *Water Sanitation Health.* [Online] Available at: http://www.who.int/water_sanitation_health/diseases/lead/en/ [Accessed 27 September 2015].

Xerox, 2017. *ColorQube 8870.* [Online] Available at: http://www.office.xerox.com/printers/color-printers/colorqube-8870/spec-enus.html [Accessed 14 October 2017].

Yang, X., 2013. *Microfluidic paper-based analytical devices: Sample preparation, medical monitoring and diagnostics.* Ph.D Thesis: Tulane University.

Yang, X., Forouzan, O., Brown, T. & Shevkoplyas, S., 2012. Integrated separation of blood plasma from whole blood for microfluidic paper-based analytical devices. *Lab on a Chip,* 12(2), pp. 274-280.

Yetisen, A., Akram, M. & Lowe, C., 2013. Paper-based microfluidic point-of-care diagnostic devices. *Lab on a Chip,* Volume 12, pp. 2210-2251.

Yuan, Y. & Lee, T., 2013. *Surface Science Techniques: Contact Angle and Wetting Properties.* Heidelberg: Springer.

Yu, J., Ge, L., Huang, J., Wang, S. & Ge, S., 2011. Microfluidic paper-based chemiluminescence biosensor for simultaneous determination of glucose and uric acid. *Lab on a Chip,* 11(7), pp. 1286-1291.

Yu, L. & Shi, Z., 2015. Microfluidic paper-based analytical devices fabricated by low-cost photolithography and embossing of Parafilm. *Lab on a Chip,* Volume 15, pp. 1642-1645.

Zhang, Y., Zhou, C., Nie, J., Le, S., Qin, Q., Liu, F., Li, Y. & Li, J., 2014. Equipment-Free Quantitative Measurement for Microfluidic Paper-Based Analytical Devices Fabricated Using Principles of Movable-Type Printing. *Analytical Chemistry,* Volume 86, pp. 2005-2012.

Zhong, Z., Wang, Z. & Huang, G., 2012. Investigation of wax and paper materials for the fabrication of paper-based microfluidic devices. *Microsystem Technologies,* Volume 18, pp. 649-659.

Zhu, C. & Takatera, M., 2013. Effect of Fabric Structure and Yarn on Capillary Liquid Flow within Fabrics. *Journal of Fiber Bioengineering and Informatics,* 6(2), pp. 205-215.

Zhu, Y., Xu, X., Brault, N.D., Keefe, A.J., Han, X., Deng, Y., Xu, J., Yu, Q. & Jiang, S., 2014. Cellulose Paper Sensors Modified with Zwitterionic Poly(carboxybetaine) for Sensing and Detection in Complex Media. *Analytical Chemistry,* 86(6), pp. 2871-2875.

APPENDIX A: EQUIPMENT DESCRIPTION

A.1 Introduction

This appendix gives an overview of the major equipment used in this study, which is an extension of the information given in Chapter 3. The structure of appendix follows the testing methodology, whereby the main equipment used in each test will be described, together with figures.

A.2 Handsheet Making

The Rapid-Köthen Sheet Former was used in the production of handsheets to be used in the study. The work table unit of the forming machine consists of a pump, hot water bath, a control unit, return water filter and a water container. The main structure of the machine comprises of a forming column, dryer and water circulation system, which is used in the formation of handsheets from pulp. The controls, mounted on the panel adjacent to the dryers, display the temperature and pressure, as well as a timer for each dryer. The former was set at a standard 93ºC with a time of 4 minutes.

Figure A.1: Rapid-Köthen Sheet Former.

A.3 Nanofibrillation

Nanofibrillation was conducted using a super mass colloider, model MKCA6-3, manufactured by Masuko Sangyo Co, Ltd., Japan. This equipment uses friction grinding to produce ultra-fine particles, with a paste-like consistency. The colloider consists of two ceramic, adjustable, non-porous grinders. The ceramic grinders allow for creation of more round and smoother particles with a uniform size. The space between the grinders can be adjusted to determine the size and quality of the particles. A handle is attached, which moves vertically, to adjust the clearance between grinders in 1/100 mm increments.

Figure A.2: Super mass colloider (Masuko Sangyo Co., Ltd, 2017).

A.4 Field emission gun-scanning electron microscopy (FEG-SEM)

Field emission gun-scanning electron microscopy was conducted using a Carl Zeiss Ultra Plus FEG-SEM. The equipment was used to obtain micrographs for purposes of analysing the pore sizes of the sheets. The equipment allows for high electron imaging with low acceleration voltages to capture detailed images for analysis. In addition, the FEG-SEM has the functionality of an Energy-Dispersive X-ray Spectroscopy) analyser and an Electro-Backscatter Diffraction camera to provide analysis on crystal structures. The technical features of the equipment are listed:

- ✓ Acceleration voltage: 0.02 – 30 kV
- ✓ Resolution: 1.0 nm/ 15 kV, 1.7 nm/ 1 kV, 4.0 nm/ 0.1 kV

(University of Oulu, 2013)

Figure A.3: Carl Zeiss Ultra Plus FEG-SEM (Research Equipment Database, 2017).

A.5 Contact angle measurements

A DataPhysics Optical Contact Angle 15EC was used to determine the contact angles. The equipment has the option to measure contact angle as well as provide a drop shape analysis. The set-up consists of a sample table, which contains a magnetic horizontal slide system and a vertical alteration. The camera has a video measuring system with a high-performance zoom lens, which can magnify up to 6 times. The observation angle is adjustable, with an integrated fine focus. Other features include LED-lighting used to control the temperature.

The available software which can be used for the instrument are:

- ✓ SCA 20 – for contact angle determination
- ✓ SCA 21 – for surface free energy determination
- ✓ SCA 22 – for surface/interfacial tension determination
- ✓ SCA 23 – for liquid bridge analysis
- ✓ SCA 26 – for oscillation/relaxation

Figure A.4: DataPhysics Optical Contact Angle 15EC (DataPhysics, 2017).

A.6 Solid wax printing

The Xerox ColorQube 8870 printer was used to conduct the solid wax printing experiment. The printer features five trays, each with a capacity of 525 sheets each, with the exception of the first multipurpose tray, which has a limit of 100 sheets. The trays can handle paper weights of between 60 – 220 g/m^2, and has the ability to print on a wide variety of paper types. Solid ink cartridges are used for printing, which are melted and deposited onto the paper sheets.

The operational specifications of the printer are as follows:

- ✓ Temperature (operating): 10 - 32ºC
- ✓ Temperature (non-operating): -30 - 60 ºC
- ✓ Relative humidity (operating): 10 - 80%

- ✓ Relative humidity (non-operating): 10 - 95%
- ✓ Power consumption (operating): 252 W

Figure A.5: Wax printer Xerox ColorQube 8870 (Xerox, 2017).

A.7 Conclusion

This appendix gives an overview of the main pieces of equipment used in this study. The equipment specifications and operations are described to provide a background to methodology found in Chapter 3.

APPENDIX B: FIELD EMISSION GUN-SCANNING ELECTRON MICROSCOPY

B.1 Introduction

This appendix contains the additional micrographs obtained from the FEG-SEM experiments, to support the results from Chapter 4. The images have various magnifications, ranging from 100 × to 20 000 ×. The appendix is split into the base substrate micrographs and NFC substrate micrographs, where it is subsectioned into the various substrates.

B.2 Base substrates

The morphological studies conduction on the substrates, discussed in Chapter 4, showed the comparison of the various pore sizes within the sheets, which was then related to the wicking ability of the sheet. Numerous micrographs were obtained at different magnifications, to find the most suitable image for comparison. It was seen in Chapter 4 that the 200 × magnification for the surface images and 500 × magnification for the cross-sectional image were chosen as the basis for discussion. In this section, the other images from the experiment can be observed. In general, the images showed a sequence from low magnification to a high magnification, allowing for a view of the pore sizes, eventually leading up to a view of the individual fibres.

This section is split up according to the substrates, which each subsection containing the surface and cross-sectional images, similar to that of Chapter 4. These images could assist in future studies of the similar nature, as a source for comparison.

B.2.1 Sulphite

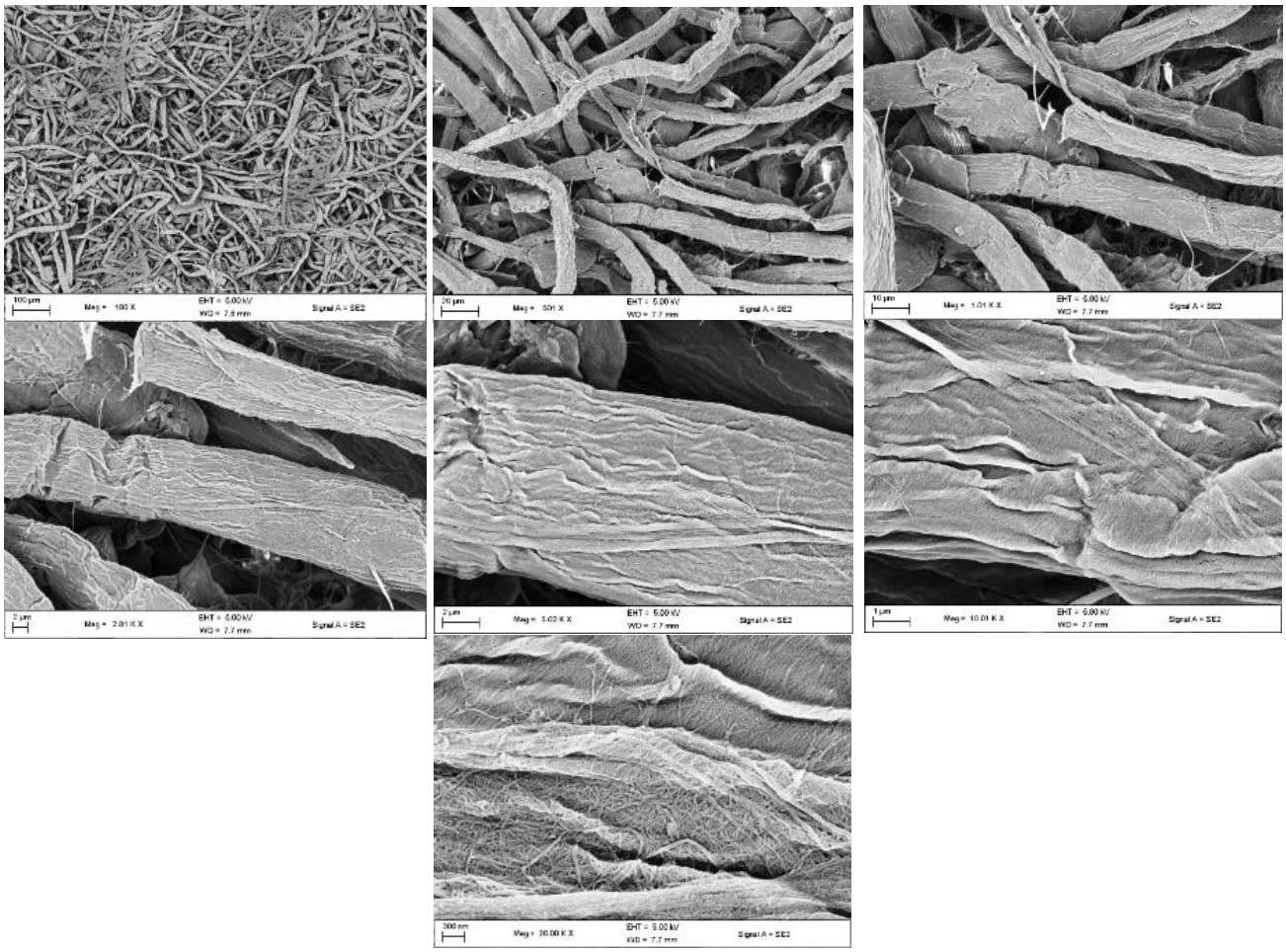

Figure B.1: FEG-SEM images of SULP sheet showing surface images at various magnifications.

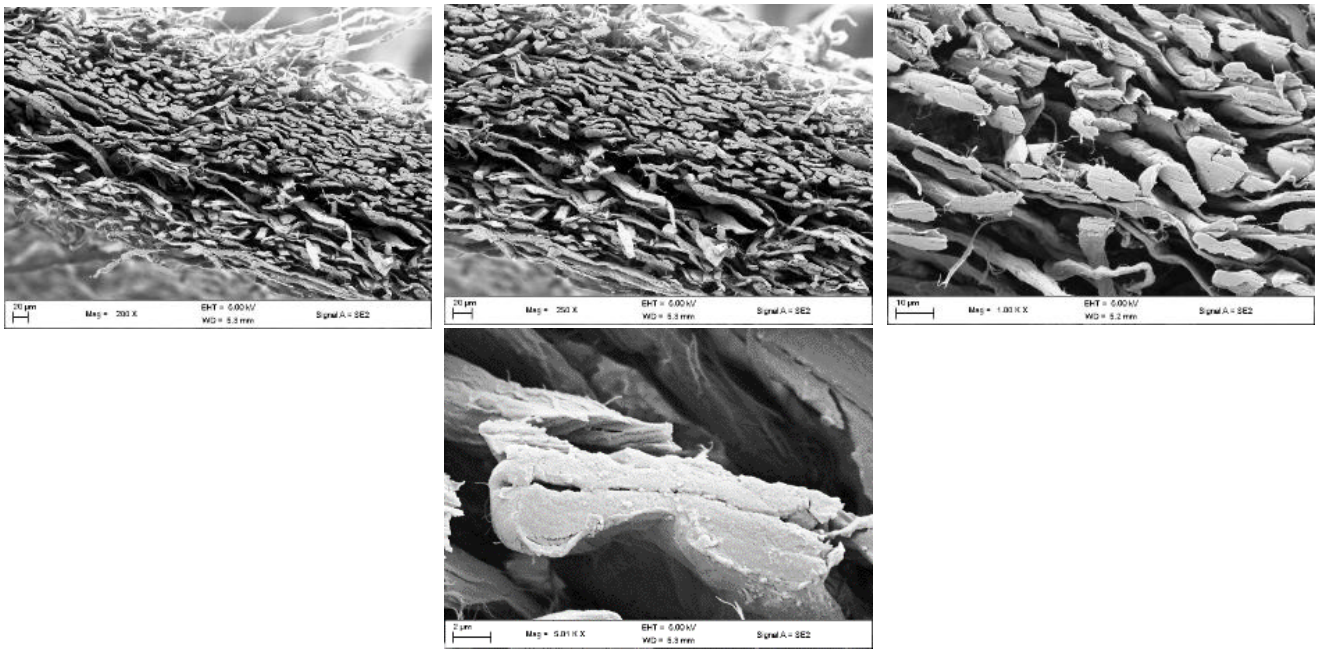

Figure B.2: FEG-SEM images of SULP sheet showing cross-sectional images at various magnifications.

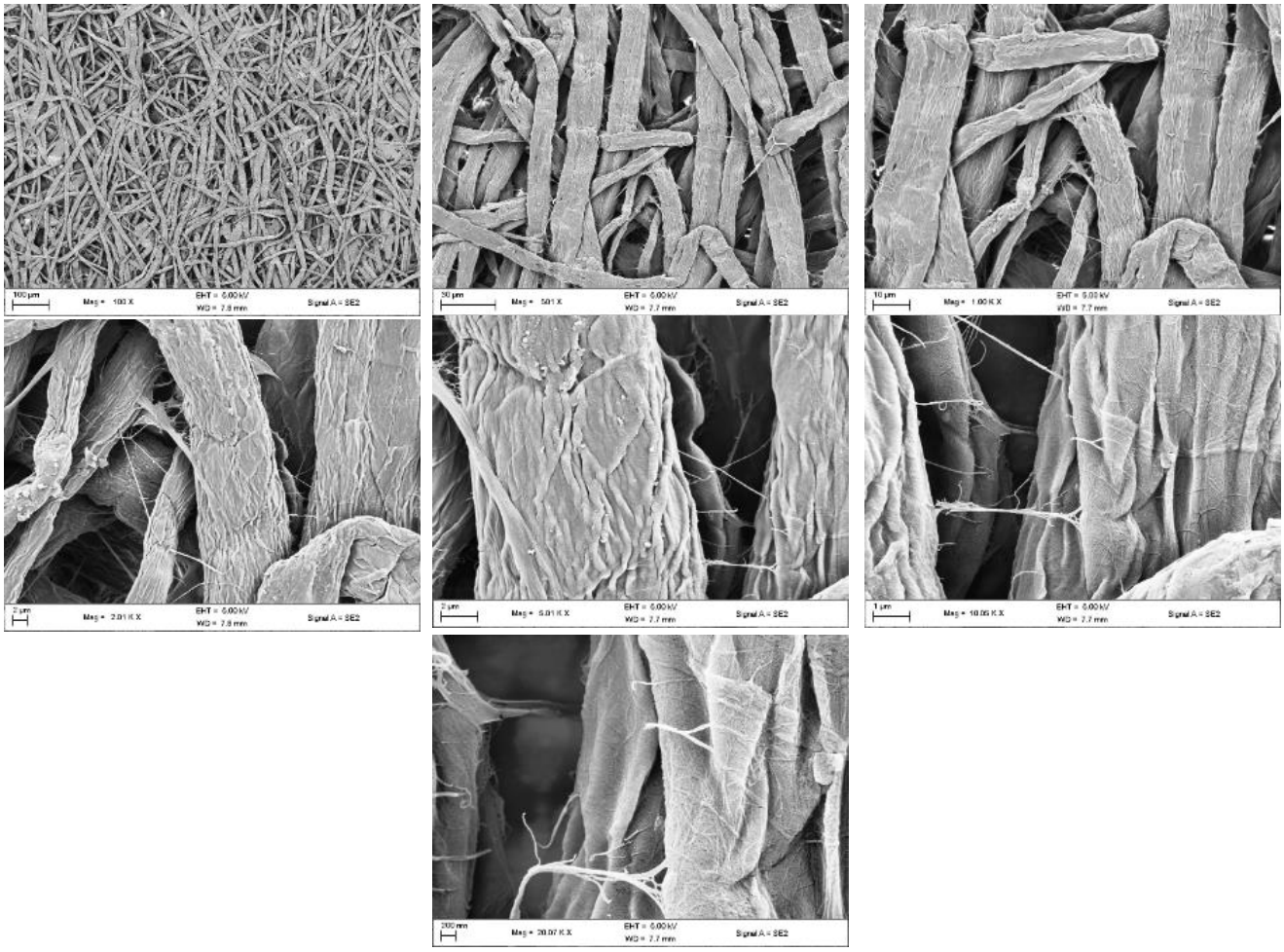

Figure B.3: FEG-SEM images of BK sheet showing surface images at various magnifications.

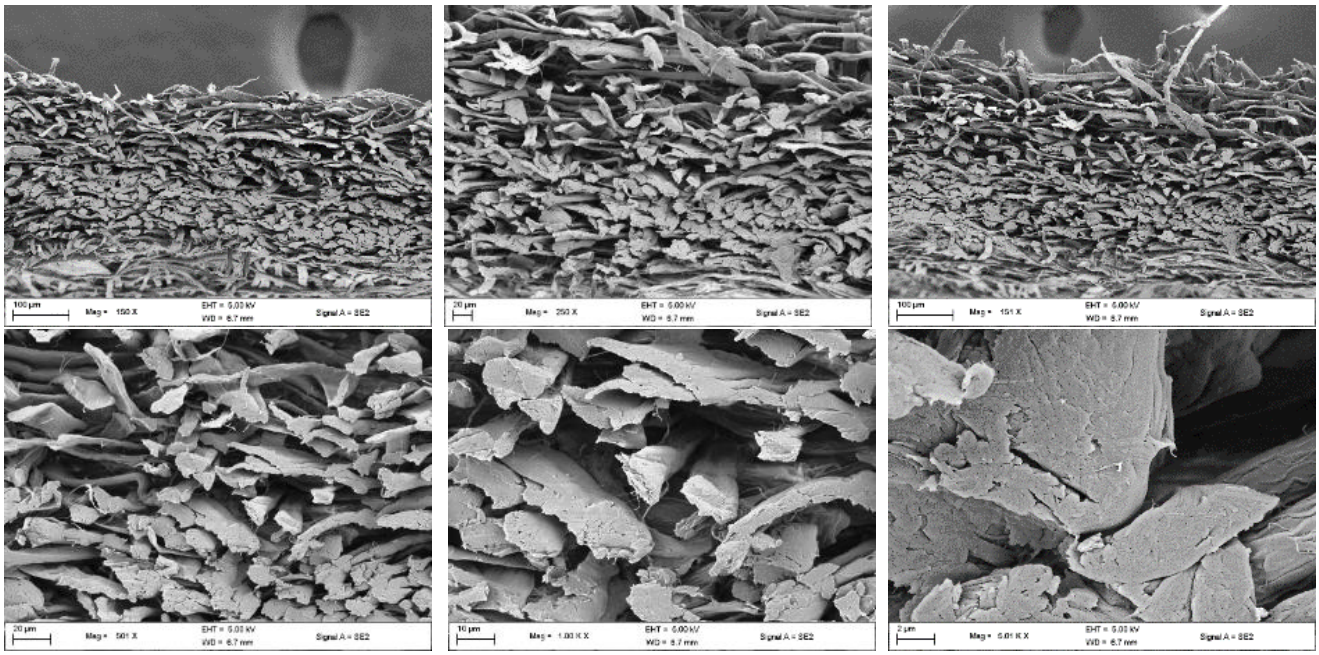

Figure B.4: FEG-SEM images of BK sheet showing cross-sectional images at various magnifications.

B 2.3 Unbleached Kraft

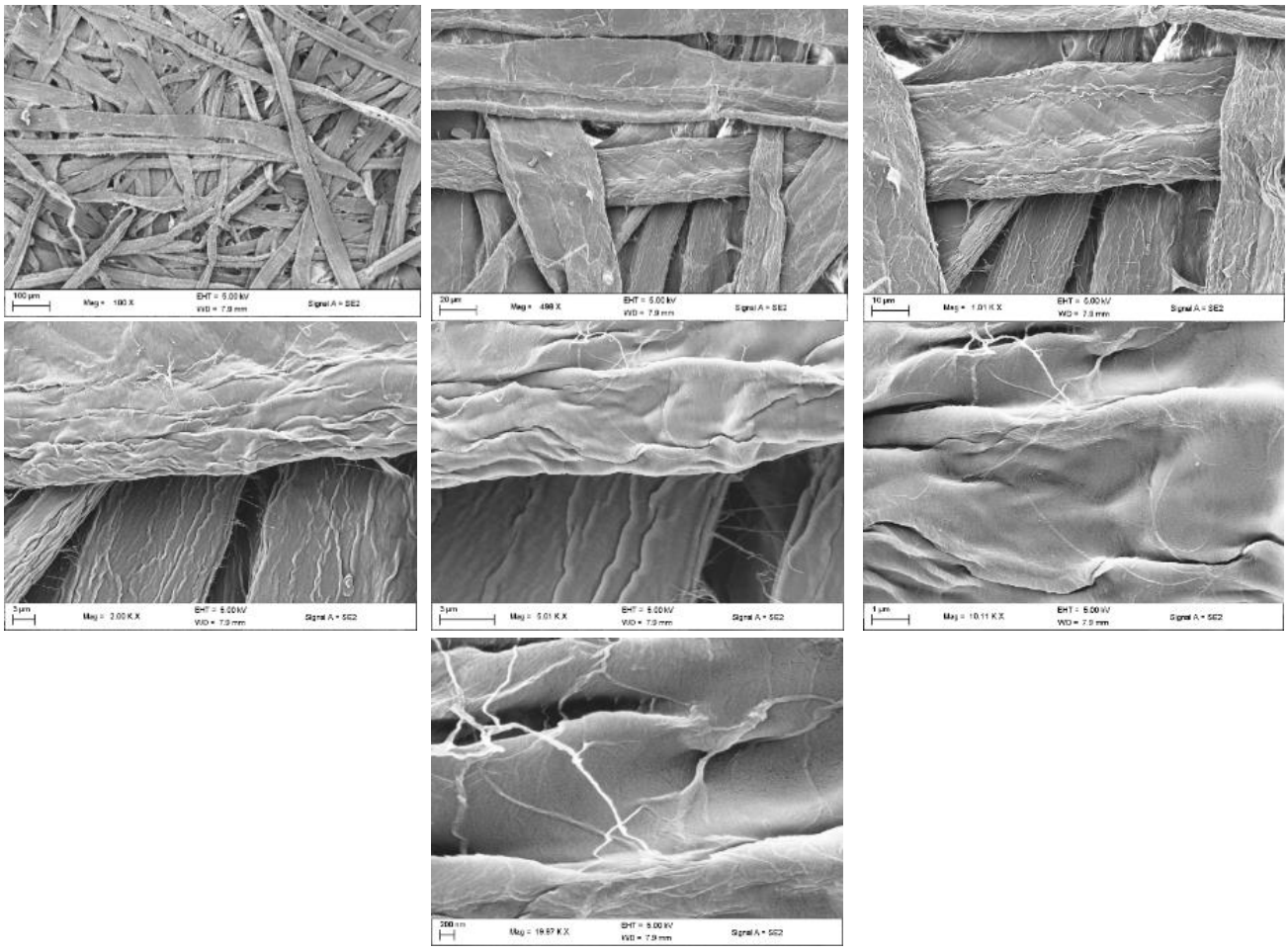

Figure B.5: FEG-SEM images of UBK sheet showing surface images at various magnifications.

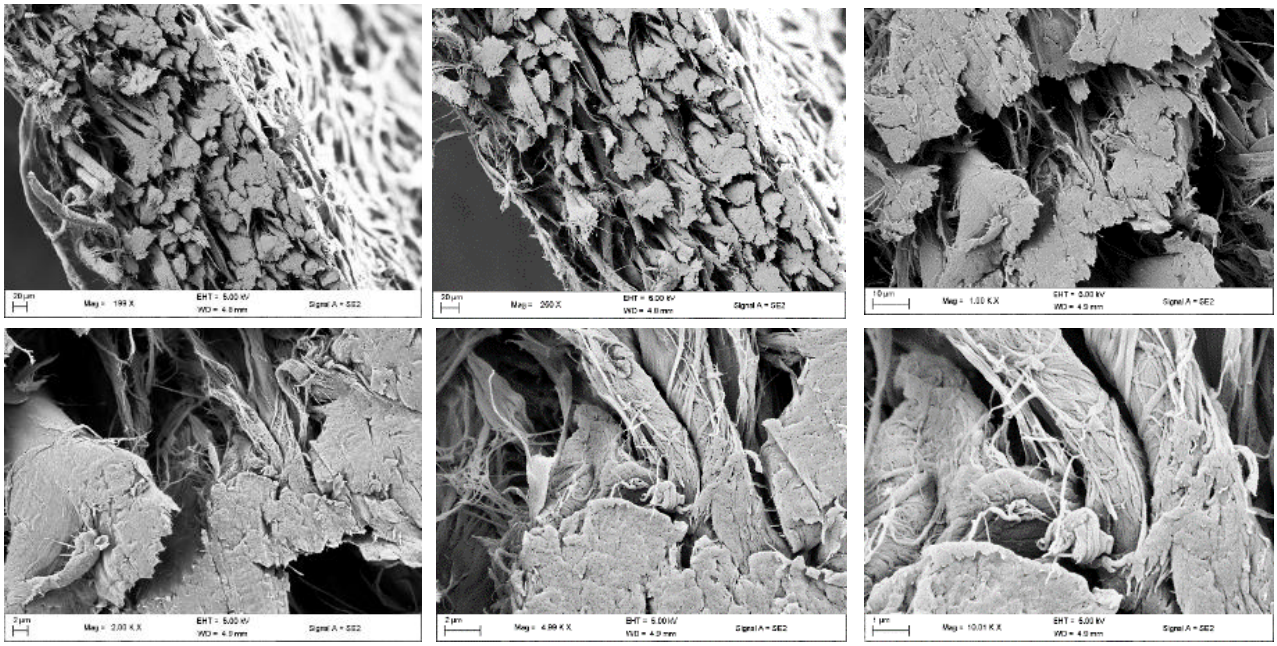

Figure B.6: FEG-SEM images of UBK sheet showing cross-sectional images at various magnifications.

B 2.4 Chromatography No.1 Filter Paper

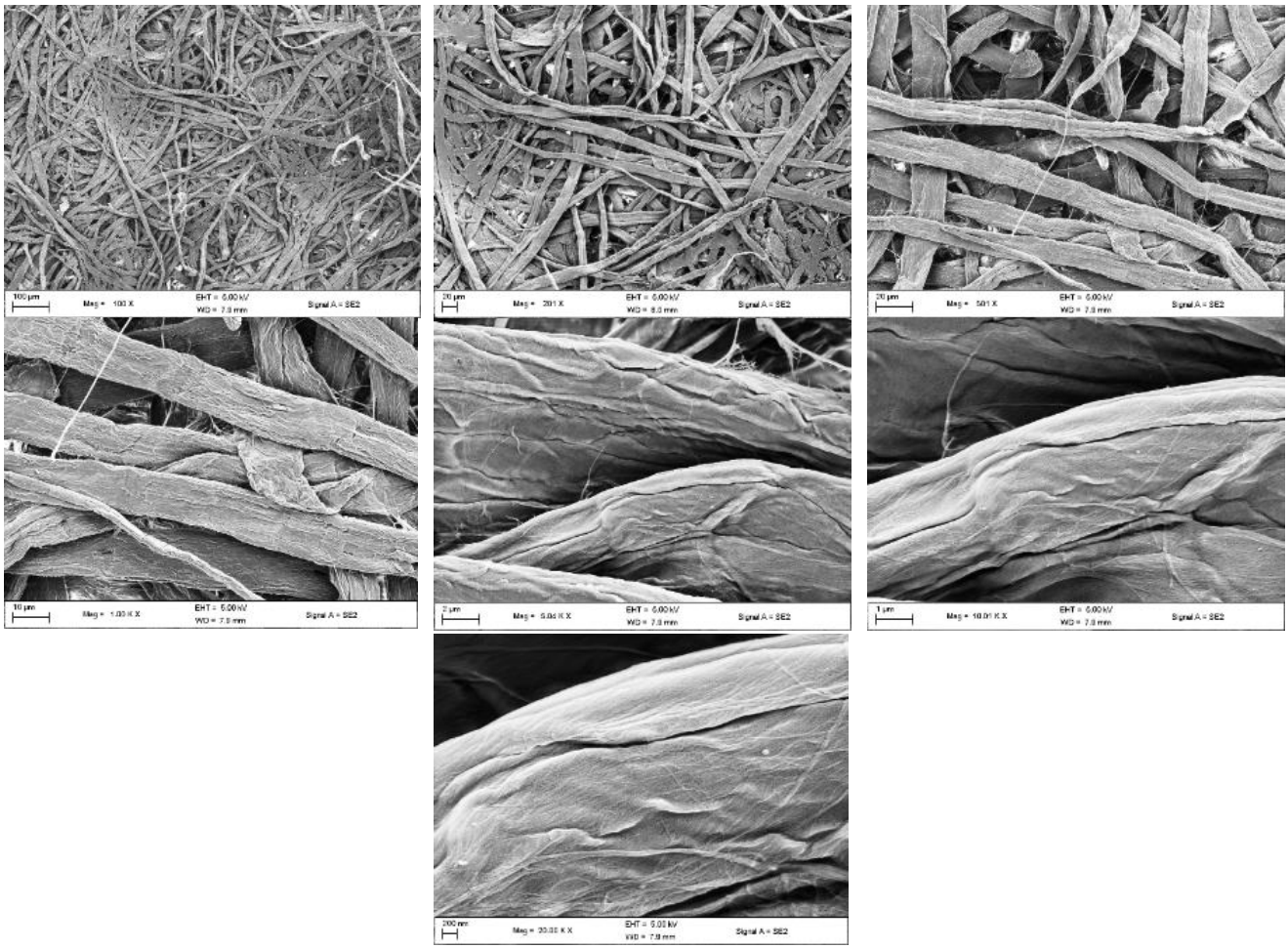

Figure B.7: FEG-SEM images of CHR sheet showing surface images at various magnifications.

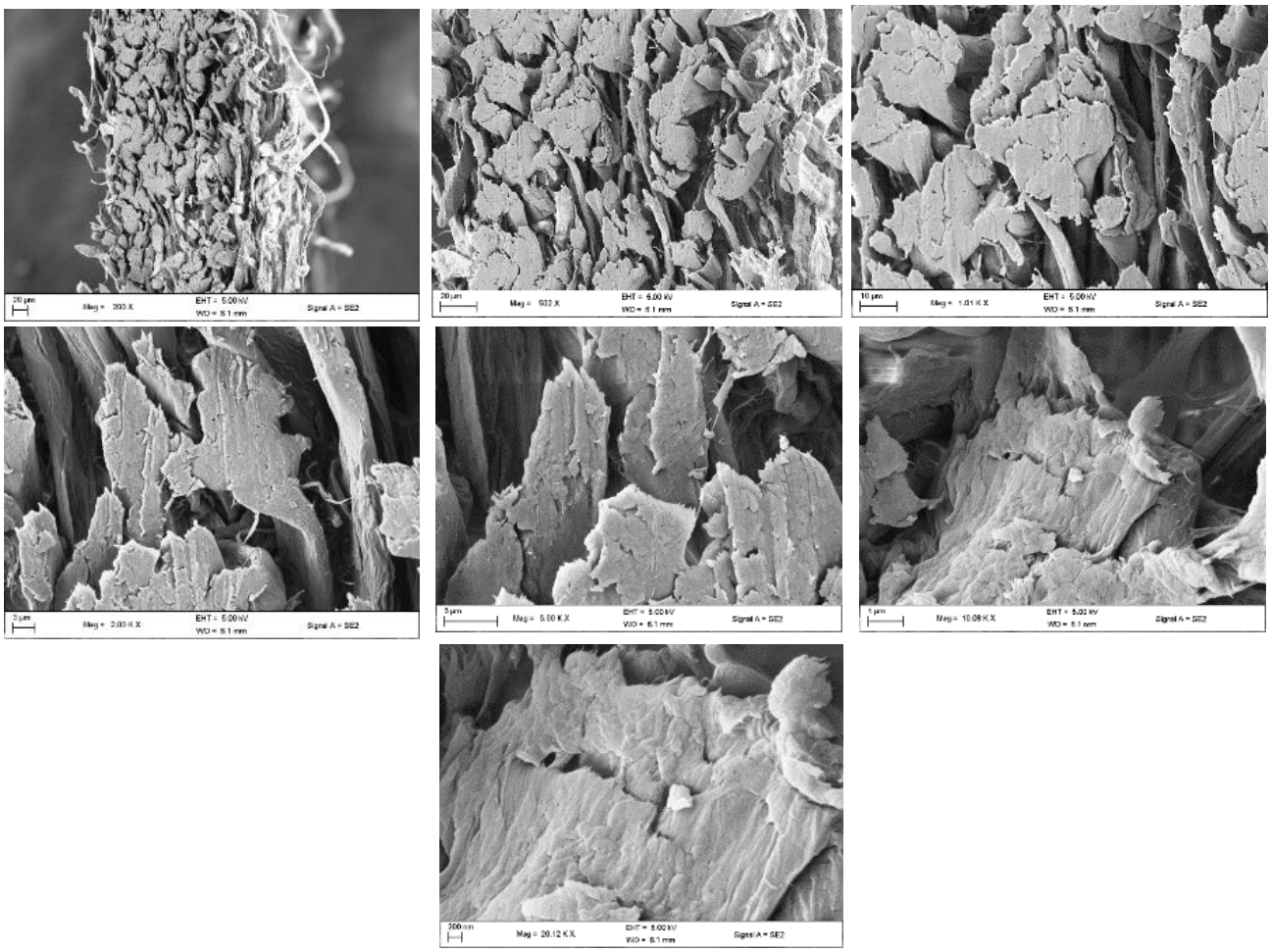

Figure B.8: FEG-SEM images of CHR sheet showing cross-sectional images at various magnifications.

B 2.5 Chromatography 3MM Filter Paper

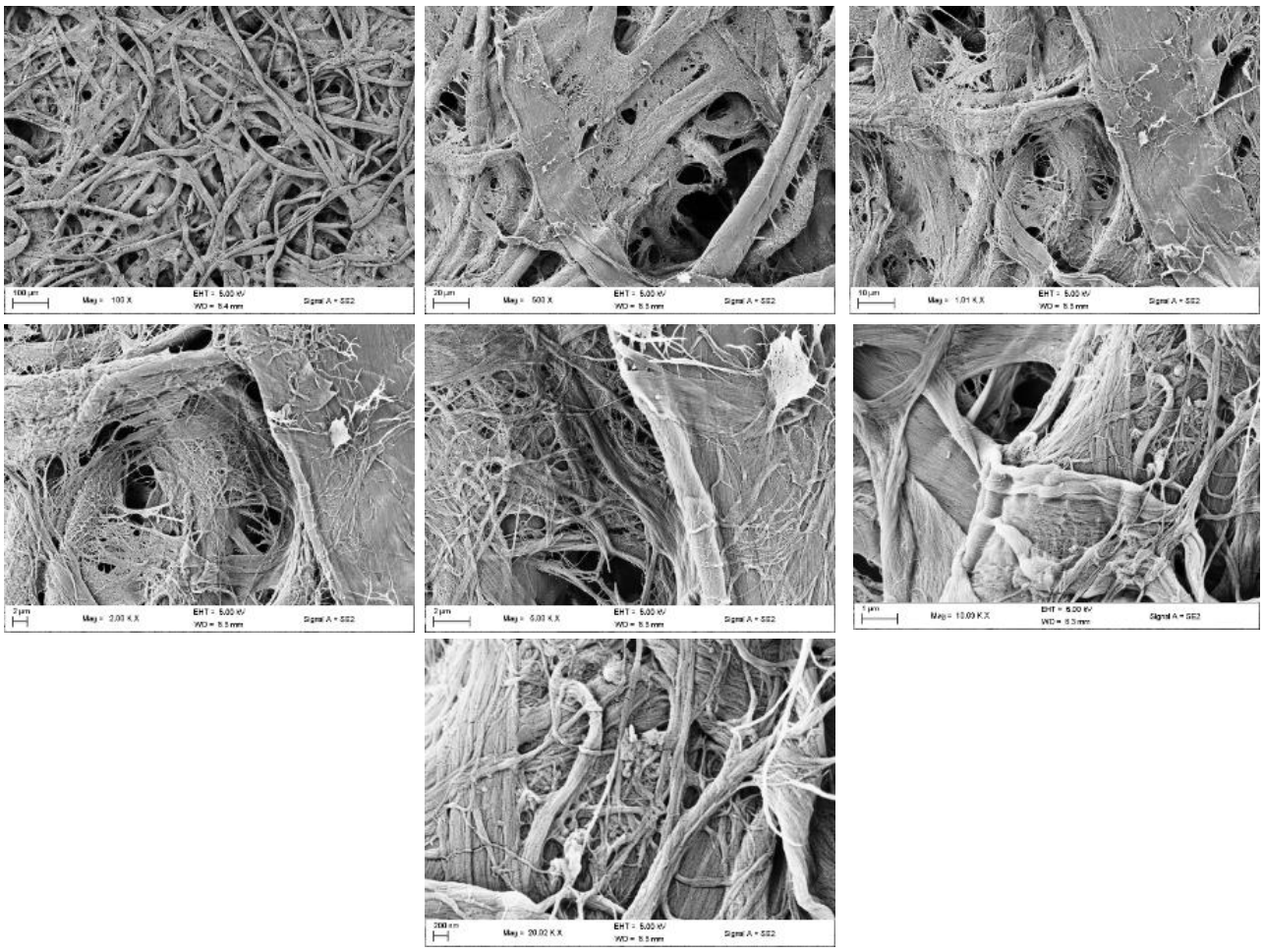

Figure B.9: FEG-SEM images of CHR3 sheet showing surface images at various magnifications.

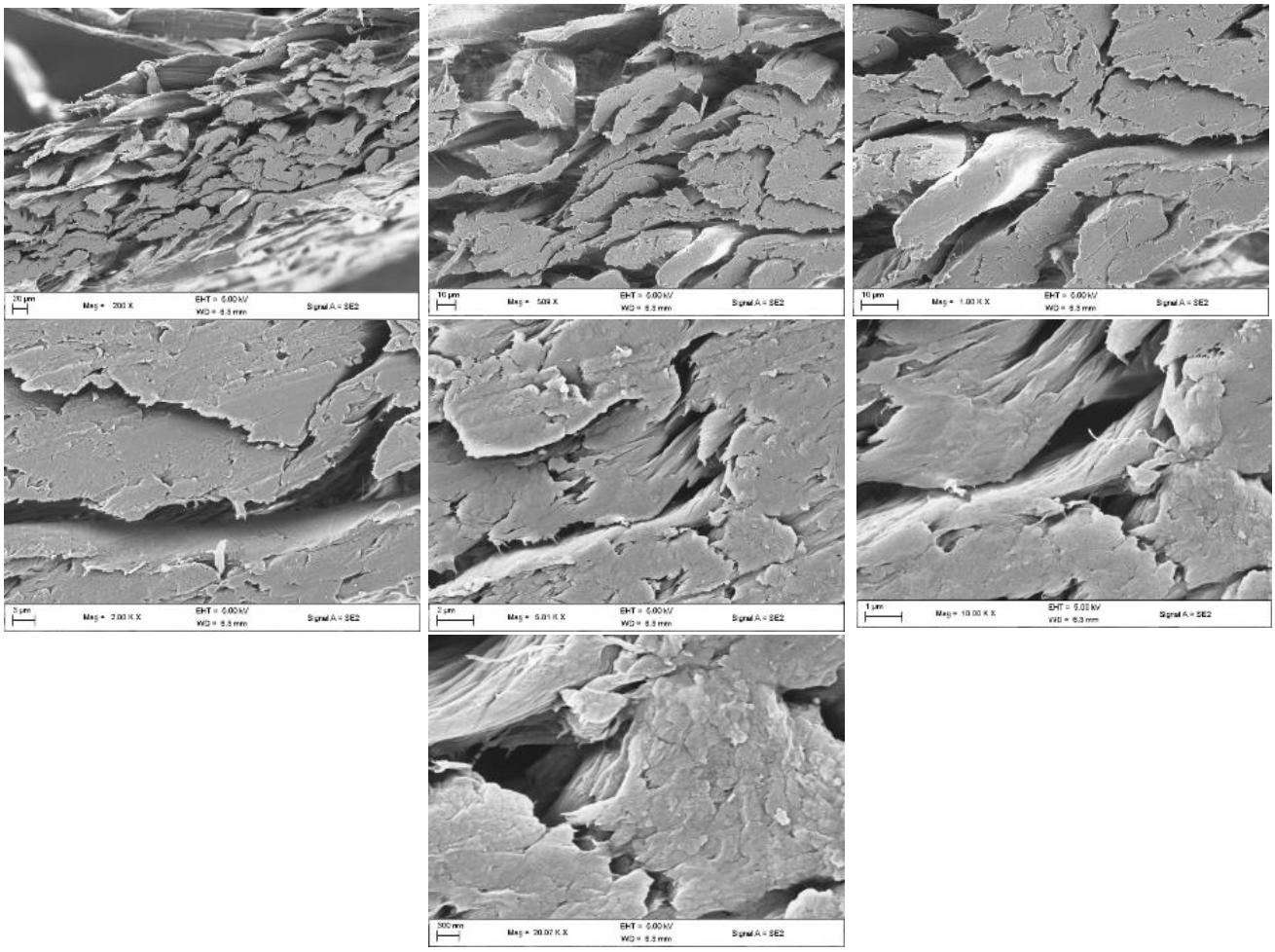

Figure B.10: FEG-SEM images of CHR3 sheet showing cross-sectional images at various magnifications.

B 2.6 Thermo-mechanical

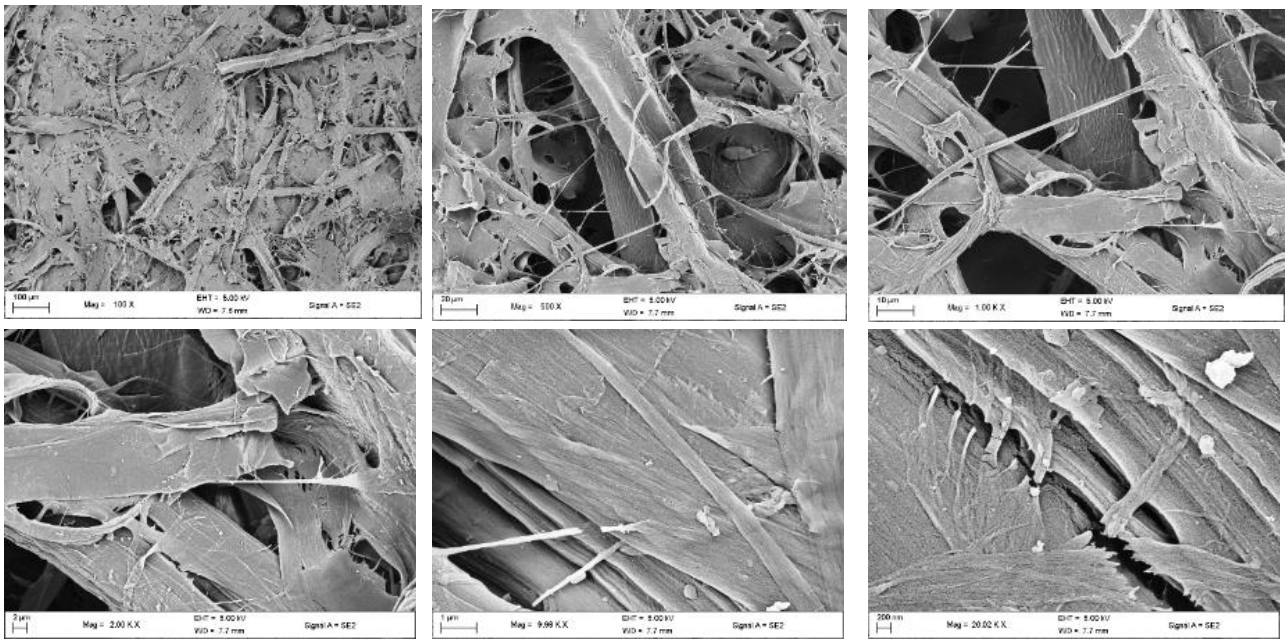

Figure B.11: FEG-SEM images of TMP sheet showing surface images at various magnifications.

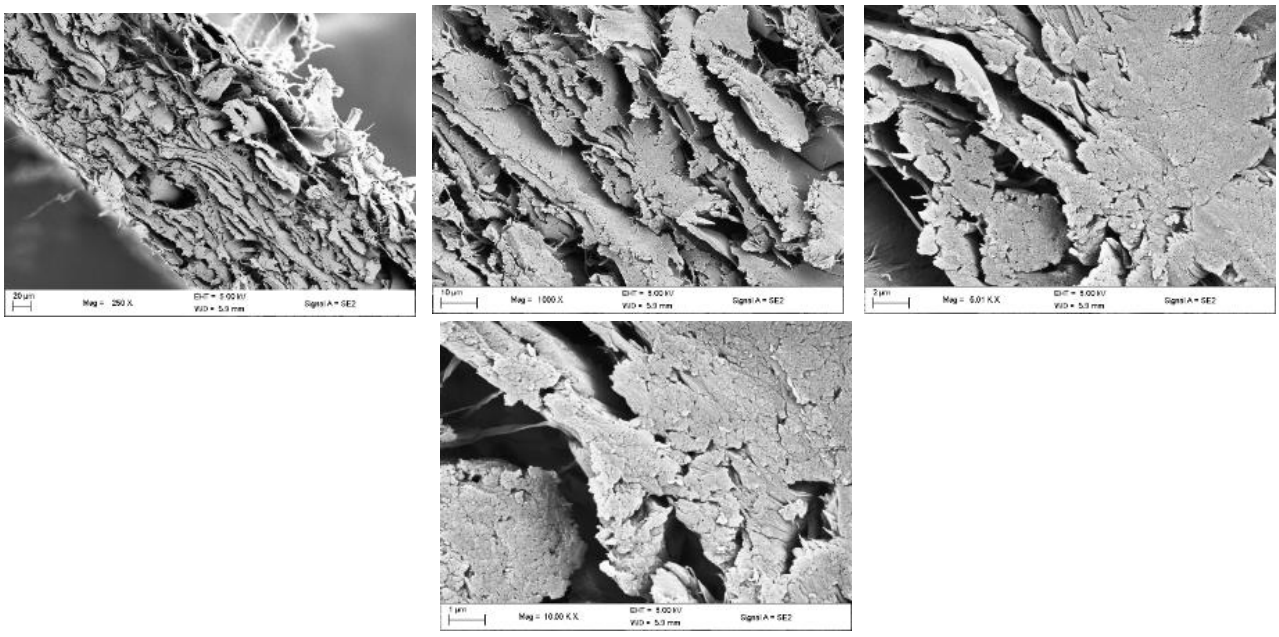

Figure B.12: FEG-SEM images of TMP sheet showing cross-sectional images at various magnifications.

B 2.7 Recycled

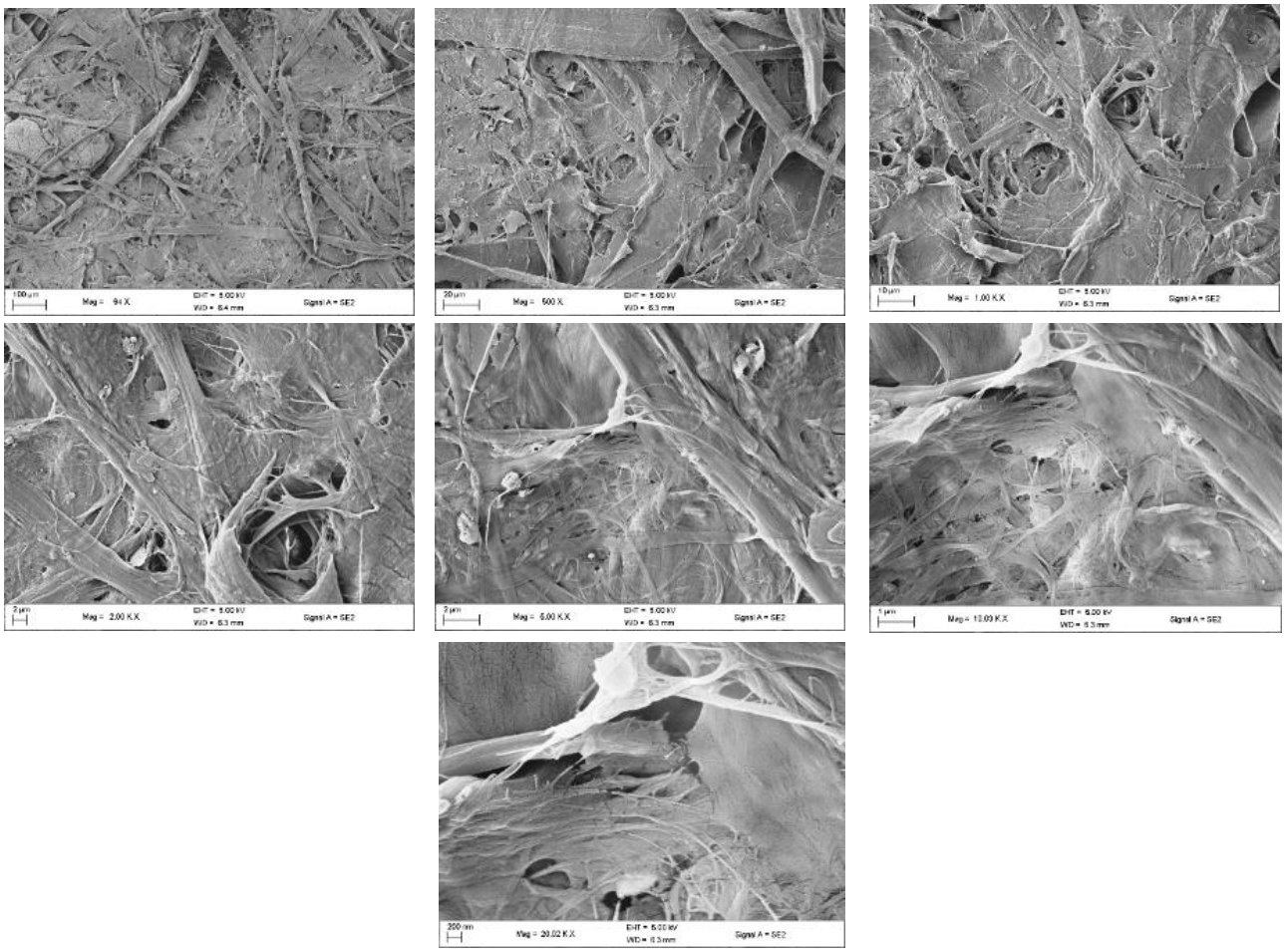

Figure B.13: FEG-SEM images of REC sheet showing surface images at various magnifications.

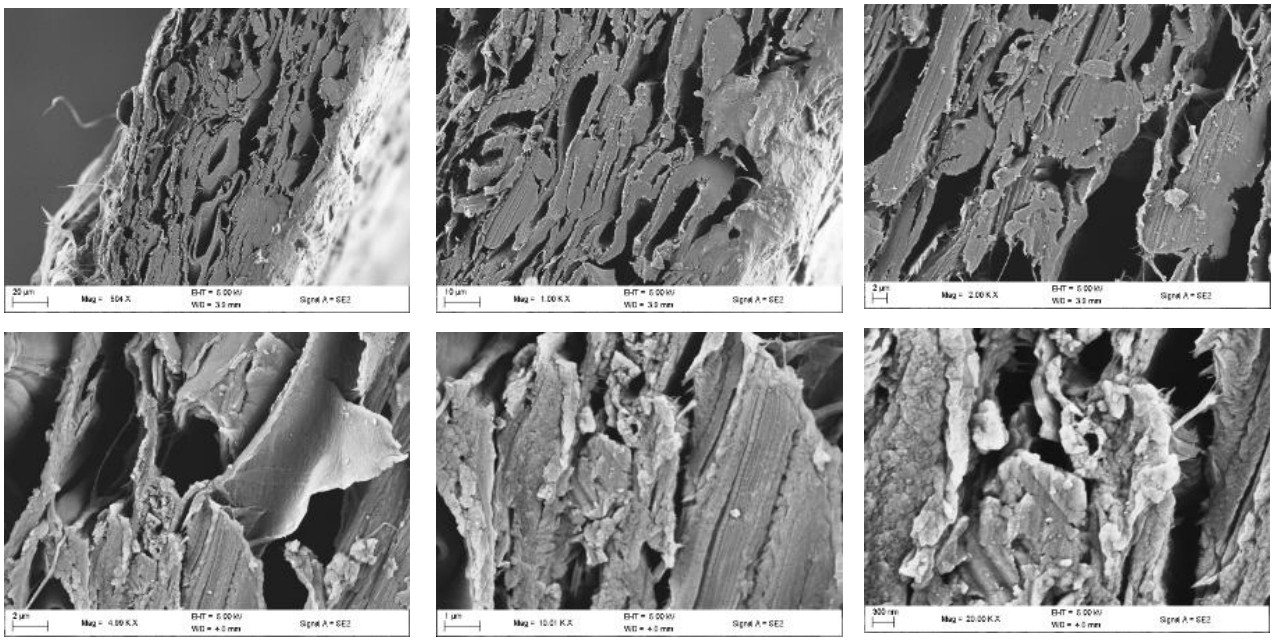

Figure B.14: FEG-SEM images of REC sheet showing cross-sectional images at various magnifications.

B.3 NFC Substrates

This section contains the micrographs of the NFC sheets, obtained during experimentation. The micrographs are ordered from lowest magnification to highest magnification, where the overall pore size could be observed, and a detailed picture of the fibre strands can be seen.

Similar to that of section B.2, this section is split up into the substrate type, and further being broken down into the NFC substitution amounts, these being either 20%, 50% or 100%.

B.3.1 Sulphite

B.3.1.1 20% NFC

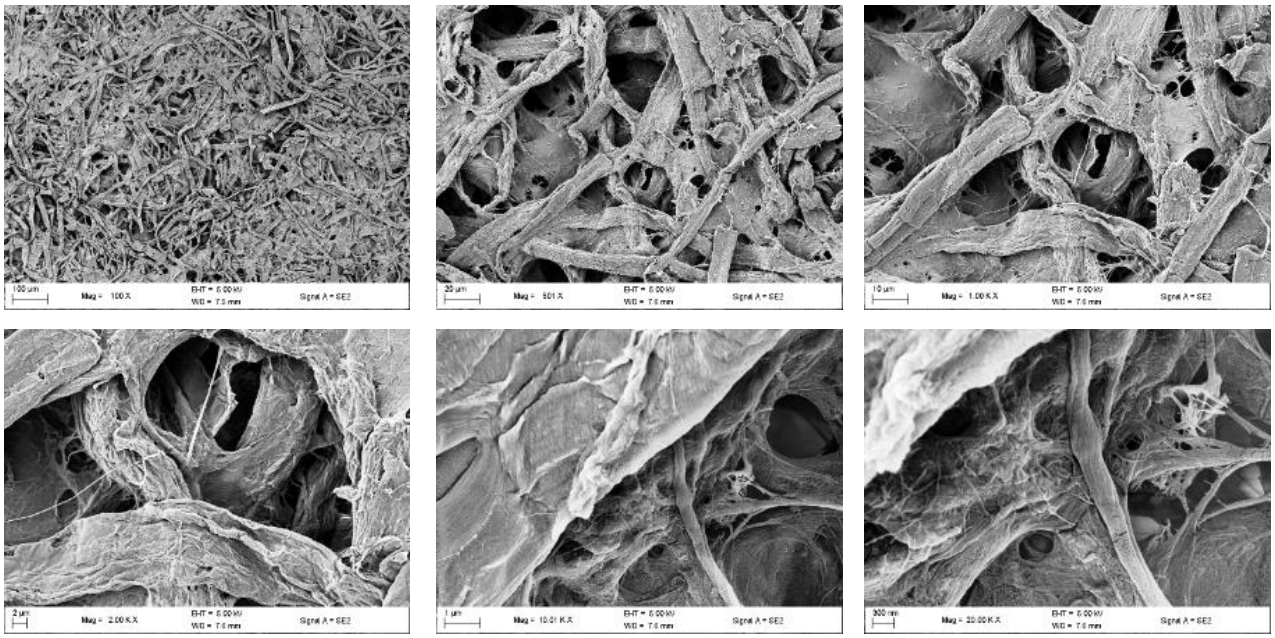

Figure B.15: FEG-SEM images of 20% NFC SULP sheet showing surface images at various magnifications.

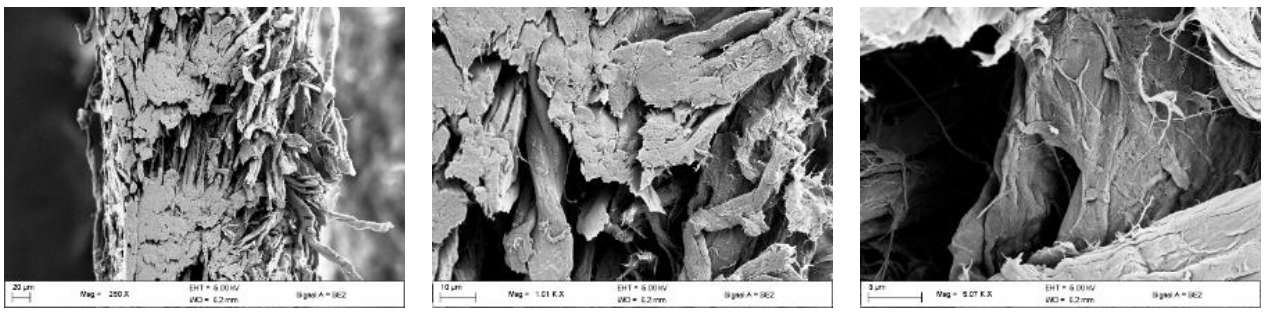

Figure B.16: FEG-SEM images of 20% NFC SULP sheet showing cross-sectional images at various magnifications.

B.3.1.2 50% NFC

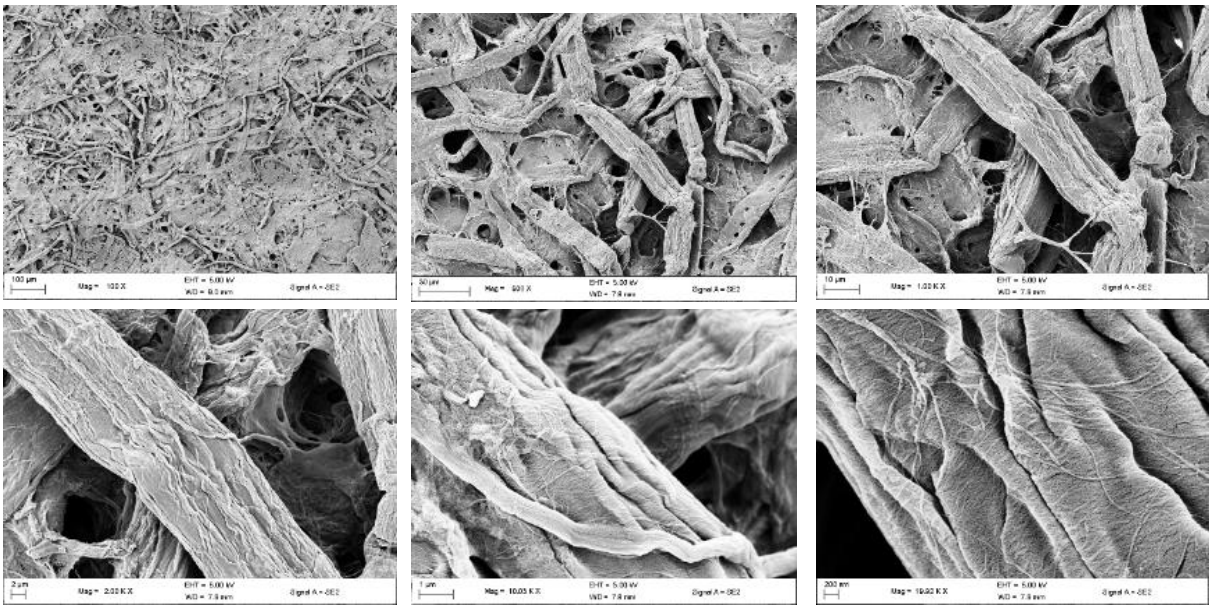

Figure B.17: FEG-SEM images of 50% NFC SULP sheet showing surface images at various magnifications.

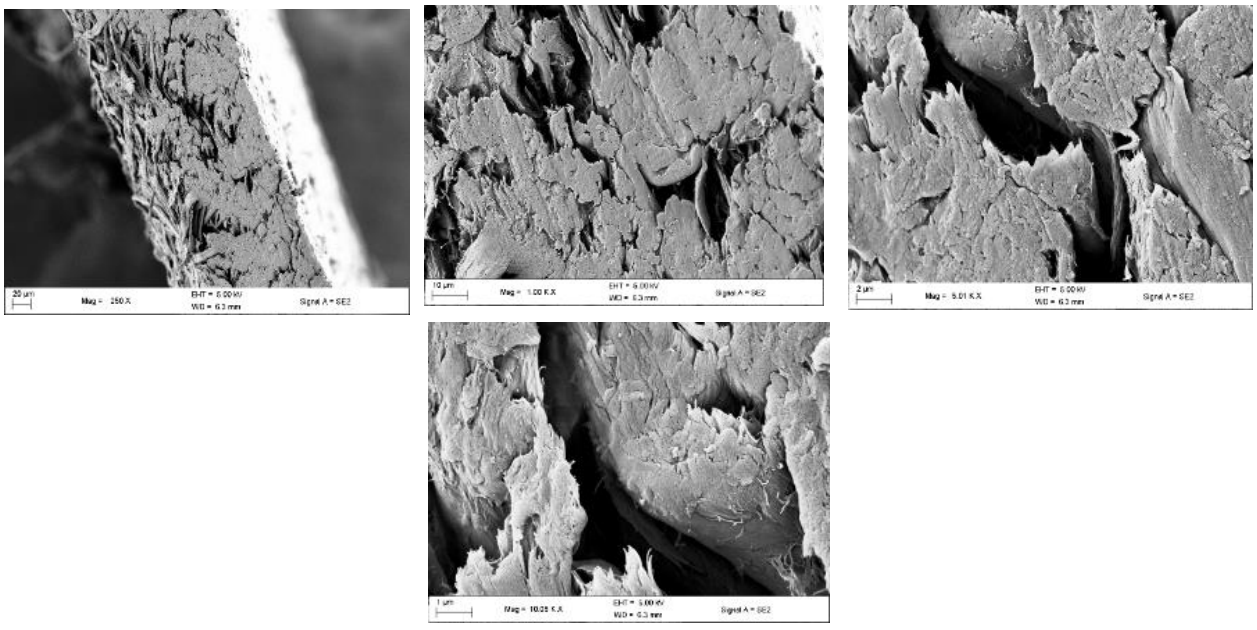

Figure B.16: FEG-SEM images of 50% NFC SULP sheet showing cross-sectional images at various magnifications.

B 3.2 Unbleached Kraft

B 3.2.1 20% NFC

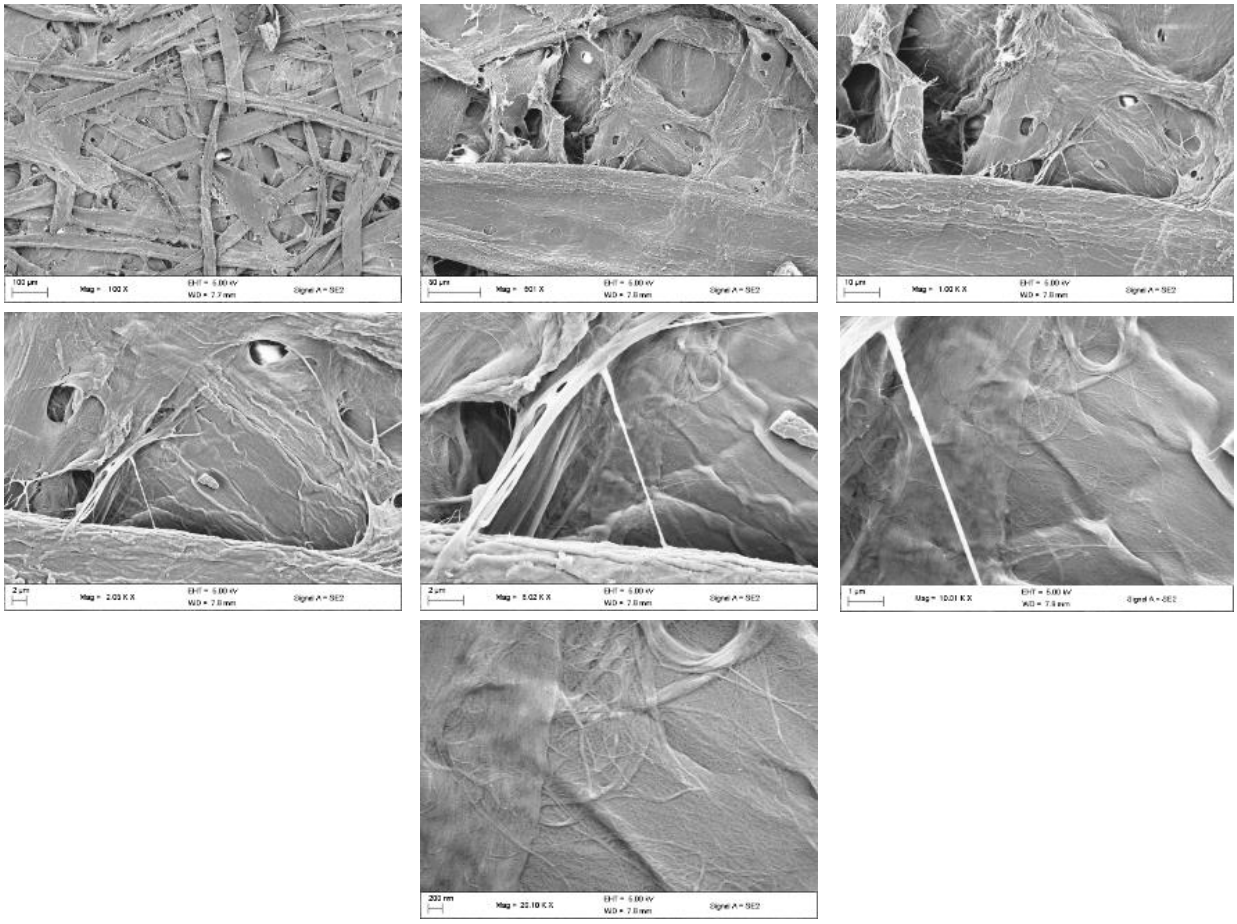

Figure B.17: FEG-SEM images of 20% NFC UBK sheet showing surface images at various magnifications.

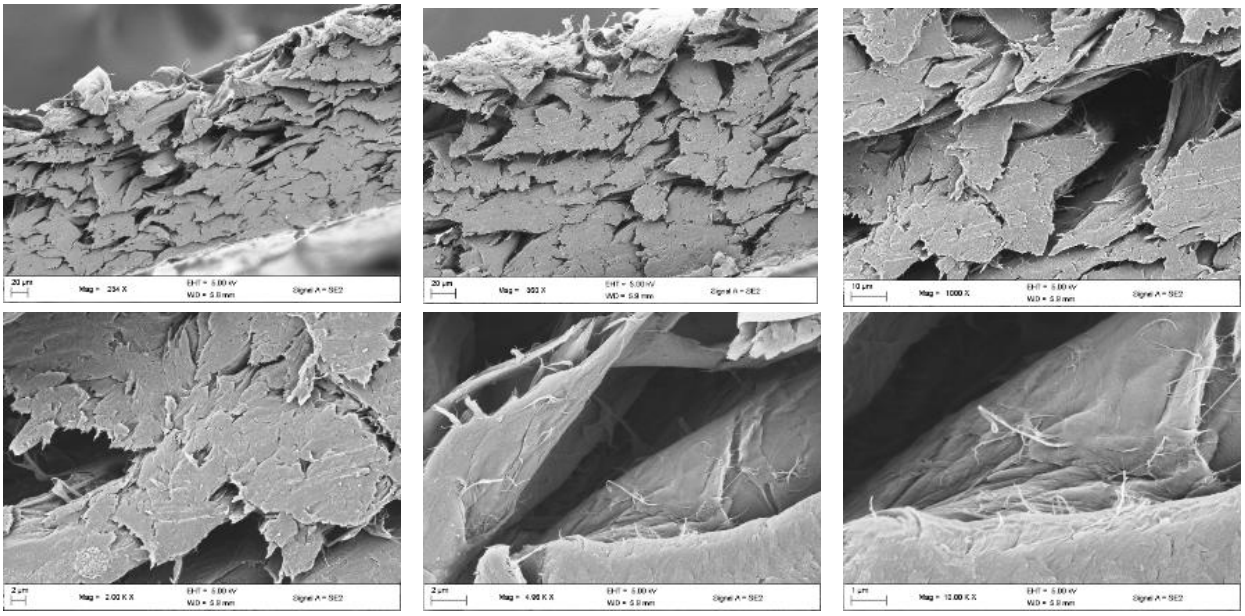

Figure B.18: FEG-SEM images of 20% NFC UBK sheet showing cross-sectional images at various magnifications.

B 3.2.2 50% NFC

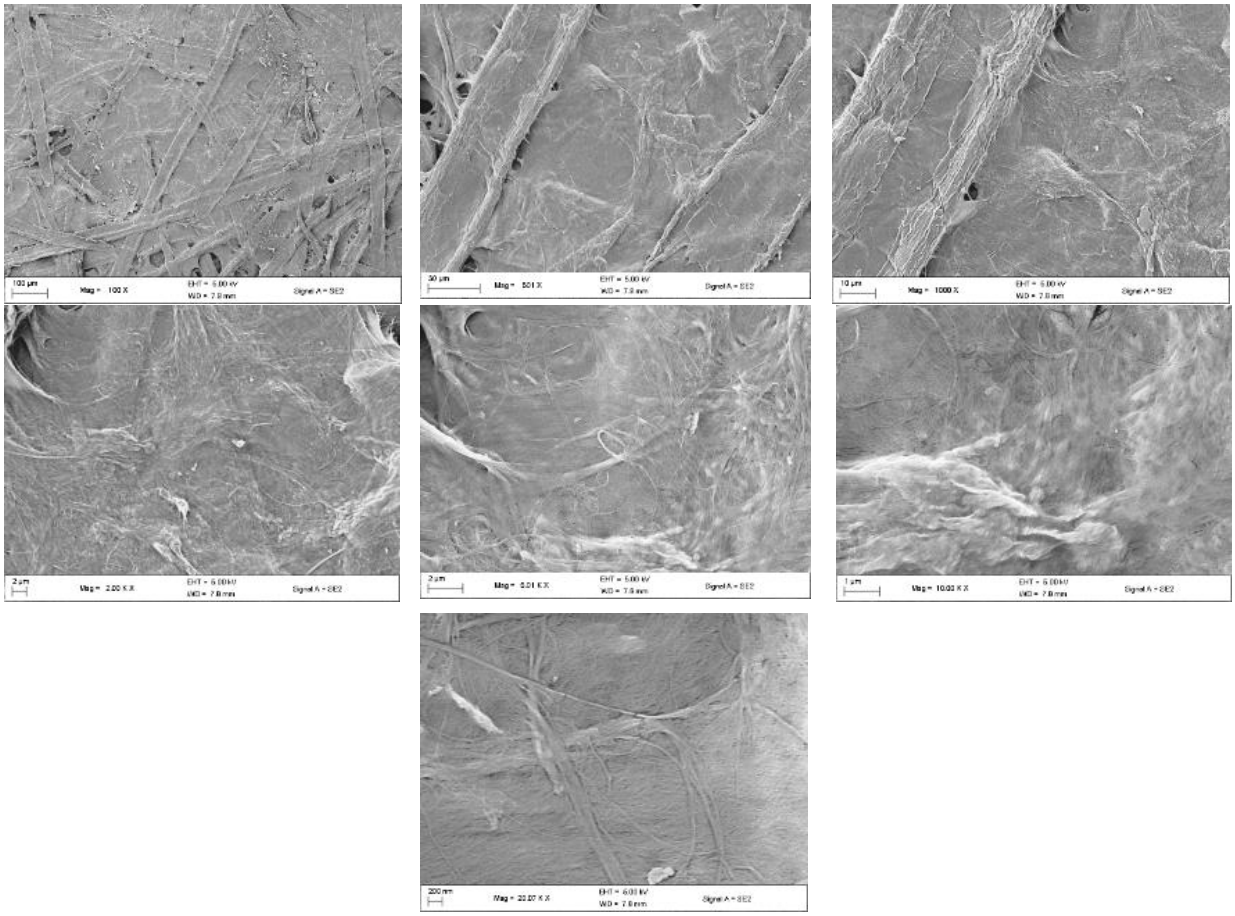

Figure B.19: FEG-SEM images of 50% NFC UBK sheet showing surface images at various magnifications.

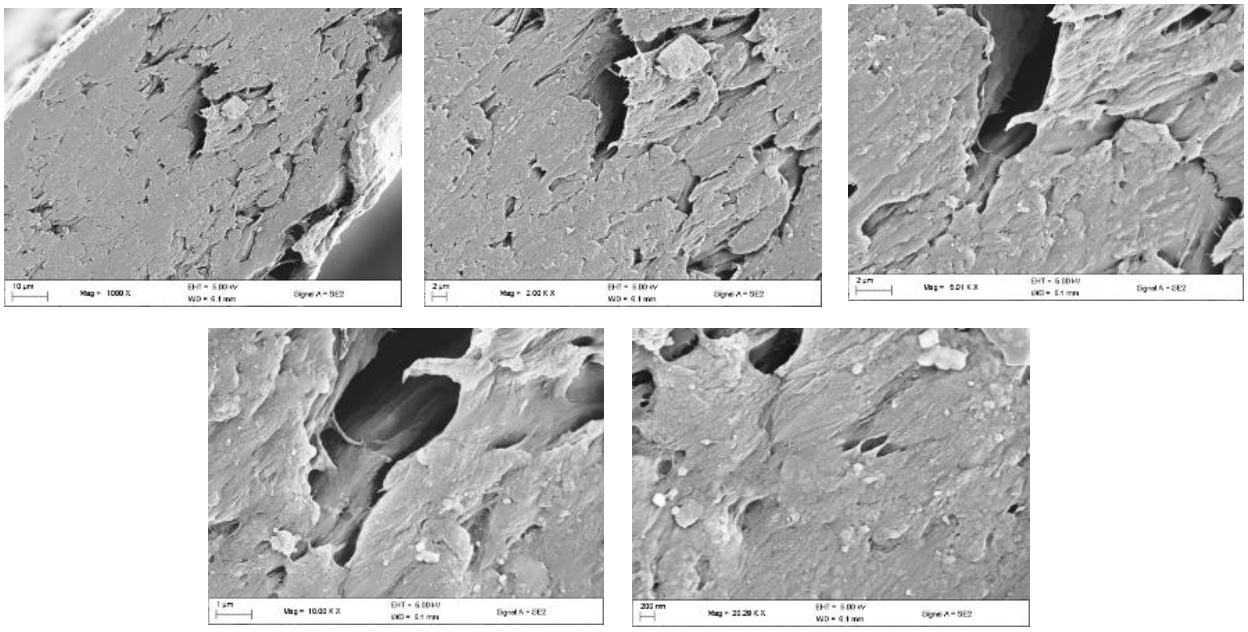

Figure B.20: FEG-SEM images of 50% NFC UBK sheet showing cross-sectional images at various magnifications.

B 3.2.3 100% NFC

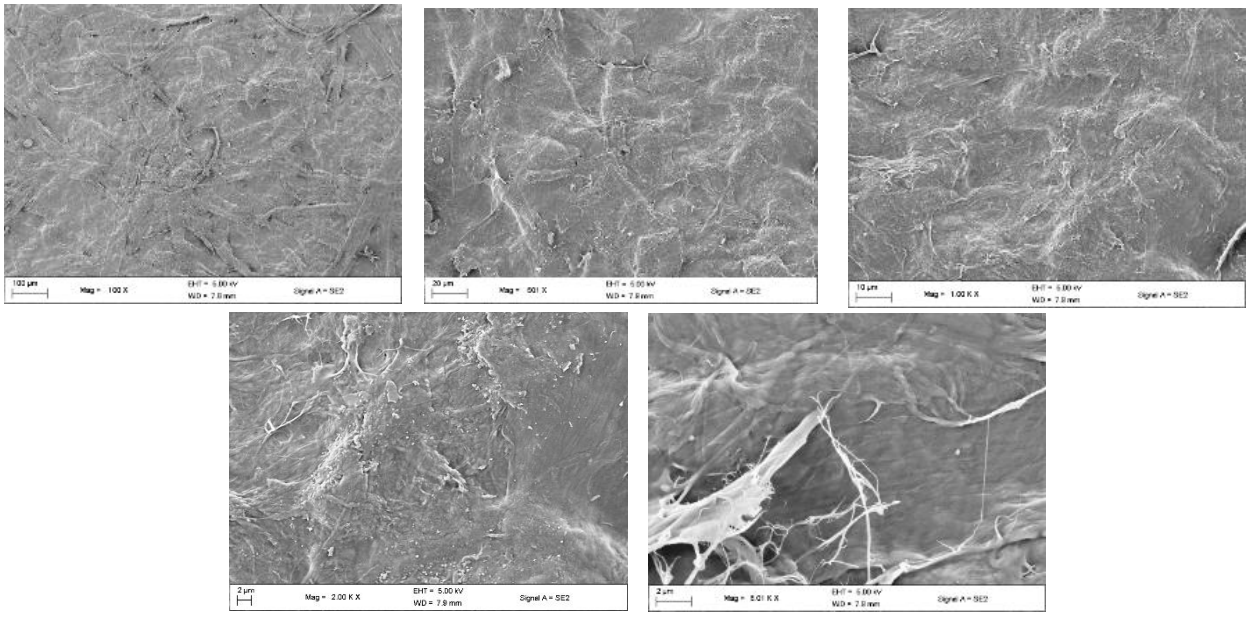

Figure B.21: FEG-SEM images of 100% NFC UBK sheet showing surface images at various magnifications.

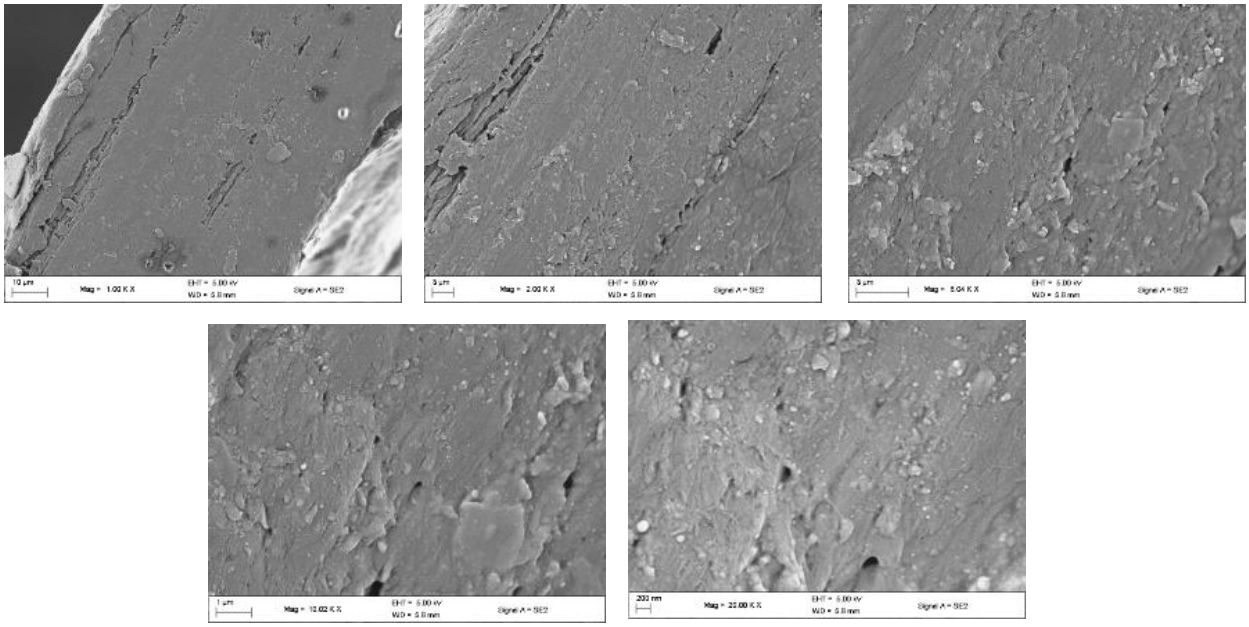

Figure B.22: FEG-SEM images of 100% NFC UBK sheet showing cross-sectional images at various magnifications.

B 3.3 Chromatography No.1 Filter Paper

B 3.3.1 20% NFC

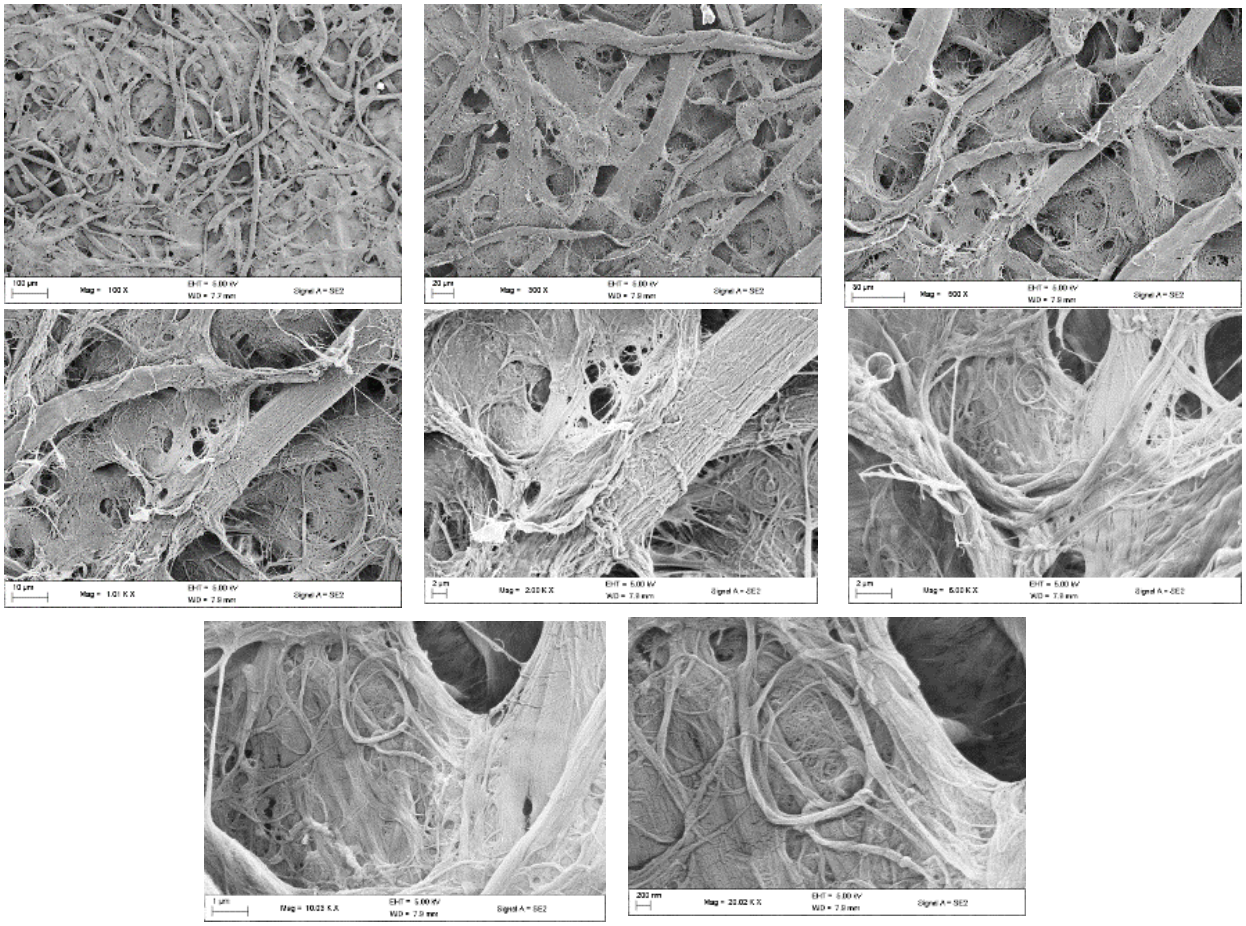

Figure B.23: FEG-SEM images of 20% NFC CHR sheet showing surface images at various magnifications.

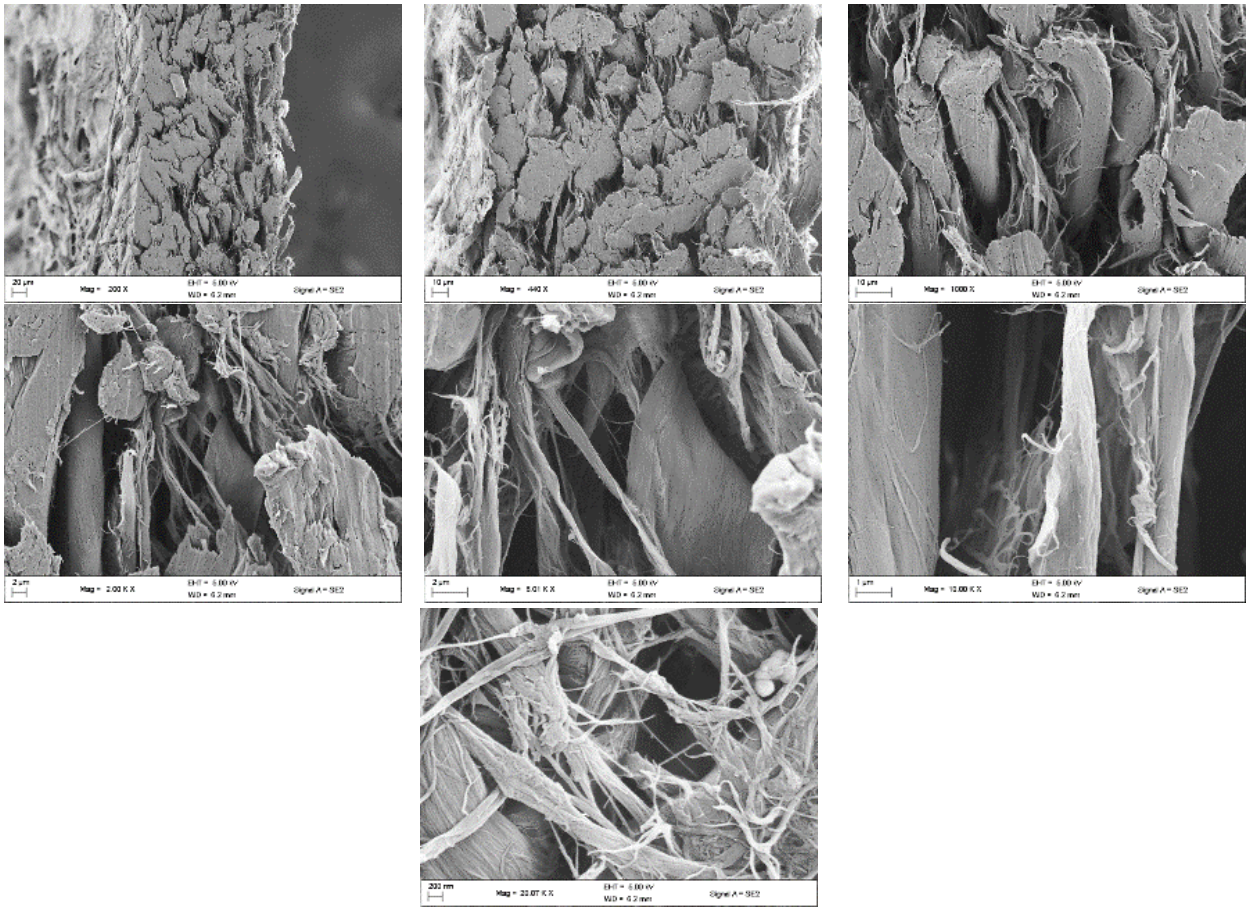

Figure B.24: FEG-SEM images of 20% NFC CHR sheet showing cross-sectional images at various magnifications.

B 3.3.2 50% NFC

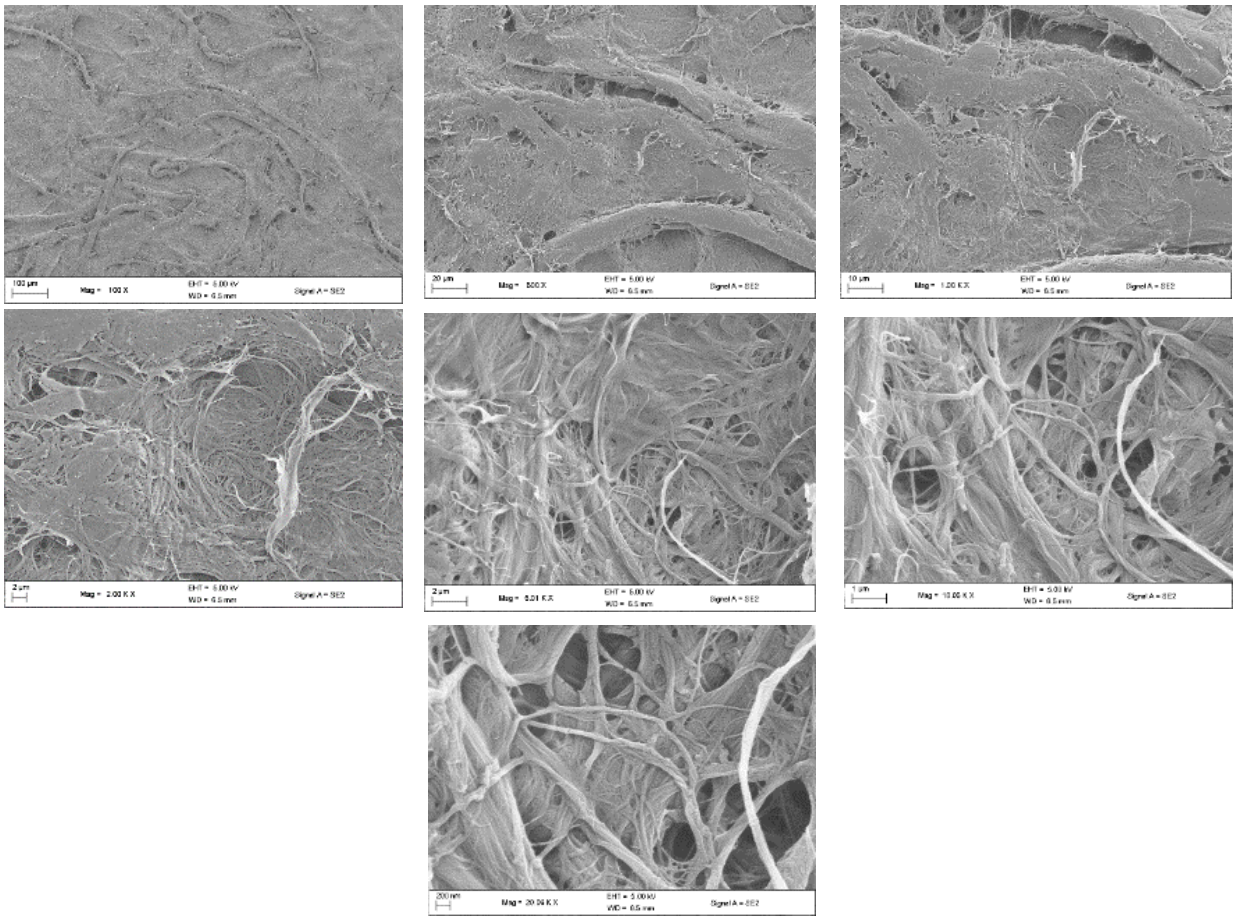

Figure B.25: FEG-SEM images of 50% NFC CHR sheet showing surface images at various magnifications.

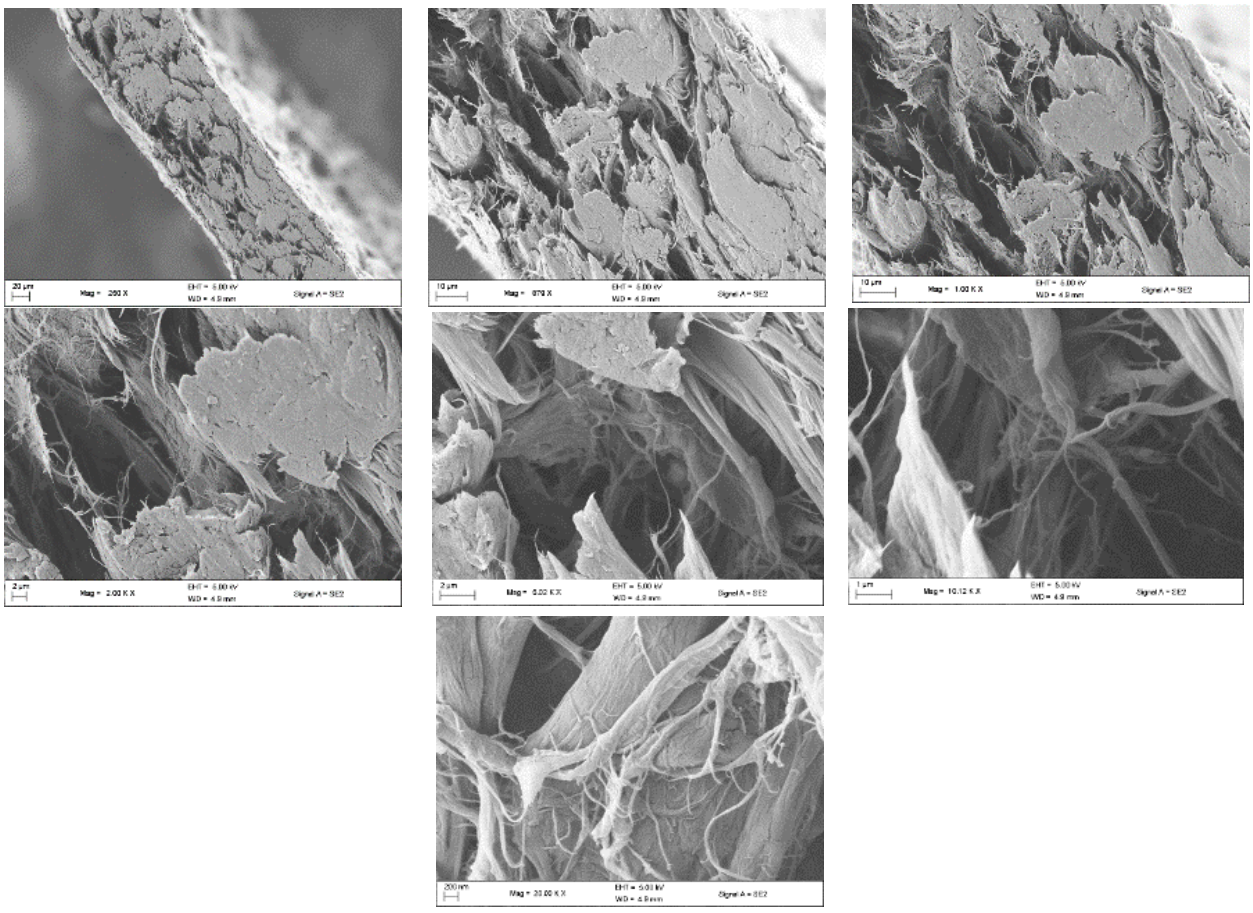

Figure B.26: FEG-SEM images of 50% NFC CHR sheet showing cross-sectional images at various magnifications.

B 3.3.3 100% NFC

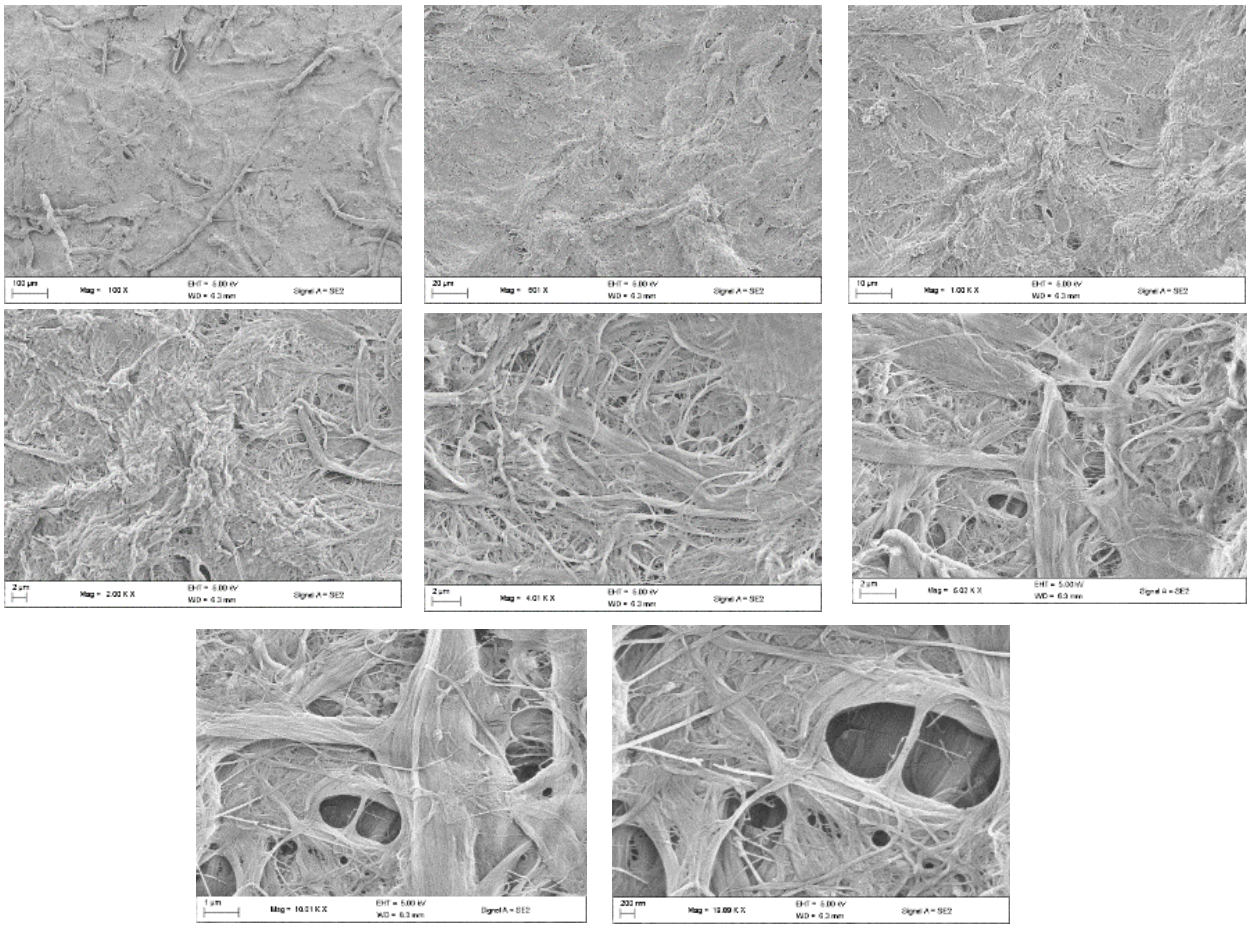

Figure B.27: FEG-SEM images of 100% NFC CHR sheet showing surface images at various magnifications.

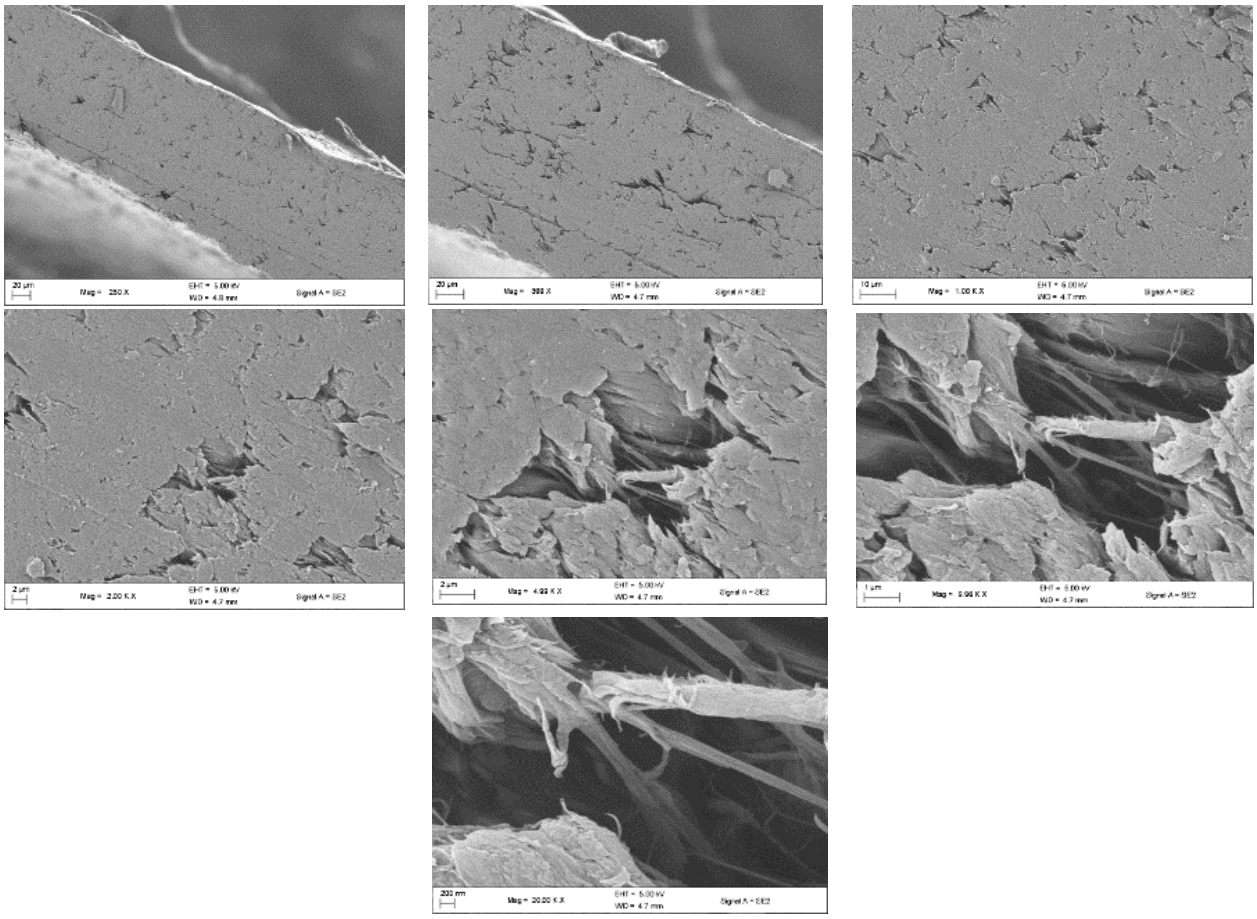

Figure B.28: FEG-SEM images of 100% NFC CHR sheet showing cross-sectional images at various magnifications.

B 3.4 Chromatography 3MM Filter Paper

B 3.4.1 20% NFC

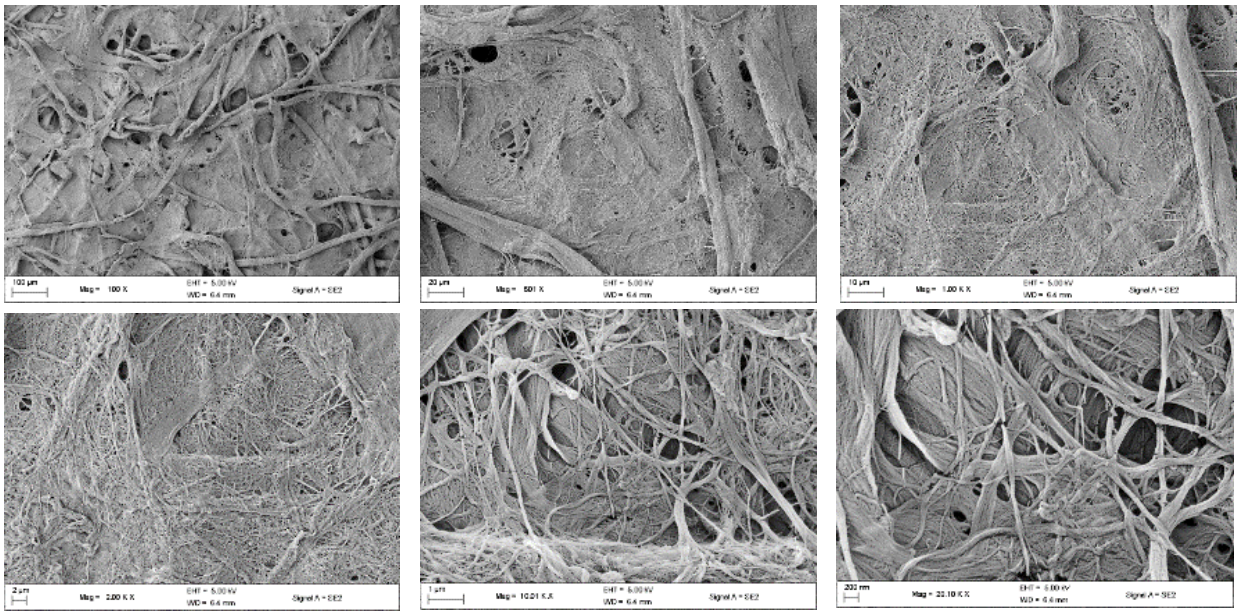

Figure B.29: FEG-SEM images of 20% NFC CHR3 sheet showing surface images at various magnifications.

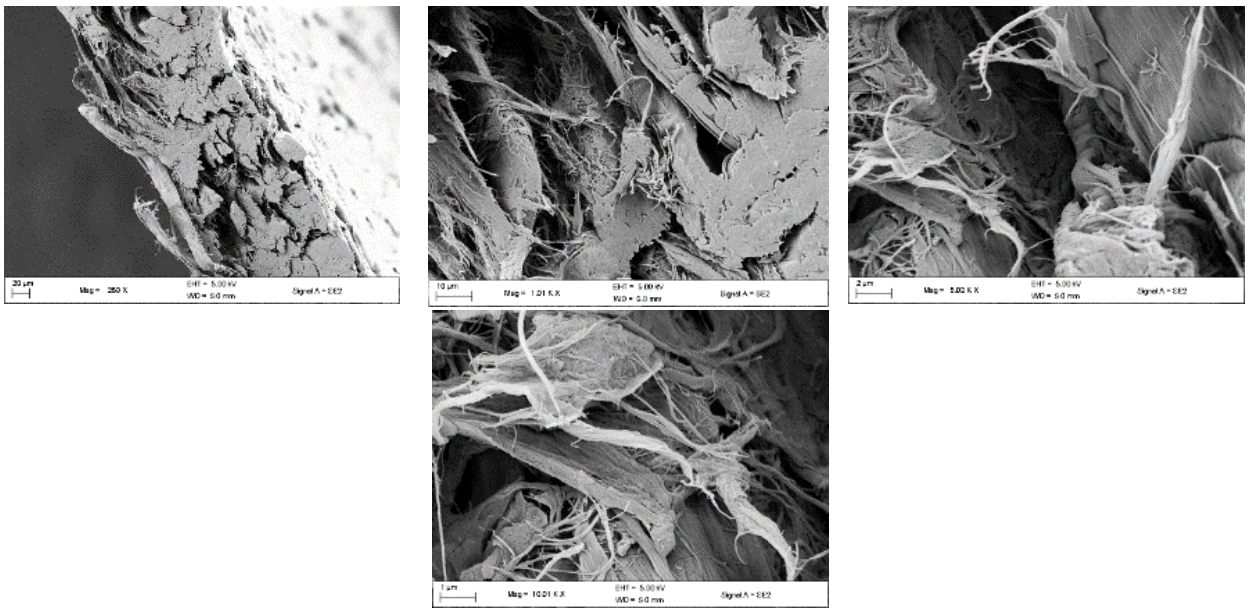

Figure B.30: FEG-SEM images of 20% NFC CHR3 sheet showing cross-sectional images at various magnifications.

B 3.4.2 50% NFC

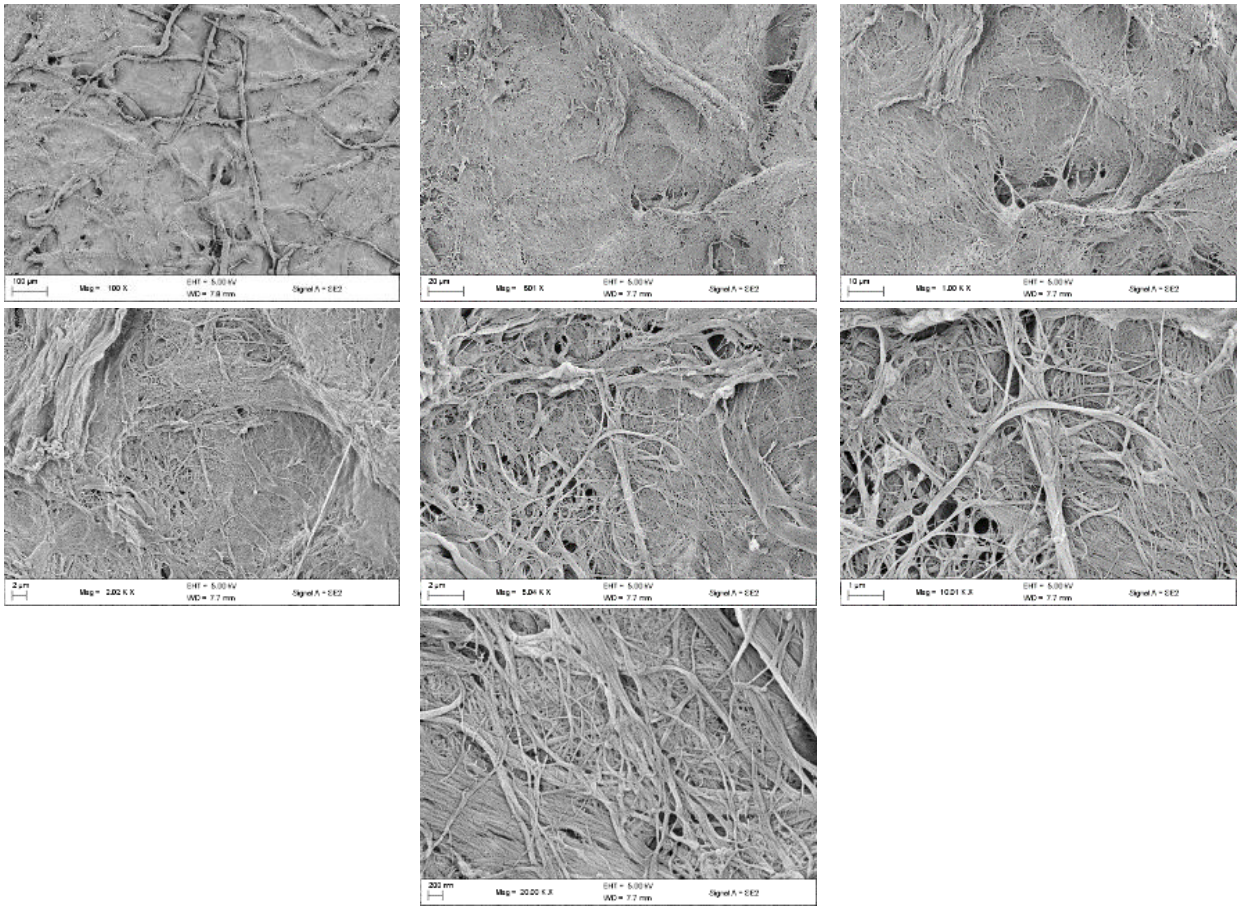

Figure B.31: FEG-SEM images of 50% NFC CHR3 sheet showing surface images at various magnifications.

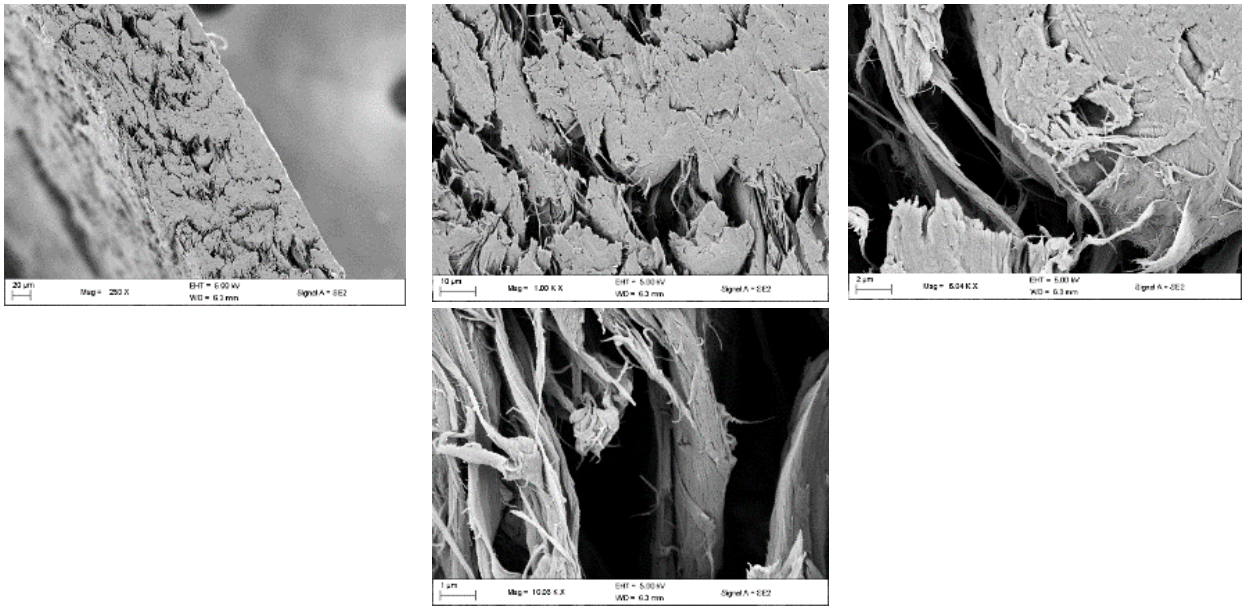

Figure B.32: FEG-SEM images of 50% NFC CHR3 sheet showing cross-sectional images at various magnifications.

B 3.4.3 100% NFC

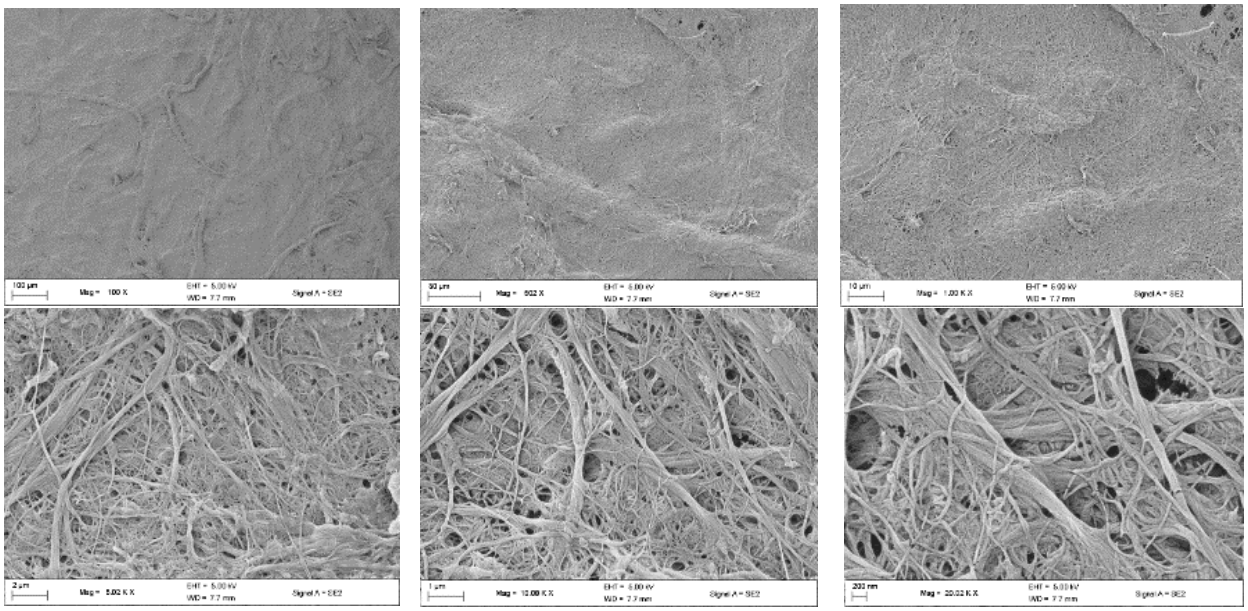

Figure B.33: FEG-SEM images of 100% NFC CHR3 sheet showing surface images at various magnifications.

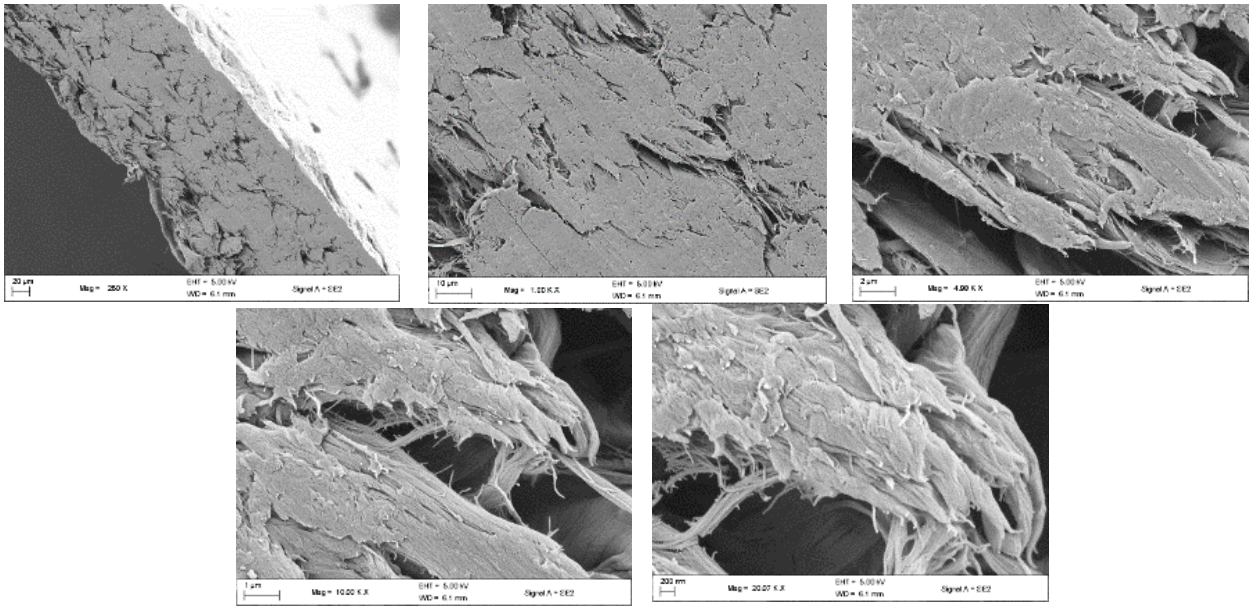

Figure B.34: FEG-SEM images of 100% NFC CHR3 sheet showing cross-sectional images at various magnifications.

B 3.5 Recycled

B 3.5.1 20% NFC

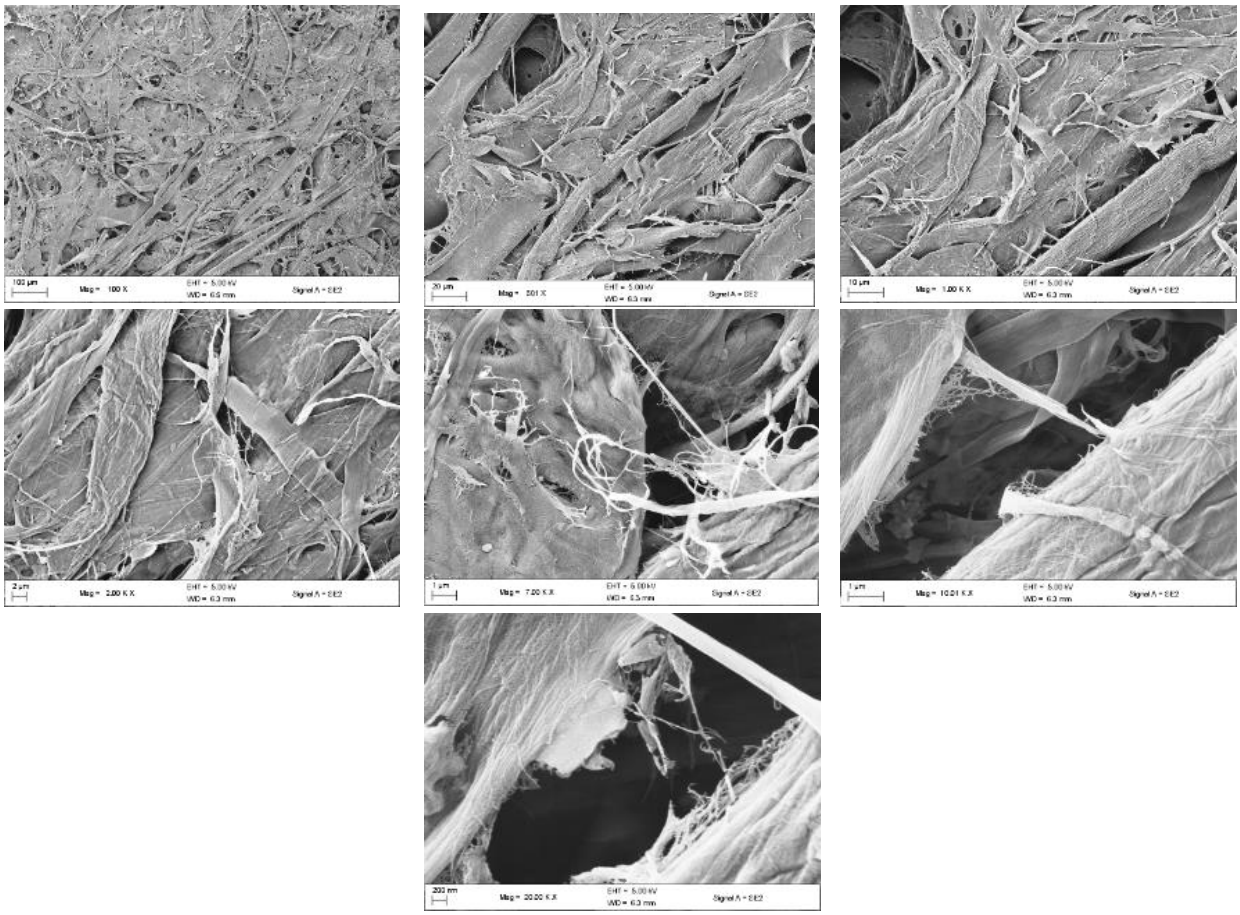

Figure B.35: FEG-SEM images of 20% NFC REC sheet showing surface images at various magnifications.

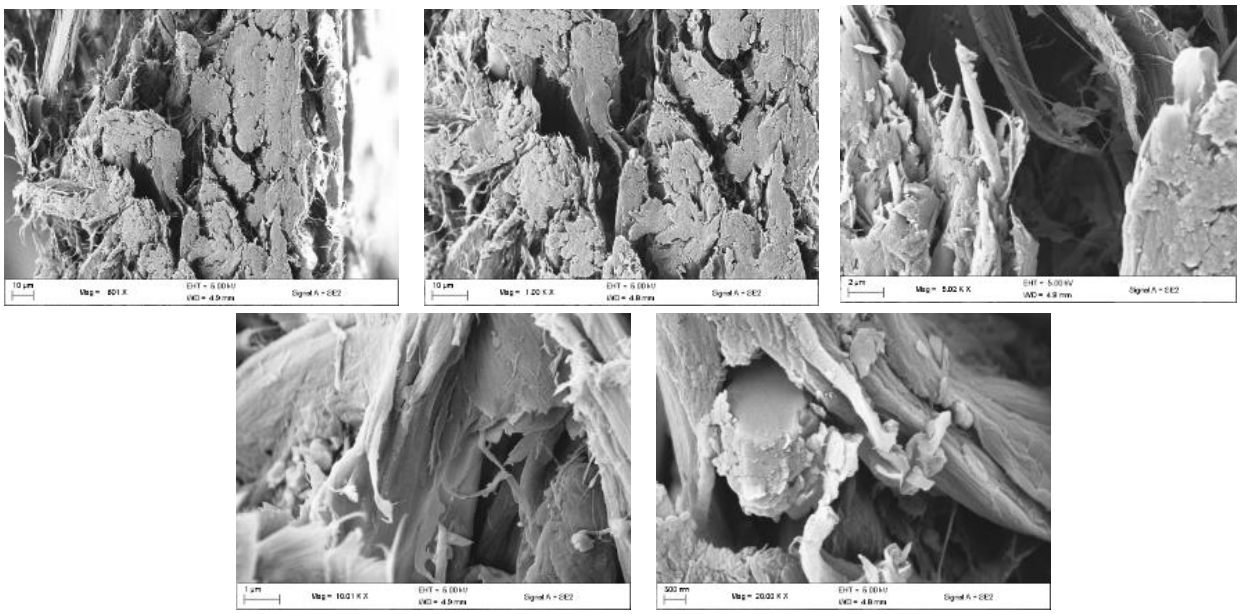

Figure B.36: FEG-SEM images of 20% NFC REC sheet showing cross-sectional images at various magnifications.

B 3.5.2 50% NFC

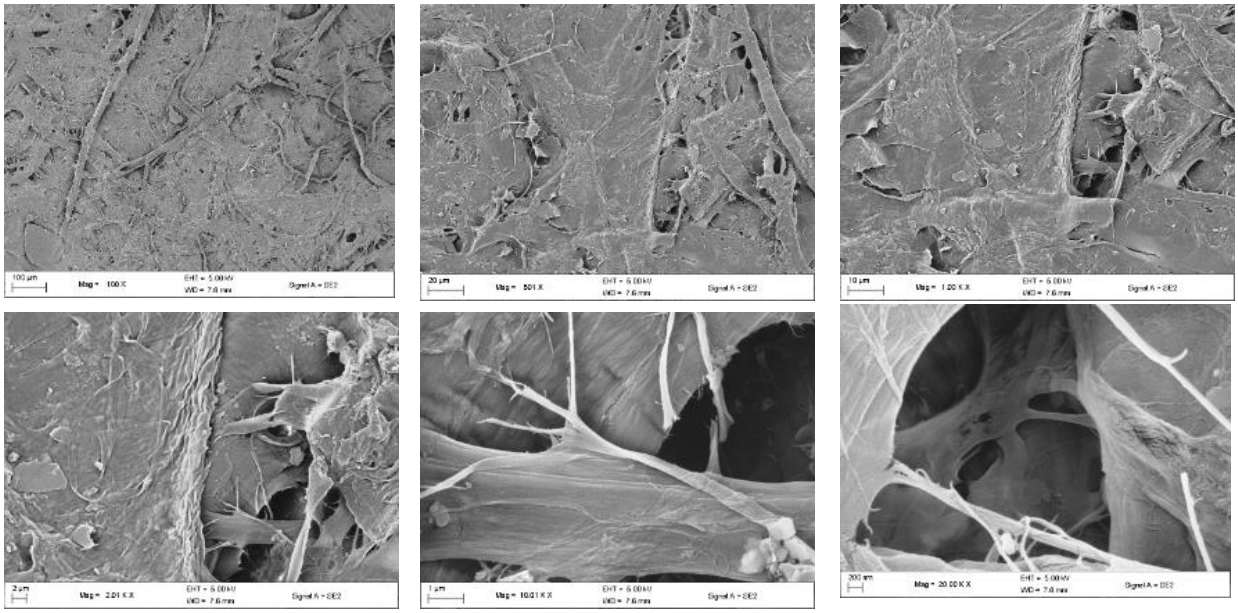

Figure B.37: FEG-SEM images of 50% NFC REC sheet showing surface images at various magnifications.

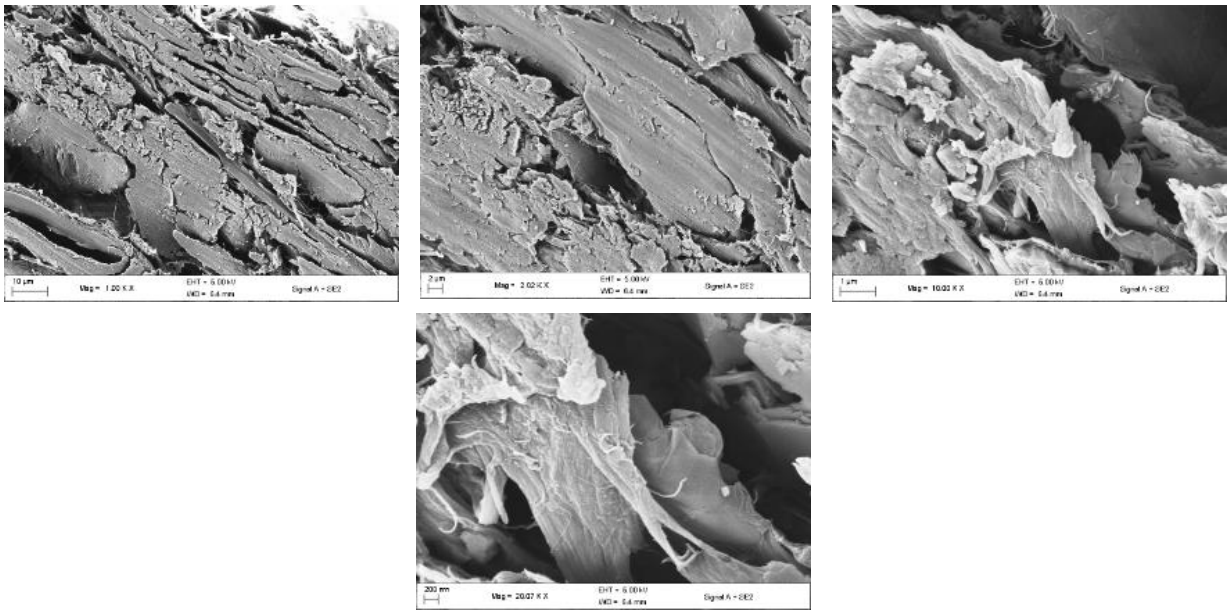

Figure B.38: FEG-SEM images of 50% NFC REC sheet showing cross-sectional images at various magnifications.

B 3.5.3 100% NFC

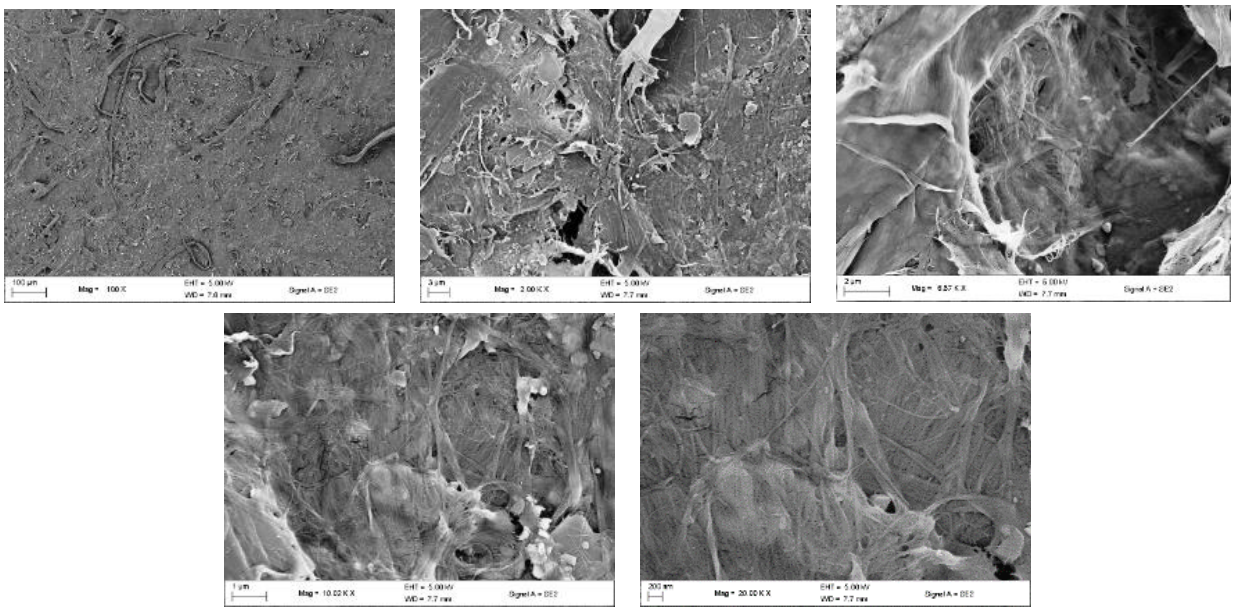

Figure B.39: FEG-SEM images of 100% NFC REC sheet showing surface images at various magnifications.

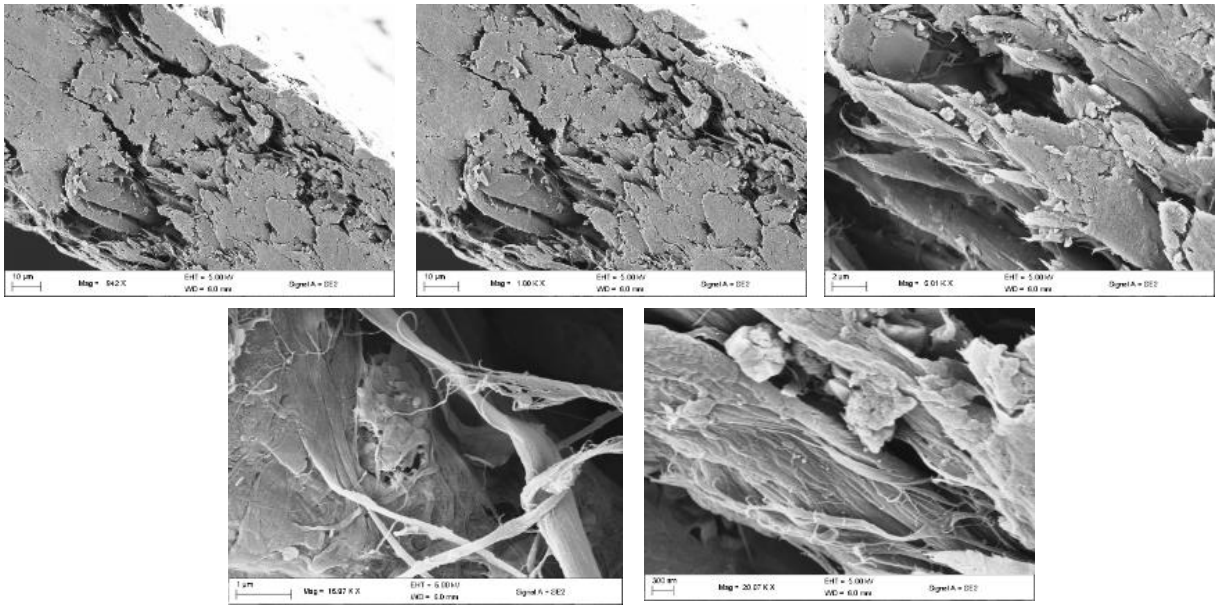

Figure B.40: FEG-SEM images of 100% NFC REC sheet showing cross-sectional images at various magnifications.

B.4 Conclusion

This Appendix gives the micrographs obtained from the FEG-SEM experiments conducted in this study. The images aim to give additional information to the reader on morphology of the sheet, as well as a view of the individual fibre structures, which could be used as a basis for future and expansion of data in this field.

APPENDIX C: SOLID WAX PRINTING

C.1 Introduction

This appendix serves a supporting function to the solid wax printing results from Chapter 7. The appendix contains images of the base substrate sheets after wax printing using a line width of 0.4 mm, with the front and back of the sheet being shown to observe the penetration of wax through the sheet. The results stated in this appendix can be correlated with the results presented in Chapter 7. Which presented the penetration ability of each sheet.

The appendix is broken down into one section, whereby the images for SULP, BK, UBK, CHR, CHR3, TMP and REC are displayed.

C.2 Wax printing images

Figure C.1 shows the solid wax printing results for the SULP substrate. Here, it can be seen that the wax had penetrated through the sheet, however can be observed to have a lighter wax line on the back of the sheet, indicating that the wax had not fully penetrated through the depth of the sheet.

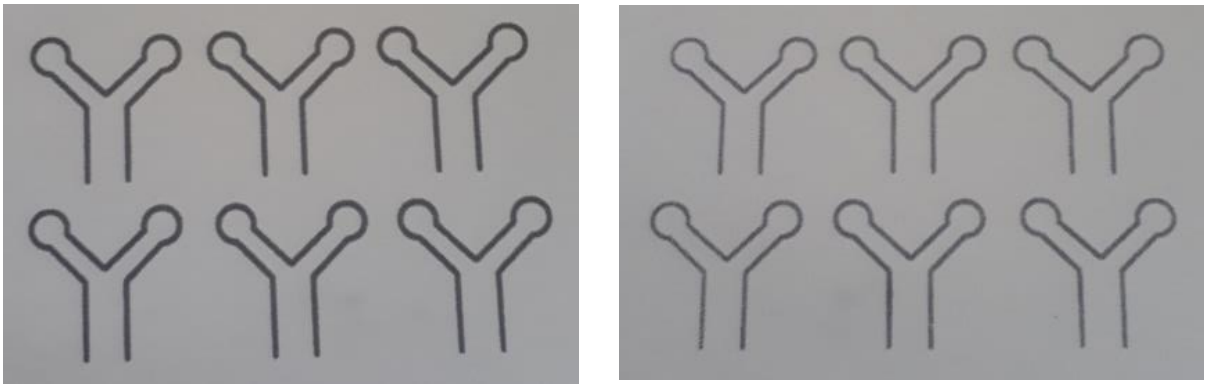

Figure C.1: SULP sheet images with solid wax printing showing the front (left) and back (right) of the sheet.

The UBK substrate, shown in Figure C.2, can be seen to have a significantly lighter wax line on the back of the sheet. This implied that the wax did not penetrate effectively through the sheet, in comparison to the SULP sheet.

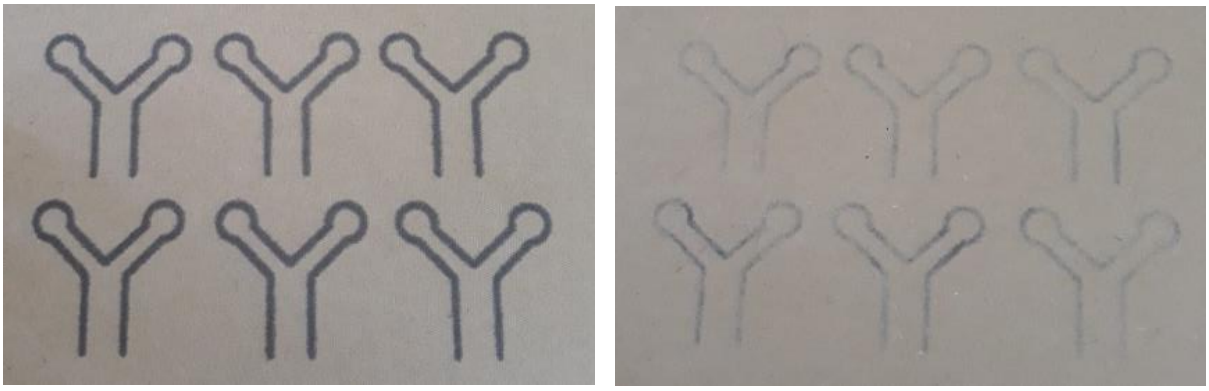

Figure C.2: UBK sheet images with solid wax printing showing the front (left) and back (right) of the sheet.

Figure C.3 showed a similar result to that of the SULP sheet, whereby it can be seen that the wax penetrated through the sheet, however not fully, due to the lighter colour observed from the back of the sheet.

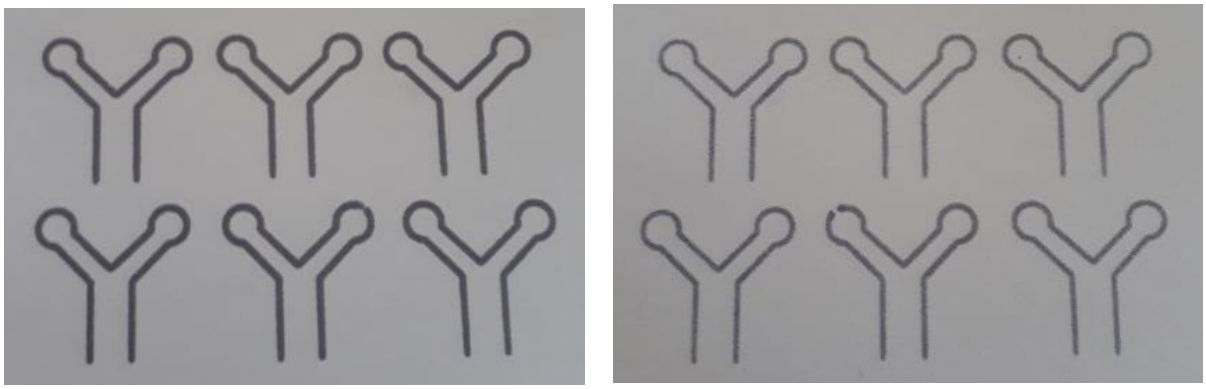

Figure C.3: BK sheet images with solid wax printing showing the front (left) and back (right) of the sheet.

Figure C.4 followed the results from the SULP and BK sheets, showing that the wax was able to penetrate through the sheet, however not through the full depth of the sheet.

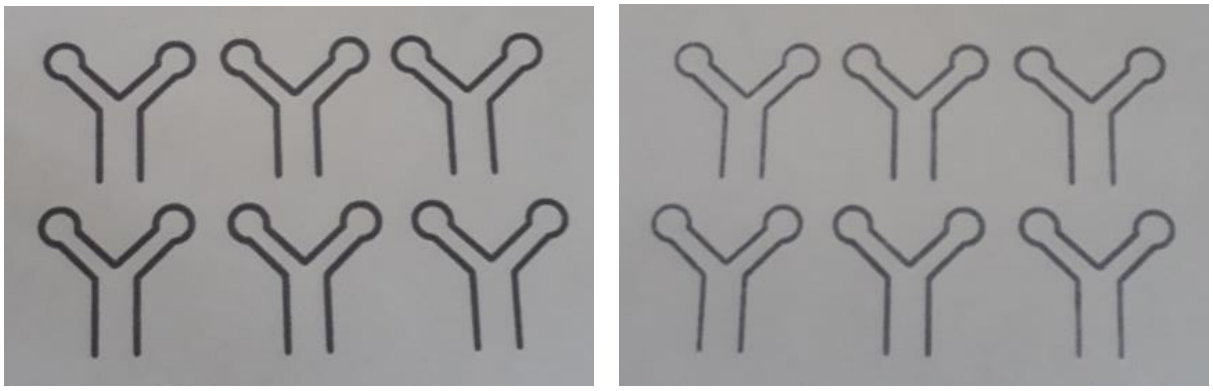

Figure C.4: CHR sheet images with solid wax printing showing the front (left) and back (right) of the sheet.

From Figure C.5, it can be observed that there was a light outline of the wax line from the back of the CHR3 sheet. Thus, it can be concluded that the wax did not penetrate well through the sheet, in comparison to the previous substrates.

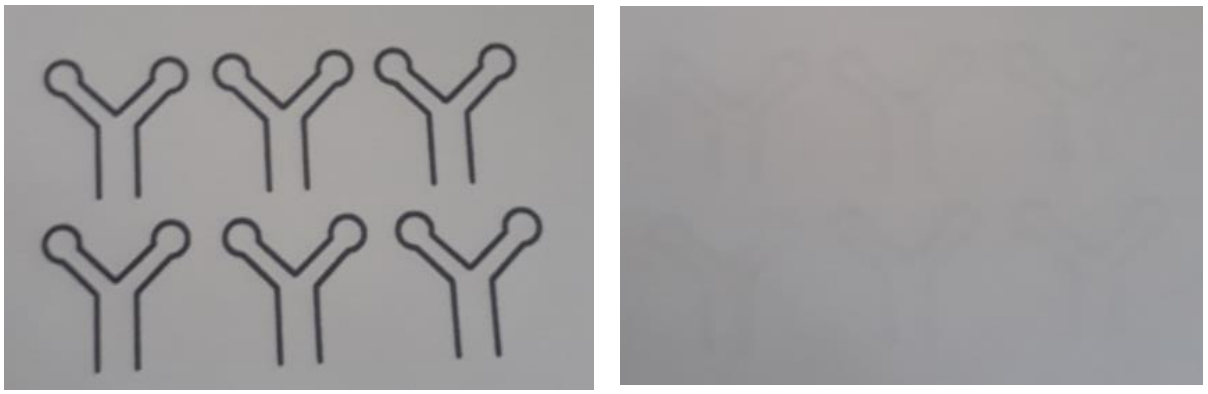

Figure C.5: CHR3 sheet images with solid wax printing showing the front (left) and back (right) of the sheet.

The TMP sheet, in Figure C.6, followed a similar wax penetration as that of the UBK sheet. It can be seen although the wax penetrates through the sheet, the image of the back of the sheet showed a faded wax line, leading to the conclusion that the wax did not penetrate fully through the sheet.

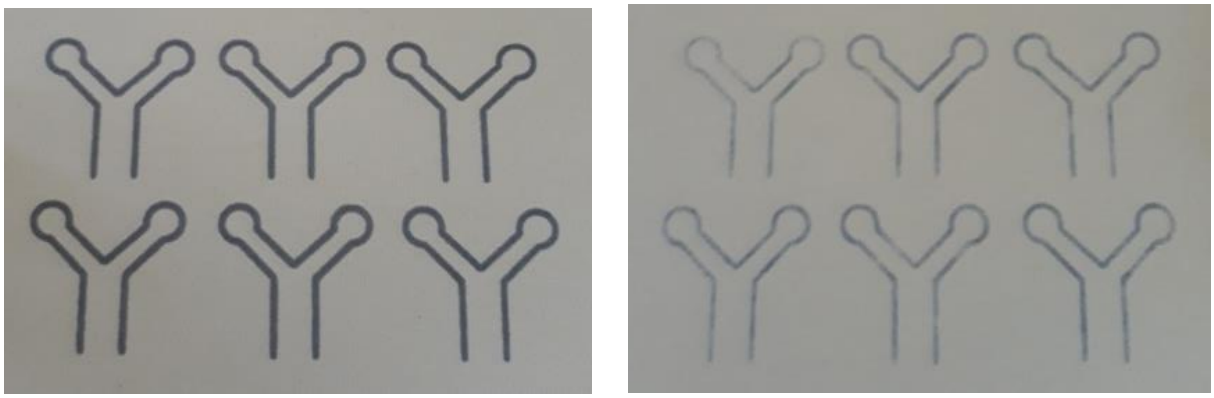

Figure C.6: TMP sheet images with solid wax printing showing the front (left) and back (right) of the sheet.

Figure C.7 showed the REC wax penetration ability. From the image, it can be seen that the wax penetrated through the sheet, however not 100%, due the lightened wax line.

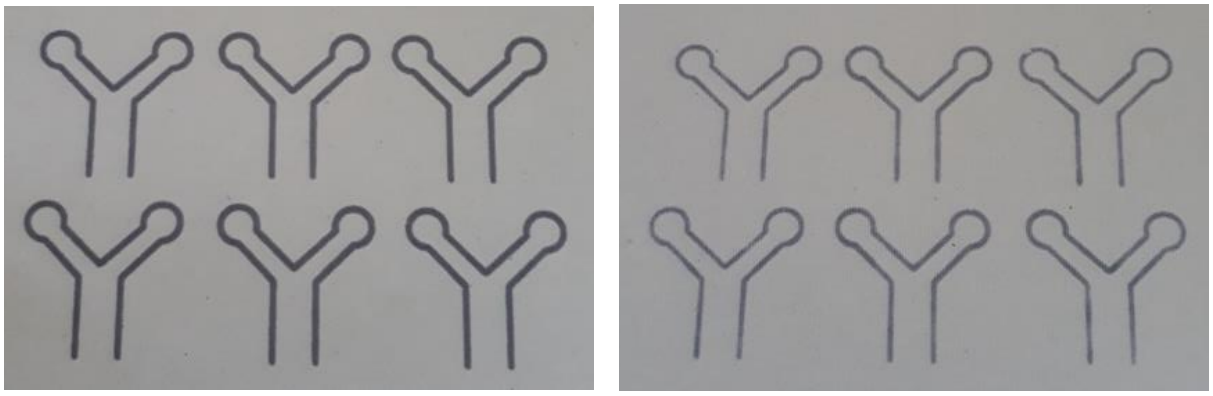

Figure C.7: REC sheet images with solid wax printing showing the front (left) and back (right) of the sheet.

C. 3 Conclusion

This appendix presents the sheets images after the solid wax printing. The images show the ability of wax to penetrate the sheet, which is an important consideration when fabricating µPADs. The lightness of the wax line on the back of the sheet was related to the penetration of wax through the sheet, which supported the results found in Chapter 7.

APPENDIX D: WICKING EXPERIMENT RAW DATA

D.1 Introduction

This appendix contains the raw data obtained from the horizontal and vertical wicking experiments conducted for this study. Three runs were conducted for each of the experiments, where averages were used for graphical purposes in Chapter 6. In addition, the standard deviation was calculated, which was discussed in Chapter 6, together with the wicking results.

The appendix is divided into base substrates and NFC substrates, which is further split into horizontal and vertical wicking data, according to the wicking liquid used, i.e. dye or blood simulant.

D.2 Base substrates

D 2.1 Horizontal

D 2.1.1 Whatman Glass Fibre Filters GF/D

Table D.1 showing the raw data for GM substrate for horizontal wicking using dye as a wicking liquid.

Distance (cm)	Time (s) Run 1	Run 2	Run 3	Average (s)	Standard deviation (s)
0	0	0	0	0	0
1	5	4	4	4	1
2	11	10	9	10	1
3	19	18	17	18	1
4	33	31	30	31	2
5	48	44	46	46	2
6	66	62	63	64	2
7	89	87	90	89	2
8	113	110	112	112	2
9	132	128	130	130	2
10	162	155	159	159	4

Table D.2 showing the raw data for GM substrate for horizontal wicking using blood simulant as a wicking liquid.

Distance (cm)	Time (s) Run 1	Run 2	Run 3	Average (s)	Standard deviation (s)
0	0	0	0	0	0
1	24	28	28	27	2
2	85	97	95	92	6
3	174	186	183	181	6
4	336	358	350	348	11
5	513	524	518	518	6
6	769	783	772	775	7
7	1082	1128	1125	1112	26
8	1518	1597	1562	1559	40
9	2137	2164	2151	2151	14
10	2792	2831	2803	2809	20

D 2.1.2 Sulphite

Table D.3 showing the raw data for SULP substrate for horizontal wicking using dye as a wicking liquid.

Distance (cm)	Time (s) Run 1	Run 2	Run 3	Average (s)	Standard deviation (s)
0	0	0	0	0	0
1	10	10	11	10	1
2	32	36	33	34	2
3	75	81	76	77	3
4	123	126	123	124	2
5	194	196	191	194	3
6	286	283	280	283	3
7	369	370	369	369	1
8	483	482	482	482	1
9	616	609	608	611	4

10	776	772	779	776	4

Table D.4 showing the raw data for SULP substrate for horizontal wicking using blood simulant as a wicking liquid.

Distance (cm)	Time (s) Run 1	Run 2	Run 3	Average (s)	Standard deviation (s)
0	0	0	0	0	0
1	94	100	98	97	3
2	289	294	290	291	3
3	632	645	634	637	7
4	1127	1146	1136	1136	10
5	1816	1885	1825	1842	38
6	3131	3180	3149	3153	25
7	5465	5473	5468	5469	4
8	9113	9142	9121	9125	15
9	15538	15607	15553	15566	36
10	22633	22711	22655	22666	40

D 2.1.3 Bleached Kraft

Table D.5 showing the raw data for BK substrate for horizontal wicking using dye as a wicking liquid.

Distance (cm)	Time (s) Run 1	Run 2	Run 3	Average (s)	Standard deviation (s)
0	0	0	0	0	0
1	11	13	14	13	2
2	40	40	43	41	2
3	87	89	91	89	2
4	159	150	156	155	5
5	232	233	235	233	2
6	332	336	331	333	3
7	463	460	459	461	2

8	591	587	589	589	2
9	736	731	731	733	3
10	944	946	941	944	3

Table D.6 showing the raw data for BK substrate for horizontal wicking using blood simulant as a wicking liquid.

Distance (cm)	Time (s) Run 1	Run 2	Run 3	Average (s)	Standard deviation (s)
0	0	0	0	0	0
1	169	170	171	170	1
2	494	507	510	504	9
3	1137	1148	1145	1143	6
4	2374	2390	2384	2383	8
5	4777	4785	4781	4781	4
6	8876	8888	8812	8859	41
7	14544	14623	14613	14593	43
8	22803	22856	22895	22851	46

D 2.1.4 Unbleached Kraft

Table D.7 showing the raw data for UBK substrate for horizontal wicking using dye as a wicking liquid.

Distance (cm)	Time (s) Run 1	Run 2	Run 3	Average (s)	Standard deviation (s)
0	0	0	0	0	0
1	13	14	14	14	1
2	35	36	38	36	2
3	78	81	80	80	2
4	125	127	129	127	1
5	184	190	191	188	4
6	261	283	276	273	11
7	402	404	399	402	3

8	555	553	558	555	3
9	752	750	769	757	10
10	993	997	996	995	2

Table D.8 showing the raw data for UBK substrate for horizontal wicking using blood simulant as a wicking liquid.

Distance (cm)	Time (s) Run 1	Run 2	Run 3	Average (s)	Standard deviation (s)
0	0	0	0	0	0
1	190	198	215	201	13
2	671	673	689	678	10
3	1390	1384	1400	1391	8
4	2345	2302	2349	2332	26
5	3534	3491	3513	3513	22
6	4924	4954	4988	4955	32
7	6840	6769	6814	6808	36
8	9243	9261	9292	9265	25
9	11870	11811	11854	11845	31
10	15001	14957	14923	14960	39

D 2.1.5 Chromatography No.1 Filter Paper

Table D.9 showing the raw data for CHR substrate for horizontal wicking using dye as a wicking liquid.

Distance (cm)	Time (s) Run 1	Run 2	Run 3	Average (s)	Standard deviation (s)
0	0	0	0	0	0
1	26	29	28	28	2
2	96	108	94	99	8
3	172	198	180	183	13
4	275	265	269	270	5

5	408	403	418	410	8
6	568	579	552	566	14
7	774	775	772	774	2
8	986	998	1013	999	14
9	1239	1256	1217	1237	20
10	1528	1543	1538	1536	8

Table D.10 showing the raw data for CHR substrate for horizontal wicking using blood simulant as a wicking liquid.

Distance (cm)	Time (s) Run 1	Run 2	Run 3	Average (s)	Standard deviation (s)
0	0	0	0	0	0
1	618	610	615	614	4
2	2500	2442	2461	2468	30
3	5479	5361	5390	5410	61
4	11260	11216	11248	11241	23
5	19736	19654	19703	19698	41

D 2.1.6 Chromatography 3MM Filter Paper

Table D.11 showing the raw data for CHR3 substrate for horizontal wicking using dye as a wicking liquid.

Distance (cm)	Time (s) Run 1	Run 2	Run 3	Average (s)	Standard deviation (s)
0	0	0	0	0	0
1	26	29	28	28	2
2	96	107	103	102	6
3	172	182	180	178	5
4	275	284	269	276	8
5	408	403	398	403	5
6	578	579	562	573	10

7	774	781	772	776	5
8	986	1006	1013	1002	14
9	1239	1254	1217	1237	19
10	1528	1555	1538	1540	14

Table D.12 showing the raw data for CHR3 substrate for horizontal wicking using blood simulant as a wicking liquid.

Distance (cm)	Time (s) Run 1	Run 2	Run 3	Average (s)	Standard deviation (s)
0	0	0	0	0	0
1	243	243	244	243	1
2	724	743	734	734	10
3	1550	1532	1556	1546	12
4	3014	3062	3045	3040	24
5	5002	5022	5022	5015	12
6	7354	7429	7382	7388	38
7	10467	10438	10443	10449	16
8	13716	13777	13758	13750	31
9	17666	17711	17695	17691	23
10	21854	21949	21941	21915	53

D 2.1.7 Thermo-mechanical

Table D.13 showing the raw data for TMP substrate for horizontal wicking using dye as a wicking liquid.

Distance (cm)	Time (s) Run 1	Run 2	Run 3	Average (s)	Standard deviation (s)
0	0	0	0	0	0
1	93	104	99	99	6
2	400	395	387	394	7
3	872	869	868	870	2

4	1624	1638	1640	1634	9
5	2820	2838	2831	2830	9
6	4683	4671	4740	4698	37
7	7916	7902	7978	7932	40

Table D.14 showing the raw data for TMP substrate for horizontal wicking using blood simulant as a wicking liquid.

Distance (cm)	Time (s) Run 1	Run 2	Run 3	Average (s)	Standard deviation (s)
0	0	0	0	0	0
1	2792	2815	2812	2806	13
2	10040	10009	10064	10038	28
3	24015	23988	24047	24017	30

D 2.1.8 Recycled

Table D.15 showing the raw data for REC substrate for horizontal wicking using dye as a wicking liquid.

Distance (cm)	Time (s) Run 1	Run 2	Run 3	Average (s)	Standard deviation (s)
0	0	0	0	0	0
1	547	539	547	544	5
2	1514	1449	1492	1485	33
3	3374	3263	3363	3333	61
4	6123	6069	5989	6060	67

Table D.16 showing the raw data for TMP substrate for horizontal wicking using blood simulant as a wicking liquid.

Distance (cm)	Time (s) Run 1	Run 2	Run 3	Average (s)	Standard deviation (s)
0	0	0	0	0	0
1	5051	5002	5124	5059	61
2	11212	11334	11271	11272	61

D 2.2 Vertical

D 2.2.1 Whatman Glass Fibre Filters GF/D

Table D.17 showing the raw data for GM substrate for vertical wicking using dye as a wicking liquid.

Distance (cm)	Time (s) Run 1	Run 2	Run 3	Average (s)	Standard deviation (s)
0	0	0	0	0	0
1	3	3	3	3	0
2	9	9	10	9	1
3	18	18	18	18	0
4	29	31	29	30	1
5	44	46	46	45	1
6	61	66	65	64	3
7	85	88	90	88	3
8	115	112	118	115	3
9	147	145	148	147	2
10	181	177	182	180	3

Table D.18 showing the raw data for GM substrate for vertical wicking using blood simulant as a wicking liquid.

Distance (cm)	Time (s) Run 1	Run 2	Run 3	Average (s)	Standard deviation (s)
0	0	0	0	0	0
1	27	28	28	28	1
2	84	85	82	84	2
3	179	181	176	179	3
4	285	297	280	287	9
5	452	459	446	452	7
6	651	660	649	653	6
7	927	946	931	935	10
8	1261	1272	1262	1265	6
9	1535	1601	1579	1572	34
10	1924	1928	1918	1923	5

D 2.2.2 Sulphite

Table D.19 showing the raw data for SULP substrate for vertical wicking using dye as a wicking liquid.

Distance (cm)	Time (s) Run 1	Run 2	Run 3	Average (s)	Standard deviation (s)
0	0	0	0	0	0
1	12	12	14	13	1
2	30	38	35	34	4
3	62	77	73	71	8
4	109	132	139	127	16
5	169	201	206	192	20
6	245	275	271	264	16
7	328	371	368	356	24
8	457	538	490	495	41
9	586	613	616	605	17

10	750	743	748	747	4

Table D.20 showing the raw data for SULP substrate for vertical wicking using blood simulant as a wicking liquid.

Distance (cm)	Time (s) Run 1	Run 2	Run 3	Average (s)	Standard deviation (s)
0	0	0	0	0	0
1	109	111	109	110	1
2	337	351	340	343	7
3	707	735	702	715	18
4	1214	1255	1216	1228	23
5	1771	1804	1789	1788	17
6	2789	2811	2803	2801	11
7	3601	3672	3624	3632	36
8	4812	4844	4832	4829	16
9	6307	6359	6319	6328	27
10	8285	8342	8317	8315	29

D 2.2.3 Bleached Kraft

Table D.21 showing the raw data for BK substrate for vertical wicking using dye as a wicking liquid.

Distance (cm)	Time (s) Run 1	Run 2	Run 3	Average (s)	Standard deviation (s)
0	0	0	0	0	0
1	16	12	15	14	2
2	50	43	41	45	5
3	111	86	87	95	14
4	207	189	188	195	11
5	327	311	320	319	8
6	459	426	431	439	18

7	609	574	598	594	18
8	806	776	785	789	15
9	989	953	967	970	18
10	1238	1200	1204	1214	21

Table D.22 showing the raw data for BK substrate for vertical wicking using blood simulant as a wicking liquid.

Distance (cm)	Time (s) Run 1	Run 2	Run 3	Average (s)	Standard deviation (s)
0	0	0	0	0	0
1	130	128	131	130	2
2	397	408	405	403	6
3	861	887	852	867	18
4	1426	1442	1449	1439	12
5	2272	2246	2317	2278	36
6	3170	3159	3228	3186	37
7	3833	3887	3875	3865	28
8	5509	5591	5563	5554	42

D 2.2.4 Unbleached Kraft

Table D.23 showing the raw data for UBK substrate for vertical wicking using dye as a wicking liquid.

Distance (cm)	Time (s) Run 1	Run 2	Run 3	Average (s)	Standard deviation (s)
0	0	0	0	0	0
1	9	12	12	11	2
2	29	34	36	33	4
3	72	70	78	73	4
4	126	125	131	127	3
5	191	194	205	197	7
6	263	268	280	270	9

7	359	356	363	359	4
8	474	480	484	479	5
9	609	614	621	615	6
10	730	768	774	757	24

Table D.24 showing the raw data for UBK substrate for vertical wicking using blood simulant as a wicking liquid.

Distance (cm)	Time (s) Run 1	Run 2	Run 3	Average (s)	Standard deviation (s)
0	0	0	0	0	0
1	173	179	171	174	4
2	537	559	546	547	11
3	913	935	915	921	12
4	1682	1697	1709	1696	14
5	2527	2522	2551	2533	16
6	3835	3861	3894	3863	30
7	5132	5158	5168	5153	19
8	6902	6942	6935	6926	21
9	8809	8795	8876	8827	43
10	11626	11655	11700	11660	37

D 2.2.5 Chromatography No.1 Filter Paper

Table D.25 showing the raw data for CHR substrate for horizontal wicking using dye as a wicking liquid.

Distance (cm)	Time (s) Run 1	Run 2	Run 3	Average (s)	Standard deviation (s)
0	0	0	0	0	0
1	60	58	61	60	2
2	209	195	215	206	10
3	434	422	437	431	8

4	661	645	674	660	15
5	1154	1177	1198	1176	22
6	1799	1752	1816	1789	33
7	2488	2413	2500	2467	47
8	4179	4144	4221	4181	39
9	7081	7136	7147	7121	35

Table D.26 showing the raw data for CHR substrate for vertical wicking using blood simulant as a wicking liquid.

Distance (cm)	Time (s) Run 1	Run 2	Run 3	Average (s)	Standard deviation (s)
0	0	0	0	0	0
1	321	348	336	335	14
2	1088	1133	1098	1106	24
3	1996	2031	1993	2007	21
4	3786	3815	3807	3803	15
5	5596	5556	5564	5572	21
6	8247	8321	8274	8281	37
7	11686	11792	11692	11723	60
8	15888	15855	15841	15861	24
9	21090	21127	21012	21076	59

D 2.2.6 Chromatography 3MM Filter Paper

Table D.27 showing the raw data for CHR3 substrate for horizontal wicking using dye as a wicking liquid.

Distance (cm)	Time (s) Run 1	Run 2	Run 3	Average (s)	Standard deviation (s)
0	0	0	0	0	0
1	19	19	19	19	0
2	70	67	68	68	2

3	158	133	138	143	13
4	266	255	257	259	6
5	395	388	388	390	4
6	553	539	558	550	10
7	747	711	713	724	20
8	875	859	895	876	18
9	1115	1078	1100	1098	19
10	1360	1340	1355	1352	10

Table D.28 showing the raw data for CHR3 substrate for vertical wicking using blood simulant as a wicking liquid.

Distance (cm)	Time (s)			Average (s)	Standard deviation (s)
	Run 1	Run 2	Run 3		
0	0	0	0	0	0
1	228	240	237	235	6
2	775	793	786	785	9
3	1695	1736	1732	1721	23
4	2879	2903	2882	2888	13
5	4616	4637	4623	4625	11
6	6482	6547	6539	6523	35
7	8596	8647	8625	8623	26
8	11173	11227	11194	11198	27
9	14143	14175	14123	14147	26
10	17665	17704	17700	17690	21

D 2.2.7 Thermo-mechanical

Table D.29 showing the raw data for TMP substrate for vertical wicking using dye as a wicking liquid.

Distance (cm)	Time (s) Run 1	Run 2	Run 3	Average (s)	Standard deviation (s)
0	0	0	0	0	0
1	206	211	232	216	14
2	652	689	700	680	25
3	1238	1277	1294	1270	29
4	2270	2311	2345	2309	38
5	4867	4889	4915	4890	24
6	7498	7510	7600	7536	56

Table D.30 showing the raw data for TMP substrate for vertical wicking using blood simulant as a wicking liquid.

Distance (cm)	Time (s) Run 1	Run 2	Run 3	Average (s)	Standard deviation (s)
0	0	0	0	0	0
1	2195	2187	2182	2188	7
2	6338	6328	6314	6327	12
3	12665	12627	12608	12633	29
4	18521	18613	18536	18557	49
5	27094	27110	27187	27130	50

D 2.2.8 Recycled

Table D.31 showing the raw data for REC substrate for vertical wicking using dye as a wicking liquid.

Distance (cm)	Time (s) Run 1	Run 2	Run 3	Average (s)	Standard deviation (s)
0	0	0	0	0	0
1	533	555	567	552	17
2	1713	1724	1753	1730	21
3	5272	5346	5275	5298	42
4	0	0	0	0	0

Table D.32 showing the raw data for REC substrate for vertical wicking using blood simulant as a wicking liquid.

Distance (cm)	Time (s) Run 1	Run 2	Run 3	Average (s)	Standard deviation (s)
0	0		0	0	0
1	4642	4656	4691	4663	25
2	12491	12535	12561	12529	35
3	21491	21546	21560	21532	36

D. 3 NFC Substrates

D 3.1 Horizontal

D 3.1.1 Sulphite

Table D.33 showing the raw data for 20% NFC SULP substrate for horizontal wicking using dye as a wicking liquid.

Distance (cm)	Time (s) Run 1	Run 2	Run 3	Average (s)	Standard deviation (s)
0	0	0	0	0	0
1	42	38	40	40	2
2	92	96	95	94	2
3	173	213	189	192	20
4	300	316	320	312	11
5	444	466	459	456	11
6	647	654	658	653	6
7	925	940	951	939	13
8	1329	1219	1204	1251	68
9	1832	1595	1623	1683	130
10	2554	2066	2115	2245	269

Table D.34 showing the raw data for 20% NFC SULP substrate for horizontal wicking using blood simulant as a wicking liquid.

Distance (cm)	Time (s) Run 1	Run 2	Run 3	Average (s)	Standard deviation (s)
0	0	0	0	0	0
1	89	91	88	89	2
2	767	745	764	759	12
3	2673	2734	2716	2708	31
4	5126	4989	5047	5054	69
5	8109	8006	8110	8075	60

6	11377	11023	11254	11218	180
7	14885	14634	14744	14754	126
8	17984	17806	17855	17882	92

Table D.35 showing the raw data for 50% NFC SULP substrate for horizontal wicking using dye as a wicking liquid.

Distance (cm)	Time (s) Run 1	Run 2	Run 3	Average (s)	Standard deviation (s)
0	0	0	0	0	0
1	155	160	149	155	6
2	380	396	385	387	8
3	735	749	726	737	12
4	1422	1464	1403	1430	31
5	2723	2793	2701	2739	48
6	8901	9002	8894	8932	60

Table D.36 showing the raw data for 50% NFC SULP substrate for horizontal wicking using blood simulant as a wicking liquid.

Distance (cm)	Time (s) Run 1	Run 2	Run 3	Average (s)	Standard deviation (s)
0	0	0	0	0	0
1	2061	1844	1987	1964	110
2	6002	5622	5666	5763	208
3	12840	12741	12964	12848	112
4	21656	21496	21963	21705	237

Table D.37 showing the raw data for 100% NFC SULP substrate for horizontal wicking using dye as a wicking liquid.

Distance (cm)	Time (s) Run 1	Run 2	Run 3	Average (s)	Standard deviation (s)
0	0	0	0	0	0
1	1863	1761	1823	1816	51
2	5994	5789	5947	5910	107

Table D.38 showing the raw data for 100% NFC SULP substrate for horizontal wicking using blood simulant as a wicking liquid.

Distance (cm)	Time (s) Run 1	Run 2	Run 3	Average (s)	Standard deviation (s)
0	0	0	0	0	0
1	16638	16716	16658	16671	41

D 3.1.2 Unbleached Kraft

Table D.39 showing the raw data for 20% NFC UBK substrate for horizontal wicking using dye as a wicking liquid.

Distance (cm)	Time (s) Run 1	Run 2	Run 3	Average (s)	Standard deviation (s)
0	0	0	0	0	0
1	126	130	134	130	4
2	326	329	339	331	7
3	675	689	697	687	11
4	1172	1197	1205	1191	17
5	1823	1867	1886	1859	32
6	2646	2794	2874	2771	116
7	3432	3569	3571	3524	80
8	5118	5247	5311	5225	98

9	7117	7498	7487	7367	217
10	10080	10312	10225	10206	117

Table D.40 showing the raw data for 20% NFC UBK substrate for horizontal wicking using blood simulant as a wicking liquid.

Distance (cm)	Time (s) Run 1	Run 2	Run 3	Average (s)	Standard deviation (s)
0	0	0	0	0	0
1	832	846	844	841	8
2	2458	2567	2569	2531	64
3	6004	5874	5935	5938	65
4	9896	10002	9990	9963	58
5	14670	14525	14593	14596	73

Table D.41 showing the raw data for 50% NFC UBK substrate for horizontal wicking using dye as a wicking liquid.

Distance (cm)	Time (s) Run 1	Run 2	Run 3	Average (s)	Standard deviation (s)
0	0	0	0	0	0
1	883	803	864	850	42
2	2194	2054	2103	2117	71
3	5529	5468	5497	5498	31

Table D.42 showing the raw data for 50% NFC UBK substrate for horizontal wicking using blood simulant as a wicking liquid.

Distance (cm)	Time (s) Run 1	Run 2	Run 3	Average (s)	Standard deviation (s)
0	0	0	0	0	0
1	5493	5502	5107	5367	226
2	15734	15489	16255	15826	391

Table D.43 showing the raw data for 100% NFC UBK substrate for horizontal wicking using dye as a wicking liquid.

Distance (cm)	Time (s) Run 1	Run 2	Run 3	Average (s)	Standard deviation (s)
0	0	0	0	0	0
1	65461	65168	65615	65415	227

Table D.44 showing the raw data for 100% NFC UBK substrate for horizontal wicking using blood simulant as a wicking liquid.

Distance (cm)	Time (s) Run 1	Run 2	Run 3	Average (s)	Standard deviation (s)
0	0	0	0	0	0
1	164027	164061	164195	164094	89

D 3.1.3 Chromatography No.1 Filter Paper

Table D.45 showing the raw data for 20% NFC CHR substrate for horizontal wicking using dye as a wicking liquid.

Distance (cm)	Time (s) Run 1	Run 2	Run 3	Average (s)	Standard deviation (s)
0	0	0	0	0	0
1	92	100	95	96	4
2	269	193	210	224	40
3	493	383	419	432	56
4	760	652	709	707	54
5	1008	946	966	973	32
6	1535	1492	1530	1519	24
7	2251	1971	2246	2156	160
8	3761	3858	3655	3758	102
9	0	0	0	0	0
10	92	100	95	96	4

Table D.46 showing the raw data for 20% NFC CHR substrate for horizontal wicking using blood simulant as a wicking liquid.

Distance (cm)	Time (s) Run 1	Run 2	Run 3	Average (s)	Standard deviation (s)
0	0	0	0	0	0
1	541	552	536	543	8
2	2675	2703	2640	2673	32
3	6651	6549	6565	6588	55
4	10744	10552	10499	10598	129
5	15302	15208	15295	15268	52

Table D.47 showing the raw data for 50% NFC CHR substrate for horizontal wicking using dye as a wicking liquid.

Distance (cm)	Time (s) Run 1	Run 2	Run 3	Average (s)	Standard deviation (s)
0	0	0	0	0	0
1	298	340	315	318	21
2	1068	1152	1090	1103	44
3	2235	2310	2264	2270	38
4	6245	6376	6283	6301	67

Table D.48 showing the raw data for 50% NFC CHR substrate for horizontal wicking using blood simulant as a wicking liquid.

Distance (cm)	Time (s) Run 1	Run 2	Run 3	Average (s)	Standard deviation (s)
0	0	0	0	0	0
1	3420	3605	3000	3342	310
2	12692	12887	12431	12670	229
3	24362	24550	24265	24392	145

Table D.49 showing the raw data for 100% NFC CHR substrate for horizontal wicking using dye as a wicking liquid.

Distance (cm)	Time (s) Run 1	Run 2	Run 3	Average (s)	Standard deviation (s)
0	0	0	0	0	0
1	8249	8153	8178	8193	50

Table D.50 showing the raw data for 100% NFC CHR substrate for horizontal wicking using blood simulant as a wicking liquid.

Distance (cm)	Time (s) Run 1	Run 2	Run 3	Average (s)	Standard deviation (s)
0	0	0	0	0	0
1	17343	17275	17360	17326	45

D 3.1.4 Chromatography 3MM Filter Paper

Table D.51 showing the raw data for 20% NFC CHR3 substrate for horizontal wicking using dye as a wicking liquid.

Distance (cm)	Time (s) Run 1	Run 2	Run 3	Average (s)	Standard deviation (s)
0	0	0	0	0	0
1	81	95	86	87	7
2	279	227	245	250	26
3	549	435	497	494	57
4	973	734	833	847	120
5	1578	1400	1428	1469	96
6	2343	2023	2140	2169	162
7	3483	3217	3398	3366	136
8	10709	10293	10114	10372	305

Table D.52 showing the raw data for 20% NFC CHR3 substrate for horizontal wicking using blood simulant as a wicking liquid.

Distance (cm)	Time (s) Run 1	Run 2	Run 3	Average (s)	Standard deviation (s)
0	0	0	0	0	0
1	1388	1397	1406	1397	9
2	4252	4301	4296	4283	27
3	8050	8120	8093	8088	35
4	12435	12607	12598	12547	97
5	17886	17760	17796	17814	65

Table D.53 showing the raw data for 50% NFC CHR3 substrate for horizontal wicking using dye as a wicking liquid.

Distance (cm)	Time (s) Run 1	Run 2	Run 3	Average (s)	Standard deviation (s)
0	0	0	0	0	0
1	487	471	483	480	8
2	1496	1432	1452	1460	33
3	4735	4702	4699	4712	20

Table D.54 showing the raw data for 50% NFC CHR3 substrate for horizontal wicking using blood simulant as a wicking liquid.

Distance (cm)	Time (s) Run 1	Run 2	Run 3	Average (s)	Standard deviation (s)
0	0	0	0	0	0
1	5465	4897	5510	5291	342
2	15617	14654	15333	15201	495

Table D.55 showing the raw data for 100% NFC CHR3 substrate for horizontal wicking using dye as a wicking liquid.

Distance (cm)	Time (s) Run 1	Run 2	Run 3	Average (s)	Standard deviation (s)
0	0	0	0	0	0
1	1945	2055	1911	1970	75

Table D.56 showing the raw data for 100% NFC CHR3 substrate for horizontal wicking using blood simulant as a wicking liquid.

Distance (cm)	Time (s) Run 1	Run 2	Run 3	Average (s)	Standard deviation (s)
0	0	0	0	0	0
1	17127	17085	17210	17141	64

D 3.1.5 Recycled

Table D.57 showing the raw data for 20% NFC REC substrate for horizontal wicking using dye as a wicking liquid.

Distance (cm)	Time (s) Run 1	Run 2	Run 3	Average (s)	Standard deviation (s)
0	0	0	0	0	0
1	1063	989	1014	1022	38
2	1685	1560	1611	1619	63
3	2655	2894	2444	2664	225
4	3912	4052	3835	3933	110
5	6371	6987	6464	6607	332
6	11792	11007	11163	11321	416

Table D.58 showing the raw data for 20% NFC REC substrate for horizontal wicking using blood simulant as a wicking liquid.

Distance (cm)	Time (s) Run 1	Run 2	Run 3	Average (s)	Standard deviation (s)
0	0	0	0	0	0
1	3196	3221	3154	3190	34
2	8464	8553	8269	8429	145
3	15900	15822	15845	15856	40

Table D.59 showing the raw data for 50% NFC REC substrate for horizontal wicking using dye as a wicking liquid.

Distance (cm)	Time (s) Run 1	Run 2	Run 3	Average (s)	Standard deviation (s)
0	0	0	0	0	0
1	750	712	806	756	47
2	2241	2056	2296	2198	126
3	4320	4217	4364	4300	75
4	9316	9270	9409	9332	71

Table D.60 showing the raw data for 50% NFC REC substrate for horizontal wicking using blood simulant as a wicking liquid.

Distance (cm)	Time (s) Run 1	Run 2	Run 3	Average (s)	Standard deviation (s)
0	0	0	0	0	0
1	5224	4789	5398	5137	314
2	16732	15903	16544	16393	435

Table D.61 showing the raw data for 100% NFC REC substrate for horizontal wicking using dye as a wicking liquid.

Distance (cm)	Time (s) Run 1	Run 2	Run 3	Average (s)	Standard deviation (s)
0	0	0	0	0	0
1	4029	4168	4015	4071	85
2	14206	14222	14135	14188	46

Table D.62 showing the raw data for 100% NFC REC substrate for horizontal wicking using blood simulant as a wicking liquid.

Distance (cm)	Time (s) Run 1	Run 2	Run 3	Average (s)	Standard deviation (s)
0	0	0	0	0	0
1	42092	42146	42045	42094	51
2	135794	135784	135699	135759	52

D 3.2 Vertical

D 3.2.1 Sulphite

Table D.63 showing the raw data for 20% NFC SULP substrate for vertical wicking using dye as a wicking liquid.

Distance (cm)	Time (s) Run 1	Run 2	Run 3	Average (s)	Standard deviation (s)
0	0	0	0	0	0
1	33	36	35	35	2
2	72	74	72	73	1
3	171	179	176	175	4
4	337	360	359	352	13
5	500	542	512	518	22

6	712	756	726	731	22
7	960	971	972	968	7
8	1344	1397	1388	1376	28
9	1788	1806	1787	1794	11
10	2152	2232	2160	2181	44

Table D.64 showing the raw data for 20% NFC SULP substrate for vertical wicking using blood simulant as a wicking liquid.

Distance (cm)	Time (s) Run 1	Run 2	Run 3	Average (s)	Standard deviation (s)
0	0	0	0	0	0
1	198	183	207	196	12
2	650	638	669	652	16
3	1725	1705	1740	1723	18
4	3192	3130	3278	3200	74
5	5829	5815	5843	5829	14
6	8874	8895	8881	8883	11
7	11786	11806	11801	11798	10
8	15504	15415	15610	15510	98

Table D.65 showing the raw data for 50% NFC SULP substrate for vertical wicking using dye as a wicking liquid.

Distance (cm)	Time (s) Run 1	Run 2	Run 3	Average (s)	Standard deviation (s)
0	0	0	0	0	0
1	123	137	131	130	7
2	418	438	422	426	11
3	980	1013	993	995	17
4	1668	1766	1679	1704	54
5	2397	2473	2409	2426	41
6	3595	3708	3621	3641	59

7	4849	4990	4898	4912	72
8	6653	6792	6685	6710	73
9	9115	9291	9173	9193	90
10	12236	12356	12289	12294	60

Table D.66 showing the raw data for 50% NFC SULP substrate for vertical wicking using blood simulant as a wicking liquid.

Distance (cm)	Time (s) Run 1	Run 2	Run 3	Average (s)	Standard deviation (s)
0	0	0	0	0	0
1	1869	1874	1906	1883	20
2	5849	5859	5949	5886	55
3	10920	10959	11033	10971	57
4	17118	17186	17253	17186	68
5	26238	26303	26368	26303	65
6	38400	38468	38589	38486	96
7	51428	51468	51589	51495	84
8	66369	66406	66493	66423	64
9	81571	81614	81632	81606	31
10	97251	97315	97353	97306	52

Table D.67 showing the raw data for 100% NFC SULP substrate for vertical wicking using dye as a wicking liquid.

Distance (cm)	Time (s) Run 1	Run 2	Run 3	Average (s)	Standard deviation (s)
0	0	0	0	0	0
1	2378	2369	2415	2387	24
2	7216	7281	7285	7261	39

Table D.68 showing the raw data for 100% NFC SULP substrate for vertical wicking using blood simulant as a wicking liquid.

Distance (cm)	Time (s) Run 1	Run 2	Run 3	Average (s)	Standard deviation (s)
0	0	0	0	0	0
1	10250	10212	10297	10253	43
2	51360	51355	51470	51395	65
3	91721	91767	91815	91768	47
4	154625	154594	154744	154654	79

D 3.2.2 Unbleached Kraft

Table D.69 showing the raw data for 20% NFC UBK substrate for vertical wicking using dye as a wicking liquid.

Distance (cm)	Time (s) Run 1	Run 2	Run 3	Average (s)	Standard deviation (s)
0	0	0	0	0	0
1	157	164	155	159	5
2	494	506	487	496	10
3	1176	1215	1164	1185	27
4	1868	1964	1886	1906	51
5	2907	2977	2841	2908	68
6	3805	3964	3627	3799	169
7	4822	4997	4775	4865	117
8	6191	6235	5932	6119	164
9	8601	8714	8766	8694	84
10	12817	12947	12812	12859	77

Table D.70 showing the raw data for 20% NFC UBK substrate for vertical wicking using blood simulant as a wicking liquid.

Distance (cm)	Time (s)			Average (s)	Standard deviation (s)
	Run 1	Run 2	Run 3		
0	0	0	0	0	0
1	982	997	978	986	10
2	3303	3390	3275	3323	60
3	6681	6728	6576	6662	78
4	12555	12614	12501	12557	57
5	17472	17509	17332	17438	93

Table D.71 showing the raw data for 50% NFC UBK substrate for vertical wicking using dye as a wicking liquid.

Distance (cm)	Time (s)			Average (s)	Standard deviation (s)
	Run 1	Run 2	Run 3		
0	0	0	0	0	0
1	1046	1254	1206	1169	109
2	2721	3089	2914	2908	184
3	5306	5681	5569	5519	193
4	9414	9710	9701	9608	168
5	15930	16212	15856	15999	188

Table D.72 showing the raw data for 50% NFC UBK substrate for vertical wicking using blood simulant as a wicking liquid.

Distance (cm)	Time (s) Run 1	Run 2	Run 3	Average (s)	Standard deviation (s)
0	0	0	0	0	0
1	2599	2615	2633	2616	17
2	10551	10567	10608	10575	29
3	24691	24718	24759	24723	34
4	42937	43019	43096	43017	80
5	61225	61281	61310	61272	43
6	87126	87192	87282	87200	78
7	128883	128919	129018	128940	70
8	163539	163612	163682	163611	72

Table D.73 showing the raw data for 100% NFC UBK substrate for vertical wicking using dye as a wicking liquid.

Distance (cm)	Time (s) Run 1	Run 2	Run 3	Average (s)	Standard deviation (s)
0	0	0	0	0	0
1	11309	11192	11358	11286	85

Table D.74 showing the raw data for 100% NFC UBK substrate for vertical wicking using blood simulant as a wicking liquid.

Distance (cm)	Time (s) Run 1	Run 2	Run 3	Average (s)	Standard deviation (s)
0	0	0	0	0	0
1	206669	206443	206577	206563	114

D 3.2.3 Chromatography No.1 Filter Paper

Table D.75 showing the raw data for 20% NFC CHR substrate for vertical wicking using dye as a wicking liquid.

Distance (cm)	Time (s) Run 1	Run 2	Run 3	Average (s)	Standard deviation (s)
0	0	0	0	0	0
1	67	65	64	65	2
2	321	311	315	316	5
3	640	612	622	625	14
4	1125	1064	1103	1097	31
5	1662	1574	1590	1609	47
6	2232	2195	2213	2213	19
7	2983	2880	2928	2930	52
8	4060	3996	4009	4022	34
9	5657	5447	5552	5552	105
10	7383	7200	7295	7293	92

Table D.76 showing the raw data for 20% NFC CHR substrate for vertical wicking using blood simulant as a wicking liquid.

Distance (cm)	Time (s) Run 1	Run 2	Run 3	Average (s)	Standard deviation (s)
0	0	0	0	0	0
1	824	818	824	822	3
2	2367	2332	2376	2358	23
3	5651	5617	5632	5633	17
4	9133	9087	9193	9138	53
5	13987	13919	14010	13972	47

Table D.77 showing the raw data for 50% NFC CHR substrate for vertical wicking using dye as a wicking liquid.

Distance (cm)	Time (s) Run 1	Run 2	Run 3	Average (s)	Standard deviation (s)
0	0	0	0	0	0
1	173	162	172	169	6
2	744	721	743	736	13
3	1705	1668	1694	1689	19
4	2838	2812	2850	2833	19
5	4467	4406	4488	4454	43

Table D.78 showing the raw data for 50% NFC CHR substrate for vertical wicking using blood simulant as a wicking liquid.

Distance (cm)	Time (s) Run 1	Run 2	Run 3	Average (s)	Standard deviation (s)
0	0	0	0	0	0
1	3580	3410	3666	3552	130
2	12668	12473	12960	12700	245

Table D.79 showing the raw data for 100% NFC CHR substrate for vertical wicking using dye as a wicking liquid.

Distance (cm)	Time (s) Run 1	Run 2	Run 3	Average (s)	Standard deviation (s)
0	0	0	0	0	0
1	11288	11311	11207	11269	55

Table D.80 showing the raw data for 100% NFC CHR substrate for vertical wicking using blood simulant as a wicking liquid.

Distance (cm)	Time (s) Run 1	Run 2	Run 3	Average (s)	Standard deviation (s)
0	0	0	0	0	0
1	6405	6358	6393	6385	24
2	51217	51073	51199	51163	78
3	104887	104715	104857	104820	92

D 3.2.4 Chromatography 3MM Filter Paper

Table D.81 showing the raw data for 20% NFC CHR3 substrate for vertical wicking using dye as a wicking liquid.

Distance (cm)	Time (s) Run 1	Run 2	Run 3	Average (s)	Standard deviation (s)
0	0	0	0	0	0
1	97	107	108	104	6
2	338	360	362	353	13
3	781	794	799	791	9
4	1335	1387	1370	1364	27
5	1942	2004	1988	1978	32
6	2716	2854	2805	2792	70
7	3677	3790	3715	3727	58
8	4609	4782	4693	4695	87
9	5936	5989	5966	5964	27
10	7625	7688	7679	7664	34

Table D.82 showing the raw data for 20% NFC CHR3 substrate for vertical wicking using blood simulant as a wicking liquid.

Distance (cm)	Time (s) Run 1	Run 2	Run 3	Average (s)	Standard deviation (s)
0	0	0	0	0	0
1	997	995	1015	1002	11
2	3431	3398	3455	3428	29
3	6947	6905	7023	6958	60
4	11447	11427	11525	11466	52
5	15771	15772	15803	15782	18

Table D.83 showing the raw data for 50% NFC CHR3 substrate for vertical wicking using dye as a wicking liquid.

Distance (cm)	Time (s) Run 1	Run 2	Run 3	Average (s)	Standard deviation (s)
0	0	0	0	0	0
1	438	490	412	447	40
2	1413	1503	1387	1434	61

Table D.84 showing the raw data for 50% NFC CHR3 substrate for vertical wicking using blood simulant as a wicking liquid.

Distance (cm)	Time (s) Run 1	Run 2	Run 3	Average (s)	Standard deviation (s)
0	0	0	0	0	0
1	5997	6213	5714	5975	250
2	19354	19830	19521	19568	242

Table D.85 showing the raw data for 100% NFC CHR3 substrate for vertical wicking using dye as a wicking liquid.

Distance (cm)	Time (s) Run 1	Run 2	Run 3	Average (s)	Standard deviation (s)
0	0	0	0	0	0
1	1237	1215	1212	1221	14
2	5333	5374	5303	5337	36
3	11768	11693	11661	11707	55

Table D.86 showing the raw data for 100% NFC CHR3 substrate for vertical wicking using blood simulant as a wicking liquid.

Distance (cm)	Time (s) Run 1	Run 2	Run 3	Average (s)	Standard deviation (s)
0	0	0	0	0	0
1	10546	10568	10641	10585	50
2	53591	53607	53685	53628	50

D 3.2.5 Recycled

Table D.87 showing the raw data for 20% NFC REC substrate for vertical wicking using dye as a wicking liquid.

Distance (cm)	Time (s) Run 1	Run 2	Run 3	Average (s)	Standard deviation (s)
0	0	0	0	0	0
1	3448	3502	3432	3461	37
2	6520	6604	6541	6555	44

Table D.88 showing the raw data for 20% NFC REC substrate for vertical wicking using blood simulant as a wicking liquid.

Distance (cm)	Time (s) Run 1	Run 2	Run 3	Average (s)	Standard deviation (s)
0	0	0	0	0	0
1	3140	3155	3070	3122	45
2	10245	10194	10111	10183	68
3	17737	17816	17621	17725	98

Table D.89 showing the raw data for 50% NFC REC substrate for vertical wicking using dye as a wicking liquid.

Distance (cm)	Time (s) Run 1	Run 2	Run 3	Average (s)	Standard deviation (s)
0	0	0	0	0	0
1	4273	4181	4122	4192	76
2	9638	9556	9533	9576	55
3	16946	16804	16843	16864	73

Table D.90 showing the raw data for 50% NFC REC substrate for vertical wicking using blood simulant as a wicking liquid.

Distance (cm)	Time (s) Run 1	Run 2	Run 3	Average (s)	Standard deviation (s)
0	0	0	0	0	0
1	2482	2468	2492	2481	12
2	10113	10109	10191	10138	46
3	24470	24425	24517	24471	46
4	42454	42422	42576	42484	81
5	64498	64405	64506	64470	56
6	95569	95508	95650	95576	71

Table D.91 showing the raw data for 100% NFC REC substrate for vertical wicking using dye as a wicking liquid.

Distance (cm)	Time (s) Run 1	Run 2	Run 3	Average (s)	Standard deviation (s)
0	0	0	0	0	0
1	2862	2715	2836	2804	78
2	12017	11886	12042	11982	84

Table D.92 showing the raw data for 100% NFC REC substrate for vertical wicking using blood simulant as a wicking liquid.

Distance (cm)	Time (s) Run 1	Run 2	Run 3	Average (s)	Standard deviation (s)
0	0	0	0	0	0
1	9355	9361	9417	9378	34
2	57720	57732	57839	57764	66

D.4 Conclusion

This appendix supports Chapter 6 and contains the relevant raw data obtained from wicking experiments. Statistical elements, such as the average and standard deviation were calculated and presented together with the raw data.

APPENDIX E: TAPPSA CONFERENCE POSTER PRESENTATION

The TAPPSA Conference took place in September 2016. The preliminary results from this study were presented. The poster can be seen below.

Evaluation of paper substrates for microfluidic application in medical diagnostic kits

Revesa Moodley[1, 2], Bruce Sithole[1, 2], Jerome Andrew[1], Werner van Zyl[3]
[1]University of KwaZulu-Natal/CSIR Natural Resources and the Environment: Forestry and Forest Products Research Centre
[2]Discipline of Chemical Engineering, University of KwaZulu-Natal
[3]School of Chemistry and Physics, University of KwaZulu-Natal
Email: bsithole@csir.co.za

1. BACKGROUND

Millions of people worldwide die from preventable diseases each year. Accurate diagnosis is of utmost importance for proper and effective treatment of diseases. However, currently produced diagnostic technologies which are successful in developed countries are often not well suited to developing countries, due to high costs as well as the need for trained personnel for correct diagnosis. Paper-based microfluidic analytical devices provide a disposable, simple and low-cost alternative to existing diagnostic technologies, which is advantageous in developing countries with minimal healthcare resources. Paper is considered an appropriate substrate for application in microfluidic system due to (i) its wide availability; (ii) knowledge on paper analytical techniques is extensive and can be applied; and (iii) its ability to wick aqueous fluids without the need for external forces [1]. Patterning of the paper into microfluidic hydrophilic channels and hydrophobic barriers allows the transportation of liquids in a controlled manner. Recent studies in the biomedical field have shown the use of paper in microfluidic analytical devices. However, no studies have been undertaken to ascertain what type(s) of paper substrates are ideal for such microfluidic applications. This study will be conducted to determine the feasibility of using different paper substrates for implementation in microfluidic analytical devices, as compared to currently used material such as glass, silicone, and other polymers or plastics. The current work focuses on the wickability of the paper substrates.

2. METHODOLOGY

2.1 Paper substrates

Handsheets were produced using the Rapid-Köthen Sheet Machine from various pulp types, these being: sulphite, kraft, thermo-mechanical and recycled pulp. The recycled pulp was bleached before handsheet making use of a 3 stage bleaching process of PYP (hydrogen peroxide, sodium hydrosulfite and hydrogen peroxide). Seven paper substrates were used for experimentation, these being:

- Sulphite pulp handsheet
- Kraft pulp handsheet
- Thermo-mechanical pulp handsheet
- Recycled pulp handsheet
- Whatman No. 1 Chromatography Paper (CHR No. 1)
- Whatman 3MM Chromatography Paper (CHR 3MM)
- Whatman Glass microfiber GF/D Filters

Figure 1: Rapid-Köthen Sheet Former

2.2 Wicking tests

Vertical and horizontal wicking tests were conducted on the paper substrates, using yellow food dye and a glycerol – water mixture as wicking liquids.
Wicking tests were conducted by dipping the paper substrate in a reservoir of wicking liquid. Time was recorded for every 1 cm of liquid wicked. The food dye was used to simulate bodily fluids with a viscosity similar to that of water, i.e. tears, saliva and urine. A mixture of glycerol and water, in a ratio of 52:48, was used to simulate blood (in terms of viscosity). Triplicate experiments were done for each substrate for horizontal and vertical wicking tests.

2.3 Thin-Layer Chromatography

TLC experiments were conducted using the wicking liquids. Yellow food dye and glycerol – water mixture were used as the spotting materials. After trial and error, solvent systems of ammonia - isopropanol at a ratio of 63:37 and butanol – water at a ratio of 83:17 were chosen. The Rf values were determined using the ratio of distance travelled by the spot to the distance travelled by the solvent. The experiment was conducted in triplicate for each substrate.

3. RESULTS

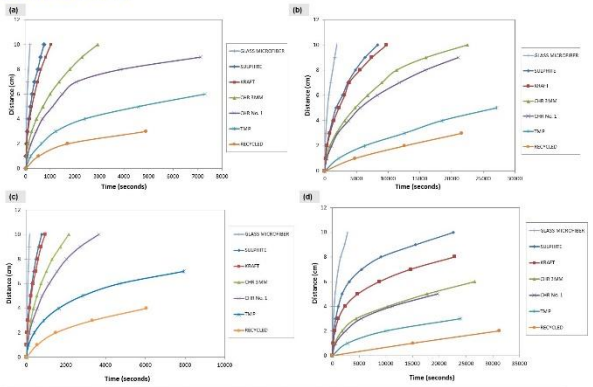

Figure 2 (a): Vertical wicking for different paper substrates using yellow food dye
Figure 2 (b): Vertical wicking for different paper substrates using glycerol mixture
Figure 2 (c): Horizontal wicking for different paper substrates using yellow food dye
Figure 2 (d): Horizontal wicking for different paper substrates using glycerol mixture

From the distance-time graphs above (**Figures 2a-d**), it can be seen that vertical and horizontal wicking follows the same trend for both liquids, with regard to the order of substrates from fastest to slowest wicking times. The food dye wicked the fastest in the glass microfiber filters due to its high porosity. Sulphite and kraft handsheets had similar wicking times, followed by CHR 3MM, CHR No. 1 and TMP. Recycled handsheets wicked the slowest. This could be attributed to the fact that recycled pulp contains lignin and other contaminants, such as ash and inks, which retards the motion of liquids through the paper. The glycerol mixture followed the same trends; however, the time for the liquid to wick was much longer due to its high viscosity.

Table 1 Results from TLC using yellow food dye as spotting material

Substrate	*Rf Value*
Glass microfiber	1
Recycled	0.846
Kraft	0.758
CHR No. 1	0.725
Sulphite	0.678
TMP	0.588
CHR 3MM	0.444

Table 2 Results from TLC using glycerol mixture as spotting material

Substrate	*Rf Value*
Glass microfiber	0.89
CHR No. 1	0.883
TMP	0.564
Kraft	0.458
Sulphite	0.398
Recycled	0.397
CHR 3MM	0.24

TLC was conducted to determine the wickability of the paper substrate with respect to the spotting material. The TLC results for food dye, using ammonia and isopropanol solvent system, from **Table 1**, showed that glass microfiber had the highest Rf value, followed by recycled, kraft and CHR No. 1. TMP and CHR 3MM had the lowest Rf values. **Table 2** shows the results from the TLC for the blood simulant, using a butanol – water system. The glass microfiber filter had the highest Rf value followed closely by CHR No. 1. The other substrates had significantly lower Rf values in comparison, these being TMP, kraft, sulphite, recycled and CHR 3MM.

4. REFERENCES

[1] MARTINEZ, A.W., PHILLIPS, S.T., NIE, Z., CHENG, C., CARRILHO, E., WILEY, B.J. & WHITESIDES, G.M., 2010. Programmable diagnostic devices made from paper and tape. *Lab on a Chip,* **10**(19), pp. 2499-2504.

Acknowledgments

The authors would like to thank NRF for financial assistance during this project.